COMPARISON OF DOUBLY-FED INDUCTION GENERATOR AND BRUSHLESS DOUBLY-FED RELUCTANCE GENERATOR FOR WIND ENERGY APPLICATIONS

Wenjun Chen

A thesis submitted for the degree of

Philosophy Doctorate

June 2014

Newcastle University

School of Electrical & Electronic Engineering

ABSTRACT

The Doubly-fed Induction Generator (DFIG) is the dominant technology for variable-speed wind power generation due in part to its cost-effective partially-rated power converter.

However, the maintenance requirements and potential failure of brushes and slip rings is a significant disadvantage of DFIG. This has led to increased interest in brushless doubly-fed generators. In this thesis a Brushless Doubly-Fed Reluctance Generator (BDFRG) is compared with DFIG from a control performance point of view.

To compare the performance of the two generators a flexible 7.5kW test facility has been constructed. Initially, a classical cascade vector controller is applied to both generators. This controller is based on the stator voltage field orientation method with an inner rotor (secondary stator) current control loop and an outer active and reactive power control loop. The dynamic and steady state performance of two generators are examined experimentally. The results confirm that the BDFRG has a slower dynamic response when compared to the DFIG due to the larger and variable inductance.

Finally a sensorless Direct Power Control (DPC) scheme is applied to both the DFIG and BDFRG. The performance of this scheme is demonstrated with both simulation and experimental results.

TABLE OF CONTENTS

ACKNOWLEDGEMENTS

The author would like to thank the Engineering and Physical Sciences Research Council (EPSRC) and Overseas Researcher Scholarship (ORS) for their financial support.

I would like to give special thanks to Northumbria University (UK), Shenyang University of Technology (China) and Scottish-Southern Energy Group (UK) for their contrbution of this collaborative project.

Thanks go of course to my supervisor, Dave Atkinson and Bashar Zahawi, for their guidance and encourangement. Special thanks are given to Dave due to his work of designing the DSP control board interface.

I must also acknowledge the support of Darren for his work of making the control board and initial test, Wu Hao and Hamza for all their efforts in building and testing the test rigs. Special thanks go to Min Zhang and Steven Hong for their patience of helping me with C Code Studio utilization and sharing their experience of C programme with me. The acknowledgements are also given to Yutana, who provide advice and information on DFIG experments to me.

I would like to thank the administrative and IT-support staff in the department, the whole technical support team, in particular the technicians in both Newcastle University and Northumbria University lab for their assistances for the safety and health. Thanks are due to given to all the friends in the labs and schools, for making life easier and more colourful.

GLOSSARY AND SYMBOLS

Glossary and commonly used acronyms

BDFRG	Brushless Doubly-Fed Reluctance Generator
Crowbar	Rotor-windings temporary short-circuit device.
DC-brake	DC-link power sink
DC-Link	DC connection of the back-back DFIG power converter arrangement
DFIG	Doubly Fed Induction Generator
DSP	Digital Signal Processor
emf	Electromagnetic Force
EMI	Electromagnetic Interference
FRT	(Grid) Fault Ride Through
GSC	DFIG/BDFRG Grid-side Converter =DFIG/BDFRG Line-side Converter
GTO	Gate Turn-Off
IGBT	Insulated Gate Bipolar Transistor
I/O	Input and output interface
LC	Inductor-capacitor filter
LCL	Inductor-capacitor-inductor (‘T’-shaped) filter
LSC	DFIG/BDFRG Line-side Converter
MMF	Magneto-Motive Force
PI	Proportional-Integral (Controller)
PIC	Programmable Interrupt Controller
PLL	Phase Locked Loop
PM	Permanent Magnet
p.u.	per-unit(s)
PWM	Pulse Width Modulation
RFI	Radio Frequency Interference
rms	root-mean-square average value

RSC	DFIG/BDFRG Rotor-side Converter
SFIG	Singly-Fed Induction Generator (shorted rotor)
UPS	Uninterruptible Power Supply
Variac	Variable auto-transformer
VPLL	Space-Vector based PLL
VSC	Voltage-Source Converter
WT	Wind Turbine

Labelling of space vectors

Space Vector $\overrightarrow{u_b^a}$

Reference Frame

Circuit Reference

Space vector of Variables $\boldsymbol{u}$ on circuit $\boldsymbol{b}$ measured in the reference frame $\boldsymbol{a}$

Space vector component u_{bd}^a u_{bda}

Direct or Quadrature axis component

Direct-axis, $\boldsymbol{d}$, or Quadrature-axis, $\boldsymbol{q}$, component of space vector of Variables $\boldsymbol{u}$ on circuit $\boldsymbol{b}$ measured in the reference frame $\boldsymbol{a}$

Superscripts (reference frames)

s	DFIG stationary reference frame with respect to the stator circuit
r	DFIG stationary reference frame with respect to the rotor circuit
p	BDFRG stationary reference frame with respect to the primary circuit
c	BDFRG stationary reference frame with respect to the secondary circuit

e excitation reference frame, aligned with stator (DFIG) or primary (BDFRG) voltage

g general reference frame

Other Superscripts

⊗ controller reference quantity

$*$ complex conjugate

Subscripts

0 initial conditions, i.e. the state of the variable at time zero

0 zero sequence component

1 positive sequence component

2 negative sequence component

σ leakage quantity

mag, μ magnetising quantity

a, b, c electrical phases in three-phase system

d d-axis or ‘direct-axis’ quantity: aligned with the orthogonal ref. frame

q q-axis quantity: aligned in quadrature with the direct axis of the same reference frame

s DFIG stator circuit quantity

r DFIG rotor circuit quantity

l DFIG/BDFRG line-side converter circuit quantity

p BDFRG primary circuit quantity

c BDFRG secondary circuit quantity

BC DC-link brake-chopper quantity

cb rotor crowbar-circuit quantity

ref a controller reference value

ph a phase quantity

ph-ph a phase to phase quantity

L-L a line to line quantity

L	mechanically the low-speed (hub) side of the turbine gearbox
m	mechanically the high-speed (generator) side of the turbine gearbox

Symbols

Electrical Variables

DFIG Variables

$\overrightarrow{u_s^e}$	space vector of stator voltage viewed in the excitation reference frame
u_{sa}, u_{sb}, u_{sc}	phase *a, b* and *c* instantaneous stator voltages
u_{sd}^e, u_{sq}^e	d-q components of stator voltage viewed in the excitation frame
$\overrightarrow{u_r^e}$	space vector of rotor voltage viewed in the excitation reference frame
u_{ra}, u_{rb}, u_{rc}	phase *a, b* and *c* instantaneous rotor voltages
u_{rd}^e, u_{rq}^e	d-q components of rotor voltage viewed in the excitation frame
$\overrightarrow{i_s^e}$	space vector of stator current viewed in the excitation reference frame
i_{sa}, i_{sb}, i_{sc}	phase *a, b* and *c* instantaneous stator currents
i_{sd}^e, i_{sq}^e	d-q components of stator current viewed in the excitation frame
$\overrightarrow{i_r^e}$	space vector of rotor current viewed in the excitation reference frame
i_{ra}, i_{rb}, i_{rc}	phase *a, b* and *c* instantaneous rotor currents
i_{rd}^e, i_{rq}^e	d-q components of rotor current viewed in the excitation frame

BDFRG Variables

$\overrightarrow{u_p^e}$ space vector of primary stator voltage viewed in the excitation reference frame

u_{pa}, u_{pb}, u_{pc} phase *a, b* and *c* instantaneous primary stator voltages

u_{pd}^e, u_{pq}^e d-q components of primary stator voltage viewed in the excitation frame

$\overrightarrow{u_c^e}$ space vector of secondary stator voltage viewed in the excitation reference frame

u_{ca}, u_{cb}, u_{cc} phase *a, b* and *c* instantaneous secondary stator voltages

u_{cd}^e, u_{cq}^e d-q components of secondary stator voltage viewed in the excitation frame

$\overrightarrow{i_p^e}$ space vector of primary stator current viewed in the excitation reference frame

i_{pa}, i_{pb}, i_{pc} phase *a, b* and *c* instantaneous primary stator currents

i_{pd}^e, i_{pq}^e d-q components of primary stator current viewed in the excitation frame

$\overrightarrow{i_c^e}$ space vector of secondary stator current viewed in the excitation reference frame

i_{ca}, i_{cb}, i_{cc} phase *a, b* and *c* instantaneous secondary stator currents

i_{cd}^{e}, i_{cq}^{e} d-q components of secondary stator current viewed in the excitation frame

The superscript and subscript of voltages, currents and other variables could be replaced, thus any space vector and three-phase quantity can be represented in any combination of reference frame and electrical circuit or axis. The examples are given in 'labelling of space vectors' above. From here onwards, therefore, only the single example of each parameter is generally given. Certain stator, rotor or primary, secondary stator parameters are repeated or permuted, and would be never reaffirmed.

$\overrightarrow{\varphi_s^e}$ space vector of stator flux linkage viewed in the excitation frame

$\overrightarrow{u_{s0}^e}, \overrightarrow{i_{s0}^e}, \overrightarrow{\varphi_{s0}^e}$ initial conditions of stator voltage, current, flux linkage viewed in the rotor frame

$\overrightarrow{\Theta_r^e}$ space vector of rotor MMF viewed in the excitation frame

$\overrightarrow{B_r^e}$ space vector of rotor magnetic flux density in the excitation frame

$\overrightarrow{H_r^e}$ space vector of rotor magnetic field strength in the excitation frame

V_{dc} DC-link voltage

Frequency speed and angle

f frequency

f_0 frequency of electrical system, normally 50Hz

f_s Stator side frequency of DFIG in Hz;

f_r Rotor side frequency of DFIG in Hz;

f_{slip} Slip Frequency of DFIG in Hz;

f_m Mechanical Rotor Frequency of DFIG in Hz;

t time elapsed

Ω_r mechanical angular frequency of rotor in mechanical rad/s

ω angular frequency

ω_r angular frequency of DFIG rotor in electrical rad/s

ω_s angular frequency of DFIG stator in elec. rad/s

ω_e, angular frequency of the excitation reference frame in elec. rad/s

ω_χ relative rotor frequency from the excitation reference frame in elec. rad/s

ω_{slip} slip frequency from the excitation reference frame in elec. rad/s, negative of ω_χ

N_m Mechanical Rotor Speed in 1/min;

N_{syn} Synchronous Speed in 1/min;

θ angle

θ_r angle of the rotor frame with respect to the stationary

θ_e angle of the excitation frame with respect to the stationary

θ_χ angle of the rotor frame with respect to the excitation frame

θ_{slip} slip angle, negative of θ_{χ}

θ_{r0} initial angle of the rotor frame (at time zero).

θ_{e0} initial angle of the excitation frame.

$\theta_{\chi 0}$ initial angle of the rotor frame with respect to the excitation frame.

θ_{slip0} initial slip angle.

Machine and circuit parameters

a effective turns ratio, stator:rotor

a_1 effective turns ratio of DFIG, stator:rotor

a_2 effective turns ratio of BDFRG, primary stator:secondary stator

N_s effective number of DFIG stator winding coils per phase

N_r effective number of DFIG rotor winding coils per phase

N_p effective number of BDFRG primary stator winding coils per phase

N_c effective number of BDFRG secondary stator winding coils per phase

p_A magnetic pole pair number

p_{A1} DFIG magnetic pole pair number

p_{A2} BDFRG magnetic pole pair number

s slip

s_1 DFIG's slip

s_2	BDFRG's slip
R	resistance
R_s, R_r	per-phase resistance of DFIG respective winding
R_p, R_c	per-phase resistance of BDFRG respective winding
Z	impedance
C	capacitance
X	reactance
L	inductance
L_s, L_r	per-phase inductance of DFIG respective winding
L_p, L_c	per-phase inductance of BDFRG respective winding
L_{es}, L_{er}	per-phase leakage inductance of DFIG respective winding
L_{ep}, L_{ec}	per-phase leakage inductance of BDFRG respective winding
L_{m1}	per-phase mutual inductance of DFIG
L_{m2}	per-phase mutual inductance of BDFRG
${L_s}', {L_r}'$	operational inductance of DFIG respective winding
${L_p}', {L_c}'$	operational inductance of BDFRG respective winding
k_s	ratio of DFIG mutual / stator inductance p.u. values
k_r	ratio of DFIG mutual / rotor inductance p.u. values

k_p ratio of BDFRG mutual / primary stator inductance p.u. values

k_c ratio of BDFRG mutual / secondary stator inductance p.u. values

σ dimensionless machine leakage factor

τ_s, τ_r transient time constant of respective circuit

τ_s', τ_r' effective transient time constant of respective circuit

τ_T torque transient time constant

τ_{cb} crowbar application period

ς_f complex frequency adjustment factor

κ timescale adjustment factor

δ frequency adjustment factor

$\Re$ magnetic reluctance

μ_0 permeability of free space

Space

A area

h average width of the rotating machine's airgap

l length

r radius

Power and Torque

E energy

F force

T torque

T_L load torque

T_m Mechanical torque applying to the rotor;

T_e Electromagnetic torque applying to the rotor by the generator;

P power

P_m mechanical power

P_s, P_r DFIG active power of electrical machine stator / rotor

P_{grid} Grid Power;

Q_s, Q_r DFIG reactive power of electrical machine stator / rotor

Q_{sr} Sum of Reactive Power;

Q_{grid} Reactive power flowing into the grid;

Q_g Reactive power flowing from the grid-side converter into the grid;

S_s, S_r DFIG apparent power of electrical machine stator / rotor

P_p, P_c BDFRG active power of electrical machine primary stator / secondary stator

Q_p, Q_c BDFRG reactive power of electrical machine primary stator / secondary

stator

S_p, S_c BDFRG apparent power of electrical machine primary stator / secondary stator

Mecahnical

B mechanical friction coefficient

D mechanical damping coefficient

K mechanical shaft stiffness

J mechanical moment of inertia

Feedback Control

$1/s$ integration operator

$PI(x)$ PI feedback control performed on the error feedback of 'x'

k_p, k_i proportional & integral control constants

m_a, m_b, m_c modulation signal for PWM generation

m_i modulation index

Mathematical artifices (for DFIG fault analysis)

A, B, C general-use coefficients

$f(x)$ general function of 'x'

x general variable

i, j imaginary number operator, +90° phase shift in a complex plane

A_s^s stator-circuit natural fault response coefficient in the stator frame

A_r^r rotor-circuit natural fault response coefficient in the rotor frame

A_1^s, B_1^s stator flux linkage fault response solution coefficients in the stator frame

A_2^r, B_2^r rotor flux linkage fault response solution coefficients in the rotor frame

$k_x(u)$ a derived coefficient: a function of the voltage u

k_σ derived leakage factor, a combination of σ, τ_s, τ_r

α, β complex roots of the induction machine natural fault response (in stator frame unless otherwise notated)

ρ_s, ρ_r complex factors of stator and rotor flux linkage equations

$\Gamma\{f(t)\}$ Laplace transform operation

$F(v)$ Laplace transform (denoted by capitalisation of the variable)

v Laplace variable

$\frac{d}{dt}$ time differential operator

Vectors

Vector definition

Space vector: $\overrightarrow{u_b^a} = u_{bd}^a + j u_{bq}^a$

Complex conjugate $\overrightarrow{u_b^a}^* = u_{bd}^a - j u_{bq}^a$

Reference frame example

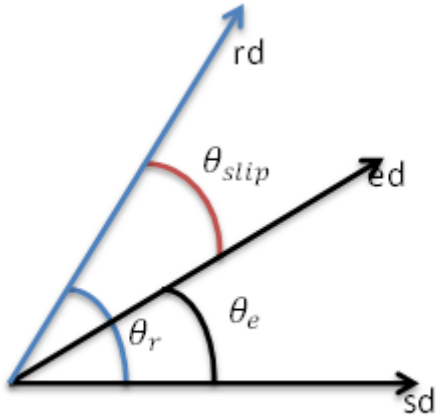

Figure i. Direct or ‘d’ axes of commonly used reference frames.

Normally, there are three reference frames, stationary, excitation and rotor reference frames, commonly used in the machine circuit analysis. Their direct axes’ relationships are shown in Figure 1.1. The relative quadrature axis is defined as $90°$ ahead of the d axis. The velocities for these three frames canbe defined as below:

$\omega_e = \frac{d\theta_e}{dt}$ Excitation frame angular velocity with respect to the stator frame.

$\omega_r = \frac{d\theta_r}{dt}$ Rotor frame angular velocity with respect to the stator frame

The rotor would rotate at the electrical rotor frequency. Compared to the mechanical rotation, the electrical rotor frequency would accomplish a 2π radian in each magnetic pole pair. Thus the relationship between the mechanical speed and electrical speed are denoted as $\omega_r = p_A \Omega_r$.

As told above, the parameters measured in different reference frames are distinguished by their superscripts. Then the transformation of different reference frames can be inferred by an appropriate angle. Take the voltage vector as an example, the transformations of the vector measured in stator (s), rotor (r) and excitation (e) frame can be deduced by:

$$\overrightarrow{u^s} = \overrightarrow{u^e} exp(j\theta_e) \qquad (i)$$

$$\overrightarrow{u^r} = \overrightarrow{u^e} exp\left(j\theta_{slip}\right) = \overrightarrow{u^e} exp(j\{\theta_e - \theta_r\}) \qquad (ii)$$

1. Introduction

1.1. The comparison of DFIG and BDFRG

1.1.1. Background

Due to the increasing price of the oil and the environmental impact, governments all over the world have made many great efforts to exploit renewable energies, for example, solar energy, wind power and hydro-electric power [1]. With improved techniques, reduced cost and environmental pollution, wind energy has undergone a remarkable improvement over the last two decades, developing from a fringe science in the *1970s* to flourish and industrialization. The production of wind turbines has grown in size from *20kW* to *5MW* [2], and in some cases even up to *10MW* class. So far, a rate of annual growth of worldwide wind power has reached approximately *25%* [3]. Germany is a case in point as the most significant user of wind energy in Europe today. Approximately *18.427GW* in operation contrasting with scarcely any wind power ten years ago shows a large transformation of energy structure. In Denmark, more than *15%* of electrical energy of country is now supplied by *3GW* of wind power [4]. It seems that wind power has played a significant role in the world's energy and will continue this action.

1.1.1.1. Wind generation development

The wind generators have gone through several generations. In the early stage of wind power developments, most wind turbines were equipped with the low-power squirrel-cage induction machine, with one side connected to the fixed-ratio gearbox and the other side directly coupled with the three phase grid [5]. This generator basically operates close to a constant synchronous speed through pole-adjustable winding configurations [6]. However, this fix-speed generator is found to be largely affected by the characteristics of mechanical sub-systems, for example, the pitch control time constants and main breaker maximum switching rate etc [5]. The

response time of mechanical drive train leads to a fast and strong variation of electrical output power when the blade is hit by the gust. Two results appear. One is the rather low efficiency for most wind speeds. The other is fairly expensive mechanical structure, especially at the full-rated power. A stiff power grid is required due to the stable operation under variation loads and a sturdy mechanical construction is designed for the absorption of high mechanical stress [5]. The low efficiency and high cost of this system motivated the development of the adjustable speed turbine.

The adjustable-speed generator emerged with improved performance. A so-called ‘elasticity’ is created by the absorbed energy in mechanical inertia which not only leads to the reduction of torque pulsation but also eliminates the electrical power variations [6]. The mechanical loads and stresses are reduced due to the lower variation of torque caused by the ‘elasticity’ and the power quality is improved because of lower fluctuation of output power [5][6]. Besides, the system efficiency is much higher and the cost of electricity is lower compared to the fixed speed generators, since the speed can be adjusted to maximize power capture and the cheaper structure is designed due to less variation under stead-state operation [5]. Additionally, owing to the longer time constant and less control complexity allowed in speed control, simple pitch control can be employed. What is more, other benefits of variable-speed generators are demonstrated in numerous aspects: reduction of acoustic noise and island-operation capability etc [5].

Nowadays, Permanent Magnet Generator (PMG) and Doubly-Fed Induction Generator (DFIG) have the best prospects due to their improved performance. However, compared to the large-volume, high-weigh and expensive PMG, DFIG has better cost performance. The comparison of Permanent Magnet Generator (PMG) and DFIG will be introduced below.

1.1.1.2. Comparison of DFIG and PMG

The DFIGs and PMGs play the major roles in modern wind energy industry. Both generators have the same features as the wind generators:

①. A large wind turbine is needed in order to capture large wind power
②. The wind speed and direction are variable and cannot be controlled
③. Variable speed constant frequency (VSCF) technology is usually needed for the wind power generation system

But DFIG and PMG have two ways to achieve VSCF as graphically demonstrated in Figure 1.1. DFIG uses the variable frequency excitation current. For a DFIG, an AC/DC/AC converter will be connected with rotor and be controlled to produce the frequency f_2 as shown in the left graph of Figure 1.1. The constant frequency f_1 equals to $\frac{p_A n}{60} \mp f_2$. However, PMG uses AC/DC/AC power converter to change the output power from variable frequency f_v to constant frequency f_c. Thus DFIG VSCF achievement is more difficult than PMG. Additionally, as f_2 is a fraction of f_1, the power capacity of DFIG's converter is a fraction of generator's, typically requiring a *25%*-rated converter. However, PMG's AC/DC/AC converter is a fully-rated power converter. Conclusively the two VSCF generator systems bring about the lower cost but with more difficult VSCF achievement of DFIG compared to the PMG.

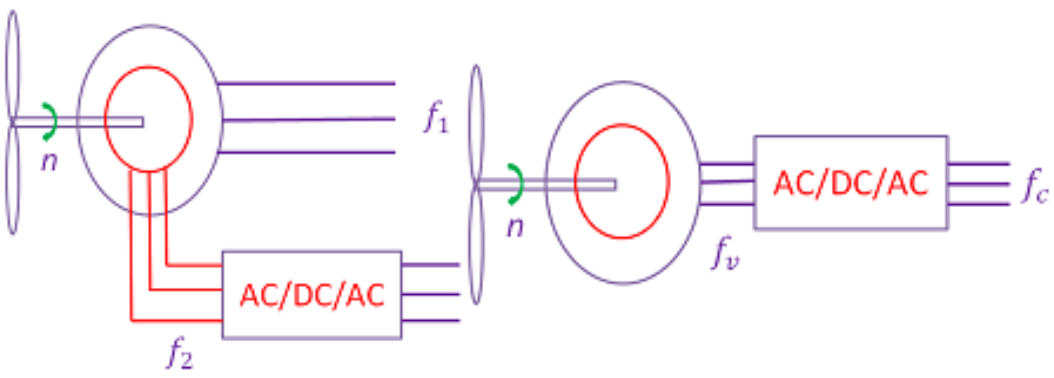

Figure 1.1 (left) DFIG VSCF (right) PMG VSCF

Table 1.1 compares the DFIG and PMG advantages and disadvantages. It is clear that the reliability and VSCF complications can be overcome by adding the appropriate controller or protection scheme. But the cost of PMG is of concern after the Chinese government increases the price of the rare-earth permanent magnet materials.

	DFIG	PMG
Advantages	• Small size • Low cost • Cheaper power converter	• High reliability and performance • Easier VSCF achievement
Drawbacks	• Poor reliability • Complicated VSCF achievements	• Large size • High cost • Expensive power converter

Table 1.1 The advantages and drawbacks comparison of DFIG and PMG

China once owned *80%* of the known rare earth metal ore deposits in the world. But following the numerous export and utilization of the rare-earth permanent magnet materials, the storage of the rare-earth materials drops remarkably to *30%*. As a result, the Chinese government applies the several times price increase and exportation restriction. As the largest exporter of permanent magnet materials, Chinese policy causes the significant price raise of rare-earth permanent magnet, and indirectly results in the less utilization of PMG. That is the reason why this research focuses on DFIG.

However, the maintenance requirements and potential failure of the brushes and slip-rings is still a significant disadvantage of DFIG. This led to increased interest in the Brushless Doubly-Fed Generator (BDFG) for wind power.

1.1.1.3. Brushless Doubly-Fed Generator (BDFG)

BDFG has two standard, sinusoidally distributed, stator windings of different pole numbers and applied frequencies. The BDFG with a cage-less reluctance rotor is known as the Brushless Doubly-Fed Reluctance Generator (BDFRG) and the other type having a special cage rotor is termed as the Brushless Doubly-Fed Induction Generator (BDFIG).

As any with other doubly–fed machines, BDFG has similar basic advantages as the DFIG. Firstly, the cost of power electronics hardware (especially larger scale) is often the dominant component of the total system costs. The fact that the power converter only has to handle the slip power implies the possibility for significant capital cost savings compared to systems with a fully-rated inverter. Secondly, the BDFG can operate in sub-synchronous and super-synchronous modes in both motoring and generating regimes. Besides, the BDFG is brushless and therefore more reliable, mechanically robust and maintenance-free for slips and brushes. This is one of the key arguments for using the BDFG in all applications traditionally served by the DFIG or the classical wound rotor synchronous machine, such as off-shore wind turbines where reliability issues and associated operation and maintenance costs become increasingly important. All the merits above encourage the motivation for the growing attention to the BDFGs.

Both BDFG versions, the BDFIG and the BDFRG, share all the above salient features, the focus of this thesis is on the BDFRG as this machine has some additional favourable properties such as:

A synchronous reluctance machine rotor should offer the BDFRG greater efficiency [7], improved reliability and much easier control with respect to the BDFIG [8]. The advances in BDFRG rotor design have indicated the potential of achieving competitive performance when compared to the DFIG [9].

The BDFRG can be operated stably over the entire speed range in both motoring and generating modes whereas the BDFIG suffers from the inherent stability problems around the synchronous speed of the mains field when it produces no torque [10].

Therefore, in this thesis, BDFRG is compared with DFIG from a control performance point of view.

1.1.2. The research project

Three academic institutions and one industrial partner participated in this collaborative project — Newcastle University (UK), University of Northumbria (UK), Shenyang University of Technology (China) and Scottish-Southern Energy Group (UK).

The main aim of the project is to compare two generators technologies for a wind power application — Brushless Doubly-Fed Reluctance Generator (BDFRG) and Doubly-Fed Induction Generator (DFIG).

Newcastle University focuses on the DFIG, while the University of Northumbria concentrates on the BDFRG. The BDFRG is designed and manufactured by Shenyang University of Technology. Scottish-Southern Energy assisted with power network expertise and project management.

BDFRG is compared with DFIG under a parameter independent vector controller in this thesis. To date, this kind of work has not been carried out. Only a similar work has been done by Dr. Teng Long in Cambridge University. But he made a comparison between BDFIG and DFIG whereas I compared the difference between BDFRG and DFIG, for the BDFRG has some additional advantages than BDFIG as mention before.

Besides, a robust and versatile sensorless Direct Power Control (DPC) scheme has been applied to Brushless Doubly-Fed Reluctance Machine by my collaborator, Chaal Hamza in Northumbria University. Further research has been done by me to compare the DFIG and BDFRG performance when DPC is applied to them. Although the experiment implementation is not successful in DFIG because of the limitation of IGBT module, the simulation comparison of two generators under DPC has been done. And the results are presented in chapter 6. This work has never been carried out before either.

1.1.3. Research objectives

The objectives of the research project are:

- To build a DFIG simulation model by Matlab/Simulink and validate this model by comparing model fault response and crowbar performance to Pannell's experiment results [11].
- To develop and evaluate by simulation studies a machine parameter independent field orientation vector control for decoupled real and reactive power of both DFIG and closely related BDFRG in grid-connected wind energy conversion systems (WECS).
- To develop a BDFRG/DFIG laboratory test facility in variable speed constant frequency (VSCF) applications.
- To implement and test the developed controller in real time on a custom designed and built BDFRG prototype and equivalent, commercially available DFIG of the same size.
- To perform a comparative performance analysis, and assess performance of the two generators controller response in order to establish BDFRG viability as a brushless alternative to slip ring doubly fed induction generator (DFIG) for wind turbines.

- To investigate a Direct Power Control (DPC) scheme for both BDFRG and DFIG and examine the control quality by computer simulations and experimental testing.

1.2. Thesis overview

1.2.1. Thesis layout

The thesis is organised as follows:

Chapter 2 provides an overview of the theory and principles of DFIG and BDFRG operation and control. The aim is to cover the necessary background to analyse the control response of a conventional DFIG/BDFRG. Space vector analysis is introduced and used to demonstrate vector control of DFIG/BDFRG system. The DFIG and BDFRG different structures — wound rotor induction machine and reluctance machine are discussed separately. The difference inductance determinations of induction machine and reluctance machine are detailed as inductance will affect the control response. However, the power converter and wind turbine transformer are introduced which are common knowledge to both generator systems.

Chapter 3 studies the grid fault and fault-ride-through requirements, followed by the analytical solution of induction machine fault response and timer action crowbar methods. A DFIG computer model is described in this chapter which simulates the fault response and crowbar performance. The simulation results are compared with the analytical solution and Pannell's experiment results [11] to validate the model accuracy. This DFIG model is used in Chapter 6 as well to simulate DPC response.

Chapter 4 introduces the DFIG and BDFRG test facility which was built and commissioned in Northumbria University and referred to throughout this work as 'test rig'. The test rig includes a DFIG/BDFRG, a prime drive made up of commercial

Altivar 71, an induction machine and a control cabinet. The entire system is controlled by an *eZdsp F28335* board. The controller is programmed with C language in the Code Composer debugger. Two LabVIEW interfaces are designed to keep communication with DSP via *RS232* and control the systems during the tests.

Chapter 5 and 6 present the vector control and direct power control principles and experimental implementation. Vector control test responses of both DFIG and BDFRG are graphically demonstrated in Chapter 5. The results from the two generators are compared and analysed. The experimental results for the DPC scheme are described in Chapter 6, but DFIG results are not satisfactory due to the sampling frequency limitation.

1.2.2. Publications

[12] WenJun Chen; Atkinson, David; Chaal, H.; Jovanovic, M., "Experimental and Simulation Comparison for Timer Action Crowbar of Doubly-Fed Induction Generator," Power and Energy Engineering Conference (APPEEC), 2011 Asia-Pacific , vol., no., pp.1,5, 25-28 March 2011 doi: 10.1109/APPEEC.2011.5748822

[13] Chaal, H.; Jovanovic, M.; Atkinson, D.; Wenjun Chen, "A simple yet efficient doubly-fed drive/generator controller," Power Electronics and Applications (EPE 2011), Proceedings of the 2011-14th European Conference on , vol., no., pp.1,6, Aug. 30 2011-Sept. 1 2011

2. DFIG and BDFRG concepts

This chapter gives an overview of DFIG and BDFRG operations and their theories. This material provides the necessary background knowledge for the analysis in the following chapters.

The first section explicates the space vector analysis. The next two sections provide an overview of the theories and principles of DFIG and BDFRG separately.

In Section 2.2, the power electronic converters and wind turbine transformers of the DFIG have been introduced. The performance and power flow characteristics of the DFIG have been described. They are common knowledge for both generator systems. Thus Section 2.3 does not repeat these contexts.

Besides these similarities, the wound rotor induction machine and reluctance machine are discussed separately. The different inductance determinations of induction machine and reluctance machine are detailed as the inductance will affect the control response. Additionally, the control methods of both DFIG and BDFRG have been demonstrated in this chapter as the background knowledge.

2.1. Space vector analysis

The space vector is a mathematical abstract concept. It facilitates the analysis of the electrical machine, by representing the three-phase quantities, such as the voltage, current and flux in vector form. The three-phase components can also be represented by two orthogonal quantities in a rectangular coordinate system which is called ‘reference frame’.

The use of rectangular co-ordinate axis helps to simplify the derivation of the mathematic model. The book [14] documents the advantages of space vector analysis. All the information of real three-phase waveforms, including the zero

sequence components, is represented by the space vector in the orthogonal two-axis system. Normally, in a reference frame, the vector can be described as a complex number, $d + jq$, where real part d represents direct axis value and imaginary part q is the quadrature axis number. Secondly, the complicated calculations of two or more electrical parameters can be replaced by simply using the four arithmetic operations of matrix, complex number and trigonometric function. So, the utilization of the different reference frames to analyse and control the same machine becomes much easier because it is convenient to transform the expression of any vector from one reference frame to the other by using the space vector representation. Besides, the space vectors can consist of a matrix which describes the status of the electrical machine on both steady-state and transient response, whereas they may be resolved immediately via a reverse of the matrix transformation. Thus, the space vector model is, therefore, “valid for any instantaneous variation of voltage and current and adequately describes the performance of the machine under both steady-state and transient operation” [15]. From the advantages above, it is worth analysing the electrical machine by the use of the orthogonal space vector representation.

Generalised electrical machine theory, including the space vector analysis, is based on the following simplifying hypothesis shown in [16][17]:

① Flux and MMF distributions are represented by their fundamental harmonic component alone.

② Slotting and other geometric winding distribution effects are neglected.

③ Commutation effects and brush-connections are considered ideal.

④ The eddy currents and hysteresis effects of the magnetic materials are neglected.

⑤ Magnetic saturation is not present.

The assumptions ①-④ are reasonable approximations of the practical cases. Magnetic linearity is assumed. Thus the different magnetic fields may be linearly superposed, which simplifies model development considerably. However, the actual machine situation contradicts the hypothesis ⑤. Magnetic saturation definitely impacts all practical machines. The concentration of magnetic flux is restricted at any one point due to the saturation. But it has less impact in the later analysis and conclusions. Practically, if the magnetic saturation has the effects on machine, it will limit the transient over-shoot current and power on step response of the vector control, and restrict the instant excesses of fault response. The linear magnetic analysis will therefore derive a worst case response in terms of transient response on both control and fault. In conclusion, the simplification of linear space vector analysis is reasonable and could be used in fault discussion in Chapter 3 and the control analysis in Chapters 5 and 6.

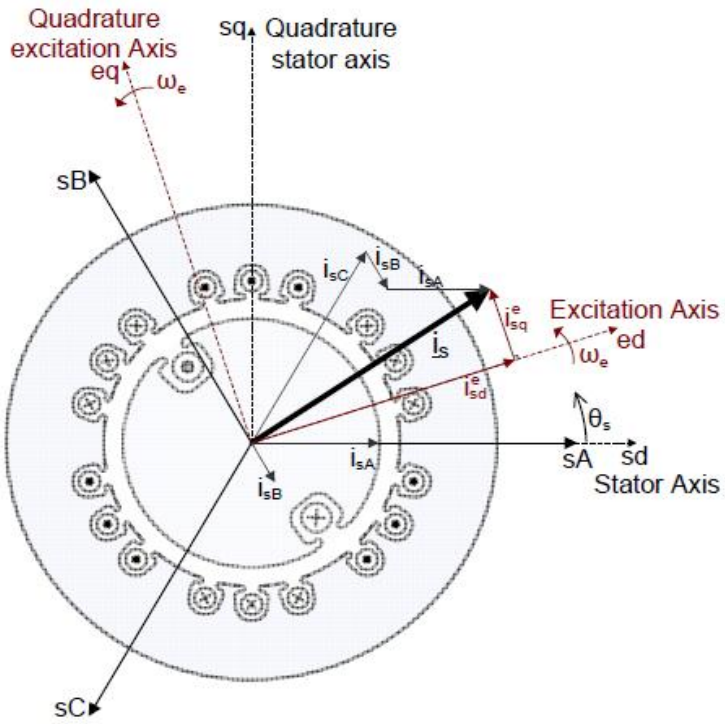

Figure 2.1 Space vector of stator current

An example of the space vector analysis is illustrated in Figure 2.1 where a stator current space vector is mapped onto a cross-section of a symmetrical two-pole, three-phase non-salient AC machine. The three-phase *a-b-c* components are drawn as *sA*, *sB* and *sC* axes with 120° difference between them, while the stationary stator axis *sd* is along with *sA*, and the excitation reference frame is pictured with an angle θ_s between the *sA* and its *d* axis. The Quadrature axes of stator and excitation reference frame is shown 90° ahead of themselves Direct axes respectively. The excitation axes rotate at speed ω_e, whereas the stator *d-q* axes are stationary. The vector stator current i_s which consists of three-phase *sA-sB-sC* (Equation 2.1), is discomposed as i_{sd}^e and i_{sq}^e along with the direction of excitation frame *d-q* axes. This set of stationary three-phase *sA-sB-sC* axes, stationary *sd-sq* axes, excitation reference frame *ed-eq* axse and the stator current i_s with its discomposed value i_{sd}^e and i_{sq}^e explicate the space vector analysis.

$$\overrightarrow{i_s}(t) = i_{sa}(t) + a i_{sb}(t) + a^2 i_{sc}(t) \tag{2.1}$$

Where

$$a = \exp(-j\,2\pi/3) \tag{2.2}$$

For the balanced three-phase currents, we have:

$$i_{sa} + i_{sb} + i_{sc} = 0 \tag{2.3}$$

Similar to the two components of stator current in excitation reference, i_{sd}^e and i_{sq}^e, the stator current also can be resolved in stationary reference frame to i_{sd}^s and i_{sq}^s. These two components have the following relationships to the three-phase quantities:

$$i_{sd}^s = \frac{2}{3} i_{sa} - \frac{1}{3} i_{sb} - \frac{1}{3} i_{sc} \tag{2.4}$$

$$i_{sq}^s = \frac{\sqrt{3}}{3} i_{sb} - \frac{\sqrt{3}}{3} i_{sc} \tag{2.5}$$

And the two reference frames have the transformation below:

$$\begin{cases} i_{sd}^{e} = i_{sd}^{s} cos\theta_s + i_{sq}^{s} sin\theta_s \\ i_{sq}^{e} = -i_{sd}^{s} sin\theta_s + i_{sq}^{s} cos\theta_s \end{cases} \quad (2.6)$$

$$\begin{cases} i_{sd}^{s} = i_{sd}^{e} cos\theta_s - i_{sq}^{e} sin\theta_s \\ i_{sq}^{s} = i_{sd}^{e} sin\theta_s + i_{sq}^{e} cos\theta_s \end{cases} \quad (2.7)$$

The details of reference frame and the transformations are explained in Appendix A.

2.2. Doubly-Fed Induction Generator (DFIG)

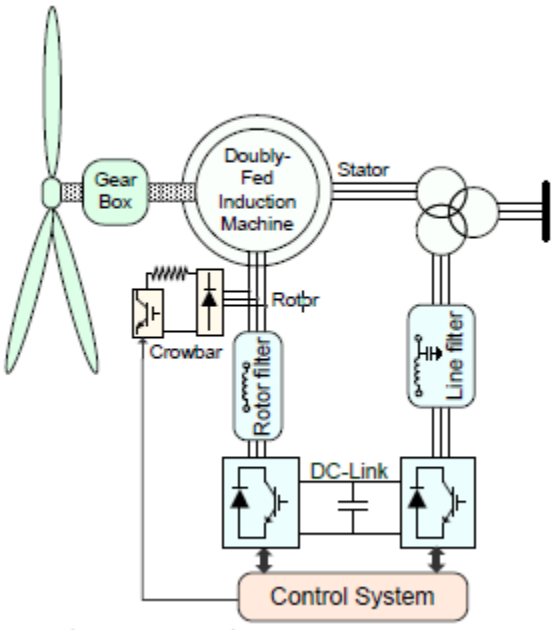

Figure 2.2 Schematic of wind turbine DFIG including a back-to-back power converter [11]

As is well known, a most widespread DFIG scheme, as shown schematically in Figure 2.2, consists of a poly-phase wound rotor induction generator with direct grid connection on stator side and variable frequency power converter on rotor side [11]. The frequency converter is built by a pair of three phase bridge PWM converters arranged as ‘back-to-back’ structure with a dc voltage link created by a capacitor in

the middle [18]. The generator will be controlled by applying the control scheme to the IGBT power converter and connected to the grid via a transformer.

2.2.1. Wound rotor induction generator

A wound rotor induction machine is common terms used to describe an electrical machine with the following characteristics [19]. The machine has a cylindrical stator and rotor with a set of slots in the internal face of the stator and the external face of the rotor. In the slots, three phase windings are located to create the magnetic field in the airgap with poles. Typically, there are thirty-six to forty-eight slots and two or three pole pairs [19] on the stator and the rotor has the same pole pair number as the stator. The two magnetic field produced by both stator and rotor windings will turn at the same speed with some degree phase shift between them as the function of the torque. The slip rings are necessary to feed the rotor as the rotor is moving. But the slip ring assembly requires maintenance, therefore, will increase the cost and reduce the reliability and efficiency of the system. That is the reason why the brushless machine appears. Figure 2.3 explains the structure of a wound rotor induction machine.

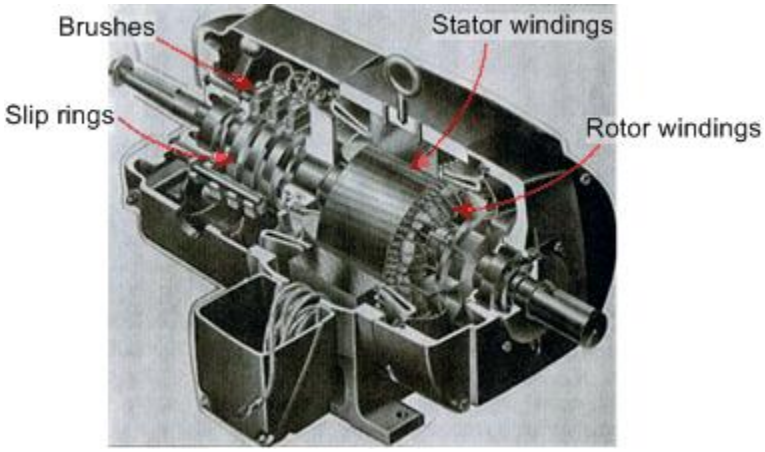

Figure 2.3 Cutway section of a wound-rotor induction machine [20]

The wound-rotor induction machine offers the option of rotor-field control with the decoupling of the output power and permits the variable speed option in comparison

to the squirrel-cage machine. Thus the DFIG has the merits of adjustable speed generators, for example, high efficiency, less loss and stress of mechanical shaft and simple control, etc. The chief disadvantage is the slip ring.

2.2.1.1. DFIG inductances

In determining the machine inductance, an idealised three phase AC machine is firstly considered. The machine has sinusoidally distributed windings and flux density. Taking account of a single stator phase winding, the flux linkage around it consists of one leakage and three mutual fluxes. The leakage flux contribution is driven by this stator phase current itself without any link to any other phase. One mutual flux contribution is encouraged by the same stator phase but linking the other stator phases. The other two mutual fluxes thread the stator and rotor. One is driven by the stator phase currents with link to the rotor, the other is obliged by the rotor currents and linking the stator.

From here we can see that the circuits in the machine may have the magnetic coupling between each other. This will cause the complicated circuit equation [21] However, the book [22] substantially simplifies this by using an orthogonal two-axis representation to describe machine and expressing the magnetic couplings of each circuit separately by their relevant impedance parameters.

In order to eliminate the turns ratio effects, the parameters here are all referred to *'per-unit'* value. The relations between the inductance and current are independent of reference frame. Thus, here a general frame is used in the equations below by the superscripts $'g'$. The three following equations describe the leakage flux driven by the stator (Eq. 2.15), mutual component encouraged by both currents (Eq. 2.16) and the stator total flux linkage (Eq. 2.17).

$$\overrightarrow{\varphi_{es}^{g}} = L_{es}\overrightarrow{\iota_{s}^{g}} \tag{2.15}$$

$$\overrightarrow{\varphi_m^g} = L_m\left(\overrightarrow{\imath_s^g} + \overrightarrow{\imath_r^g}\right) \tag{2.16}$$

$$\overrightarrow{\varphi_s^g} = L_{es}\overrightarrow{\imath_s^g} + L_m\left(\overrightarrow{\imath_s^g} + \overrightarrow{\imath_r^g}\right) \tag{2.17}$$

The total stator inductance combines the stator leakage and mutual elements, expressed as:

$$L_s = L_{es} + L_m = (1 + \sigma_s)L_m \tag{2.18}$$

$$\sigma_s = {}^{L_{es}}\!/_{L_m} = -\left(1 - {}^{L_s}\!/_{L_m}\right) \tag{2.19}$$

$$\overrightarrow{\varphi_s^g} = L_s\overrightarrow{\imath_s^g} + L_m\overrightarrow{\imath_r^g} \tag{2.20}$$

Similar, for the rotor flux linkage, we have:

$$\overrightarrow{\varphi_r^g} = L_{er}\overrightarrow{\imath_r^g} + L_m\left(\overrightarrow{\imath_s^g} + \overrightarrow{\imath_r^g}\right) \tag{2.21}$$

$$L_r = L_{er} + L_m = (1 + \sigma_r)L_m \tag{2.22}$$

$$\sigma_r = {}^{L_{er}}\!/_{L_m} = -\left(1 - {}^{L_r}\!/_{L_m}\right) \tag{2.23}$$

$$\overrightarrow{\varphi_r^g} = L_r\overrightarrow{\imath_r^g} + L_m\overrightarrow{\imath_s^g} \tag{2.24}$$

For the simplification of the expressions, a useful measurement of the ratio between the leakage and mutual fields in machine is derived in Equation 2.25, called ‘leakage factor’. The stator and rotor leakage factor is defined in above equation 2.19 and 2.23

$$\sigma = 1 - \frac{L_m^2}{L_s L_r} \tag{2.25}$$

The flux and inductance equation above are all valid in transient condition [23]. Although the saturation is general insignificant for a simpler analysis, it, in practical, may reduce the relevant inductance values [16].

As the description above, we know that the linking flux strength varies around the rotor surface in a saliency machine. This leads to the variations of the inductance values [17]. In a salient induction machine, the inductance is possible to be resolved against the *d-q* axes of the rotor and the stator reference frame, which will result in a complicated impedance expression.

However, we also know that a poly-phase winding distribution is able to eliminate the saliency effect due to its multiple slots per phase and the narrow and identical airgap width. Even if the small, ripple-like deviations happen occasionally as the slots align and mis-align in, these ‘slot effects’ do not seriously impact. Inductance values, therefore, may ignore its variations with position and be considered as an approximate constant.

All wind turbine DFIGs are poly-phase induction machines. Typically, for the sake of maximum efficiency, DFIG is designed with a large number of slots and windings, and narrow smooth airgap [20]. Thus, DFIG has minimal saliency and it can be assumed that the machine inductances are independent of rotor position. This important conclusion provides us the support of considering the DFIG inductances as constant when viewed in a stator, rotor or synchronously-rotating reference frame.

2.2.2. DFIG power converter

2.2.2.1. Converter types

The DFIG converter has previously been based on three types before the back-to-back PWM converter that is used nowadays [20].

In the early years, the naturally commutated DC-link converter was commonly used. It consisted of voltage controlled inverters [1]. But, this converter was superseded due to many drawbacks. Initially, it has problems at synchronous speed, since a rectangular current waveform was drawn through the converter from the supply. This problem gave rise to an extra commutation circuit for the operation at synchronous speed. However, this strategy still had poor performance at low slip speed [1]. In addition, the DC-link choke was expensive, which led to a high cost. Moreover, additional transformers were needed not only for the neutral connection but also voltage matching [1].

Gradually, the direct AC to AC frequency converter known as a cyclocnverter replaced the DC-link converter [1]. The cycloconverter has two main types; a 6-pulse converter, and a 3-pulse converter. Although cycloconverter had excellent attributes, it also had many weaknesses, for example, increased machine complexity, difficulty of current harmonic elimination and the extra transformers [1].

Nowadays, the back-to-back PWM converter is the preferred option. It is also called a self-commutated PWM converter, a four-quadrant converter or a bi-directional power converter. This converter is made up by two voltage-fed, current-regulated inverters connected back to back sharing the DC bus. This converter allows the DFIG a more versatile and flexible operation compared to the Single-Fed Induction Generator (SFIG) [1]. At any time, one of converter will operate as a rectifier and the other is an inverter. This design allows the sub- and super- synchronous modes operation in DFIG. Speed variability is also made possible by the directly dependent transfer of slip power via the frequency converter [25]. Besides, these two converters can be controlled separately. They enable the decoupled control of real and reactive power. When the converter has to provide only excitation energy, the DFIG has the similar operation of synchronous machine and results in a simple power factor control which can be implemented at low cost [5][26]. In addition, the converter’s power rating is a fraction of the generator rating. The reasonable operating speed range is typically

within ±*25%* around synchronous speed and requiring a *25%*-rated converter which is the dominant virtue of DFIG giving significant cost savings [5][27]. The low rated converter of course leads to the *0.25 p.u*. rating inverter filters and EMI filters which has reduced cost and less *p.u.* harmonic [5].

2.2.2.2. Voltage source converter

Figure 2.4 illustrates the two-level, three-phase IGBT bridge converter used in the DFIG. A pair of such converters is connected back to back sharing a DC-link bus to allow the bi-directional power flow. The power flow characteristics will be introduced in the Section 2.2.5.

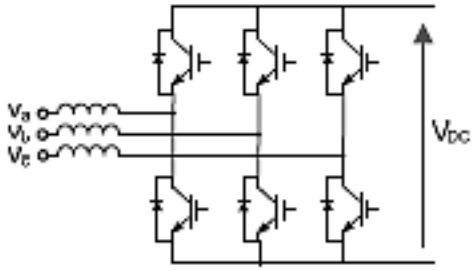

Figure 2.4 Three-phase IGBT bridge converter used in DFIG

The two voltage source converters are called rotor-side and grid-side converters according to their position and can be controlled separately by two sets of independent three-phase modulation indexes. The supply frequency (eg *50Hz*) is injected to both the generator stator windings and the grid side converter. The rotor-side converter supplies slip frequency voltages/currents to the rotor circuit via the slip-rings.

With this structure, DFIG is an attractive option for the applications of large capacity and is widely adopted for different kinds of variable speed constant frequency turbines. The primary advantage of DFIG is its best cost performance due to the reduced power converter rating. Compared to the fully-rated back-to-back converters, partly-rated converters would have the cheaper converter devices and cause the

lower DC bus voltage. Further, the lower voltage results in low cost of capacitor bank [26][27][28][29].These reductions give the important capital saving on both converter, the filters and other relative hardwares compared to fully-rated power converter since the cost of hardware is usually the dominant component of total cost [19][26]. In addition, unlike the SFIG, the DFIG can operate in both sub- and super- synchronous speed modes. The similarity of operation to that of a synchronous generator permits the implementation of power factor control at low cost and the possibility of decoupled active and reactive power control [1][27]. What is more, constant stator flux linkage over entire operation range causes high utilization ratio of generator [26][27][28][29].

All of these contributions are given by this compact design with minimal size of components. Actually, this design is based on several reformations, especially the innovations of the converter. The reasons why this modern converter design gives so many advantages have been included in the process of converter changes and introduced above.

The DC-link capacitance maintains the DC voltage and decouples the operation of the two converters. It permits the independent control of two converters and allows the power flow in either direction. In the experiment, the DC voltage will be controlled by the grid side converter through the direct axis line current. The details will be given in Chapter 5.

2.2.3. Wind turbine transformer

Most European wind power generators are designed to operate with *690V* phase to phase voltage. One reason for this design is safety regulations for a wind turbine tower. The other is the flexibility and cost-effectiveness of production for cables and switchgear at low voltages [30]. Hence, in general, an LV:MV transformer would be included in all large DFIG wind turbines, as the output voltage of wind turbine is lower than the distribution network level.

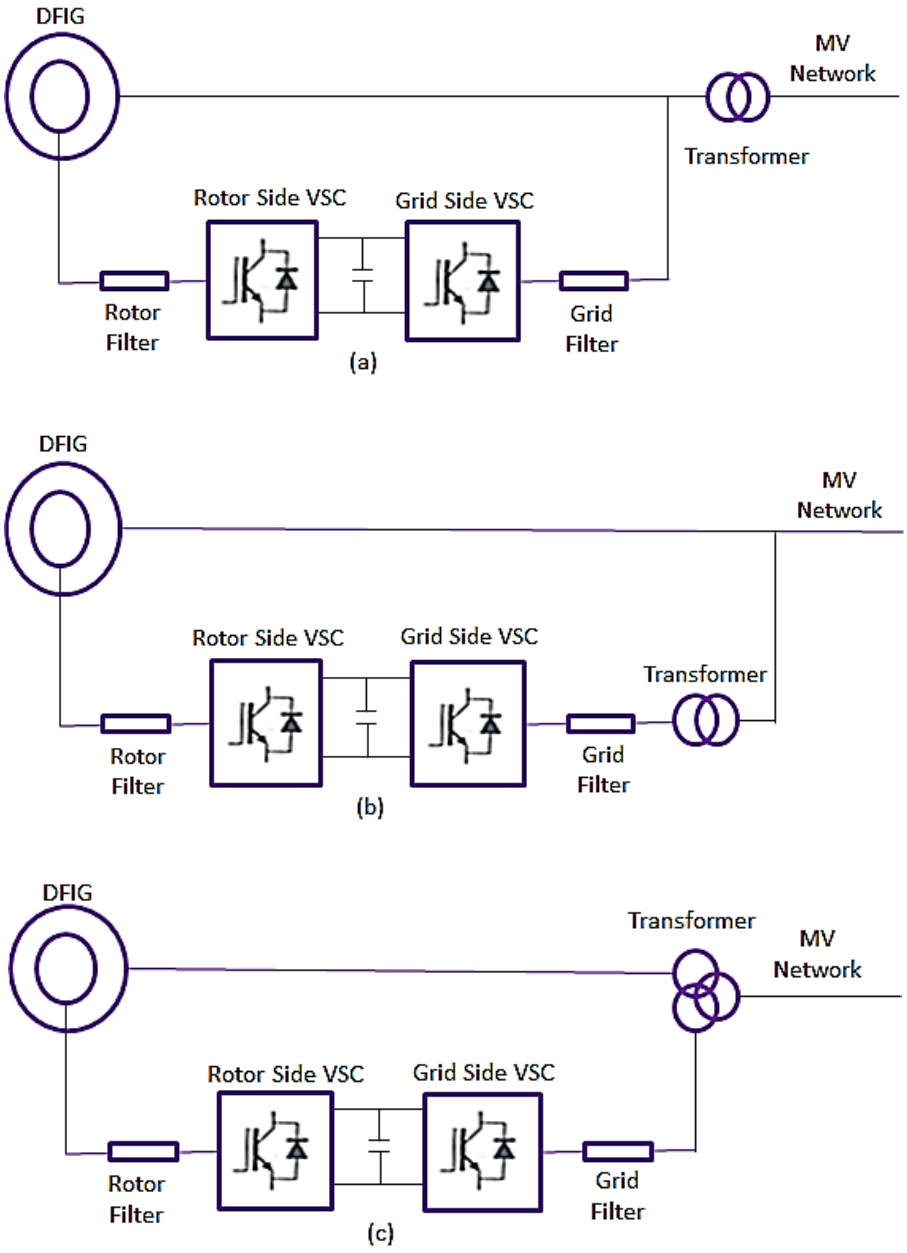

Figure 2.5 Different transformer connections

There are several ways to connect the stator and the converter to the grid as shown in Figure 2.5. If the stator and converter have the same voltage level, one transformer rated at full power is used as shown in Figure 2.5 (a). If the stator voltage is in the range of MV, the transformer like the middle picture is used at the rated rotor power level. In this case, the stator voltage is direct connected to a medium voltage distribution grid or the medium voltage grid of a wind farm. If the stator and converter

voltages are both in the low voltage range but different value, two secondary windings are used.

All three transformer configurations have merits. Table 2.1 summarizes the main advantages and disadvantages.

Option	Advantages	Disadvantages
a	● One single secondary winding ● The MV winding can be adapted to different MV grids	● Full power transformer
b	● The transformer is rated at *30%* of the wind turbine power ● Less transformer loses ● Stator electrical design	● The transformer leakage impedance limits the short-circuit current ● The MV grid must fit the stator MV voltage
c	● The stator voltage and the power electronics can be designed with different voltage	● The transformer is more expensive

Table 2.1 Transformer topology comparison [19]

2.2.4. Performance of DFIG operation

As demonstrated above, DFIG can operate in synchronous, sub- and super-synchronous modes. The performance of DFIG in these modes will be discussed below, however, before the discussion, the frequency relationship between stator and rotor need be introduced below. The symbols can be found in glossary and symbols section.

$f_s = f_r + p_A f_m$

$$f_{slip} = f_r$$

$$s_1 = \frac{f_r}{f_s} = \frac{N_{syn} - N_m}{N_{syn}} = \frac{f_s - p_A f_m}{f_s} = 1 - \frac{p_A f_m}{f_s}$$

$$N_{syn} = \frac{60 \times f_s}{p_A}$$

$$n_m = 60 f_m$$

$$\omega_{slip} = \omega_s - \omega_r$$

$$\omega_s = \frac{2\pi f_s}{p_A}$$

$$\omega_{slip} = \frac{2\pi f_{slip}}{p_A} = \frac{2\pi f_r}{p_A}$$

$$\omega_r = 2\pi f_m$$

The generalised slip is from *-1* to *1*, however as is well known, DFIG's slip range is typically ± 0.25. Normally, the SFIG's slip is smaller than *0* to make sure the rotor field is ahead of the stator field. But the DFIG has the positive slip. How does it operate as a generator? At this time, the phase position of rotor current need be adjusted to control the rotor field is dragged ahead of the stator field to keep the generation modes. The performance of DFIG could be discussed as the slip is changed: [31]

The slip is started from negative. The first operation DFIG experienced is super-synchronous mode. In this mode, the rotor mechanical speed is above the synchronous speed. That means the further acceleration after synchronism. That is the reason why this mode is called 'super-'. The slip frequency is under zero since the rotor windings "overtake" the stator flux due to the 'super-'. The negative frequency causes the reversed rotor phase sequence. After the rise of slip, it arrives to zero which indicates the slip frequency is zero and the mechanical rotor speed is the same

as the synchronous speed. Thus this mode is called ‘synchronous’. In this condition, the rotor windings rotate synchronism with the stator flux. In other word, the rotor windings have no relative movements to the stator flux. Therefore no voltage is induced in rotor windings. The slip continues rising over the zero. When the slip is positive, the stator frequency is larger than the rotor frequency and mechanical rotor speed is smaller than the synchronous speed, thus this operation is called sub-synchronous.

With the slip climbing up and approaching to the stator frequency, the distance of the relative position of rotor and stator flux increases. When the slip reaches *1*, the stator and rotor voltages have the same frequency which is determined by the *50Hz* mains supply connected to stator, and the mechanical rotor frequency and speed are zero. The DFIG operates at the stationary state. Not only the stator but also the rotor voltage is supplied by a positive phase sequence “*a*-*b*-*c*”. In this condition, the machine behaves merely as a transformer.

Besides, there is an exceptional mode called ‘counter-synchronous’ operation when the slip is over *1*. The slip frequency is bigger than the stator frequency and the mechanical rotor speed is negative which indicates the rotor rotates in opposite direction to stator flux. It would not be discussed in this thesis.

2.2.5. Power flow characteristics of DFIG

For a conventional wound rotor induction machine, the rotor windings are normally shorted at the slip rings so that there is no power outputted from the rotor except rotor loss only. For a DFIG, however, to obtain sub- and super- synchronous speed operation, the converter must be able to handle slip power in both directions [32] and therefore both real and reactive power P and Q could be conveyed in either direction at grid frequency. When the power loss is ignored, the real power P and reactive power Q can be expressed as: [31]

$$P_m = T_m \omega_r$$

$$P_s = T_e \omega_s$$

$$J\frac{d\omega_r}{dt} + B\omega_r = T_m - T_e$$

Where J is inertia coefficient and B represents friction. At the steady-state for the loss less generator, when the friction is ignored ($B = 0$):

$$T_m = T_e$$

$$P_m = P_s + P_r$$

$$P_r = P_m - P_s = T_m\omega_r - T_e\omega_s = -T_m\left(\frac{\omega_s - \omega_r}{\omega_s}\right)\omega_s = -s_1 T_m \omega_s = -s_1 P_s$$

$$P_m = (1 - s_1)P_s$$

$$Q_{sr} = Q_s + \frac{Q_r}{s_1}$$

$$P_{grid} \approx P_s + P_r$$

On one hand, when slip is *0* at synchronous speed, the power only transfers between stator and mechanical shaft, while at stationary state whose slip is *1* and mechanical rotor frequency is *0*, the power flow only takes place in the stator and the rotor. Besides, depending on the DFIG operating in sub- or super- synchronous modes, the mechanical shaft would feed energy to the stator and the stator real power P_s is always flowing from the stator to the grid, whereas the rotor power P_r would change the direction at different modes. As Figure 2.6 illustrates, power flow conveys towards the grid and increases linearly when the slip is negative at over-synchronous speed, while reverses to the rotor at the sub-synchronous with positive slip and reduces linearly with the rise of mechanical power P_m. The real power delivered to the rotor at sub-synchronous speed depends primarily on the amplitude of the voltage injected

into rotor and the peak rotor power absorbed from the converter occurs around the synchronous speed. At that time, the slip is near zero and the rotor is close to a short circuit. In other words, to prevent such high peak rotor power or current, the DFIG should not be operated near synchronous speed [31].

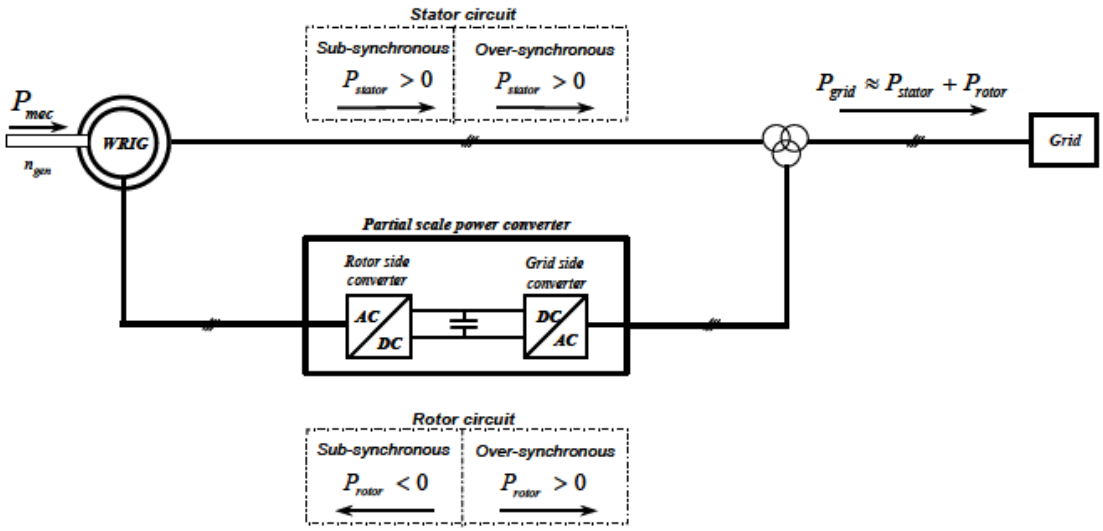

Figure 2.6 Principle diagram of power flow [31]

On the other hand, the rotor reactive power Q_r and Q_g should be adjusted by the controller to make sure that the grid reactive power Q_{grid} is zero and to reduce the reactive power Q_r transmitted between the rotor and the converter. Actually, although the reactive power Q_r is not conveyed to the grid through the grid-side converter under the constant DC-link voltage condition, it may cause overall rotor power to exceed the power ratings of rotor-side converter and therefore influence the effective DFIG control objectives [31].

Explicitly, the biggest characteristic of DFIG is the transportation of the real and reactive power between rotor and rotor-side converter. However, it may become the bottleneck for the effective vector control of DFIG owing to the rated power limitation of converter [34].

2.2.6. Mathematical Model of DFIG

2.2.6.1. Different Order Model of DFIG

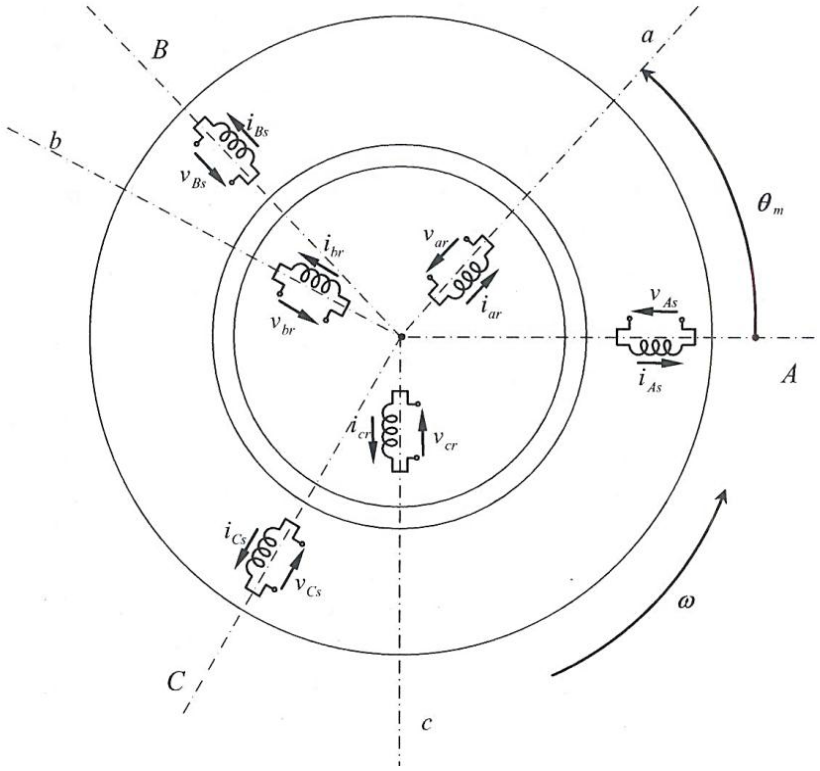

Figure 2.7 Ideal three-phase windings (stator and rotor) of the DFIG [19]

An ideal DFIG model can be described as three windings in the stator and three windings in the rotor as illustrated in Figure 2.7. Three windings are an ideal representation of the real machine which helps to derive the three-phase machine model. The instantaneous stator voltages, currents and flux linkages of the machine can be expressed by the following electric equations:

$$u_{sa} = R_s i_{sa} + \frac{d\varphi_{sa}}{dt} \tag{2.26}$$

$$u_{sb} = R_s i_{sb} + \frac{d\varphi_{sb}}{dt} \tag{2.27}$$

$$u_{sc} = R_s i_{sc} + \frac{d\varphi_{sc}}{dt} \tag{2.28}$$

Similarly, the rotor magnitudes are described by:

$$u_{ra} = R_s i_{ra} + \frac{d\varphi_{ra}}{dt} \tag{2.29}$$

$$u_{rb} = R_s i_{rb} + \frac{d\varphi_{rb}}{dt} \tag{2.30}$$

$$u_{rc} = R_s i_{rc} + \frac{d\varphi_{rc}}{dt} \tag{2.31}$$

This model can transfer to the *d-q* model based on the excitation reference frame. The equivalent circuit is shown in Figure 2.8 which is similar to an induction machine.

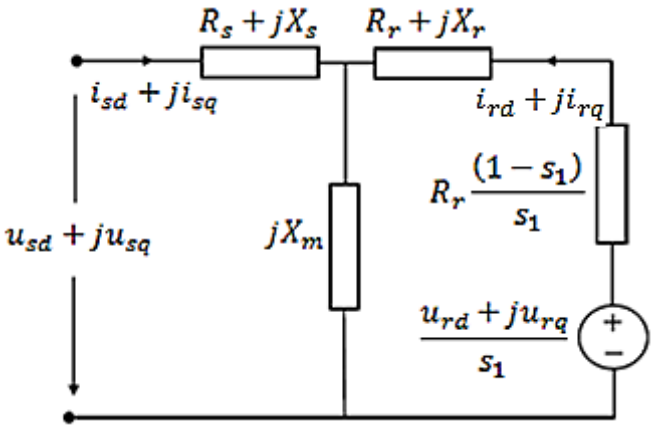

Figure 2.8 Steady-State Equivalent Circuit of DFIG [35]

Depending on this circuit, the fundamental equations of DFIG are given [36]:

1) Voltage equations:

$$\overrightarrow{u_s} = R_s \overrightarrow{i_s} + \frac{d\overrightarrow{\varphi_s}}{dt} + j\omega_e \overrightarrow{\varphi_s} \tag{2.32}$$

$$\overrightarrow{u_r} = R_r \overrightarrow{i_r} + \frac{d\overrightarrow{\varphi_r}}{dt} + j\omega_{slip} \overrightarrow{\varphi_r} \tag{2.33}$$

2) Flux equations:

$$\overrightarrow{\varphi_s} = L_s \overrightarrow{i_s} + L_m \overrightarrow{i_r} \tag{2.34}$$

$$\overrightarrow{\varphi_r} = L_m\overrightarrow{\imath_s} + L_r\overrightarrow{\imath_r} \tag{2.35}$$

From the flux equations, the current can be expressed by the flux, so the current equations are:

$$\overrightarrow{\imath_s} = \frac{L_m}{L_m^2 - L_sL_r}\overrightarrow{\varphi_r} - \frac{L_r}{L_m^2 - L_sL_r}\overrightarrow{\varphi_s} \tag{2.36}$$

$$\overrightarrow{\imath_r} = \frac{L_m}{L_m^2 - L_sL_r}\overrightarrow{\varphi_s} - \frac{L_s}{L_m^2 - L_sL_r}\overrightarrow{\varphi_r} \tag{2.37}$$

And the relationship between stator and rotor flux is:

$$\overrightarrow{\varphi_s} = (L_s - \frac{L_m^2}{L_r})\overrightarrow{\imath_s} + \frac{L_m}{L_r}\overrightarrow{\varphi_r} \tag{2.38}$$

Define a constant $K = \frac{1}{L_m^2 - L_sL_r}$, then the current equations can be expressed as:

$$\overrightarrow{\imath_s} = KL_m\overrightarrow{\varphi_r} - KL_r\overrightarrow{\varphi_s} \tag{2.39}$$

$$\overrightarrow{\imath_r} = KL_m\overrightarrow{\varphi_s} - KL_r\overrightarrow{\varphi_r} \tag{2.40}$$

Substitute the voltage equations by current equations 2.39 and 2.40, they can be described by:

$$\frac{d\overrightarrow{\varphi_s}}{dt} = \overrightarrow{u_s} + (KL_rR_s - j\omega_e)\overrightarrow{\varphi_s} - KL_mR_s\overrightarrow{\varphi_r} \tag{2.41}$$

$$\frac{d\overrightarrow{\varphi_r}}{dt} = \overrightarrow{u_r} + \left(KL_sR_r + j\omega_{slip}\right)\overrightarrow{\varphi_r} - KL_mR_r\overrightarrow{\varphi_s} \tag{2.42}$$

3) Motion equation:

$$\frac{d\omega_r}{dt} = \frac{1}{J}\left(T_m + Im\left(\overrightarrow{\varphi_s^*} \times \overrightarrow{\imath_s}\right)\right) \tag{2.43}$$

The equation of motion adds the equation 2.41 and 2.42 could be used for the instantaneous performance or dynamic simulation of DFIG and be called ‘Full Order

Model' (FOM) of the DFIG [36]. This model presents an induction machine type circuit, it, therefore, could be described as the vector diagram shown in Figure 2.9.

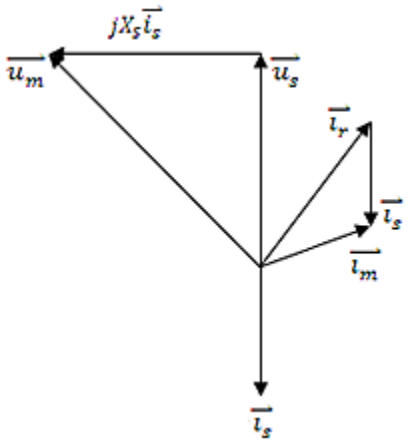

Figure 2.9 Vector Diagram of (induction) DFIG

Although the FOM is a perfect model and could operate under the small time constants involved small integration time step, it includes a large number of differential equations to eliminate the stator voltage. This will limit the application of FOM due to the complex analysis [36].

The equation $\frac{d\vec{\varphi_s}}{dt} = 0$ is warranted in the reference frame rotating at a speed close to synchronous speed. The DFIG model can be changed to '5th Order Model' (5th OM) shown below:

Depending on 2.38, equation 2.41, 2.42 and 2.43 can be changed to:

$$\vec{u_s} = \left[R_s + j\omega_e\left(L_s - \frac{L_m^2}{L_r}\right)\right]\vec{i_s} + j\omega_e\frac{L_m}{L_r}\vec{\varphi_r} \tag{2.44}$$

$$\frac{d\vec{\varphi_r}}{dt} = \vec{u_r} + \left(-\frac{R_r}{L_r} + j\omega_{slip}\right)\vec{\varphi_r} + \frac{L_m}{L_r}\vec{i_s} \tag{2.45}$$

$$\frac{d\omega_r}{dt} = \frac{1}{J}\left(T_m + Im\left(\frac{L_m}{L_r}\vec{\varphi_r^*} \times \vec{i_s}\right)\right) \tag{2.46}$$

Define $Z' = \left[R_s + j\omega_e\left(L_s - \frac{L_m^2}{L_r}\right)\right]$, $\overrightarrow{u'} = j\omega_e \frac{L_m}{L_r}\overrightarrow{\varphi_r}$, then Figure 2.10 can express the circuits of 5th OM.

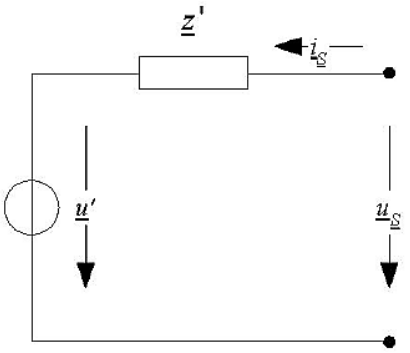

Figure 2.10 Equivalent Circuit of 5th OM [36]

When $\frac{d\overrightarrow{\varphi_r}}{dt} = 0$, the '3rd Order Model' (3rd OM) was created. The equation 2.44 and 2.45 is changed to:

$$\overrightarrow{u_s} = R_s\overrightarrow{i_s} + j\omega_e L_s\overrightarrow{i_s} + j\omega_e L_m\overrightarrow{i_r} \tag{2.47}$$

$$\frac{\overrightarrow{u_r}}{s_A} = \frac{R_r}{s_A}\overrightarrow{i_r} + j\omega_e L_r\overrightarrow{i_r} + j\omega_e L_m\overrightarrow{i_s} \tag{2.48}$$

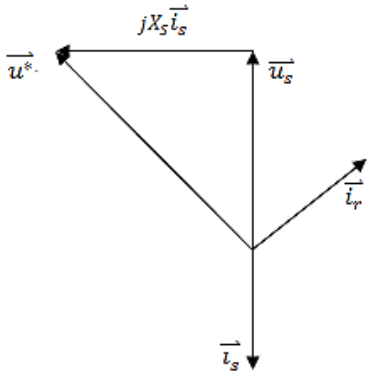

Figure 2.11 Vector Diagram of (synchronous) DFIG

If the stator resistance is neglected, and define $\overrightarrow{u^*} = j\omega_e L_m\overrightarrow{i_r}$, it would be found that $\overrightarrow{u_s} = j\omega_e L_s\overrightarrow{i_s} + \overrightarrow{u^*}$, where the $\overrightarrow{u^*}$ could present the back EMF induced by the rotor current $\overrightarrow{i_r}$, and the rotor current can be considered as the field current. At this time,

the model looks like the circuit presented in Figure 2.10, and its vector diagram can be obtained by Figure 2.11.

The 3rd OM can be used to the steady state analysis. Both 3rd OM and 5th OM are the reduced order models (ROM). Without the rotor crowbar, not only the FOM but also the ROM will give the similar performance. However, when the grid is disturbed and the rotor crowbar is switched on, the ROM has not been covered the considerable alternating components of the rotor flux, and an extra DC components can be captured on both stator and rotor side in FOM which is not a part of ROM solution. That indicates the ROM does not provide the correct information for the initializing crowbar control. All of the research under the grid disturbance would be analysed in the near future.

2.2.6.2. D-Q Component Model at Excitation Reference Frame

The equivalent circuits of *d, q* components are illustrated in Figure 2.12 (a) and (b)

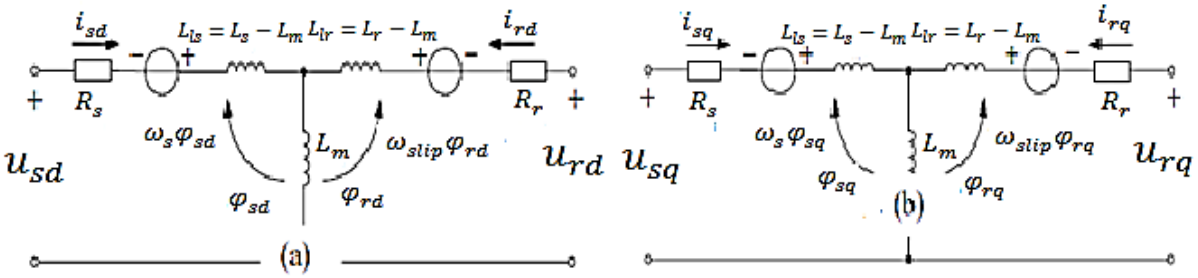

Figure 2.12 (a) D–axis Equivalent Circuits of DFIG [37]; (b) Q-axis Equivalent Circuits of DFIG [37]

In the picture, a definition is given by:

$$\begin{cases} L_{ls} = L_s - L_m & (a) \\ L_{lr} = L_r - L_m & (b) \end{cases} \tag{2.49}$$

Based on the circuits, the stator and rotor voltage equations of *d-q* components are:

$$\begin{cases} u_{sd} = R_s i_{sd} + \dfrac{d\varphi_{sd}}{dt} - \omega_e \varphi_{sq} & (a) \\ u_{sq} = R_s i_{sq} + \dfrac{d\varphi_{sq}}{dt} + \omega_e \varphi_{sd} & (b) \end{cases} \quad (2.50)$$

$$\begin{cases} u_{rd} = R_r i_{rd} + \dfrac{d\varphi_{rd}}{dt} - \omega_{slip} \varphi_{rq} & (a) \\ u_{rq} = R_r i_{rq} + \dfrac{d\varphi_{rq}}{dt} + \omega_{slip} \varphi_{rd} & (b) \end{cases} \quad (2.51)$$

The flux equations of stator and rotor are expressed by:

$$\begin{cases} \varphi_{sd} = L_s i_{sd} + L_m i_{rd} & (a) \\ \varphi_{sq} = L_s i_{sq} + L_m i_{rq} & (b) \end{cases} \quad (2.52)$$

$$\begin{cases} \varphi_{rd} = L_m i_{sd} + L_r i_{rd} & (a) \\ \varphi_{rq} = L_m i_{sq} + L_r i_{rq} & (b) \end{cases} \quad (2.53)$$

The torque and power equations are:

$$T_e = \frac{3}{2} p_A \left(\varphi_{rq} i_{rd} - \varphi_{rd} i_{rq}\right) \quad (2.54)$$

$$= \frac{3}{2} p_A L_m \left(i_{sq} i_{rd} - i_{sd} i_{rq}\right) \quad (2.55)$$

$$= -\frac{3}{2} p_A \times Im\left(\overrightarrow{\varphi_s} \times \overrightarrow{i_s^*}\right) \quad (2.56)$$

$$P_s = \frac{3}{2} p_A (u_{sd} i_{sd} + u_{sq} i_{sq}) \quad (2.57)$$

$$Q_s = \frac{3}{2} p_A (u_{sq} i_{sd} - u_{sd} i_{sq}) \quad (2.58)$$

$$P_s + jQ_s = \overrightarrow{u_s} \times \overrightarrow{i_s^*} \quad (2.59)$$

$$P_r + jQ_r = \overrightarrow{u_r} \times \overrightarrow{i_r^*} \quad (2.60)$$

$$P_r = -s_1 P_s \quad (2.61)$$

Rotor copper power loss is:

$$P_{rcl} = i_r^2 R_r \tag{2.62}$$

The airgap power is:

$$P_{ag} = Re\left[\overrightarrow{E_{sm}} \times (-\overrightarrow{\iota_r})^*\right] \tag{2.63}$$

2.2.7. Control Methods Review of DFIG

As demonstrated above, the DFIG has more freedom of control. Of the two converters, the grid side converter acts as unity power factor interface to the grid for either direction of power flow to regulate the dc bus voltage while the rotor side inverter controls the machine [38].

2.2.7.1. Vector Control

Vector control is the earliest and simplest control method for DFIG. In early 1990s', the speed and grid power factor or alternatively efficiency control was most representative control method because of its low-cost micro-controller [26][39].

Field Oriented Control (FOC) of DFIG obtains almost as quick torque response as a dc machine [40], and improved the performance for fast changes in desired frequency. However, this torque response is unsatisfactory when the PWM inverter saturates. And the increase of inverter switch frequency, torque ripples and harmonic loss at steady state operation is hardly avoided [40]. Besides, in order to decide the gains or the expression of the PI controller, accuracy of machine parameters such as stator, rotor resistance and inductance, or mutual inductance, etc, is required [24][41]. The performance therefore degrades when the actual machine parameters are different from the values used in FOC system owing to magnetic saturation, temperature variation, etc [24][41]. In addition, to ensure system stability and adequate response

within the entire speed range, the current controller needs to be carefully turned [24]. What is more, FOC usually employs a position sensor to obtain the rotor angle for coordinate transformation between *d*-*q* and three-phase reference frame. Thus, the performance of system is dependent on the accuracy of the rotor position information derived from the position encoder [38]. DFIG sensorless scheme has several benefits in terms of robustness, cost, cabling and maintenance [42][43].

In many DFIG systems, there is a large physical separation between the generator and the back-to-back PWM inverter. The minimum interface between two equipments is therefore possible and so is a control without shaft position sensor [44].

Open loop method is the most popular strategy to construct a Position Sensorless Scheme (PSS) system where the estimated and measured rotor values are compared to derive the rotor position [32] [43]-[52]. There are two major estimators. One is based-on-rotor-current estimator [42],[43],[45]-[49]. In [48], the rotor current is estimated in the stator reference frame using stator variables. In [46], the most comprehensive system is proposed in 1998. In this system, a commercial product — ROTORDRIVE is presented in which an alternative rotor current estimator is proposed using load active and reactive power [42]. The other is rotor flux based estimator [32][50]. The rotor flux is obtained by integrating the rotor back EMF. This suffers from the integration problems — unexpected performance at or near synchronous speed due to the low or zero rotor frequency — which is one of the major challenges to design a PSS for a DFIG [42]-[44]. So the flux cannot be accurately estimated by integrating the PWM rotor voltage. Paper [32] reveals a case in point. It is not only the earliest research of rotor flux based estimator, but also a special study of PSS. In this paper, a dynamic torque angle controller is proposed [38]. The torque angle is defined as the spatial angle between the airgap flux and rotor current vector seen in synchronous reference frame. It sed FOC to align the airgap flux to *d*-axis of reference frame, the torque angle must be maintained at *90* degree. In other words, the current vector and airgap flux are vertical, and then the torque

angle can be found by two equations derived from torque and stator reactive power. However, in all of these papers or publications, the accuracy of rotor position and effect of parameter errors have not been addressed [42]. And the modelling, bandwidth, system dynamics, formal design procedures and methodology for whole PSS system are not considered as well [42][43].

So a new concept “Model Reference Adaptive System” (MRAS) appeared. In MRAS-based schemes, the rotor flux, stator current, stator flux and rotor current MRAS observer are applied to grid-connected system [42][43].

2.2.7.2. Direct Torque Control (DTC)

DTC concept is proposed in 1986 in paper [40]. It needs less dependence on machine parameters and causes the reduction of control complexity [53]. The machine torque is controlled directly by appropriate selection of voltage vector from a look-up-table using the stator flux and torque information [24][41]. The stator flux is usually estimated by integrating the stator voltage.

It is one disadvantage of basic DTC scheme that its performance deteriorates at the low speed operation condition [24][41][53]. This is largely due to the method of repeatedly selecting zero voltage vectors at low speed causing a voltage drop across stator resistance and resulting in flux level reduction [54]. Many methods proposed to address this problem such as using a dither signal [55], a modified switching table in order to apply all available voltage vectors in appropriate sequence [23], or predictive techniques [56].

Converter switching frequency variation is another drawback for DTC. It produces the significant complication of power circuit design. The hysteresis controller bandwidth must be selected carefully [57] to ensure that the switching frequency does not increase beyond the power converter’s maximum limitation for all operating modes. Space Vector Modulation (SVM) strategy has been utilised to achieve constant

switching frequency [58]-[61]. Inverter switching duty cycles in [58] were calculated directly, based on torque and flux errors within each sample period, whereas in [59] and [60] generated from PI controllers. Output voltage vector was selected from switching table in [61] but the voltage vector duration was determined by the torque ripple minimum strategy.

Extra shortcomings were proposed in previous surveys, such as complicated online calculation [58], additional PI controller parameters [59][60] and weak robustness on machine parameter variations [58]-[61].

Similar to DTC, in Direct Self Control (DSC), the machines are controlled, within the specified error bands, proper rotor voltage from a switching table [24][62], several virtues in terms of simplicity, robustness and yields fast dynamic response. However, the switching current and flux ripples are vital [63]. Further, the inverter average switching frequency varies with the operating conditions [63]. The unequal stresses on the switching devices are generated by variation of the switching frequency and difficulties of the design of the output filter are added [63]. Moreover, the accuracy of the rotor (or stator) flux linkage estimation is affected by the system performance [64].

2.2.7.3. Direct Power Control (DPC)

Derived from the principles of DTC strategy, DPC was developed to control DFIG [53][62]. Two representative strategies were proposed in [24] and [62]. The comparison of these two schemes is presented in Table. 1. In [62], the rotor flux was computed by the reactive power/power factor. Because the rotor supply frequency, which equals the DFIG slip frequency, can become very low, rotor flux estimation is significantly impacted by the machine parameter variations, while [24] proposed the use of stator flux estimator to address the problem. Since the stator (network) voltage is relatively harmonic-free with fixed frequency, a DFIG's estimated stator flux accuracy can be guaranteed. Thus, the control system is very simple, and the machine parameters' effect on system performance could be negligible [53].

	Estimator Basement	Switch Vector Selection
Paper [24]	Stator Flux	Switching Table Using Estimated Stator Flux Position & errors of the rotor flux & active power/torque
Paper [62]	Rotor Flux	Switching Table Using Estimated Rotor Flux Position & errors of the rotor flux & active power/torque

Table 2.2 The Comparison of Two DPC Method

However, like a conventional DTC, switching frequency of DPC varies critically, leading to the impact of active and reactive power variations, machine operating speed (rotor slip), and the power controllers' bandwidth [53].

A special DPC without rotor position sensor was presented by Rajib Datta and V.T.Ranganathan in [38], and will be implemented in this thesis. In the analysis, the active power P_s will be changed due to the change of the angle between *d*-axis and rotor flux vector δ, while Q_s the can be reduced by increase of the magnitude of the rotor flux φ_r. P_s and Q_s, therefore, can be controlled by the angular position and magnitude of rotor flux vector respectively.

The application of different voltage vectors would result in the reduction or increase of P_s and Q_s. Zero vectors can make P_s increase in sub-synchronous mode and decrease in super-synchronous, but its effect on Q_s is rather small. Nevertheless, the direction of change in Q_s can help us to estimate the rotor position. The details of this DPC will be introduced in Chapter 6.

2.3. Brushless Doubly-Fed Reluctance Generator (BDFRG)

The brushless doubly-fed machine (BDFM) has two standard, sinusoidally distributed, stator windings of different pole numbers and applied frequencies. In order to provide rotor-position dependent magnetic coupling between them, which is a pre-requisite for the machine to produce useful torque, the rotor poles number must be half of the total number of stator poles. Although design solutions with odd rotor pole numbers (e.g., *3* in case of a *4*-pole/*2*-pole stator) are possible, unlike a conventional machine, the "proof-of-concept" BDFMs with *6*-pole/*2*-pole stator windings and a *4*-pole rotor have been most frequently reported in the literature. The BDFM with a cage-less reluctance rotor is known as the Brushless Doubly-Fed Reluctance Machine (BDFRM).

The brushless doubly-fed reluctance generator has the similar converters and other components compared to the doubly-fed induction generator except the machine structure. The DFIGs possess a wound rotor induction machine, while the BDFRGs own a reluctance rotor between two windings. As shown in the Figure 2.13 and Figure 2.14, the DFIG's stator and rotor windings are both of p_A pole pairs, however, the BDFRG has one $2p$ poles stator and one $2q$ poles stator. The pole-pair number of BDFRG rotor is stipulated as $\frac{p+q}{2}$ and BDFRG pole pair number is $p_B = p + q$. The stator with $2p$ poles is called first or primary stator and the other is named secondary stator. In the later sections, the primary stator is also called the main stator depending upon its importance or the power rating according to its function. Correspondingly, the secondary stator is named as auxiliary or control stator. It will be no more explanation about the appellation in the discussion below.

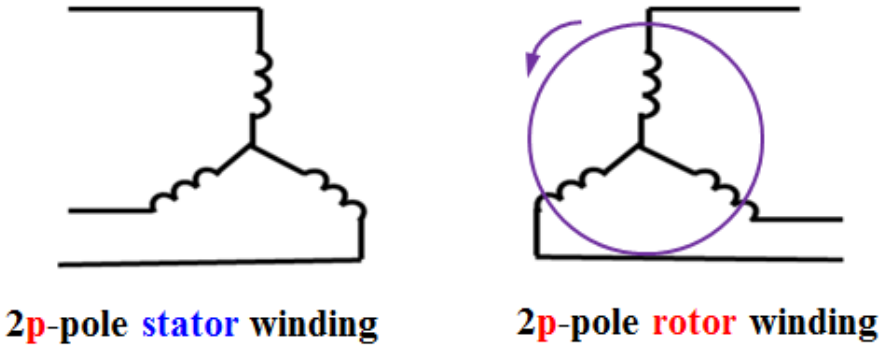

Figure 2.13 DFIG windings structure

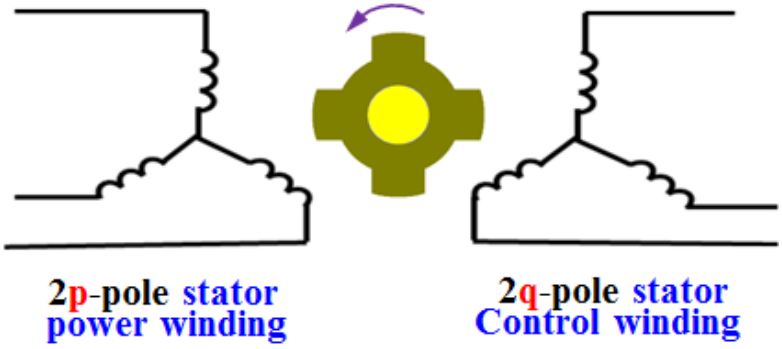

Figure 2.14 BDFRG windings structure

BDFRG has the same converters and transformer as DFIG while the performance and power flow analysis is quite similar to the DFIG. Thus, we do not state them again. What the content written here is the difference from DFIG.

2.3.1. The reluctance generator

BDFRG has eliminated the brushes and slip rings, which may increase the reliability and reduce maintenance. But, the BDFRG will be larger than the DFIG for the same power or will produce less output when the machines have the same size.

The power and control windings of the DFIG are located on the stator and rotor respectively. However, both the power winding and control winding for the BDFRG are located on the stators (primary and secondary stators). DFIG's stator and rotor

have the same pole number, but BDFRG's secondary stator normally has a lower pole number than the primary stator. This structure makes the stator slot size of BDFRG far larger than the stator slots of the DFIG when BDFRG primary stator has the same pole number as DFIG stator. The slots of the BDFRG will be deep compared to DFIG's for the same width of stator tooth.

The yoke height of stator core is inversely proportional to the pole number. Hence the BDFRG has much greater stator core yoke height compared to the DFIG with the same pole number, as the flux of the control winding needs large yoke area to pass through.

As mentioned above, the heights both of the slot and core yoke for the BDFRG are larger than DFIG's. The inner diameter of stator core for the BDFRG will be much smaller than the DFIG's. As a result, the induced back EMF of the windings for the BDFRG will be decreased due to the reduced rotor diameter for the same rotor speed in comparison with the DFIG. The power output of the machine is the product of back EMF and current of the windings. Therefore, the output power of the BDFRG will be much less than that of the DFIG.

2.3.1.1. BDFRG inductance

From the BDFRG windings picture, clearly, the machine looks like a symmetrical structure. If we 'see' this reluctance machine from one side of stator and neglected the other, it is quite similar to a switch reluctance machine. Thus this generator's inductance may be considered as superposition of two switch reluctance machines.

BDFRG's inductance is quite like the switching reluctance machine. A switching reluctance machine's inductance determination has been demonstrated in Appendix A. The superposition makes the machine flux density much higher even to the peak at the saturation. This leads to the smoother highest and lowest inductance in 'Inductance vs. rotor position' graph. Thus the BDFRG's 'Inductance vs. rotor position'

graph looks like a sinusoidal waveform. The inductance variations will be proved in the parameter test in Chapter 4.

As the BDFRG normally produces less output when the machines have the same size, in order to increase the BDFRG output power in the same size, barriers are inserted to the rotor in Prof. Wang's design. The details have been presented in Sector 2.3.1.2.

This structure brings about larger flux density and more saturation in the BDFRG. The higher flux density will lead to the higher flux and cause the larger inductance in the same power level. It will be evidenced in Chapter 4 that the BDFRG has far larger inductance than DFIG.

2.3.1.2. Rotor structure

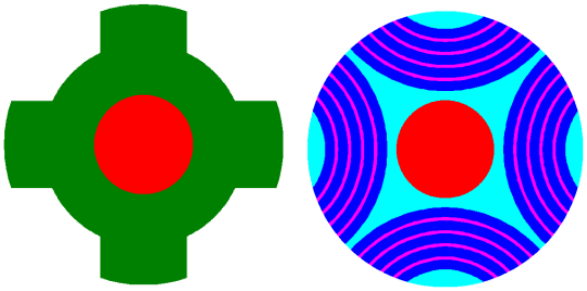

Figure 2.15 (Left) Salient pole rotor (SPR) (Right) Radially laminated rotor (RLR)

	SPR	RLR
Advantages	● Simple structure ● Low cost	● Good performance
Disadvantages	● Poor performance	● Complicated structure ● Difficult to build

Table 2.3 Comparison of two rotor structures

The most important part of BDFRG is the reluctance rotor. Its structure will affect the performance of BDFRG. Normally, BDFRG has two kinds of rotor structure: Salient Pole Rotor (SPR) and Radially Laminated Rotor (RLR) as shown in Figure 2.15. The advantages and drawbacks are demonstrated in Table 2.3.

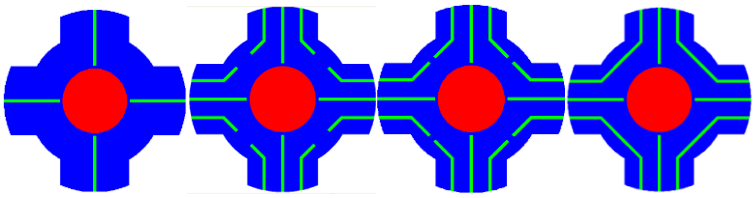

Figure 2.16 Different rotor structures within flux barriers [65]

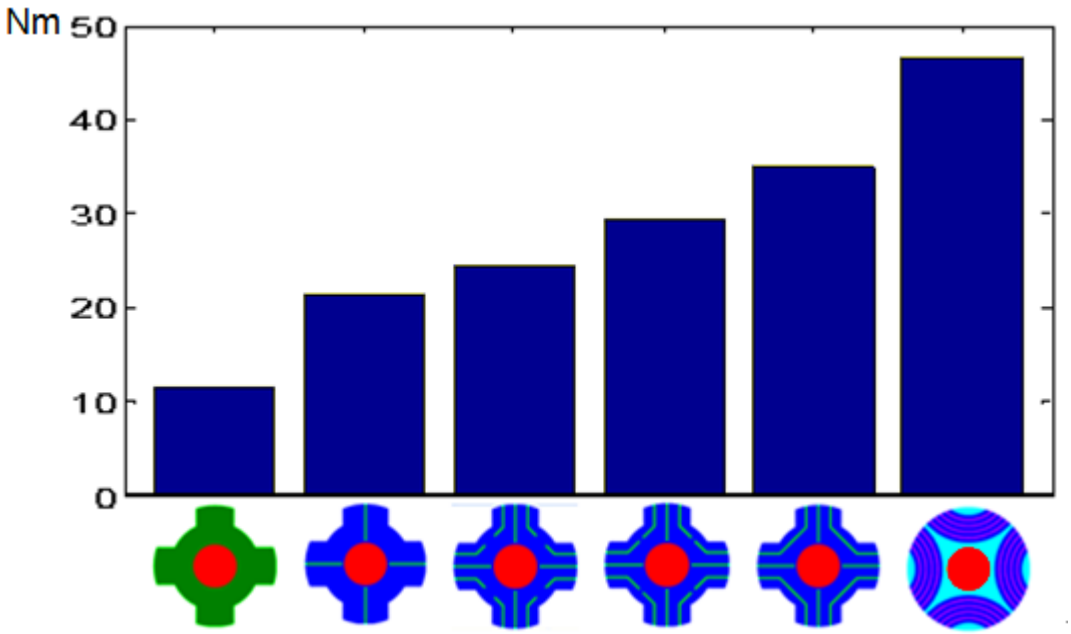

Figure 2.17 Torque comparison for different rotors [65]

In order to balance the structure and performance, the SPR has inserted flux barriers to improve the performance within reasonable cost [65]. Figure 2.16 shows the different rotor structures with increasing barriers from left to right. The research on the relationship between torque and the number of barriers has been done by the collaborator Prof. Wang in Shenyang of Technology University and illustrated in Figure 2.17. It evidences that the performance increases with more flux barriers.

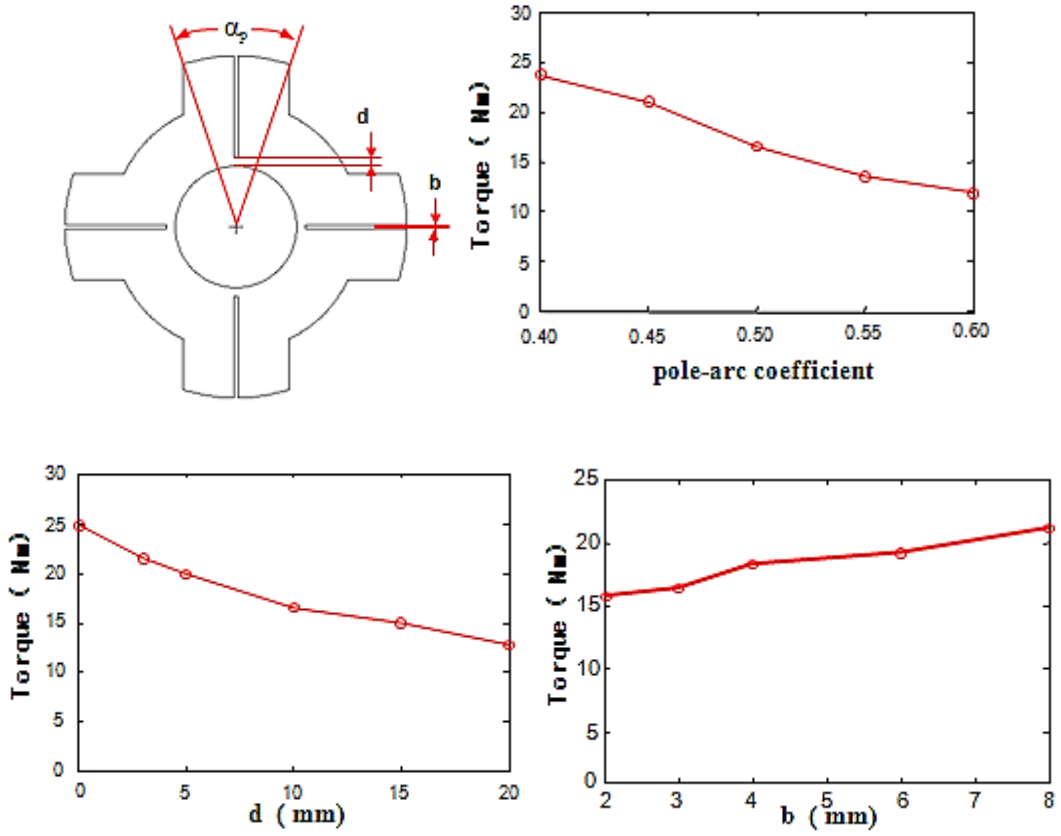

Figure 2.18 Influence of pole-arc coefficient α_p, magnetic barrier's depth d and magnetic barrier's width b on torque [65][66]

However, taking account of the costs of manufacture, the rotor with one barrier in each pole is selected by Prof. Wang for the BDFRG design [66]. The pole-arc coefficient α_p, magnetic barrier's depth d and magnetic barrier's width b all have effects on the torque as displayed in Figure 2.18 [65][66]. The machine performance would be apparently improved if the rotor has smaller pole-arc coefficient and the shorter but wider magnetic barriers.

2.3.2. BDFRG mathematic model

The BDFRG has similar mathematic model to the DFIG. Equations. 2.64 - 2.69 express the same primary stator and secondary stator space vectors viewed in three

different reference frames. Superscripts indicate which reference frame the vector is referred in, while subscripts represent the power or control windings.

Firstly in the stator frame:

$$\begin{cases} \overrightarrow{u_p^p} = R_p \overrightarrow{i_p^p} + \dfrac{d\overrightarrow{\varphi_p^p}}{dt} & (a) \\ \overrightarrow{u_c^p} = R_c \overrightarrow{i_c^p} + \dfrac{d\overrightarrow{\varphi_c^p}}{dt} - j\omega_c \overrightarrow{\varphi_c^p} & (b) \end{cases} \tag{2.64}$$

$$\begin{cases} \overrightarrow{\varphi_p^p} = L_p \overrightarrow{i_p^p} + L_m \overrightarrow{i_c^p} & (a) \\ \overrightarrow{\varphi_s^s} = L_m \overrightarrow{i_s^s} + L_r \overrightarrow{i_r^s} & (b) \end{cases} \tag{2.65}$$

Secondly, in the rotor frame:

$$\begin{cases} \overrightarrow{u_p^c} = R_p \overrightarrow{i_p^c} + \dfrac{d\overrightarrow{\varphi_p^c}}{dt} + j\omega_c \overrightarrow{\varphi_p^c} & (a) \\ \overrightarrow{u_c^c} = R_c \overrightarrow{i_c^c} + \dfrac{d\overrightarrow{\varphi_c^c}}{dt} & (b) \end{cases} \tag{2.66}$$

$$\begin{cases} \overrightarrow{\varphi_p^c} = L_p \overrightarrow{i_p^c} + L_m \overrightarrow{i_c^c} & (a) \\ \overrightarrow{\varphi_c^c} = L_m \overrightarrow{i_p^c} + L_c \overrightarrow{i_c^c} & (b) \end{cases} \tag{2.67}$$

Finally, in the excitation frame:

$$\begin{cases} \overrightarrow{u_p^e} = R_p \overrightarrow{i_p^e} + \dfrac{d\overrightarrow{\varphi_p^e}}{dt} + j\omega_e \overrightarrow{\varphi_p^e} & (a) \\ \overrightarrow{u_c^e} = R_c \overrightarrow{i_c^e} + \dfrac{d\overrightarrow{\varphi_c^e}}{dt} + j(\omega_e - \omega_c)\overrightarrow{\varphi_c^e} & (b) \end{cases} \tag{2.68}$$

$$\begin{cases} \overrightarrow{\varphi_p^e} = L_p \overrightarrow{i_p^e} + L_m \overrightarrow{i_c^e} & (a) \\ \overrightarrow{\varphi_c^e} = L_m \overrightarrow{i_p^e} + L_c \overrightarrow{i_c^e} & (b) \end{cases} \tag{2.69}$$

2.3.3. Control Methods Review of BDFRG

Till now, the published paper presented the control strategies all relative to Brushless Doubly-Fed Reluctance Motor (BDFRM) rather than BDFRG. The existing BDFRM control literature has been mostly concerned with the development of various control strategies for the optimum machine operation [67][68] and vector controllers for their implementation using a shaft position sensor [69][70]. The sensorless scheme for the BDFRM has been reported in [71] but without supporting test results to clearly demonstrate its successful practical realisation. Some papers, published by my collaborators, have also considered aspects of scalar control for “pump-alike” applications of the BDFRM [68][72], and more recently direct torque control (DTC) [72][73]. A sensorless DTC scheme proposed and experimentally verified in [72][73] does not suffer from the usual limitations of the traditional DTC concepts identified above and allows stable machine operation down to zero applied frequency of the inverter-fed (secondary) winding.

During the PhD study period, my collaborator, Chaal Hamza implemented a robust and versatile sensorless DPC on BDFRM and published a paper [74]. The DPC has never been applied to BDFRM before. Then he develops a sensorless torque and reactive power control in [75], [76] and [77].

3. DFIG Fault Response and Fault Ride Through

The experimental fault ride through performance comparison of DFIG and BDFRG was originally planned, but due to shortage of time it could not be carried out. That is the reason I dedicating a full chapter for DFIG fault response and fault ride through.

A dynamic model of the DFIG has been developed in this chapter for later used in comparisons with the BDFRG under DPC in Chapter 6. To validate the model, simulation results are compared with the experimental results produced by Pannell [11]. The experimental results in Pannell [11] are for grid fault conditions. Therefore this chapter will first review grid faults and fault ride through.

The grid faults and fault ride through requirements are introduced in the initial section of this Chapter as the preparation of the DFIG fault response and FRT method studies. A zero fault response is discussed is Section 3.2 by analytical solution with details in Appendix F and test response is validated by the simulation. A crowbar control method is studied from Graham Pannell thesis in last section. The DFIG model created by Matlab/Simulink is controlled by this crowbar method. In comparison with experiment result, the simulation model is evidenced as an almost errorless system.

3.1. Grid faults and fault ride through

A grid fault is a short circuit or earthing on one or more phases of grid system, and mainly has three situations: (i) instantaneous earthing of a single line (ii) two lines clash (iii) three-phase short circuit.

3.1.1. Fault withstand, clearance, recovery and definition

When the fault occurs, the generator close to the fault has two possible responses: disconnecting itself from the grid or continuing to operate. A synchronous generator, typically, has an inherent ability to remain connected, while the non-synchronous generators such as DFIGs disconnect from the grid. International grid codes now require generators to remain connected on transmission systems. Without this ability, the risks of widespread customer disconnection may be significant. Alternatively, the number of future wind farm installations will be severely restricted.

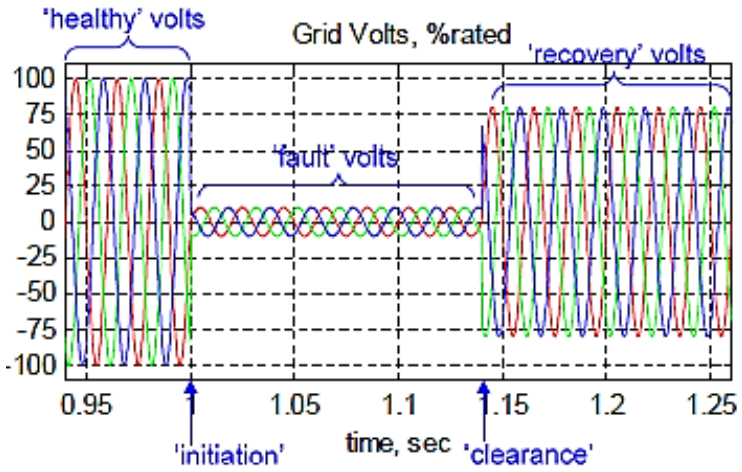

Figure 3.1 Three-phase voltage, balanced grid fault example.

A typical voltage profile during a grid fault event is shown in Figure 3.1. The fault occurs at the point labelled ‘initiation’. The fault condition persists until the point labelled ‘clearance’ where circuit breakers isolate the fault. The fault recovery period is defined as the period in which the network may continue to operate with slightly suppressed voltage after fault clearance until the isolated transmission equipment is restored.

The grid fault is characterised as a voltage dip on one or more phases of transmission line due to short circuit or earthing. The fault period would start from the ‘initiation’ point in Figure 3.1 and end at the fault clearance point. The fault recovery is not

included in the fault because the voltage returns to a much higher level than the fault voltage due to isolation of the fault. Equal dip in voltage for all three phases is called a balanced fault while different three phase voltage dips is known as an unbalance fault.

3.1.2. Fault event of wind farm in China

During the grid fault, the sensitivities to low voltages of the equipment will automatically cause the generator to disconnect from the grid, resulting in a sudden imbalance of the net power. There is a risk that a large number of the generators will be disconnected because of the uncontrolled real and reactive power and continued voltage suppression. Then the grid frequency will rapidly drop and become unstable, bringing about the cascade tripping off of the further generation units and forcing widespread consumer disconnection. In a catastrophic case, this can lead to the widespread blackouts.

A typical fault example of this situation occurred in Jiuquan of China on *24*th Feb 2011 [78]. This accident was caused by an insulation breakdown of a cable around a switch. The three-phase short circuit led to *274* wind generator systems in *10* wind farms disconnecting from the grid during the fault because of none of low voltage ride through capability. Approximate *598* wind generators tripped out of the main grid due to this malfunction. The electricity loss was over *54.4%* of wind power in entire Jiuquan area. The frequency of northwest grid of China dropped from *50.034Hz* to *49.854Hz*. This situation caused gigantic economic losses of China.

Based on the analysis of Chinese government, there were two main reasons for the problem. One reason was that a large number of wind generator systems did not have the ability to pass through the low voltage fault condition. This situation caused a high risk of dropping out from the grid during the voltage dips and a potential safety hazard for the entire system, when a wind farm was connected to the grid. The other

reason was that China did not have a unified standard of grid code. Some wind farms only had informal “generation transmission custom”. The lack of fault ride through ability and formal grid code requirements gave rise to widespread vulnerability in the Chinese power system.

3.1.3. Fault ride through requirements

In the above event, once the grid fault happened, all the wind power generators disconnected from the grid for machine equipment protection reasons. As a result, the grid voltage and frequency could not be maintained. The behaviour of a generator in the fault period acted against the stability of entire system. Thus, the new transmission system grid codes request that wind turbine machines do not disconnect themselves from power network during a fault. They remain connected and supply active and reactive power into the network to support the power system during a fault condition. This means that wind turbines must ‘ride through’ the fault.

These rules were initially described by a German expert [79]. Now they have become a common requirement in the wind energy generation systems. Many grid codes have these rules. For example, National Grid Company who supplies the electricity to the UK requires that all wind farms or electrical stations should remain connected for *140ms* when a fault occurs in transmission system rated above *200kV* [80]. Besides, Scottish Hydro Electrical Company also has similar requirements: the wind turbine was not allowed to trip out during a fault condition [81].

Nowadays, the main issues for the FRT from the point of view of the transmission system are to support grid stability. This means to remain connected during a voltage dip, and to supply the active and reactive power outputs. This will support system frequency and local voltage.

Fault ride through behaviours can be provided at wind turbine level, by engineering the individual wind turbines to provide the required response. It can also be achieved

at wind farm level, by employing additional auxiliary equipment at the wind farm substation. The former solution avoids adding potentially costly wind farm level equipment. The experiments validated in this thesis were carried out by Pannell [11] with the former FRT level.

3.2. Analytical solution for induction machine fault response

The analytical procedure is detailed in Appendix F with the induction machine response for both zero and non- zero voltage faults. However, this section only compares the stator and rotor currents fault response of both test and simulation when the fault voltage is zero.

3.2.1. Assumptions

Four key assumptions are the prerequisite for the analytical solution. Firstly, the derivation of an analytical solution is based on the generalized machine equations, thus the generator is assumed as an ideal symmetrical non-salient poly-phase induction machine with a sinusoidal MMF distribution and a narrow, uniform airgap. Secondly, the machine inductance is considered as constant in the analysis. It requests the assumption of negligible magnetic saturation. But this assumption is impossible in actual machine. However, the saturation may be better under the fault operation. So this supposition still applied for the mathematical convenience. Thirdly, the rotor speed is thought as constant under the voltage drop. Finally, the machine mechanical transient timescales are assumed to be far slower than the voltage dip.

3.2.2. Laplace-transform solution [11]

With the progress of re-arrangement, substitution and utilization of transient time constants:

$$\tau_s = \frac{L'_s}{R_s} = \frac{\sigma L_s}{R_s}, \qquad \tau_r = \frac{L'_r}{R_r} = \frac{\sigma L_r}{R_r} \tag{3.1, 3.2}$$

the generalized induction machine flux equations can be re-combined as:

$$\overrightarrow{u_s^s} = \frac{1}{\tau_s}\left(\overrightarrow{\varphi_s^s} - \frac{L_m}{L_r}\overrightarrow{\varphi_r^s}\right) + \frac{d\overrightarrow{\varphi_s^s}}{dt} \tag{3.3}$$

$$\overrightarrow{u_r^s} = \frac{1}{\tau_r}\left(\overrightarrow{\varphi_r^s} - \frac{L_m}{L_s}\overrightarrow{\varphi_s^s}\right) + \frac{d\overrightarrow{\varphi_r^s}}{dt} - j\omega_r\overrightarrow{\varphi_r^s} \tag{3.4}$$

Assume the rotor has constant speed, the linear first order differential equations 3.3 and 3.4 permits the utilization of Laplace transform, taking zero stator voltage, the stator flux linkage becomes:

$$\overrightarrow{\Psi_s^s}(v) = \frac{\left(\frac{1}{\tau_r} - j\omega_r + v\right)\overrightarrow{\varphi_{s0}^s} + \frac{L_m}{\tau_s L_r}\overrightarrow{\varphi_{r0}^s}}{\left[\left(\frac{1}{\tau_r} - j\omega_r + v\right)\left(\frac{1}{\tau_s} + v\right) - \frac{(1-\sigma)}{\tau_s\tau_r}\right]} + \frac{\frac{L_m}{\tau_s L_r}\overrightarrow{U_r^s}(v)}{\left[\left(\frac{1}{\tau_r} - j\omega_r + v\right)\left(\frac{1}{\tau_s} + v\right) - \frac{(1-\sigma)}{\tau_s\tau_r}\right]} \tag{3.5}$$

where v is the variable of the Laplace transformer. The denominator roots α and β are complex constants and determine both the rate of natural flux linkage decay and dominant frequency components of the solution. They depend upon the transient time constants, the leakage factor and the rotor speed shown in equations 3.6 and 3.7:

$$\alpha = \tau_s^{-1} - \varsigma_f \qquad\qquad \beta = \tau_r^{-1} - j\omega_r + \varsigma_f \tag{3.6, 3.7}$$

where a small complex frequency adjustment parameter is defined as :

$$\varsigma_f = \frac{(1-\sigma)/\tau_s\tau_r}{\omega_r} \angle \left(90^0 - \tan^{-1}\left\{\frac{\frac{1}{\tau_r} - \frac{1}{\tau_s}}{\omega_r}\right\}\right) \tag{3.8}$$

The real and imaginary frequency adjustment components can be estimated by the transient time constants:

$$\tau_s \approx \tau_r \gg 1 \qquad \therefore \frac{\frac{1}{\tau_r} - \frac{1}{\tau_s}}{\omega_r} \ll 1, \tag{3.9}$$

$$Re(\varsigma_f) = \kappa \approx \frac{(1-\sigma)}{{\omega_r}^2 \tau_s \tau_r}\left(\frac{1}{\tau_r} - \frac{1}{\tau_s}\right) \qquad Im(\varsigma_f) = \delta \approx \frac{(1-\sigma)}{\omega_r \tau_s \tau_r} \tag{3.10, 3.11}$$

Equation 3.8 reveals that δ is a small positive number as indicated by following equations:

$$f_{own\_circuit} = \delta \qquad f_{mutual} = (\omega_r - \delta) \tag{3.12, 3.13}$$

$$f_{own\_circuit} > 0 \qquad f_{mutual} < \omega_r \tag{3.14, 3.15}$$

The effective decay frequencies are described in the main text as ‘near-dc’ and ‘near-rotor’ speed. The real component of the complex frequency adjustment parameter κ is typically smaller than the imaginary component and its effect enlarges the difference between the effective stator and rotor transient time constants compared with the initial values as shown in equation 3.18.

$$\tau_s'^{-1} = (\tau_s^{-1} - \kappa) \qquad \tau_r'^{-1} = (\tau_r^{-1} + \kappa) \tag{3.16, 3.17}$$

$$|\tau_r' - \tau_s'| > |\tau_r - \tau_s| \tag{3.18}$$

3.2.3. Natural response analysis [11]

Looking close to stator flux equation 3.5, it can be found that two elements called ‘natural response’ and ‘forced response’ respectively comprise this equation as shown in equation 3.19. The natural response is formed by the initial conditions while the force response depends on the rotor voltage. The two components can be solved independently due to linear superposition.

$$\overrightarrow{\Psi_s^s}(v) = \frac{\left(\frac{1}{\tau_r} - j\omega_r + v\right)\overrightarrow{\varphi_{s0}^s} + \frac{L_m}{\tau_s L_r}\overrightarrow{\varphi_{r0}^s}}{\left[\left(\frac{1}{\tau_r} - j\omega_r + v\right)\left(\frac{1}{\tau_s} + v\right) - \frac{(1-\sigma)}{\tau_s\tau_r}\right]} \quad \ldots\ldots\ldots\ldots Natrual\ Response$$

$$+ \frac{\frac{L_m}{\tau_s L_r}\overrightarrow{U_r^s}(v)}{\left[\left(\frac{1}{\tau_r} - j\omega_r + v\right)\left(\frac{1}{\tau_s} + v\right) - \frac{(1-\sigma)}{\tau_s\tau_r}\right]} \quad \ldots\ldots\ldots\ldots Forecd\ Response \qquad (3.19)$$

Solving the equation 3.19 by inversing Laplace transformation will produces the equation 3.20:

$$\overrightarrow{\varphi_s^s}(t) = \left(\overrightarrow{\varphi_{s0}^s} + A_s^s\right) e^{-\frac{t}{\tau_s'^{-1}}} e^{j\delta t} \quad \ldots\ldots\ldots\ldots\ldots\ldots\ldots\ldots Near - DC$$

$$-A_s^s e^{-\frac{t}{\tau_r'^{-1}}} e^{j(\omega_r - \delta)t} \quad \ldots\ldots\ldots\ldots\ldots\ldots\ldots Near - rotor\ speed \qquad (3.20)$$

where

$$A_s^s = \frac{(\delta + j\kappa)\overrightarrow{\varphi_{s0}^s} + j\left(k_r/\tau_s\right)\left(\overrightarrow{\varphi_{r0}^s}\right)}{(\omega_r - 2\delta) + j(\tau_r'^{-1} - \tau_s'^{-1})} \qquad (3.21)$$

$$k_r = \frac{L_m}{L_r} \qquad (3.22)$$

Then the stator current can be derived by using the generalized induction machine voltage equation with zero stator voltage:

$$0 = R_s\overrightarrow{\imath_s^s} + \frac{d\overrightarrow{\varphi_s^s}}{dt} \qquad (3.23)$$

$$\overrightarrow{i_s^s}(t) = \frac{\left(\overrightarrow{\varphi_{s0}^s} + A_s^s\right)(\tau_s'^{-1} - j\delta)}{R_s} e^{-\frac{t}{\tau_s'^{-1}}} e^{j\delta t} \quad \ldots\ldots\ldots\ldots\ldots Near - DC$$

$$- \frac{A_s^s\left(\tau_r'^{-1} - j(\omega_r - \delta)\right)}{R_s} e^{-\frac{t}{\tau_r'^{-1}}} e^{j(\omega_r - \delta)t} \quad \ldots\ldots\ldots\ldots Near - rotor\ speed \qquad (3.24)$$

This expression can be simplified by using the time constant approximation from equation 3.9 and ignoring any coefficient terms of the order τ^2 or smaller.

$$A_s^s \approx j\frac{k_r \overrightarrow{\varphi_{r0}^s}}{\omega_r \tau_s} \qquad (3.25)$$

$$\overrightarrow{i_s^s}(t) \approx \frac{1}{L_s'} \overrightarrow{\varphi_{s0}^s} e^{-\frac{t}{\tau_s'^{-1}}} e^{j\delta t} - \frac{k_r}{L_s'} e^{-\frac{t}{\tau_r'^{-1}}} e^{j(\omega_r - \delta)t} \qquad (3.26)$$

Equation 3.26 gives the approximation of stator current.

Using the same method and procedures as for the stator flux solution, the rotor flux under the constant rotor speed and zero stator voltage can be derived as:

$$\overrightarrow{\varphi_r^r}(t) = A_r^r e^{-t/\tau_s'^{-1}} e^{-j(\omega_r - \delta)t} + \left(\overrightarrow{\varphi_{r0}^r} - A_r^r\right) e^{-t/\tau_r'^{-1}} e^{-j\delta t} \qquad (3.27)$$

where

$$A_r^r = \frac{-(\delta + j\kappa)\overrightarrow{\varphi_{r0}^r} + j\left(k_s/\tau_s\right)\overrightarrow{\varphi_{s0}^r}}{(\omega_r - 2\delta) + j(\tau_r'^{-1} - \tau_s'^{-1})} \qquad (3.28)$$

$$k_s = \frac{L_m}{L_s} \qquad (3.29)$$

$$0 = R_r \overrightarrow{i_r^r} + \frac{d\overrightarrow{\varphi_r^r}}{dt} \qquad (3.30)$$

$$\overrightarrow{i_r^r}(t) = \frac{(\tau_s'^{-1} - j\delta)\left(\overrightarrow{\varphi_{r0}^r} - A_r^r\right)}{R_r} e^{-\frac{t}{\tau_r'^{-1}}} e^{-j\delta t} \quad \ldots\ldots\ldots\ldots Near - DC$$

$$+ \frac{A_r^r\left(\tau_r'^{-1} - j(\omega_r - \delta)\right)}{R_r} e^{-\frac{t}{\tau_s'^{-1}}} e^{-j(\omega_r - \delta)t} \quad \ldots\ldots\ldots\ldots Near - rotor\ speed \qquad (3.31)$$

$$A_r^r \approx j\frac{k_s\overrightarrow{\varphi_{s0}^r}}{\omega_r \tau_r} \qquad (3.32)$$

$$\overrightarrow{i_r^r}(t) \approx \frac{1}{L_r'}\overrightarrow{\varphi_{r0}^r} e^{-\frac{t}{\tau_r'^{-1}}} e^{-j\delta t} - \frac{k_s}{L_r'} e^{-\frac{t}{\tau_s'^{-1}}} e^{-j(\omega_r - \delta)t} \qquad (3.33)$$

3.2.4. Comparison of experiment and simulation

The main purpose of this comparison is to validate the generalized machine simulation model under the voltage dips. The experiment is of the test rig configured as an induction machine, with the three phases of the wound-rotor physically short-circuited as shown in Pannell's thesis Chapter 4 [11].

The machine was setup to generate 7*kW* at a steady speed of *1530rpm* prior to the fault [11]. As the rated power of the experiment test generator is *7.5kW* and speed is *1500rpm*, the power and speed were set to *0.93* and *1.02* as the *p.u.* value. In the experimental test of a grid fault the stator voltage was dropped to zero *1.0s* after data-recording started. In order to compare directly with the analytical solution in section 3.2.3, only the stator and rotor currents are displayed.

3.2.4.1. The simulation parameters

The generator was modelled in Matlab/Simulink with the parameters given in the table below. In this model, the power devices were modelled as ideal switches. The voltage changed from healthy condition to fault immediately without any time delay

and the slip was fixed. The parameters are shown in table below obtained from [11], with the *p.u* value given as well.

Parameters	**Values**	**p.u value**
Power	7.5 KW	1
Pole number	4	
Stator voltage, line	415V	1
Stator current, phase (thermal)	14.7A	
Stator current, phase	10.4A	1
Rotor voltage, line (zero-speed)	1290V	1
Rotor current, phase (thermal)	3.60A	
Rotor current, phase	3.35A	1
Referred Stator Resistance (per-phase)	$0.68 \pm 0.005\Omega$	0.03
Referred Rotor Resistance (per-phase)	$0.46 \pm 0.005\Omega$	0.02
Referred Stator Leakage Inductance (per-phase)	$9.04 \pm 0.08mH$	0.0124
Referred Rotor Leakage Inductance (per-phase)	$9.04 \pm 0.08mH$	0.0124
Mutual Inductance	$226 \pm 11mH$	3.1
Turns ratio	0.32 ± 0.01	

Table 3.1 the Parameters of Machine Model [11]

The steady state equations can be obtained when the stator current and stator voltage are known:

$$\overrightarrow{\varphi_s^e} = -j\left(\overrightarrow{u_s^e} - R_s\overrightarrow{\imath_s^e}\right) \tag{3.34}$$

$$\overrightarrow{i_r^e} = \frac{1}{L_m}\left(\overrightarrow{u_s^e} - R_s\overrightarrow{i_s^e}\right) \tag{3.35}$$

$$\overrightarrow{\varphi_r^e} = L_r\overrightarrow{i_r^e} + L_m\overrightarrow{i_s^e} \tag{3.36}$$

3.2.4.2. Induction machine model

The machine model described in many papers is based on the excitation reference frame. But my model built in this thesis is based on the stator reference frame, in order to avoid the complicated stator-excitation and rotor-excitation transformation troubles. The model's stator vectors are viewed in stator reference frame, and the rotor vectors are referred to the stator reference frame by a transform. Compared to the model on excitation reference frame, my model has less transform. This causes the Matlab running time savings.

$$\begin{cases} \overrightarrow{u_s^s} = R_s\overrightarrow{i_s^s} + \dfrac{d\overrightarrow{\varphi_s^s}}{dt} & (a) \\ \overrightarrow{u_r^r} = R_s\overrightarrow{i_r^r} + \dfrac{d\overrightarrow{\varphi_r^r}}{dt} & (b) \end{cases} \tag{3.37}$$

$$\begin{cases} \overrightarrow{\varphi_s^s} = L_s\overrightarrow{i_s^s} + L_m\overrightarrow{i_r^r}e^{j\theta_r} & (a) \\ \overrightarrow{\varphi_r^r} = L_m\overrightarrow{i_s^s} + L_r\overrightarrow{i_r^r}e^{-j\theta_r} & (b) \end{cases} \tag{3.38}$$

$$\begin{cases} \overrightarrow{V^s} = \overrightarrow{V^r}\, e^{j\theta_r} & (a) \\ \overrightarrow{V^r} = \overrightarrow{V^s}e^{-j\theta_r} & (b) \end{cases} \tag{3.39}$$

Where the θ_r is the angle between the stator and rotor reference frame, the $\vec{V}$ means a vector quantity, the subscripts *s* and *r* represent the stator and rotor values, and the superscripts *s* and *r* indicate the stator or rotor reference frame. If the value is without the superscripts, it means that this value is measured under the excitation reference frame. Thus, depending upon the (3.38) and (3.39), it is obtained that:

$$\begin{cases} L_m\overrightarrow{\varphi_s^s}e^{-j\theta_r} - L_s\overrightarrow{\varphi_r^r} = K_1\overrightarrow{\imath_r^r} & (a) \\ L_m\overrightarrow{\varphi_r^r}e^{j\theta_r} - L_r\overrightarrow{\varphi_s^s} = K_1\overrightarrow{\imath_s^s} & (b) \end{cases} \quad (3.40)$$

In which $K_1 = \frac{1}{K} = L_m^2 - L_sL_r$. According to the (3.40) together with (3.37) and (3.38), the model of DFIG is constructed with the parameters in Table 3.1.

We have known from above conclusion that the forced response depends on the rotor voltage. In this model, the rotor voltage was set to zero, thus, only the natural machine response was illustrated in this case. Initial steady-state conditions were used: *1.0 p.u.* stator voltage and *0.93 p.u.* power generation to match *7kW* experimental test, corresponding to *50Hz* supply voltage. This set the *d*-component of stator current at *-0.93 p.u*. At this time, the stator current was unknown. Equations 3.34, 3.35 and 3.36 cannot be obtained when only *d*-axis of stator current is given.

The machine equations can be solved in the steady-state. In this case all time derivatives are set to zero. The equations below can be obtained from voltage and flux equations of the generalized induction machine model (noting that $\omega_e = 1\ p.u.$):

$$\begin{cases} \overrightarrow{u_s^e} = R_s\overrightarrow{\imath_s^e} + j\ L_s\overrightarrow{\imath_s^e} + jL_m\overrightarrow{\imath_r^e} & (a) \\ 0 = R_s\overrightarrow{\imath_r^e} + j\ L_r\overrightarrow{\imath_r^e} + jsL_m\overrightarrow{\imath_s^e} & (b) \end{cases} \quad (3.41)$$

Get $\overrightarrow{\imath_r^e}$ from (a) and substitute to (b), then:

$$(R_r + jsL_r)\overrightarrow{u_s^e} = \{(R_sR_r + s\sigma L_sL_r) + j(R_rL_s + sL_rR_s)\}\overrightarrow{\imath_s^e} \quad (3.42)$$

In this equation, only stator current vector $\overrightarrow{\imath_s^e}$ and slip s are unknown. If it is separated into the *d* and *q* components solve the excitation-frame per unit machine equations for slip, s:

$$\begin{aligned} (\{(\sigma L_sL_r)^2 + (L_rR_s)^2\}i_{sd0}^e - R_sL_r^2u_{s0})s^2 + (1-\sigma)R_rL_sL_r(2R_si_{sd0}^e - u_{s0})s \\ + (R_r^2R_s(R_si_{sd0}^e - u_{s0}) + (R_si_{sd0}^e - u_{s0})^2i_{sd0}^e) = 0 \end{aligned} \quad (3.43)$$

This quadratic function of slip will give two solutions – as can be deduced from the characteristic hump of an induction machine torque-slip curve. The smallest absolute slip is chosen as this value coincides with normal (stable) operation.

3.2.4.3. Analysis and discussion for comparison of experimental and simulation results

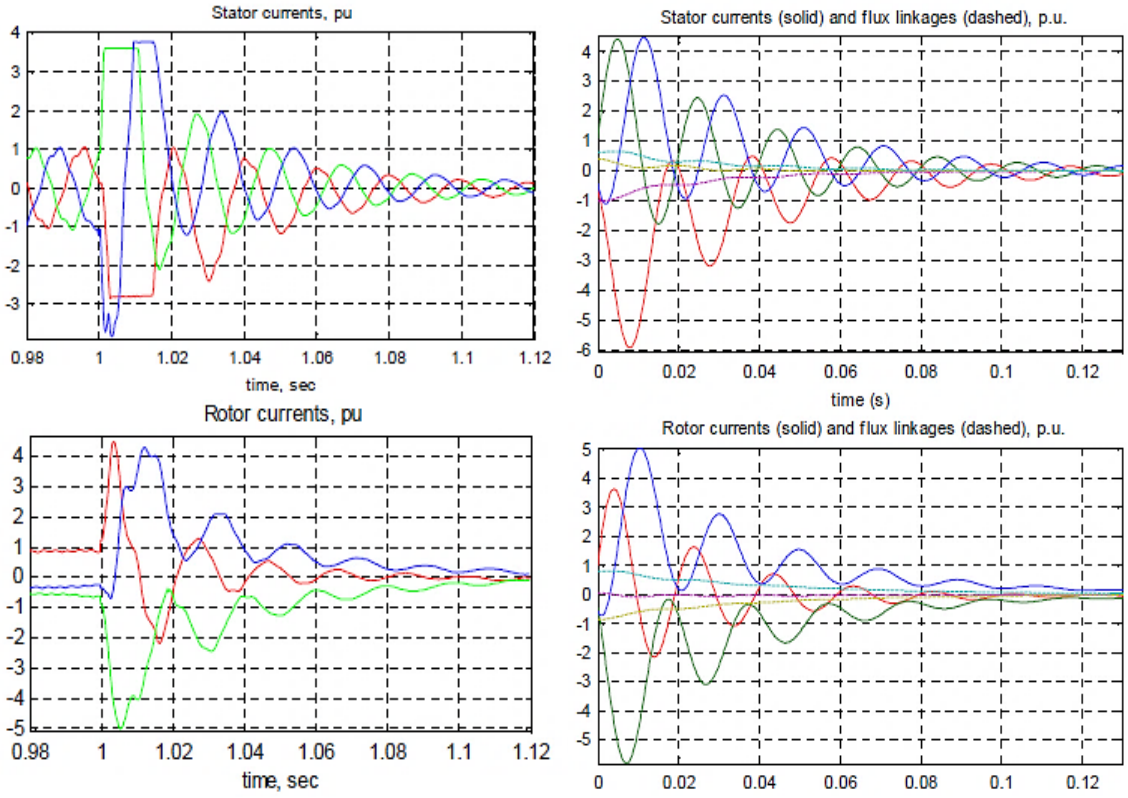

Figure 3.2 (Left) Experimental fault response shown in Pannell's thesis [11] (Right) Simulation fault response – stator (Up) and rotor (Down) currents

The test results are obtained from the Chapter 5 of Pannell's thesis [11]. The measured stator and rotor currents for the fault test are shown in the left two pictures of Figure 3.2. Compared to the stator current graph, the rotor currents emerge more dc than ac. This indicates the longer rotor transient time constant. The peak rotor current is a little less than *5 p.u*. The stator currents are saturated below peak value

by the limitation of current probe, although inspection of the waveform indicates a similar peak to the rotor currents.

The good agreement between simulated and experimental results has been shown in Figure 3.2 in terms of the relative peaks of each phase of current. The simulated currents are smoother and reach *15%* higher peak current. This is likely because of the omission of magnetic saturation in the analytical solution which would limit the real currents and the stator current probe saturation which restricts the stator current readings.

Derived Parameters		**Values**	**Decay components**		**Values**
Leakage factor	σ	0.075 p.u.	Rotor-speed frequency	f_r	51.02 Hz
Frequency adjustment factor	δ	0.0092 p.u.	Near-dc frequency	f_{self}	0.46 Hz
Timescale adjustment factor	κ	-0.0004 p.u.	Near-rotor speed frequency	f_{mutual}	50.59 Hz
Stator transient timescale	τ_s	25.8 ms	Effective stator timescale	τ_s'	25.7 ms
Rotor transient timescale	τ_r	38.7 ms	Effective rotor timescale	τ_r'	38.9 ms

Table 3.2 Machine analytically derived parameters.

Further, the machine is analysed by the analytically solution parameters discussed in Sections 3.2.2 and 3.2.23 to validate both experimental and simulation results. The computed leakage factor is *7.5%*, resulting in the complex frequency adjustment almost entirely imaginary: timescale adjustment constant $\kappa < 10^{-3}$ and frequency adjustment constant δ roughly *1%*. Referring to the stator flux natural response, the measured parameters suggested transient time-constants of *26ms* on the stator and *39ms* on the rotor, whilst the effective self and mutual decay frequencies are

calculated at *0.46Hz* and *50.59Hz*. All machine analytically derived parameters are enumerated in Table 3.2.

Based on the analytical solution stator current equation 3.24, we will have:

$$\overrightarrow{i_s^s}(t) = 4.06\angle\{\theta_{e0}-87^\circ\}e^{-t/\tau_s}@0.46Hz + 3.77\angle\{\theta_{e0}+107^\circ\}e^{-t/\tau_r}@50.59Hz \qquad (3.44)$$

The initial angle of the excitation reference frame with respect to the stator reference frame, θ_{e0}, is an arbitrary constant depending upon the moment the fault occurs: -84° was found to best match the pre-fault experimental data. A similar result can be calculated for the rotor current solution:

$$\overrightarrow{i_s^s}(t) = 3.87\angle\{\theta_{\varsigma 0}-73^\circ\}e^{-t/\tau_r}@0.46Hz + 3.96\angle\{\theta_{\varsigma 0}+92^\circ\}e^{-t/\tau_s}@50.59Hz \qquad (3.45)$$

The initial rotor slip angle, $\theta_{\varsigma 0}$, was set at -72° to best match the experimental data.

3.3. Crowbar methods

The sensitive characteristic of a standard DFIG system to the dips in the supply voltage is the reason why the protection scheme is researched. The grid disturbance would result in the over current on rotor side. At the same time, the rapid increase of the rotor current will cause the rise of the capacitor voltage in the DC-link. Then the commotion of the real and reactive power of the rotor-side converter happens. Under the voltage dips, the stator flux cannot duly change which leads to a dc component. Then a bigger slip appears. All of these reflections will bring about the over current and over voltage and damage the rotor and converters. Hence, the power electronics converter and DC-link protection by diverting or negating the over-current and over-voltage was researched. In order to protect the DFIG under the grid disturbance, the DFIGs are prevented from the impairment and could continue working should be sure. It is now a requirement that wind turbine manufacturers demonstrate what is

commonly called ‘Fault Ride Through’ (FRT) capability in their turbine systems. Rotor Crowbar, as a cost-effective and reliable method of protecting the power converters of DFIG, was employed in the previous hardware working as a part of the FRT scheme and compared with the computer model created by the software Matlab/Simulink to validate the results of software working and evaluate machine model accuracy in this thesis.

3.3.1. The crowbar in detail

In order to protect the power electronic component in the DFIG converters, a rotor crowbar is widely used in the rotor-circuit error condition. The rotor crowbar short-circuits the rotor-windings through a designed resistance, diverting the rotor currents away from the converter and rapidly de-energizing the rotor. In this manner the DFIG can ‘ride through’ the transients of fault response and resume control during the remaining period of the fault or voltage recovery.

There are several kinds of rotor crowbar structures. The simplest and earliest configuration is constituted by anti-parallel thyristors or diodes. Figure 3.3 (a) and (b) illustrate this kind of crowbar [82].

Figure 3.3 (a) reveals the anti-parallel thyristor crowbar which is constructed by two pair of anti-parallel thyristors. In the circuit, large dc component exists in the rotor current. This results in the unavailability of the thyristor turn-off characteristic. Besides, the absorber circuits for thyristors are quite hard to design.

The diodes-bridge crowbar includes one Diode Bridge to commute and one thyristor to control as shown in Figure 3.3 (b). When the dc side voltage peaks, the thyristor would turn on to conduct. Meanwhile, the rotor would be devoiced from the rotor side converter, but connect with the crowbar circuit till the stator is totally cut from the grid. This configuration excels the Figure 3.3 (a), because less thyristor is employed, easier controller is implemented. However, the current through the thyristor is

continuous in Figure 3.3 (b) configuration, thus the thyristor cannot be turned off. That means the crowbar short-circuit the rotor windings, they would remain connection till the rotor current disappears, which disobey the grid code rules. The new rules require the DFIG to resume when fault clearance. Hence, in order to remove the crowbar circuit after the fault, IGBT and GTO could be used.

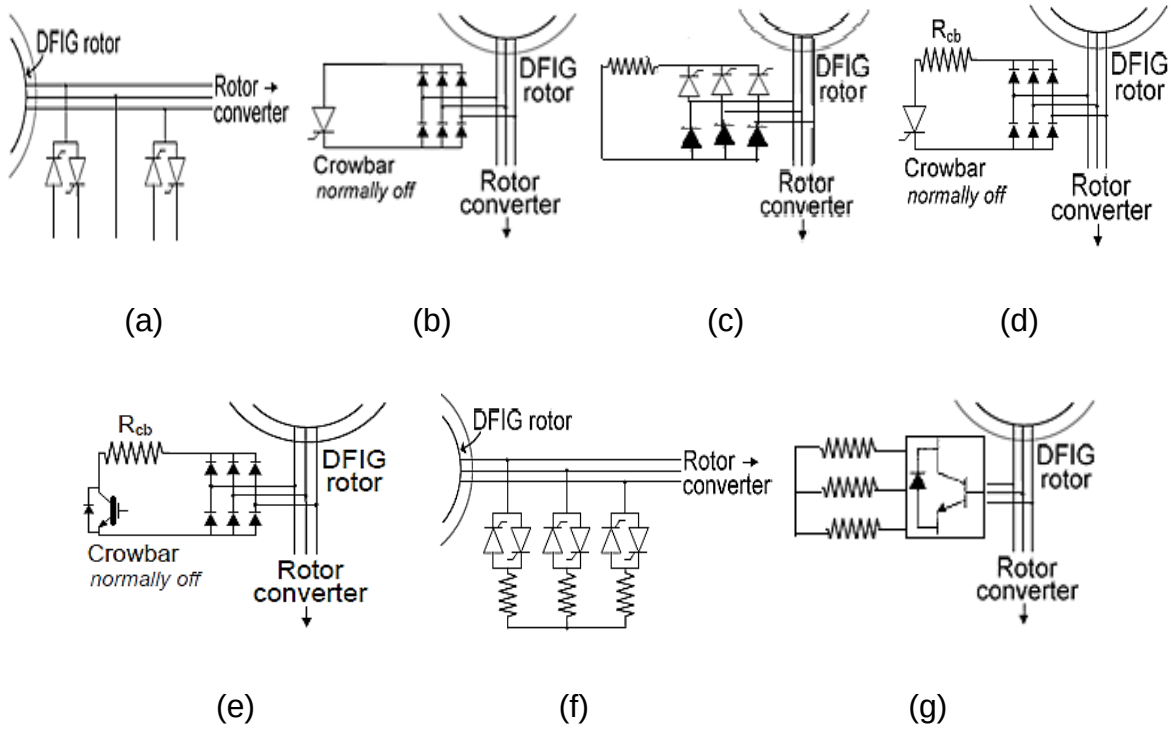

Figure 3.3 (a) Anti-Parallel Thyristor Crowbar (b) Diodes-Bridge Crowbar (c) Mixed Crowbar (d) Rectifier and Thyristor Crowbar (e) Rectifier and IGBT Crowbar (f) IGBT with Bypass Resistor Crowbar (g) Triac with Bypass Resistor Crowbar

The improved crowbar layouts are displayed in Figure 3.3 (c), (d) and (e) [82]. The mixed crowbar is designed based on the diode bridge crowbar. As shown in Figure 3.3 (c), each arm of mixed crowbar is made up of one thyristor and one diode. Figure 3.3 (d) and (e) have similar configuration. Both of them add a switch and an absorber resistor in series based on diode bridge crowbar.

In addition, with bypass resistor circuit crowbar has been used as another structure. There are two main types demonstrated in Figure 3.3 (f) and (g) [83]. When this kind

of crowbar is employed in voltage dips, the bypass resistor would be coupled with rotor windings. It supplies a bypass circuit to the over current during the grid fault. Then the target, limiting over current and protecting the power electronic converter, is achieved.

In these layouts of rotor crowbars, the structure (d), (e) and (g) have more merits and are widely used. Each silicon-controlled rectifier in configuration (g) must be rated to block maximum rotor voltage and to carry worst-case rotor over-currents. The thyristor switches can be fired by a current fed gate signal, but can only be turned off at a through-switch current zero. Alternatively, GTO thyristors offer better turn-off capabilities, but demand a far higher turn-off gate current. The configuration (d) and (e) use only one switching device. These devices must be able to block roughly *140%* of rotor phase-phase voltage. Each diode in the bridge must carry the same ratings as for the silicon-controlled rectifiers in configuration (g). The single resistor in Figure 3.3 (d) and (e) must carry an average current *135%* of the value carried by each resistor in case (g). Thermally however, grid faults cover a very short period and hence the single resistor is not rated much higher than three separate resistors. Additionally, given the relative cost of diodes, diode rectifier configurations offer a major cost saving, however, the configuration (e) with IGBT has a considerable increase in single device cost compared to (d) with the Thyristor and GTO. Moreover, turn-off of the switch device in configuration (d) must wait for a rectified current zero; this will only occur once the rotor circuit flux has completely decayed. Near-instantaneous turn-on and turn-off can be achieved by using an IGBT power switch, as shown in the rectifier-IGBT configuration in (e). However, the swift turn-off ability of an IGBT is necessary for certain fault ride through control methods. Thus configuration (e) is employed on the test rig used in this work.

3.3.2. Test rig crowbar value

Pannell used the rotor crowbar with the structure shown in (e) in his experiments [11]. With the switch fully on, the crowbar resistance behaves similarly to adding three short-circuited phase resistors in series to the rotor's windings like the configuration in Figure 3.4. An equivalent *'per-phase'* resistance of the crowbar can be approximated using this analogy.

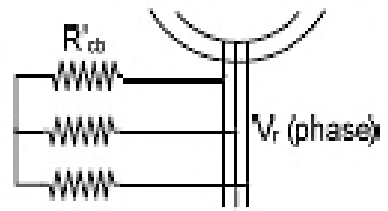

Figure 3.4 Approximate crowbar-resistance analogy [11]

Firstly, note that an ideal rectifier provides an average dc voltage of *1.35*× the line-line voltage [84]:

$$V_{dc} = \left(\frac{3\sqrt{2}}{\pi}\right) V_{line-line,\ rms} \tag{3.42}$$

The crowbar on average draws $\sqrt{3}$ times more current than the same resistance in series:

$$i_{cb} = \left(\frac{3\sqrt{2}}{\pi}\right) i_r = \frac{V_{dc}}{R_{cb}} = \left(\frac{3\sqrt{2}}{\pi}\right) \frac{\sqrt{3} V_{r,\ ph}}{R_{cb}} \quad \therefore i_r = \frac{\sqrt{3} V_{r,\ ph}}{R_{cb}} \quad \therefore R'_{cb} = \frac{R_{cb}}{\sqrt{3}} \tag{3.43}$$

The equivalent rotor crowbar resistor value

$$R'_{cb} \approx 0.58 R_{cb} \tag{3.44}$$

In terms of average power dissipated, the equivalent series resistance produces a similar relationship:

$$P_{cb} = \frac{V_{dc}^2}{R_{cb}} = \left(\frac{3\sqrt{2}}{\pi}\sqrt{3}V_{r,\ ph}\right)^2 \frac{1}{R_{cb}} = \frac{54}{\pi^2}\frac{V_{r,\ ph}^2}{R_{cb}} \tag{3.45}$$

$$P'_{cb} = 3\frac{V_{r,\ ph}^2}{R'_{cb}} \qquad \therefore R'_{cb} \approx 0.55R_{cb} \tag{3.46}$$

In this condition, the equivalent rotor crowbar resistor value is replaced by

$$R'_{cb} \approx 0.55R_{cb} \tag{3.47}$$

Both equivalent resistors can be considered as the resistance adding to the rotor in series when the crowbar works. In my simulation model, $R'_{cb} \approx 0.55R_{cb}$ is selected. Pannell chose a *25Ω, 0.6kW* power resistor in his experiments, and a *13.75 Ω* equivalent rotor crowbar resistor was added in my simulation.

3.3.3. Timer action crowbar

In the existed hardware working, a time action crowbar method was employed. That means the crowbar is activated when the magnitude of the rotor current exceeds a threshold value, and keep connection with rotor windings for a short fixed period.

While the crowbar is engaged, rotor-side PWM is disconnected. The rotor side PI controller outputs are all reset to zero. The line-side converter's controllers remain unaffected. When the crowbar is released, rotor-side converter and the inner rotor current PI control are immediately resumed. Outer control loop is resumed after a specified delay, to allow the current controllers to settle. After the crowbar disengages, if a rotor over-current persists, the crowbar is re-engaged for an additional period.

As for all of this crowbar tests, the threshold was set for the stated maximum IGBT pulse current of *2.0 p.u.* The crowbar duration is *120ms*.

3.3.3.1. Comparison of simulation and experimental results

Figure 3.5 directly compares the timer action crowbar experiment results for a *15%* fault voltage applied to a DFIG. In practical, the stator voltage shows a rapid collapse to *0.26 p.u*. After a *50ms* settling period, *28%* voltage was maintained for *500ms* throughout the fault period.

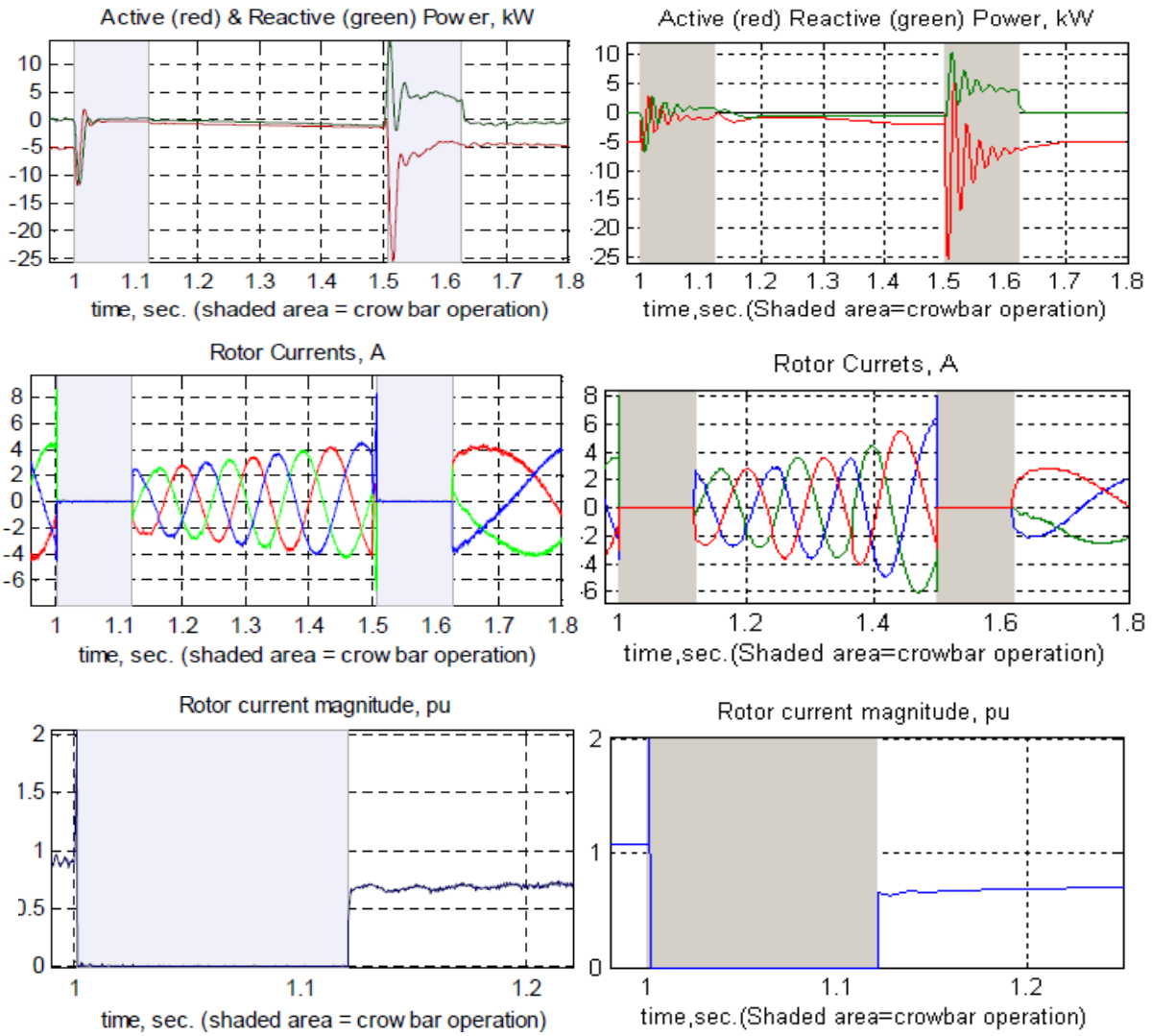

Figure 3.5 (Left) the timer action crowbar practical test and (Right) simulation results for a *15%* fault applied to a DFIG

The left picture of Figure 3.5 illustrates the hardware working outcomes, while the right graph describe the simulation results. In general, the two kinds of figures look quite similar.

In hardware tests, the current sensors were placed at the output of the rotor-converter's series filter chokes, between the crowbar and the converter. It is clear from this data that the converter leg currents were forced to zero throughout the crowbar period. The close-up graph of both rotor current magnitudes show the *2 p.u*. limit in effect. During the whole fault period the rotor currents never exceeded the computed maximum limit of *9.5A* (peak).

In the comparison of the simulation and test results, the simulation rotor current magnitude is smaller than the hardware result, when the timer action crowbar is connected with the rotor windings. Thus the three-phase rotor current graphs display the same tendency. The reason of this trend is the simulation switch device of crowbar is ideal. It has no switch time. However, although the near-instantaneous turn-on and turn-off can be achieved by using an IGBT power switch, it still takes little time to activate in practical, not none. The longer turn-on time in practical leads to the rotor current magnitude is a little over *2 p.u.* and the simulation rotor current is smaller than the hardware working result.

After the second crowbar activation period, Hardware result shows the control is regained very quickly; active and reactive power levels returned to unity power factor and *5kW* generation within tens of milliseconds. However, the simulation picture reveals that the active and reactive power takes much longer time to be constant. Because the simulation is based on the mathematic model, and it takes longer time to compute especially when the differential is used in Matlab model. The similar reason is given to the simulation rotor current magnitude graph.

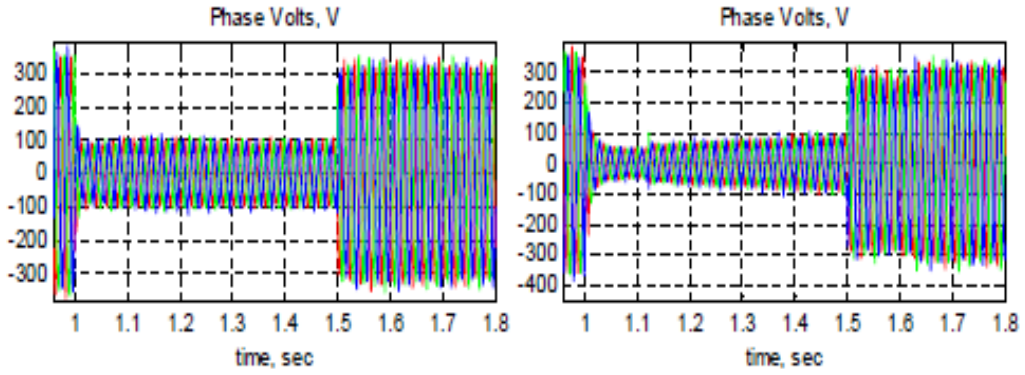

Figure 3.6 The supply voltage when *15%* fault is applied (Left) using computer simulation (Right) using experiments

After the crowbar operation, there is a short overshot period resulting from Matlab spend more time to eliminate the unstable state when the equivalent rotor resistance is changed. Besides, the computer assumes the input stator voltages always keep the same in the voltage whilst the experiment supply voltages are influenced a lot when fault simulation test devices are applied. Figure 3.6 takes a *15%* fault condition as an example. The voltages in left picture keep the phase peak value approximate *100V* during the fault period in the simulation, whereas the voltage increase generally from about *50V* to finally *100V* during the fault and slightly suppressed at the fault recovery period as displayed in right figure. The changed input will cause the small difference between the experiment and simulation result.

Figure 3.7 directly compares test and simulation results for a *0%* fault voltage applied to a DFIG. During *0%* fault voltage period, the stator voltages show a rapid collapse to below *50V* rms per-phase in *2ms*. The local voltages were maintained at around *30V* rms per-phase for *120ms*.

After the second crowbar period, control was again regained very quickly; active and reactive power levels returned to unity power factor and *5kW* generation within tens of milliseconds. But the simulation active and reactive power takes longer time to become steady state. The reason is the same as pervious discussion.

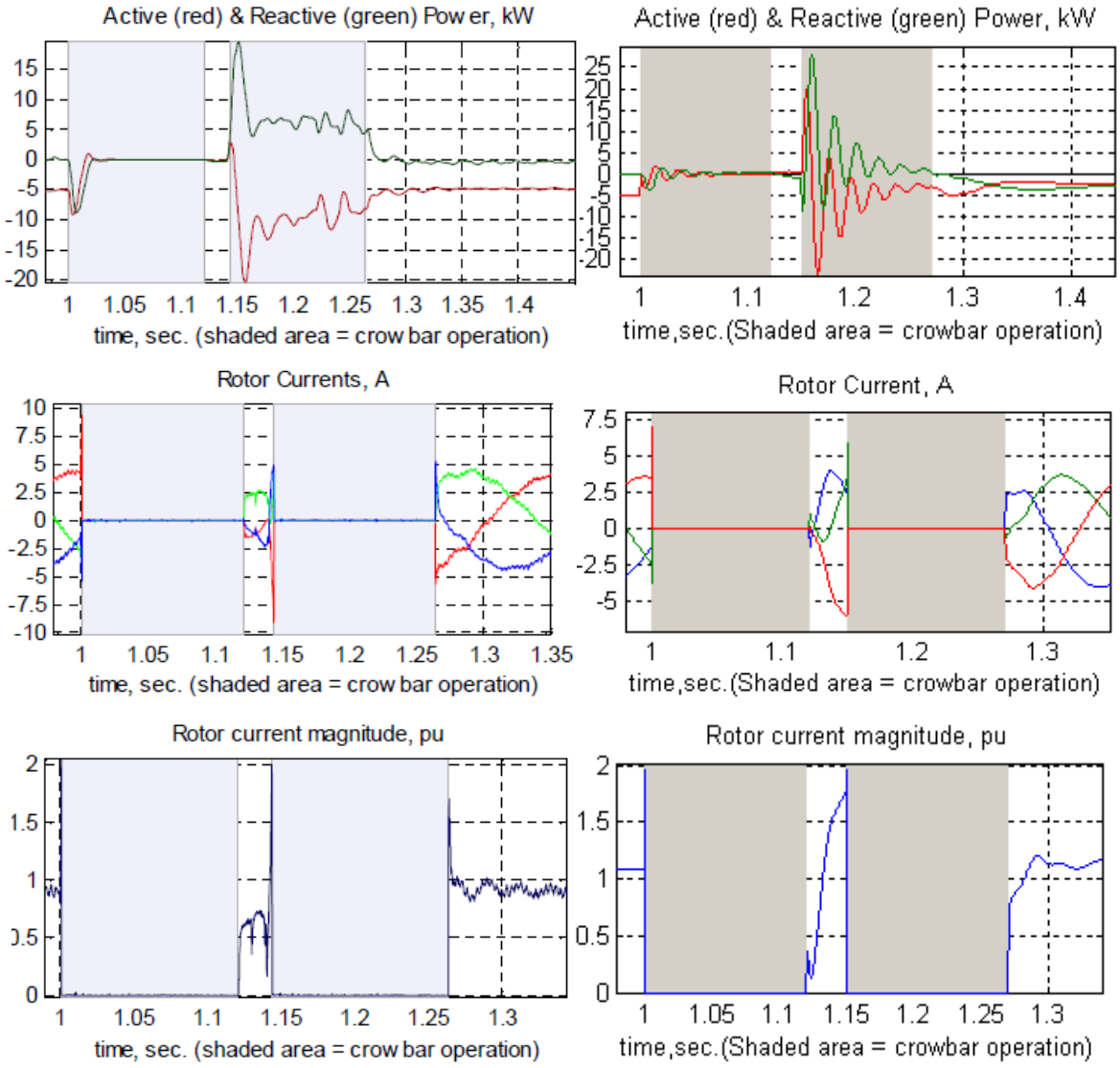

Figure 3.7 (Left) the timer action crowbar practical test and (Right) simulation results for a *0%* fault applied to a DFIG

3.3.4. Crowbar method Conclusions

Based on the discussion above, for both the *15%* fault and *0%* fault, the rotor converter devices were fully protected. The rotor converter currents were immediately diverted upon crowbar activation; at no point did they exceed the calculated *9.5A* peak limit for the converter. Therefore, the rectifier and IGBT crowbar with time action crowbar method, can be thought as a cost-effective and reliable method of protecting the DFIG's power converter from rotor over-currents and indirect DC-link protection.

Besides, the machine model simulates the accurate response with approximate none difference performance compared to the experiment results. The controller response obtained from the simulated model also can be thought similar to the experiment performance. Thus, the DFIG built by Matlab/Simulink can be considered as a correct model and would be worth to be used in Chapter 5 and 6 to simulate the response of the DFIG working in the experiments. Especially, the whole crowbar test simulation system will be used in Sector 5.3 to prove the prediction of the FRT performance difference between DFIG and BDFRG.

4. Experimental Apparatus

This Chapter details the experimental apparatus used in the tests in order to let the reader familiarise the experiments: comparing DFIG and BDFRG. For this target, there are two systems built. Because of the lab refurbishment of Newcastle University, the experimental apparatus are commissioned in Northumbria University. So thanks are given to Northumbria University and all the staff and technicians there for their cooperation.

The two test apparatus systems have the same key elements and functions except the generators. Thus, the introduction of one system and two generators will be provided separately in this Chapter. Primarily, an overview of the experiment rigs would be given. Following, two generators and the prime mover will be discussed. Then the details of controller cabinet and the setting up information of motor control board will be descried in Section 4.3 and 4.4 respectively.

4.1. Test rig overview

A test apparatus system is composed by an *Altivar 71* driver, an induction machine, a generator and a control cabinet. *Altivar 71* and induction machine consist of the primary driver for the whole system, thus they will be introduced together in the later section. The primary driver and generator are connected through a mechanical shaft with an encoder fixed on the generator side. These three elements comprise the rotating machinery. Induction machine obtains either the speed or the torque from *Altivar 71* and produces the generator's rotational speed via the shaft. The encoder will transfer the speed signal to controller board while torque transducer will convey the torque value to a software called 'torque log' self-carried by *Altivar 71*. Taking the DFIG system as example, a block diagram of the model is given in Figure 4.1.

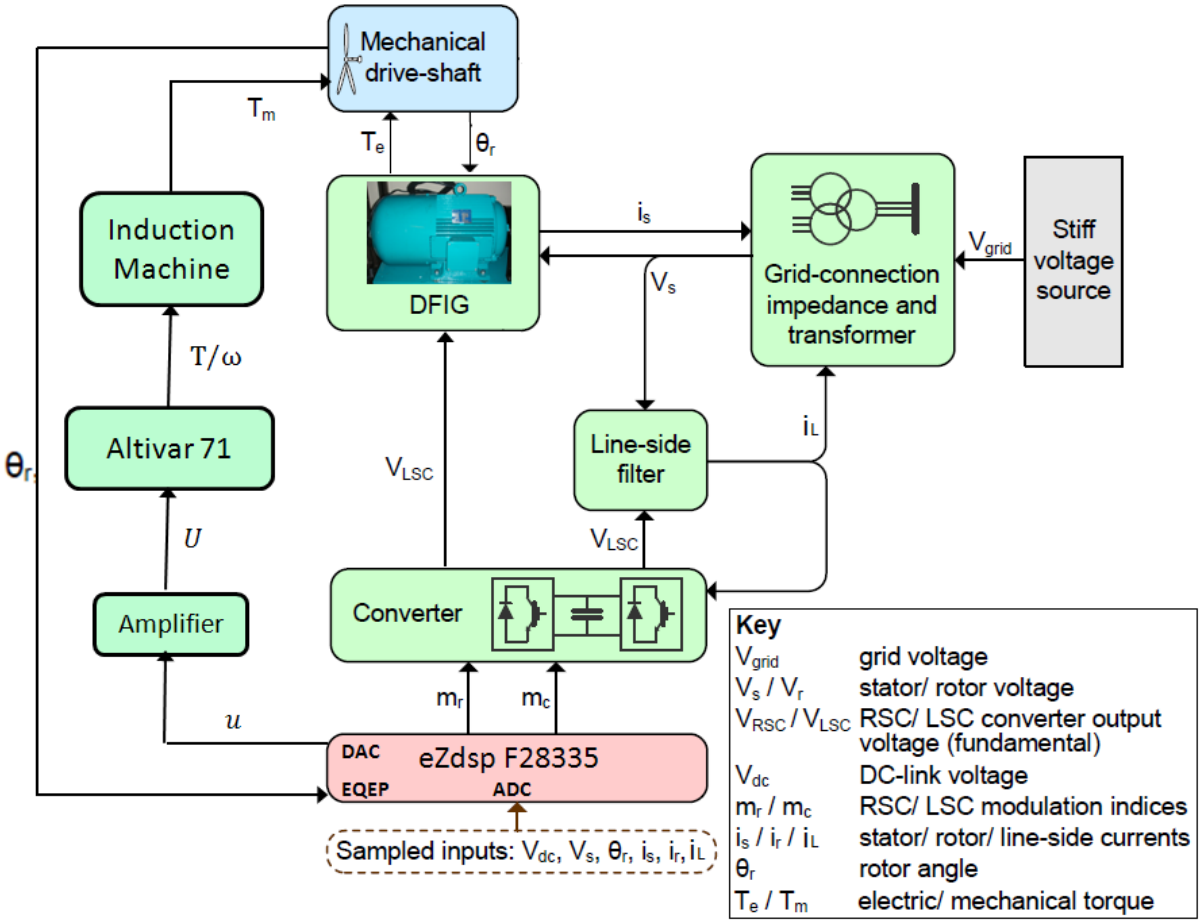

Figure 4.1 Block diagram of the DFIG system

The entire system would be controlled by an *eZdsp F28335* and its interface board fixed in the control cabinet. Two *100A*-rated Infineon IGBT modules are employed as the bi-directional power converters with a DC voltage bus made up by two capacitors. They consist of an AC/DC/AC converter system and are installed at the right bottom of control cabinet. Besides, the voltage and current sensors and other essential devices (switches, relays and so on) are all distributed in control cabinet. The details will be explained in Section 4.3.

For the contribution of the entire experimental system, Park Company and Prof. Wang would be given acknowledgement. BDFRG is designed by Prof. Wang in Shenyang Technology University, produced in China then delivered to Northumbria

University. Besides, *Altivar 71*, primary induction machine and DFIG are bought from Park Company in the UK and assembled there with a shaft and an encoder.

4.2. Rotating Machinery

As the heart of the test rig, there lays two rotating machines on a common axis with their rotor shafts joined by a short, stiff coupling. An induction machine receives the torque or the speed from an *Altivar 71* driver and provides the speed input to a *5kW*, *380V 8-pole* DFIG or BDFRG.

4.2.1. DFIG

The DFIG used in the experiments is illustrated in Figure 4.2. This DFIG is a second-hand machine, the parameters are unknown and some data are changed due to abrasion, therefore, before controlling this machine, the parameters are better to be tested.

Figure 4.2 Doubly-Fed Induction Generator used in experiments

4.2.1.1. DC Resistance Test

As we all know, the stator and rotor resistance are affected by the temperature a lot. Considering the damage of the over-current, a half of rated current is selected as the tested current and the reading of the measurement would be acquired after five minutes heating up.

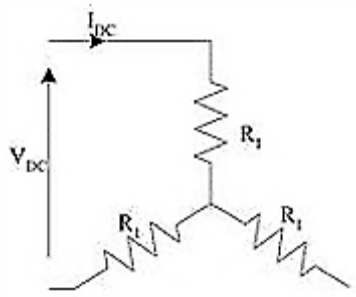

Figure 4.3 Star connection of windings

	Stator				Rotor			
	V(V)	I(A)	R(Ω)	R_s(Ω)	V(V)	I(A)	R(Ω)	R_r(Ω)
Winding 1	6.81	8.08	0.84	0.42	1.3	3.29	0.395	0.197
Winding 2	7.13	8.39	0.85	0.425	1.4	3.3	0.42	0.21
Winding 3	6.7	7.95	0.84	0.42	1.28	3.48	0.37	0.185
Average resistance (Ω)	0.42				0.198			

Table 4.1 DFIG dc resistance test results

For the machine used in the experiments, both stator and rotor windings are star connected as displayed in Figure 4.3. Thus, the stator and rotor resistance values would be the half of test results based on the principle from Appendix D.1. Hence, the stator resistance of each phase was measured separately at a test current of approximate *8A*. The stator terminals were applied with a *16V-20A* DC generator.

The current and voltage voltmeter was measured the main DC supply and the total DC current of two terminals.

A similar produce was carried out for the rotor windings which were isolated for the test current *3.3A*. However, accounting for the unbalance resistor results caused by the mechanical issues of the contacted slip rings, the rotor was moved slowly to make the current constant when the experiments were taken. The results can be found in Table 4.1.

4.2.1.2. Locked Rotor Test

A locked rotor test was carried out under *0.25 p.u*. three-phase AC stator voltage. The line voltages and currents have to be measured without the neutral terminals in the tested machine. Therefore, the 3-phase equations below were considered instead of the single-phase circuit equations according to the locked rotor test equivalent circuit given in Figure 4.4.

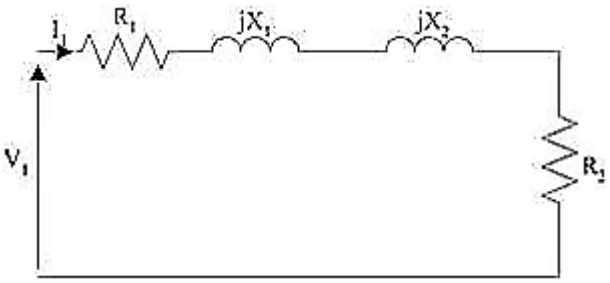

Figure 4.4 Induction Machine model equivalent circuit under the locked rotor test

$$P = 3{I_{phase\ RMS}}^2(R_1 + R_2) = \sqrt{3}|V_{line\ RMS}||I_{line\ RMS}||cos\ \varphi| \quad (4.1)$$

$$Q = 3{I_{phase\ RMS}}^2(X_1 + X_2) = \sqrt{3}|V_{line\ RMS}||I_{line\ RMS}||\sin\varphi| \quad (4.2)$$

where P and Q are the total real and reactive power. $I_{phase\ RMS}$ stands for the per-phase RMS current, while $|V_{line\ RMS}|$ and $|I_{line\ RMS}|$ are the RMS value of absolute magnitude for line voltage and current vector respectively. φ equals the

phase shift angle between the line current and voltage vector. Hence $\cos\varphi$ represents the power factor.

According to equations 4.1 and 4.2, we have:

$$R_1 + R_2 = \frac{|V_{line\ RMS}||\cos\varphi|}{\sqrt{3}|I_{line\ RMS}|} \tag{4.3}$$

$$X_1 + X_2 = \frac{|V_{line\ RMS}||\sin\varphi|}{\sqrt{3}|I_{line\ RMS}|} \tag{4.4}$$

Then the experiment readings and resistance, reactance results calculated from the equations 4.3 and 4.4 were given in Table 4.2.

	$\lvert V_{line\ RMS}\rvert$(V)	$\lvert I_{line\ RMS}\rvert$(A)	φ (°)	$(R_1 + R_2)(\Omega)$	$(X_1 + X_2)(\Omega)$
Winding 1	20.5786	2.5624	72.749	1.37	4.42
Winding 2	21.232	2.6578	74.214	1.26	4.46
Winding 3	20.7088	2.61518	73.214	1.32	4.38

Table 4.2 DFIG locked rotor test results

The average phase stator impedance was:

$$Z = (R_1 + R_2) + j(X_1 + X_2) = 1.318 + j4.4\ \Omega \tag{4.5}$$

According to

$$R_s = R_1 \qquad R_r = \frac{R_2}{a^2} \tag{4.6,4.7}$$

It could be obtained that:

$$R_1 = R_s = 0.42\ \Omega \qquad R_2 = 1.318 - 0.42 = 0.898\ \Omega \tag{4.8, 4.9}$$

$$a = \sqrt{R_2/R_r} = 2.13 \quad (4.10)$$

The common assumption of dividing the leakage reactance equally between stator and rotor was made, and then the results were:

$$X_1 = X_2 = 2.2\ \Omega \quad (4.11)$$

4.2.1.3. Synchronous Speed Test

A no load test was taken instead of a synchronous speed test, because the no load speed is so close to the synchronous speed that the torque-speed transducer used in the test equipment cannot distinguish the difference between them. The entire experiment was carried out using an AC stator main supply with line-to-line value close to the rated *380V*.

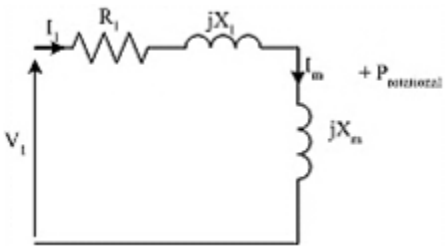

Figure 4.5 Equivalent circuit of Induction Machine under the synchronous speed test

	$\lvert V_{\text{line RMS}}\rvert$(V)	$\lvert I_{\text{line RMS}}\rvert$(A)	φ (°)	$(X_1 + X_m)(\Omega)$
Winding 1	366.72	7.43162	64.925	26
Winding 2	370.566	7.52572	69.748	26.67
Winding 3	370.674	7.67842	67.05	25.67

Table 4.3 DFIG synchronous speed test results

The similar equations as the locked rotor test can be inferred according to the equivalent circuit in Figure 4.5:

$$Q = 3{I_{phase\ RMS}}^2(X_1 + X_m) = \sqrt{3}|V_{line\ RMS}||I_{line\ RMS}||\sin\varphi| \quad (4.12)$$

$$X_m = \frac{|V_{line\ RMS}||\sin\varphi|}{\sqrt{3}|I_{line\ RMS}|} - X_1 \quad (4.13)$$

The test results were shown in Table 4.3. The average phase leakage reactance was:

$$j(X_1 + X_m) = j26\ \Omega \quad (4.14)$$

Thus,

$$X_m = 26 - 2.2 = 23.8\ \Omega \quad (4.15)$$

4.2.1.4. Open Circuit Test

Based on relationship between the stator referred equivalent circuit (Figure 4.6) parameters and the parameters suitable for the twin axis dynamic model (Figure 4.7) described in Appendix A, it can be seen that a turns ratio a is required which was measured by the open circuit test.

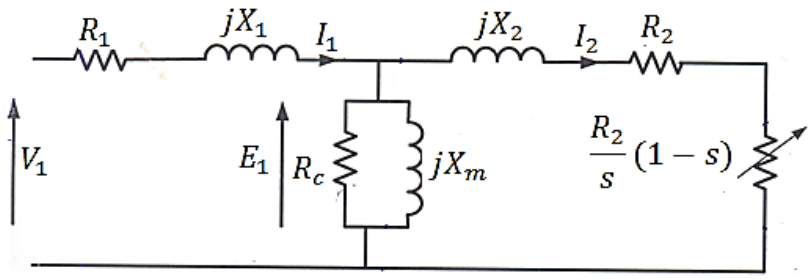

Figure 4.6 Stator referred equivalent circuit

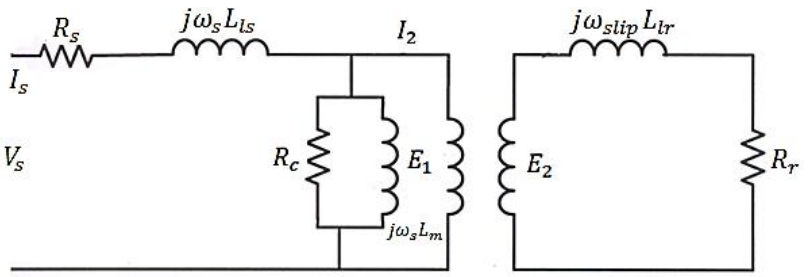

Figure 4.7 Twin axis dynamic model

This method considers the turns ratio a as the division result of the stator and rotor voltages. The turns ratio produced from this test was: $a = 2.13$. Validate with the equation 4.10, this result was reliable.

4.2.1.5. Conclusion

According to the test results we have:

$R_1 = 0.42\ \Omega \qquad R_2 = 0.898\ \Omega$

$X_1 = 2.2\ \Omega \qquad X_2 = 2.2\ \Omega \qquad X_m = 23.8\ \Omega \qquad a = 2.13$

$L_1 = \frac{X_1}{2\pi f} = 7.03mH \qquad L_2 = 7.03mH \qquad L_{mag} = \frac{X_m}{2\pi f} = 75.81mH$

Based on the knowledge of the relationship between the stator referred parameters and the two axis model machine parameters below:

$R_s = R_1 \qquad R_r = \frac{R_2}{a^2}$

$L_m = \frac{L_{mag}}{a} = \frac{X_m}{2\pi f a}$

$L_s = L_1 + L_{mag} = L_1 + aL_m$

$L_r = \frac{L_2 + L_{mag}}{a^2} = \frac{L_2}{a^2} + \frac{L_m}{a}$

It is easy to get the dynamic model parameters:

$R_s = 0.42\ \Omega \qquad R_r = 0.198\ \Omega \qquad a = 2.13$

$L_m = 35.59\ mH \qquad L_s = 82.84\ mH \qquad L_r = 18.26\ mH$

The rotor resistance got from the dc tests was *0.1978658824Ω* while the value obtained using the locked rotor test and inferred by the turns ratio was *0.197947978Ω*.

The difference between these two calculated rotor resistances was *8.2*× $10^{-5}\Omega$. The inaccuracy was less than *0.5‰*. As the core loss is not modelled in the twin axis dynamic equations, the value of R_c is not needed.

4.2.2. BDFRG

The BDFRG used in the experiments is illustrated in Figure 4.8. It is designed by Prof. Wang in Shenyang Technology University in China and manufacture there. In order to obtain the comparability of DFIG and BDFRG, Prof. Wang decided to produce a same pole number, same power rate and same size BDFRG.

Figure 4.8 Brushless Doubly-Fed Reluctance Generator used in experiments

However, the pole number of BDFRG is defined as the sum of both stator poles whereas DFIG thinks the stator pole number as machine pole number. For example, the DFIG used in the experiments has *4* stator pole pairs. Hence, BDFRG is set as *6* poles in main stator and *2* poles in auxiliary stator. Thus these two generators can be considered as the *8* poles machine and worth to be compared.

Besides, BDFRG parameter tests are quite different from DFIG's because of its different operations when one side windings are short circuited or open circuited. The details of parameter obtaining procedure are demonstrated as follows.

4.2.2.1. DC Resistance Test

Similar to the DFIG, BDFRG's resistor can be obtained by the same procedure as induction machine resistance test. The main stator and auxiliary stator winding's resistances of each phase were measured separately at a test current of approximate *8A*. The terminals were applied with a *16V-20A* DC generator. The current and voltage voltmeter measured the main DC supply and the total DC current of two terminals. Due to the star connection for both stators, the real resistance value is the half of the calculated one. The experiment results are shown in Table 4.4. As the results, we could have a conclusion that the primary side stator resistor is *1.01Ω*, and secondary side resistor is approximate *0.55Ω*.

		Primary stator			Secondary stator		
		Red	Yellow	Blue	Red	Yellow	Blue
Group 1	Voltage (V)	7.540	7.08	7.313	5.835	6.116	6.082
	Current (A)	7.567	6.973	7.148	10.994	11.045	11.036
	Resistance (Ω)	0.9964	1.015	1.023	0.531	0.554	0.551
Group 2	Voltage (V)	7.166	7.365	7.491	6.169	6.226	6.145
	Current (A)	7.173	7.265	7.307	11.345	11.260	11.158
	Resistance (Ω)	0.999	1.014	1.025	0.544	0.553	0.551
Group 3	Voltage (V)	7.322	7.733	7.718	6.227	6.34	6.333
	Current (A)	7.34	7.662	7.580	11.467	11.494	11.526
	Resistance (Ω)	0.9975	1.009	1.018	0.543	0.5516	0.549
Average resistance (Ω)		0.9977	1.013	1.022	0.539	0.5527	0.550
Total average resistance (Ω)		1.01087			0.55043		

Table 4.4 BDFRG dc resistance test results

4.2.2.2. Inductances Test

Although the BDFRG and DFIG have lots of same operation, the BDFRG also has different performances at some tests compared to the DFIG. As we all know that the wound rotor induction machine is operated at a merely synchronous speed when the stator is applied with a rated symmetrical three-phase AC voltage source with the short-circuit rotor. But, the BDFRG would start asynchronously and operate like the same pole number induction machine, if the primary stator is supplied with an AC voltage source, and the secondary winding is short circuited [7].

Thus the Synchronous Speed Test, the way to obtain inductance value of the induction machine, is not suitable for the BDFRG. However, based on the steady-state phase voltage equations of the 2*p*- and 2*q*- pole stator windings BDFRG expressed below [7][85]:

$$\begin{cases} u_p = R_p i_p + j\omega_p L_p i_p + j\omega_p \left(L_{pc}\angle\gamma\right)[i_c\angle(-\alpha)] \\ u_c = R_c[i_c\angle(-\alpha)] + j\omega_c L_c i_c\angle(-\alpha) + j\omega_c \left(L_{pc}\angle\gamma\right) i_p \end{cases} \tag{4.16}$$

Where u_p and u_c, i_p and i_c, ω_p and ω_c, L_p and L_c are the phase voltage, phase current, angular frequency and self-inductance of the power side and control side windings respectively. L_{pc} is the mutual inductance between the primary and secondary stator windings. $(-\alpha)$ is the initial angle of the auxiliary stator Magnetomotive Force (MMF) field with respect to the main stator MMF, while γ is the angle between the induced phase voltage and current.

If the secondary winding is open-circuited and the primary winding is supplied with symmetrical three-phase AC voltage, none current would flow through the secondary side windings. Hence, equation 4.16 gives conclusion below:

$$\begin{cases} u_p = R_p i_p + j\omega_p L_p i_p \\ u_c = j\omega_c \left(L_{pc}\angle\gamma\right) i_p \end{cases} \tag{4.17}$$

Considering the magnitude and the relationships in ω_p ω_c and $\angle\gamma$, the self-inductance and mutual inductance can be determined as:

$$L_1 = \left[\sqrt{\left(\frac{u_p}{i_p}\right)^2 - \left(R_p\right)^2}\right] \Big/ \omega_p \tag{4.18}$$

$$L_{12} = \left(\frac{u_{c0}}{i_p}\right) \Big/ \omega_p \tag{4.19}$$

where u_{c0} is the measured open-circuit phase voltage of secondary winding.

Similarly, if taking account to exchange the position of the main stator and auxiliary stator and doing the same procedure as above test, we will have the similar conclusion where u_{p0} is the measured open-circuit phase voltage of primary stator.

$$L_2 = \left[\sqrt{\left(\frac{u_c}{i_c}\right)^2 - (R_c)^2}\right] \Big/ \omega_c \tag{4.20}$$

$$L_{21} = \left(\frac{u_{p0}}{i_c}\right) \Big/ \omega_c \tag{4.21}$$

Therefore, the self-inductance and mutual inductance can be determined experimentally in standstill condition of the machine. The results are detailed in Table 4.5 and Table 4.6

Rotor position angle θ	Primary stator line voltage $V_{p\,line}\ (V)$	Primary Stator current I_p (A)	Secondary stator open line voltage $V_{c\,open\,line}\ (V)$	Primary stator resistor $R_p\ (\Omega)$	Primary stator phase voltage $V_{p\,phase}\ (V)$	Primary stator open phase voltage $V_{p\,open\,phase}\ (V)$	Primary stator self-inductance $L_1\ (mH)$	Mutual inductance $L_{12}\ (mH)$
0	382	4.69	312	1.01	220.5478028	180.133284	149.6512	122.2564
10	382	4.65	326	1.01	220.5478028	188.2161878	150.9391	128.8411
30	381	4.6	304	1.01	219.9704526	175.5144818	152.1809	121.4523
50	381	4.71	302	1.01	219.9704526	174.3597813	148.6252	117.8354
70	382	4.81	295	1.01	220.5478028	170.3183294	145.9159	112.7111
90	382	4.62	313	1.01	220.5478028	180.7106343	151.9197	124.5066
104	381	4.61	325	1.01	219.9704526	187.6388375	151.8506	129.5604
128	382	4.77	304	1.01	220.5478028	175.5144818	147.1402	117.1238
150	382	4.76	301	1.01	220.5478028	173.782431	147.4494	116.2116
180	380	4.53	312	1.01	219.3931023	180.133284	154.1277	126.5745
210	381	4.65	303	1.01	219.9704526	174.9371316	150.5438	119.7511
220	381	4.68	304	1.01	219.9704526	175.5144818	148	117
240	381	4.65	302	1.01	219.9704526	174.3597813	150.5438	119.3559
260	381	4.61	325	1.01	219.9704526	187.6388375	151.8506	129.5604
280	380	4.6	325	1.01	219.3931023	187.6388375	151.7813	129.8421
310	381	4.67	304	1.01	219.9704526	175.5144818	149.8988	119.6318
328	382	4.69	301	1.01	220.5478028	173.782431	147	115
350	382	4.82	294	1.01	220.5478028	169.7409791	145.6131	112.096

Table 4.5 Primary stator inductance test results

Rotor position angle θ	Secondary stator line voltage $V_{c\ line}\ (V)$	Secondary Stator current I_c (A)	Primary stator open line voltage $V_{p\ open\ line}\ (V)$	Secondary stator resistor $R_c\ (\Omega)$	Secondary stator phase voltage $V_{c\ phase}\ (V)$	Secondary stator open phase voltage $V_{c\ open\ phase}\ (V)$	Secondary stator self-inductance $L_2\ (mH)$	Mutual inductance $L_{21}\ (mH)$
0	378	2.33	226	0.55	218.2384018	130.4811608	298.1386	178.2553
20	378	2.44	194	0.55	218.2384018	112.0059522	284.6975	146.1173
40	379	2.49	195	0.55	218.815752	112.5833025	271	143.9213
60	378	2.41	224	0.55	218.2384018	129.3264603	280	170.813
80	379	2.39	199	0.55	218.815752	114.8927036	291.4227	180
100	378	2.31	204	0.55	218.2384018	117.7794549	300.72	162.2961
120	378	2.58	226	0.55	218.2384018	130.4811608	269.2482	145
150	378	2.4	224	0.55	218.2384018	129.3264603	289.4426	171.5247
180	377	2.32	225	0.55	217.6610515	129.9038106	298.6316	178.2315
200	379	2.43	195	0.55	218.815752	112.5833025	286.6254	147.4749
214	378	2.61	225	0.55	218.2384018	129.9038106	266.1532	140
232	378	2.48	195	0.55	218.2384018	112.5833025	280.1054	144.5016
260	378	2.31	195	0.55	218.2384018	112.5833025	300.72	180
290	378	2.43	193	0.55	218.2384018	111.428602	285.8691	145.9624
310	378	2.62	204	0.55	218.2384018	117.7794549	265.1373	143.0931
330	378	2.41	224	0.55	218.2384018	129.3264603	288.2416	170.813
350	378	2.31	196	0.55	218.2384018	113.1606528	300.72	180

Table 4.6 Secondary stator inductance test results

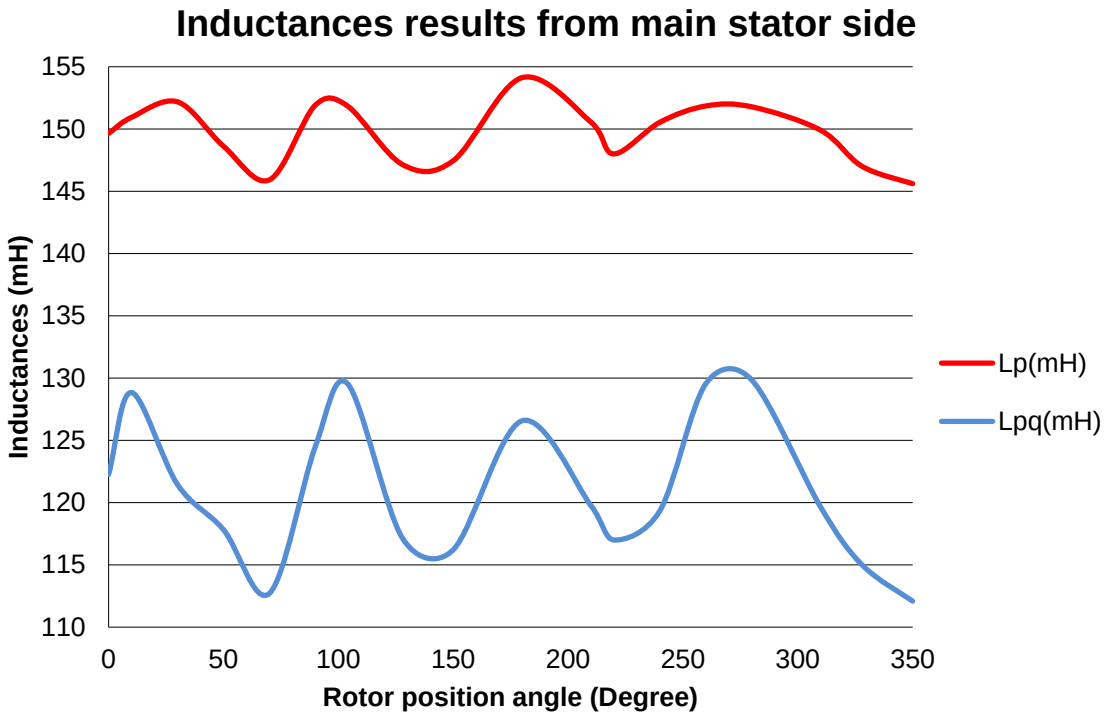

Figure 4.9 Main stator self and mutual inductances vs rotor position angle

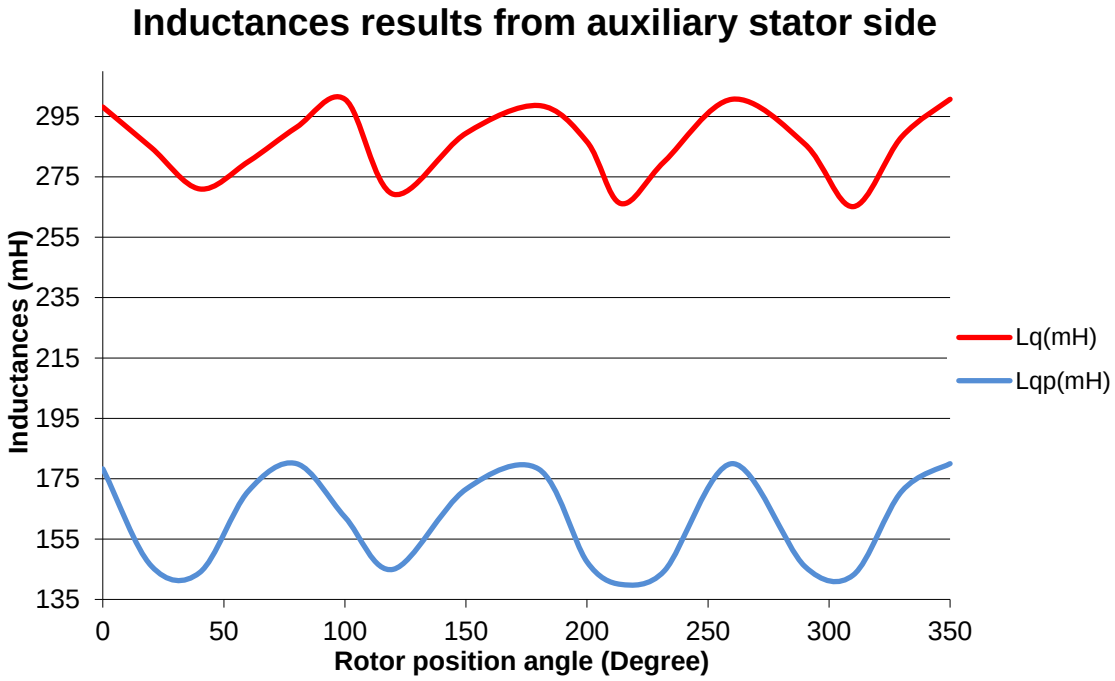

Figure 4.10 Auxiliary stator self and mutual inductances vs rotor position angle

According to the results above, two graphs are produced to demonstrate the inductance variations. It is clear that the self-inductance and mutual inductance are dependent on the rotor position. The tested main stator self-inductance and mutual-inductance curves versus the rotor position angle of the BDFRG are illustrated in Figure 4.9 while the auxiliary stator information explicated in Figure 4.10. For the sake of clarity, only the inductance of one phase (phase for the six-pole winding and phase for the two-pole winding) is displayed in both graphs.

The self-inductances in both pictures are highlighted by hot red lines and blue curves explain the mutual inductance. It is evident that the averages of the primary and secondary stator self- and mutual inductances are *0.15H*, *0.287H* and *0.14H* respectively. The parameter test results are not good enough so that the shapes have some distortions. The chief reason is the lack of the instruments for rotor angle position records. An inaccuracy reading is, therefore, caused by the utilization of protractor. Besides, the other readings, such as current and voltage value obtaining from the measurement tools, have some reasonable deviations. What is more, the environment factors will influence the experiment results as well. The errors caused by these reasons result in the distortions of inductance curve.

However, an interesting tendency is still obvious to be found in the inductance graphs. The inductance curve versus the rotor position angle emerges a shape between sinusoid and triangle. It is quite similar to the inductance wave of switched reluctance machine (SRM). Actually, BDFRG inductance curves are normally slicker and far closer to sine profile compared to the SRM inductance wave. That is because BDFRG looks quite like a superposition of two SRMs but more saturation.

4.2.2.3. Conclusion

From BDFRG parameter test, the self- and mutual inductance are:

$R_p = R_1 = 1.01\ \Omega \qquad R_c = R_2 = 0.55\ \Omega$

$L_p = 0.15\ H \qquad L_c = 0.287\ H \qquad L_m = 0.14\ H$

Compared to DFIG inductance ($L_s = 82.84\ mH, L_r = 18.26\ mH, L_m = 35.59\ mH$) The BDFRG primary stator inductance, secondary stator inductance and mutual inductance are *1.81*, *15.7* and *3.9* times respectively of relative DFIG inductance, stator, rotor and mutual inductance.

4.2.3. Altivar 71 Driver and IM Motor

As introduction above, *Altivar 71* and IM motor can be considered as an ensemble. They play a role of prime mover and provide the motive power to the generator.

Figure 4.11 shows the door layout of *Altivar 71* driver while the internal layout is displayed in Figure 4.12. The door must be kept close when the driver works. As *Altivar 71* starts, main switch will be open firstly and then press both safety reset and start button. In order to avoid the start button non-response, the red stop button should be pressed before *Altivar 71* starts. If fault occurs, the stop button turns red and the emergency stop will play a significant role at this moment.

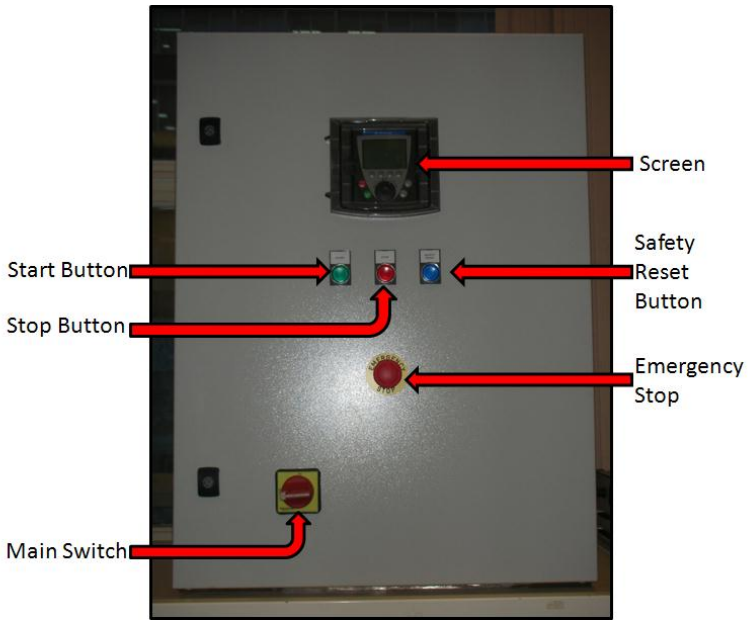

Figure 4.11 Door layout of *Altivar 71* used in experiments

Figure 4.12 Internal layout of *Altivar 71* used in experiments

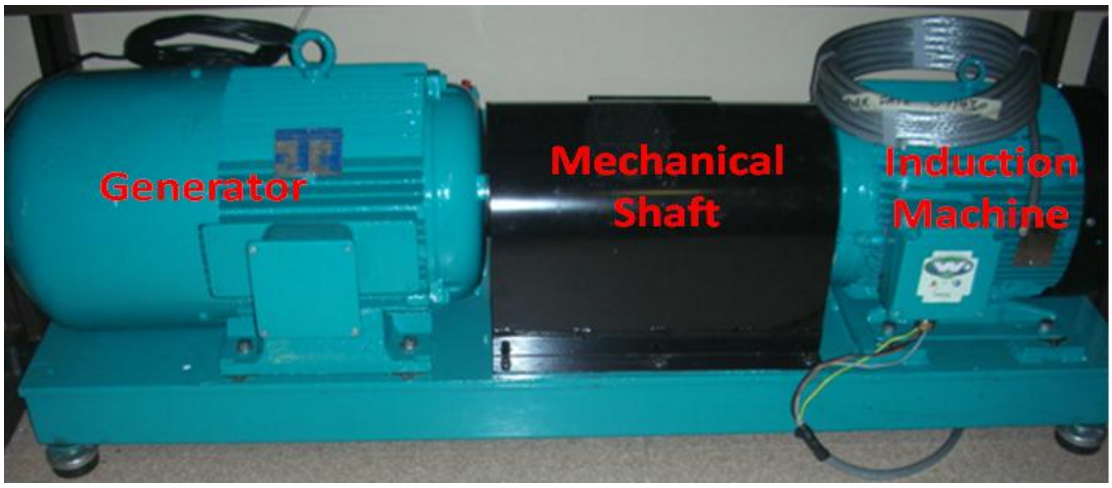

Figure 4.13 Induction machine and generator used in experiments connected by shaft

Figure 4.12 gives the internal layout of *Altivar 71*. The enlarging picture is displayed at the end of the red arrow. It is obvious a thick line connected to *Altivar 71* transfers the speed to the induction machine shown in Figure 4.13. Then the generators will rotate when it obtains the torque from induction machine through the mechanical shaft with black cover. How the *Altivar 71* controlling the speed of generator will be introduced in later section.

4.3. Control Cabinet

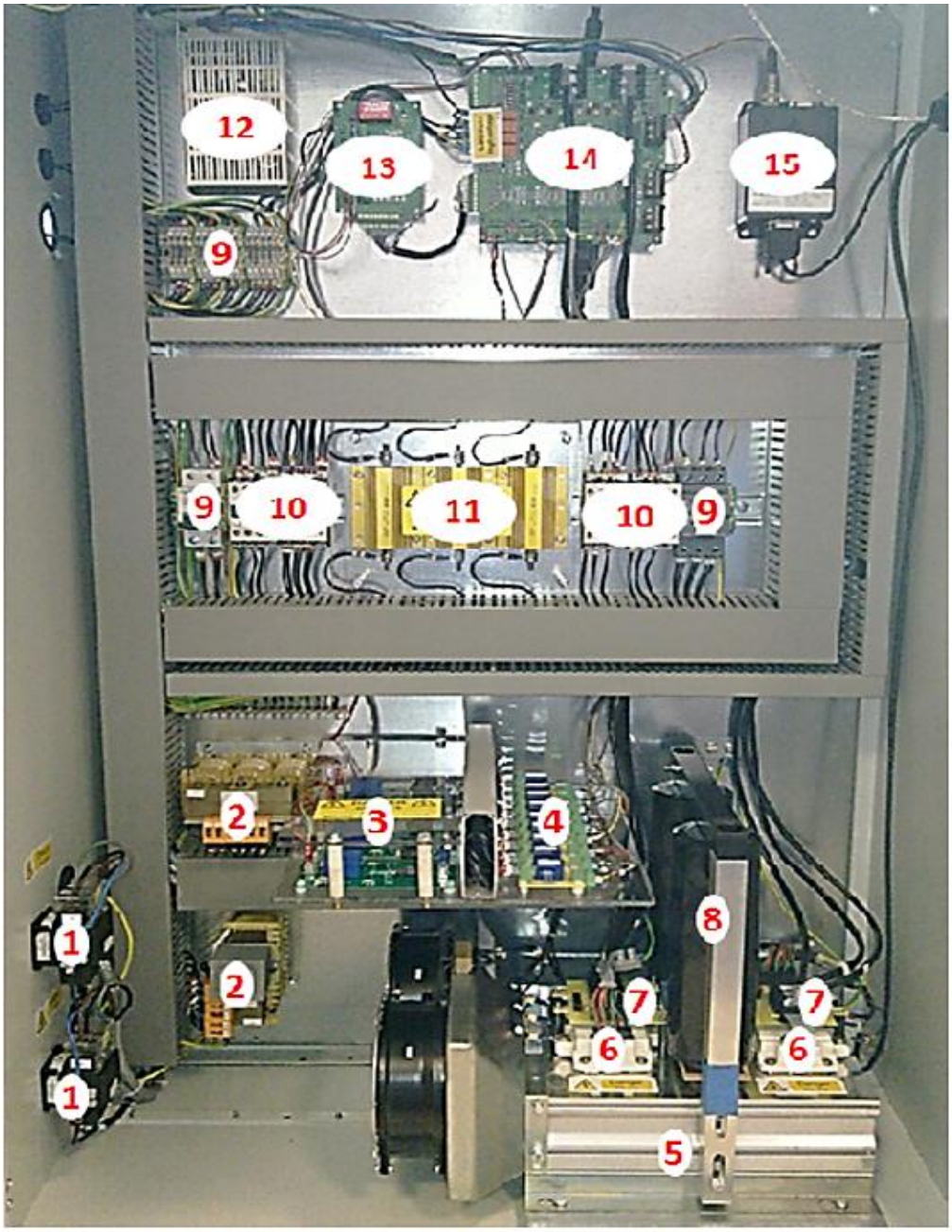

1. Main switch 2. Inductance 3. Voltage sensor 4. Current Sensor 5. Heat sink 6. Power electronics converter 7. Gate Drive Patch Board 8. DC-link Capacitor 9. Switch 10. Relay 11. Pre-charge resistor 12. Voltage supplier for DSP board 13. Expansion analogue interface 14. F28335 DSP Motor drive interface 15. Torque transducer

Figure 4.14 Internal layout of Control Cabinet used in experiments

The control cabinet inner layout has been illustrated in Figure 4.14. All components except the rotating machinery were housed in this cabinet. Every element in the cabinet has been numbered and named in the graph.

This cabinet is supplied with two separate three-phase voltages from the grid through two different variacs and passes the voltages to DFIG stator and rotor or BDFRG two stators respectively. The variac can adjust the input voltage to the generator. When it turn to *100%*, the input voltage will reach the rated level — *220V* rms value per phase.

In the expectation, both stator (primary stator) and the grid-side converter would be supplied by the rated *380V* line to line voltage and DC voltage would reach *600V*. But in fact, EMI affects the PWM fault signal LED lights. Hence, the voltage passed through the IGBT of power modules has to be restricted. In the experiments, *100%* voltage is supplied to the stator of DFIG or the primary stator of BDFRG and *50%* voltage has been provided to the grid side converter to support *300V* DC voltage. The details of the effects to PWM fault signal LED lights would be expounded in later description.

The devices marked as *1*, *9* and *10* play the roles of switches. The device *1* may connect or disconnect two routes of the cabinet to the main supply separately. Switches can be opened and closed by physically turning them, while relays have to be controlled by *eZdsp F28335*.

There are *3* AC voltage sensors and *9* current sensors which can accept up to *400V* rms voltages and *45A* rms currents, and engender *0-5V* small voltage signals to *eZdsp F28335*. One DC voltage transducer can transfer up to *800V* DC voltage to *5V* signals as well. Thus at least *13* Analogue Digital Converter (ADC) interfaces are needed to receive *0-5V* voltage signals. But the main DSP driver board only has *10* sensor interfaces, thus an expansion analogue board is made to create extra *8* sensor interfaces.

The toque transducer acquires the signals from *Altivar 71* and conveys to DSP board. Then the torque value can be read in Torque Log — the software of *Altivar 71*.

4.3.1. DSP Controller Board Overview

The whole experimental system is controlled by *eZdsp F28335*. But the *F28335* pins are too concentrated and hard to be connected. So an interface board is needed to draw out the pins of DSP. My supervisor, Dave Atkinson designed the motor driver interface shown diagrammatically in Figure 4.15 and Figure 4.16. *EZdsp F28335* is attached at the back of the interface board. The front of board displays *6* gate drives, *10* sensors, *4* digital analogue converters, *2* encoders, *4* relays and *6* sensor-out-of range trip circuits.

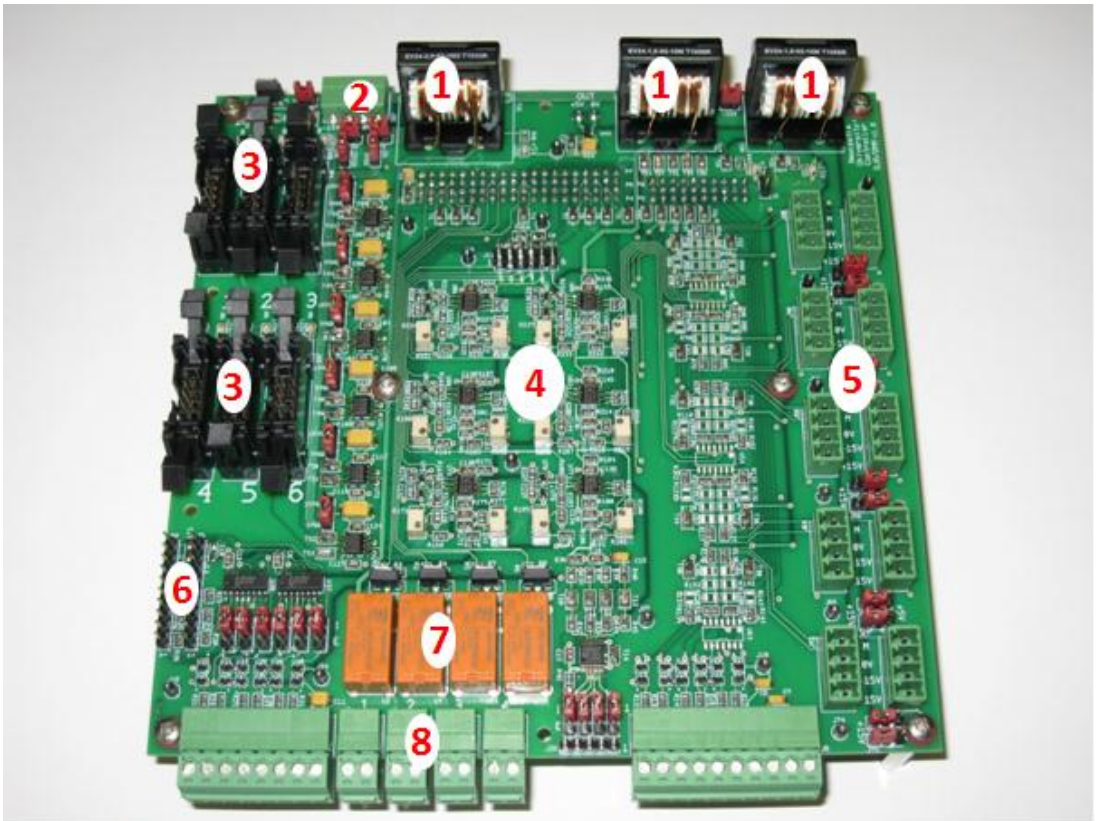

1. CM Choke (×3) 2. Aux PSU circuits 3. Gate Drive Interface (× 6) 4. Sensor out-of-range trip circuit (× 6) 5.Sensor interface (× 10) 6.Encoder interface (× 2) 7. DAC (× 4) 8.Relay (× 4)

Figure 4.15 Motor driver interface board layout

Figure 4.16 The back of motor driver interface board

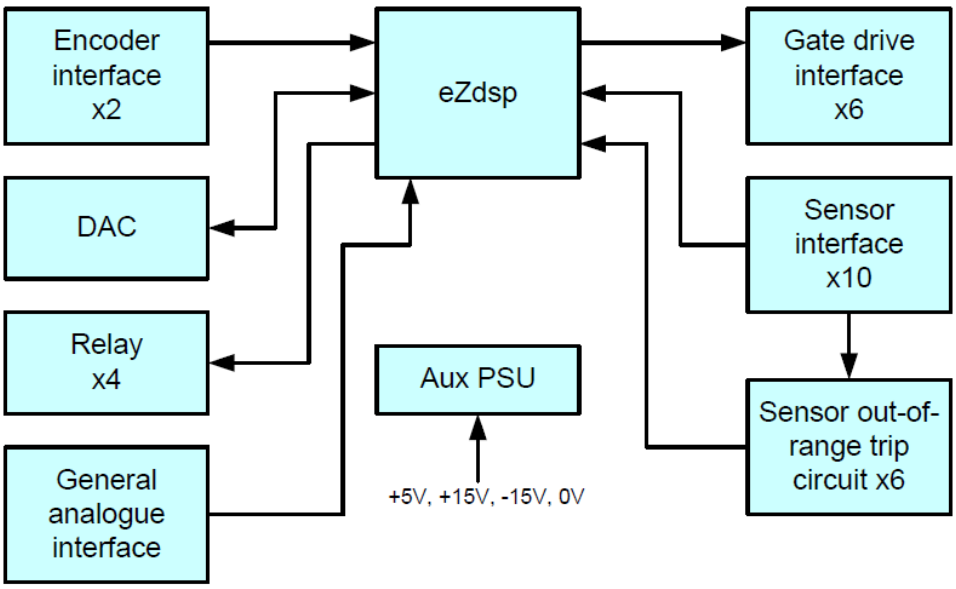

Figure 4.17 Diagram of interface board components

The functions included on the board are shown in the above diagram (Figure 4.17). The on-board interfaces have been designed to cater for a range of different external sensors and gate drive circuits.

The gate drive interface allows the *eZdsp* PWM output pins to communicate with the external gate drive boards or modules. There are *6* pairs of PWM outputs on the *F28335* microcontroller, thus 6 interface circuits are provided. Each interface includes two PWM signals. In the experiments, all gate drive channels have been utilized, *3* for rotor side converter and the other *3* for grid side converter controller.

10 identically flexible sensor interfaces are included to permit the connection of a variety of current and voltage sensors to the microcontroller ADC inputs. Every interface includes a *4*-pin connector to allow wiring to an external current or voltage sensor circuit and the supply pins to energise the sensor. For the tests, *3* DFIG stator currents (*3* primary stator currents in BDFRG), *3* rotor currents (*3* secondary stator currents in BDFRG), *3* currents between grid side converter and the grid called line currents, *3* stator voltages (*3* primary stator voltages in BDFRG) and *1* DC voltage have to be detected. Hence at least *13* sensor interfaces are needed. Hence the expansion analogue board is designed to create extra 8 uniform sensor interfaces.

To provide an overcurrent protection capability, *6* of the sensor interface circuits are connected to sensor out-of-range circuit. This trip circuit employs a voltage window detector to detect whether a sensor signal goes out of the normal range. The voltage range can be altered by regulating the adjustable resistor in window detector circuit. The most obvious application of this circuit is for fast hardware overcurrent protection. The circuit can also be used for overvoltage protection if used with a voltage sensor. Compared to the amount of sensors, *6* protection circuits seem insufficient. Therefore, selecting the most vital elements to detect is significant. Taking account of vector control in Chapter 5, rotor currents (secondary stator currents) and line currents are detected for overcurrent protection purpose as they are inner loop control components

4 DAC channels are included to allow access to internal software signals in real-time when the controller is operating. The analogue output signals from the DAC are

unipolar while ADC signals being monitored are bipolar. However, the unipolar DAC signal is sufficient in the experiments to provide the input to *Altivar 71*.

4 relay circuits are included to provide a galvanically isolated means to switch other circuits such as larger relays or contactors. The relay coil is energised by switching a discrete MOSFET. The MOSFET gate is driven from a GPIO signal configured as an output. As the DSP board will disconnect from the computer when the experiments are taken under high voltage condition, relays switching will be controlled by the Button in the LabVIEW.

Two identical shaft encoder interfaces are provided on the *eZdsp* board. As most encoders produce differential line driver output signals, the general interface board provides a differential line receiver for the *CH-A*, *CH-B* and *CH-Z* signals for two encoders.

4.3.2. Rotor Bi-directional Converter

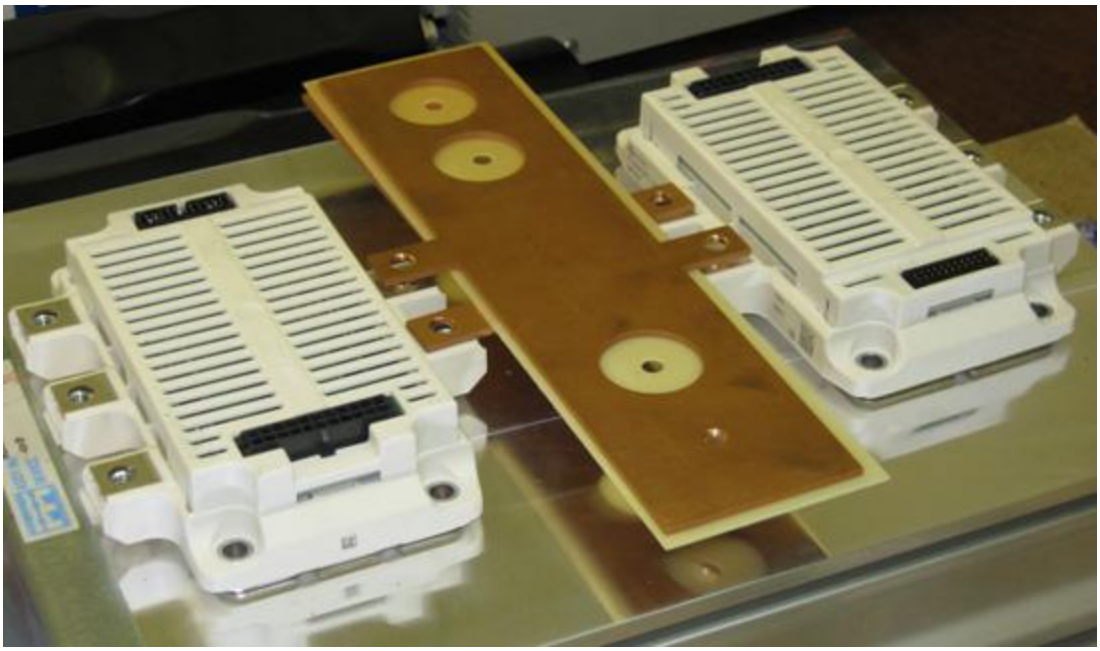

Figure 4.18 Power electronic converters used in experiments

Two *Infineon IFS100V12PT4* IGBT power modules are employed in the experimental apparatus. They have *1200V* rated voltage and *100A* rated current. Figure 4.18 explicates the two modules placed on the heat sink. Two converters connected back to back with a DC bus between them. The DC-link consists of two black capacitors as displayed in Figure 4.19. This structure allows the power bi-directionally flowing.

Figure 4.19 Back to back converters connected with DC-link

From the pictures, it is overt that *Infineon IFS100V12PT4* IGBT power module is hard to be connected to the DSP board gate drive interface, thus a gate drive patch board as shown in Figure 4.20 is lying on the IGBT module. This board plays a role of the intermediary between power converter and DSP interface board. Each module has one patch board and each board owns *3* pairs of PWM outputs.

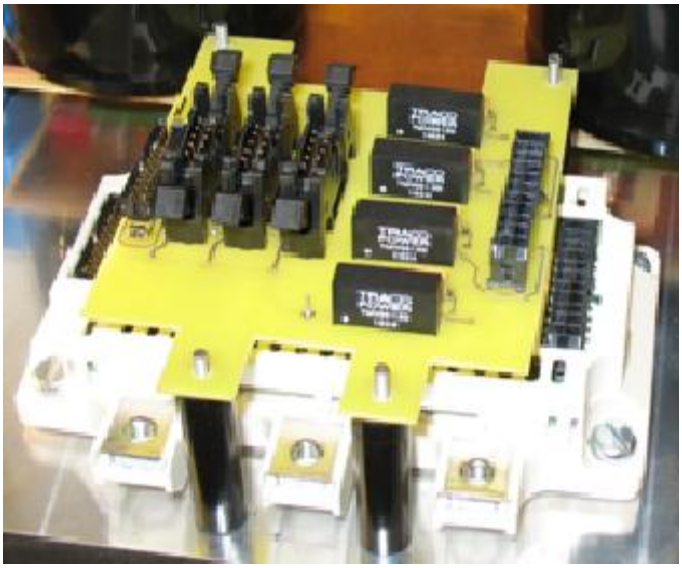

Figure 4.20 Gate drive patch board used in experiments

4.4. Basic control settings

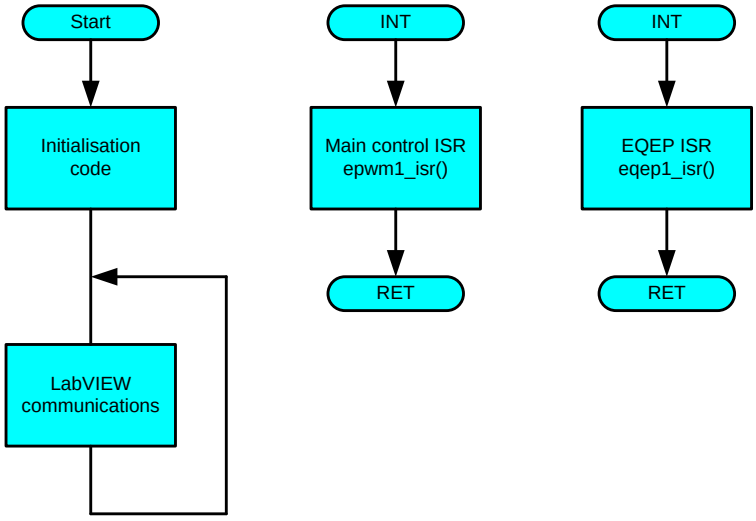

Figure 4.21 Basic structure of the code

Basically, The *F28335* has *2* serial communication interfaces (*SCI*). On the *eZdsp* board *SCI-A* is set up as an *RS232* interface. This is used for a serial link to the user interface implemented in LabVIEW. Data is sent by the user interface as a sequence of *ASCII* characters. USB connector is used to load the C programme in C code composer to DSP. However, USB connection is unstable when the experimental

voltage is high due to the noise effects. Thus, USB connector will keep disconnection during the tests after the code is loaded to the flash memory. And DSP will keep communication with the computer via *RS232*.

The basic structure of the code is shown in the following block diagram Figure 4.21). This section will introduce the basic settings of LabVIEW communications, main control *ISR* and *EQEP ISR* separately.

4.4.1. LabVIEW Communications

Execution of main program results is a series of initialisation code steps followed by the LabVIEW data exchange loop. This loop continuously communicates with the LabVIEW user control panel via the *RS232* interface. On the *F28335* microcontroller, the *RS232* interface is implemented with the Serial Communications Interface *SCI-A*.

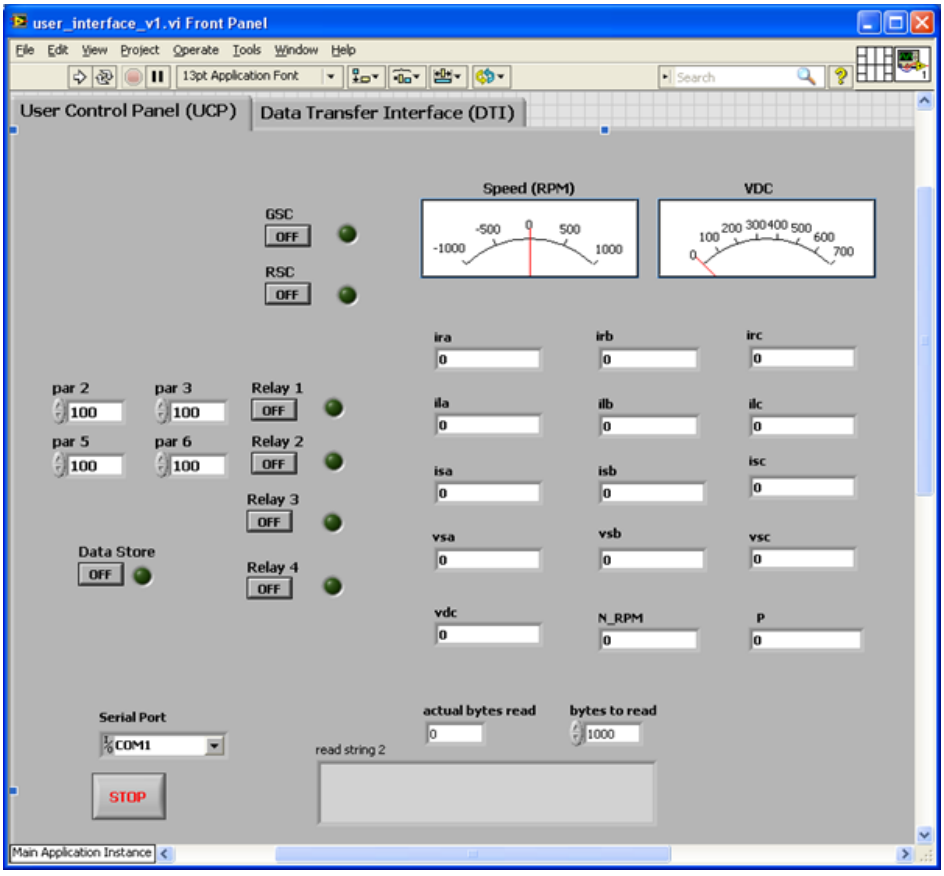

Figure 4.22 User Control Interface - UCP view

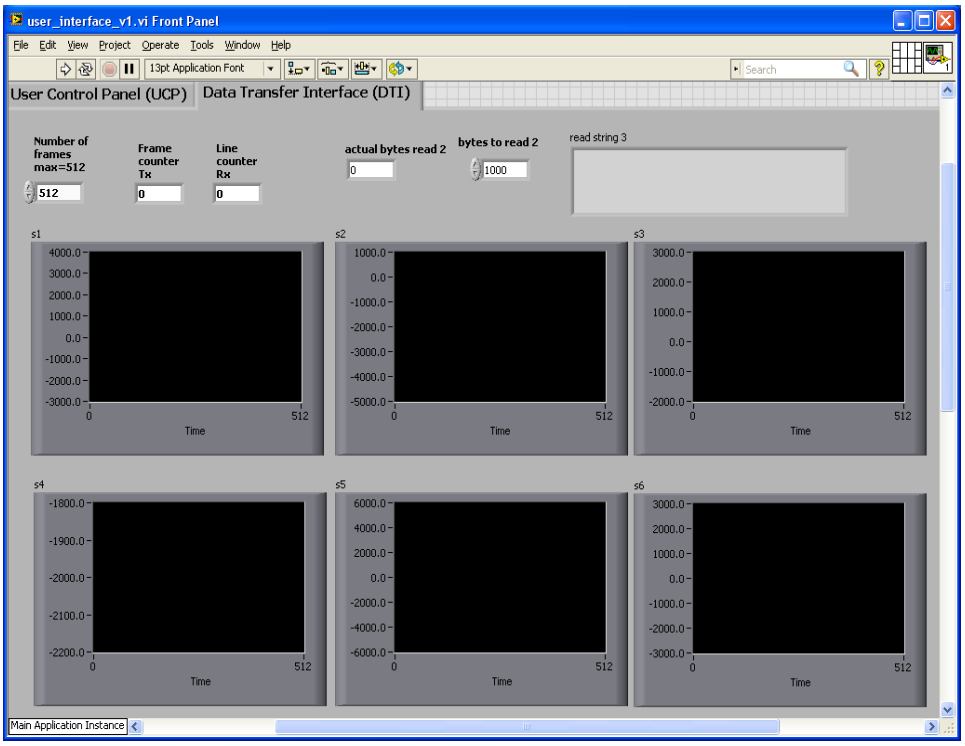

Figure 4.23 User Control Interface - DTI view

The user communicates the *eZdsp F28335* microcontroller board with the LabVIEW user interface via the *RS232* interface. The LabVIEW interface has two views depending on operating mode. The User Control Panel (UCP) view as shown in Figure 4.22 is used for continuous monitoring and control of the *eZdsp*. The Data Transfer Interface (DTI) view illustrated in Figure 4.23 is used less frequently when the data collected in the *eZdsp* RAM store requires to be transferred to the PC. The communication process between two LabVIEW user interfaces does not involve interrupts.

The communication is a bi-directional process. A Control Parameter Frame (CPF) is sent by the UCP to the *eZdsp F28335* and in return a Monitoring Parameter Frame (MPF) is sent back to the UCP. This data exchange is repeated at a rate of *5* updates per second which is determined by the LabVIEW UCP. At the time of writing the CPF contains *6* user control parameters and the MPF contains *15* monitoring parameters. Relatively simple code changes can expand or contract the number of parameters in

each frame. This data exchange process is explicated in the graph below (Figure 4.24).

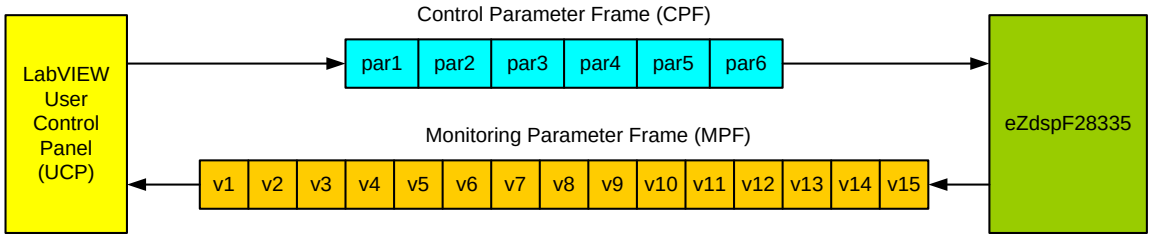

Figure 4.24 LabVIEW/*eZdsp* data exchange

Each frame of parameters is packaged as a character string for transfer over the *RS232* link. The timing of LabVIEW and *eZdsp* data exchange loop is determined by the rate at which the LabVIEW UCP sends data to the *eZdsp F28335*. The LabVIEW UCP can be modified to suit the user's requirements.

The initial loop at the beginning of the LabVIEW data exchange is used to assemble the CPF string in character array. The *6* integer data parameters (*par1*, *par2*, etc) are extracted from the input string. These data parameters are used to control the *F28335* software during execution. However, parameter *par1* is used to select the interfaces of LabVIEW. If the parameter *par1* has the coder *100*, LabVIEW UCP is exchanging the data. On the contrary, *200* code of *par1* signifies to the programme that LabVIEW DTI is transferring the data and the data will stored in a txt file which will be described later.

The *15* data variables of the MPF are sent to the *RS232* interface. The data variables are accessed as global variables. These *15* monitoring data parameters are integers as well. Thus, in order to monitor the floating data (ie. Currents, voltages) obtained from generator, normally, cut out the integer part of data when they multiply by *100* or *1000*.

There are a number of push-buttons on the LabVIEW panel. As these buttons can be pressed at any time, their status needs to be monitored continuously to ensure that

immediate action is taken by the *F28335* control software. The *16*-bit data variable *par4* contains a code representing the status of all the panel push-buttons. At present there are only *7* panel buttons so only the lower bytes of *par4* are used. A status flag (global variable) is declared for each push-button.

When using the *eZdsp F28335* to control high voltage power electronics it is advised to disconnect the USB link to the PC once the application code is running. This is because the emulator USB link is very sensitive to noise and is likely to be lost due to EMI. Even if this didn't happen it is still risky to control high power equipment with the Code Composer debugger active. For various reasons Code Composer can halt the processor and this could have catastrophic consequences for the power equipment. The LabVIEW user interface via the *RS232* link is used to control the *eZdsp* with the emulator link disconnected. The *RS232* link is not sensitive to EMI and also the *eZdsp* code can be written, such that errors in the *RS232* transmission do not result in dangerous action.

Unfortunately once the emulator link is disconnected communications cannot be re-established until the *eZdsp* is powered down and then powered up. This action would wipe the contents of the RAM data store. The *Tools=>Graph* feature of C Code Composer cannot be used to get the current or voltage waveforms. It is therefore necessary to have a means to transfer the contents from the RAM data store to the computer when the emulator link is not available. Fortunately the *RS232* link can also be used to for this purpose.

As mentioned earlier the LabVIEW user interface has a second view called the Data Transfer Interface (DTI). This is used to carry out a block transfer of the entire contents of the RAM data store to a PC text file for later graphical display or data processing.

The RAM data store contents are transferred as *512* frames, although each data store allows *2048* samples of different integer variables to be stored. Hence, the data

store function is executed *512* times to transfer the full contents for the RAM data store. It indicates data transfers to DTI every four times of its storage. Each execution of this function sends *32* words from the RAM store to the *RS232*. The DTI transfers the *512* frames of data into a text file. The data from the *26* RAM arrays are packaged in a frame. The DTI sends a frame counter value and a frame of *32* data items are sent back. The data for the first *10* arrays are shown graphically as the data is transferred, however, only *6* display in Figure 4.23. This allows a quick data health check before subsequent processing of the generated text file is carried out.

4.4.2. PWM settings (EPWM)

The *F28335* has *6* PWM units (*EPWM1 – EPWM6*). Each unit contains a pair of PWM output signals (A and B). The pair of signals can be used to drive an inverter leg. The code in this function sets up all 6 PWM units to a common time base period of $200\mu s$ with a common carrier signal of *5kHz*. The deadtime between outputs A and B is set to $1\mu s$.

The PWM carrier signal is set to a triangle. It takes half period to arrive at its peak. Thus, the interval time between the highest and lowest value is $100\mu s$. However, the basic frequency of *eZdsp F28335* is *150MHz*. Its sample time is $\frac{1}{150}\mu s$. Thus, in order to obtain *5kHz* triangle carrier signal, the peak value of PWM is set to *15000*. ($\frac{2\times 15000}{150M} = 200\mu s$)

The signal for the ADC sequencer start is set up to trigger on the positive apex of every carrier cycle. The graphical presentation is displayed in Figure 4.26.

4.4.3. Analogue digital converter (ADC)

The *F28335* ADC has *16* multiplexed inputs. The ADC sequencers on the *F28335* are set up to convert ADC inputs in simultaneous pairs. The current sensors are sampled first, followed by the AC voltages and finally the DC voltage.

The ADC timing is governed by the ADC clock (*25MHz*) which is derived from the basic frequency of DSP (*150MHz*). For good ADC performance ADC clock should not exceed *25MHz*.

The ADC sequencer is triggered on the apex of the PWM carrier. When the ADC sampling sequence is complete, an interrupt is generated for the main control ISR (epwm1_isr in Figure 4.21). This ensures that all the ADC input samples are acquired before control code execution is started.

Further details of the ADC timing are shown in the diagrams below. (Figure 4.25 and Figure 4.26)

ADC timing used on DSP board (cascaded sequencer & simultaneous sampling)

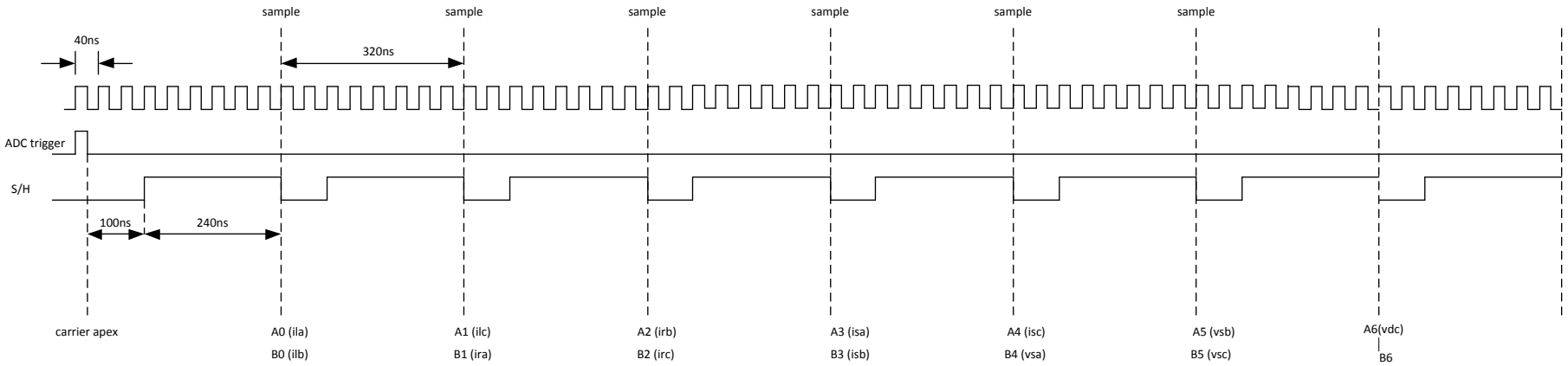

8 pairs of samples

Figure 4.25 Timing for cascaded simultaneous sampling ADC

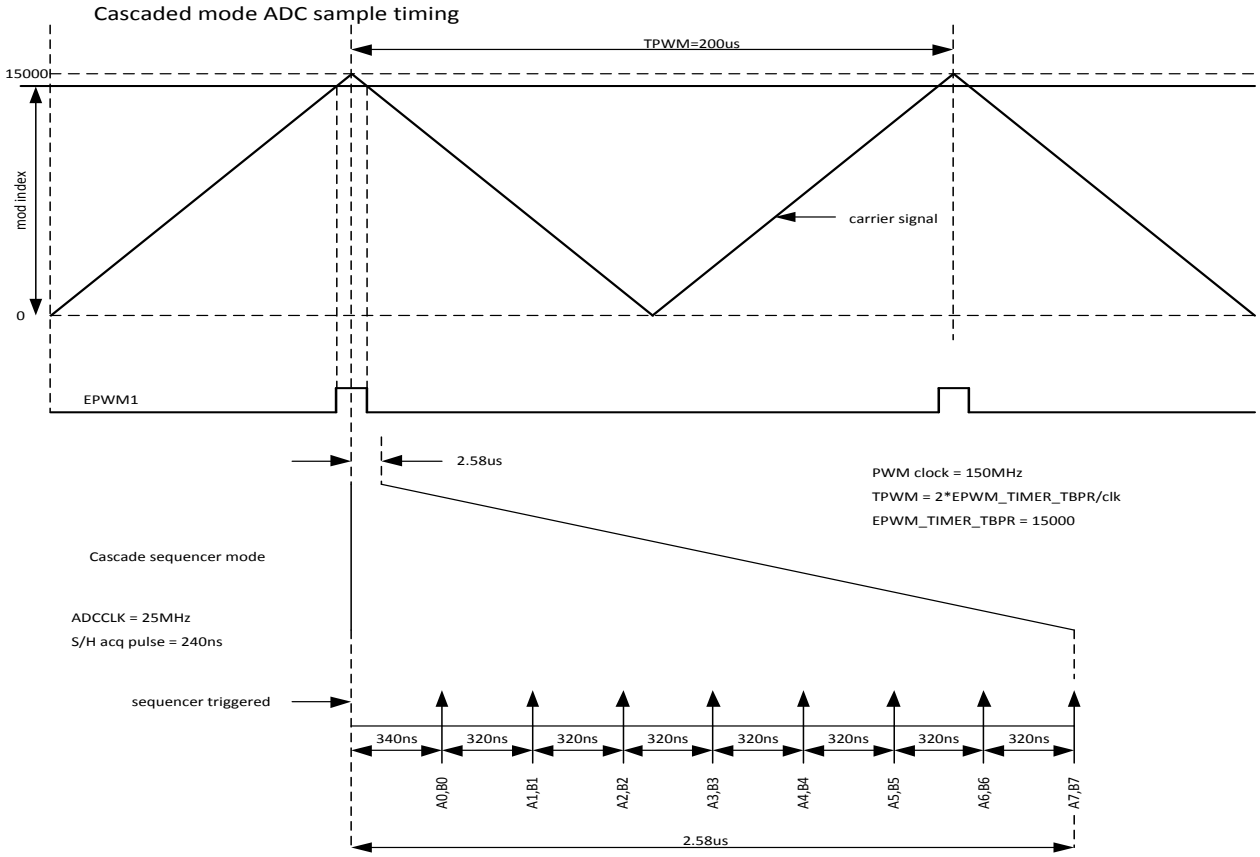

The initial 7 pairs of samples in the sequence are used. The 8th pair of sample occurs 2.58us after the carrier apex. To avoid sampling a current or a voltage on a switching event, the modulation index should be restricted to the range 0.0129 to 0.9871 p.u. (193 < mod index < 14806)

Figure 4.26 PWM-ADC sample timing

Based on the PCB controller interface board, a voltage less than *5V* is produced by the current or voltage sensor after a current or voltage passes across them. Then this small voltage signal flows to the Analogue Digital Converter (ADC). The ADC is settled to *16* bits, thus the ADC results the digital signal in the range of $\pm(2^{15}-1)$. The reading shown in the computer would be from *-32767* to *+32767*. A calibration factor is needed when the real currents and voltages are transferred to the digital signals of DSP. This factor includes the offset remover because each sensor data requires an offset to be removed to create a signed variable. The offset is different for each sensor due to small variations in the sensor offsets and associated electronic interface circuits. The offset for each sensor is determined by calibration. Besides, the ADC integer data need to be converted into floating point variables.

4.4.4. Altivar 71 controller

Altivar 71 will produce the torque and speed to the machines by supplying a DC voltage. The more input voltage, the quicker speed. The DAC can convert a digital signal to an analogue low dc voltage signal and allows software variables to be observed with an oscilloscope in real-time. Thus, it is better that provide the dc voltage to *Altivar 71* by a DAC signal through a voltage amplifier.

The advantage of doing like this is the speed can be controlled by the LabVIEW due to the linear relationship between digital signal, analogue voltage signal and speed produced by *Altivar 71*. *Par3* in UCP view can receive the demand speed value and send to DSP. DAC will transmit the analogue voltage signal after the speed value multiplies with a coefficient. Then the small voltage signal will enlarge through an amplifier and supplies to *Altivar 71*. *Altivar 71* then produces the toque and speed to the shaft. The encoder fixed on the generator side will estimate the velocity of the machine and feed the signal back to DSP for the controller.

One thing needs to be mentioned here. *Altivar 71* can only produce the torque but cannot consume it. Thus the direction of the torque or mechanical power must be kept from the induction machine to the generator. It indicates the DFIG and BDFRG can only operate at generation mode.

4.4.5. Encoder (EQEP)

The *F28335* has two incremental encoder interface units (*EQEP1* and *EQEP2*) one of which is used in the experiments. The encoder tested with the board is a *5000* line device. The quadrature encoder interface effectively multiples this by *4* to produce *20000* pulses for each revolution of the encoder shaft. The EQEP interface contains a counter which counts the encoder pulses. The counter is reset when an encoder index pulse arrives. To cope with down counting (reverse motion), the EQEP counter is set-up to reload with *19999* when the count reaches zero.

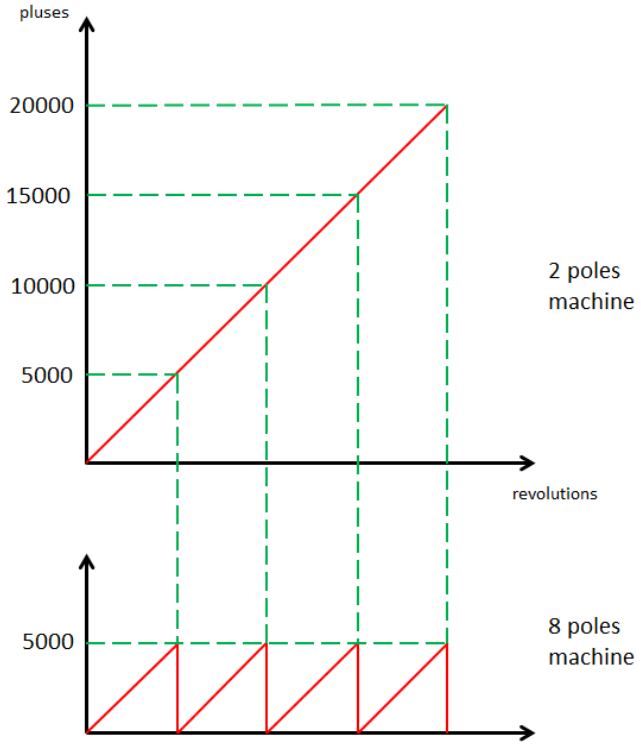

Figure 4.27 Electrical angles of 8 poles machine

When controlling machines with more than one pole pair, it is usual to convert the mechanical angle measured by the encoder to an electrical angle. As mentioned above, the *5000* line encoder produces *20000* pulses per revolution. The electrical angle is formed by dividing the *20000* pulse range into four ranges of *5000* pulses. Pulses in the range *0* to *4999* represent the angle of the first *2* poles and pulses in the range *5000* to *9999*, *10000* to *14999*, *15000* to *19999* represent the angle of the second, the third and the forth pole pair of the *8* poles machine. Graphical demonstration is given in Figure 4.27.

The EQEP unit is capable of generating an interrupt for various encoder events. The code in this function enables a direction change interrupt. When testing the board with the generator this was used to count shaft direction changes (speed reversals) for diagnostic purposes. The EQEP is also capable of estimating shaft velocity by counting encoder pulses received in a specified time interval.

4.4.6. Angle Generator

Applications based on vector control principles make use of reference frame transformations which require sine and cosine calculations. A function sets up floating-point look-up tables for one period of sine and cosine. Look-up tables execute faster than the standard sine and cosine functions implementation within a high level language. The constant TABLEN determines how many samples in the table and is currently set to *720* (i.e. 0.5 degree revolution). For example: $sin\,720 = sin\,360^{\circ} = sin\,2\pi$.

To minimise execution time, the tables are set up as global floating-point arrays and located in internal RAM. As floating-point variables occupy *4* bytes of memory, the overall memory allocated is $4 \times 720 \times 2 = 5760\,bytes$. If reduced accuracy is acceptable the memory requirement can be halved by implementing integer arrays instead.

5. Vector control response for DFIG and BDFRG

This chapter introduces the vector control schemes for both DFIG and BDFRG (taking DFIG as an example). The rotor-side and grid-side PWM converters of DFIG are controlled respectively based upon the stator voltage field orientation. A phase-locked-loop is implemented to measure the supply voltage phase angle to achieve the field orientation. The details of two controller schemes are presented followed by space vector modulation introduction.

The second part of this chapter presents the experimental results of both DFIG and BDFRG. The comparison between the control response of DFIG and BDFRG is included to show which generator has better controller performance.

According to two generators' control response and the fault response and fault ride through studies of DFIG in chapter 3, the fault response and fault ride through performance of BDFRG can be predicted in Section 5.3.

5.1. Vector control

Taking the DFIG as the example, BDFRG has the same controller scheme by replacing the subscripts and superscripts *s* and *r* to *p* and *c*. Vector control theory for electric drives is well-understood and can be applied to the control of the doubly-fed machines [86]. In general, robust and reliable control can be achieved using PI feedback controllers with machine currents or flux linkages transformed into excitation reference frame *d-q* space vectors [25][87].

The controller's excitation frame may be aligned in rotation to any particular voltage or flux linkage space-vector such that in steady-state operation all the machine currents and voltages appear as dc quantities. This approach lends itself to the application of

PI feedback controllers, in nested control loops, with independent control of active and reactive power.

5.1.1. Stator voltage field orientation

Many DFIG rotor-control schemes use an excitation-frame aligned with the stator flux linkage [25][38][24][41][45][87]. This allows clear decoupling between *d* and *q* components of rotor current. However, the alignment depends upon accurate positioning of the stator flux linkage vector. The stator flux linkage cannot be directly measured, typically estimated from integrating the stator voltage equation, although the integration process is not without drawbacks. Alternatively, it is acceptable to align the excitation-frame with the stator voltage space vector. The main advantage of stator voltage field orientation utilization emerges in using the reliable and stable output of a PLL for the field alignment.

In this thesis, the stator voltage field orientation control is selected and implemented as follows: the stator voltage is aligned to the *d*-axis as illustrated in Figure 5.1.

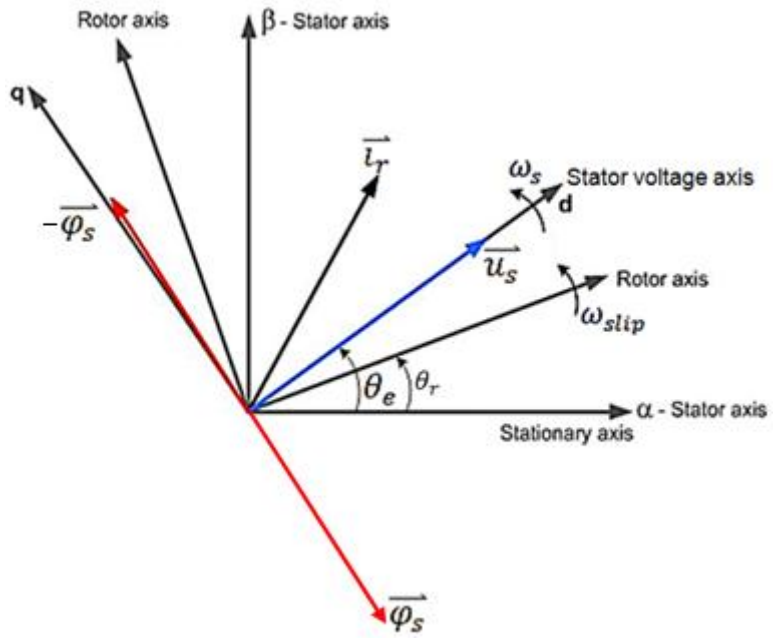

Figure 5.1 Stator Voltage Oriented Vectors Frame

According to the graph, the stator flux is more or less perpendicular to the stator voltage. The reason why the stator flux and the stator voltage are orthogonal to each other will be discussed in rotor side converter control section.

5.1.2. Phase Locked Loop (PLL)

A digital PLL is needed to provide accurate and stable information on the stator phase voltage. The excitation frame *d*-axis is aligned with the fundamental stator voltage space vector. As such, the quadrature component of stator voltage should be zero. This definition is exploited by the PLL to generate a space vector rotating synchronously with the fundamental component of the measured voltages.

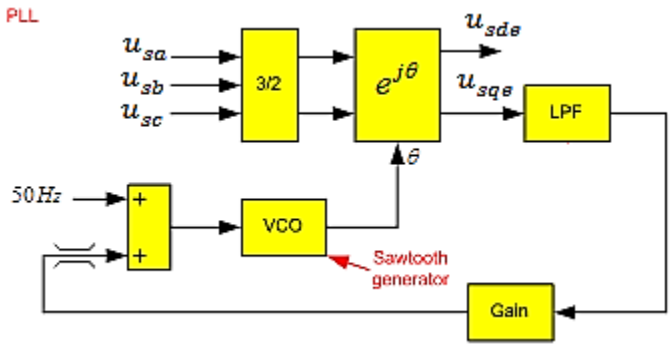

Figure 5.2 Phase Lock Loop design

The PLL scheme used in the experiments is shown in Figure 5.2. This PLL is composed of a phase detector, a low pass filter (LPF), a gain and a voltage controlled oscillator (VCO). The three-phase voltages u_{sa}, u_{sb} and u_{sc} are transformed to two-phase equivalents and then applied to a reference frame transformation. The transformation block produces u_{sde} and u_{sqe} components which are DC quantities in the steady state. The reference frame transformation block receives the angle from the VCO. The voltage u_{sqe} will be zero when the PLL is phase locked. Therefore u_{sqe} is used as a phase error signal. This error signal is low pass filtered and multiplied by a gain. The output from the gain block is used to adjust the frequency of the VCO. When the VCO is locked to the frequency of the incoming voltages, u_{sqe}

will be zero. The frequency input to the VCO is given a pre-set value of *50Hz* as this is the nominal frequency of the supply inputs. As the supply voltages are unlikely to deviate very much from *50Hz*, a limiter is put on the frequency adjust signal to limit its range. This adds to the stability of the PLL operation. The performance of the PLL can be tuned by changing the gain and the cut-off frequency of LPF.

This PLL scheme gives accurate estimation for stator voltages and angle θ_e. Figure 5.3 displays the *d-q* components of stator voltage under excitation reference frame (u_{sde} and u_{sqe}) after PLL. The test supply phase rms voltage is *220V*, which results in the *310V* peak phase voltage and magnitude of stator voltage space vector. Figure 5.3 shows the *310V* d component and approximate *0V* q element of stator voltage under excitation reference frame after PLL implementation. That evidences this PLL scheme is practicable.

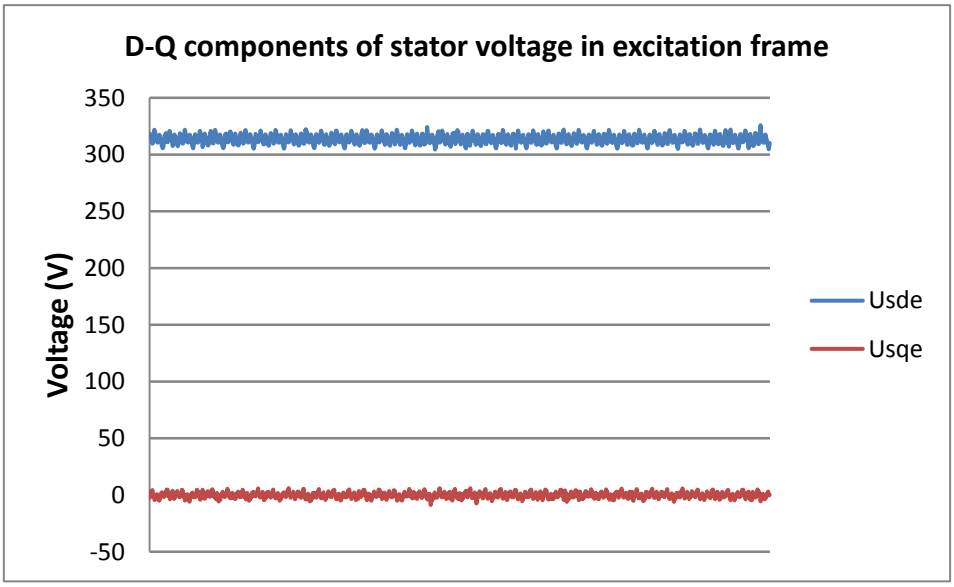

Figure 5.3 *d-q* components of stator voltage under excitation reference frame after PLL (u_{sde} and u_{sqe})

As the rotor output voltage must be applied at slip frequency, this necessitates a measurement of the rotor shaft position and the calculations of slip angle which is used to transfer the rotor reference vector to excitation reference frame. In the

experiments, the excitation-frame angle θ_e is obtained from PLL, while rotor-frame angle θ_r is acquired from the encoder. The slip angle θ_{slip} is calculated each instant from the difference between θ_e and θ_r.

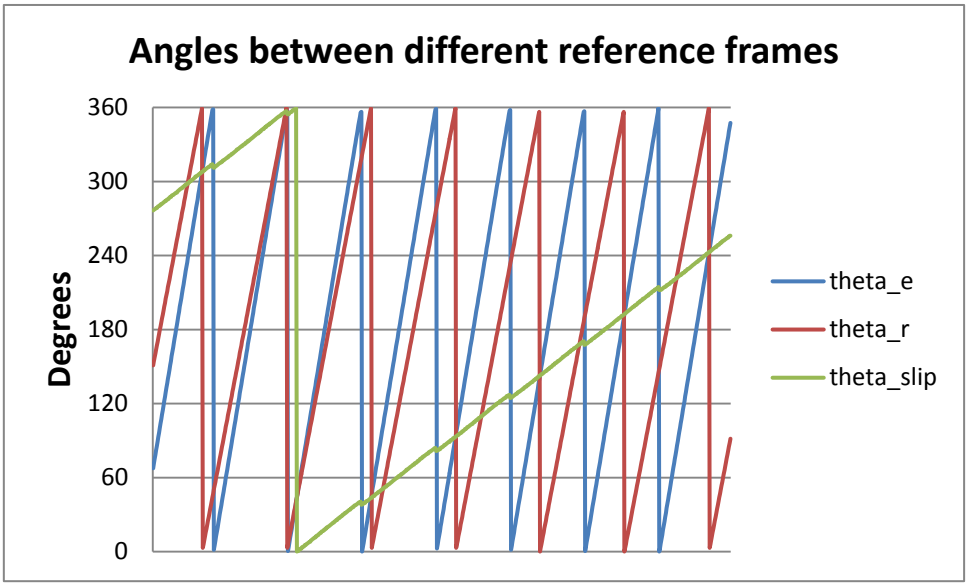

Figure 5.4 The experiment angles (θ_e, θ_r and θ_{slip})

The experimental results in Figure 5.4 indicate the relationships of excitation-frame angle θ_e, rotor-frame angle θ_r and slip angle θ_{slip}. From the graph, the excitation-frame angle θ_e rotates more quickly than the rotor-frame angle θ_r, which corresponds to $f_e > f_r$ and causes the slip frequency to be larger than zero. The machine operates at sub-synchronous speed mode with a positive slip angle θ_{slip}.

5.1.3. Space Vector Modulation (SVM)

In the experiment, the space vector modulation is used to receive the outputs of PI controller and produce the modulation index to the PWM power converter in both rotor-side and grid-side control schemes. In order to match the carrier frequency (*5kHz*) and ADC acquirement timing in the experiments. The SVM is designed as Figure 5.5 illustrated.

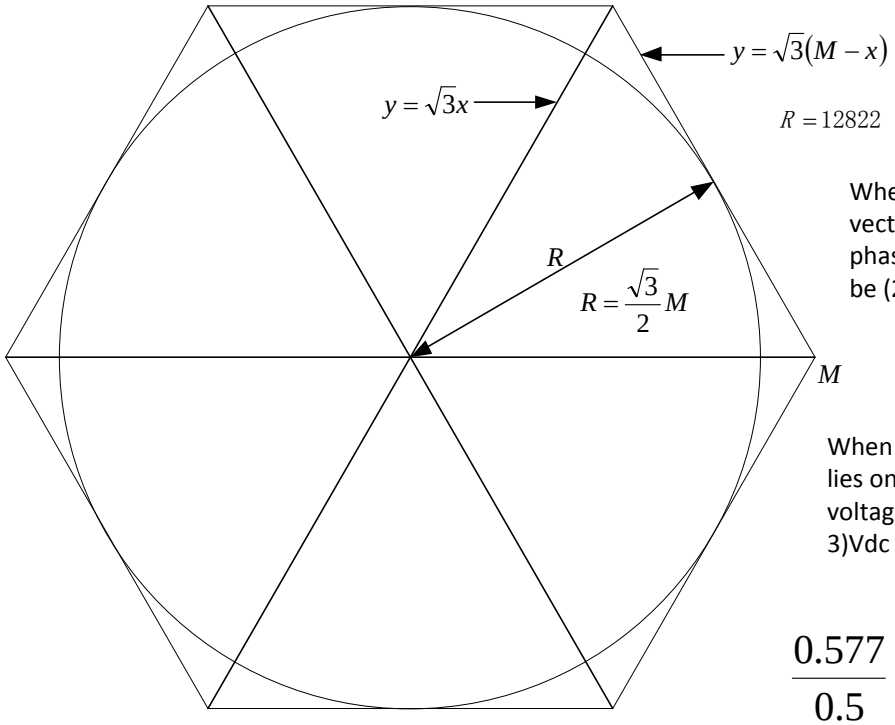

When reference vector is at M, the phase voltage will be (2/3)Vdc

When reference vector lies on circle, the phase voltage will be 0.866*(2/3)Vdc = 0.577Vdc.

$$\frac{0.577}{0.5}=1.154(15\%)$$

Clamping R within hexagon boundary

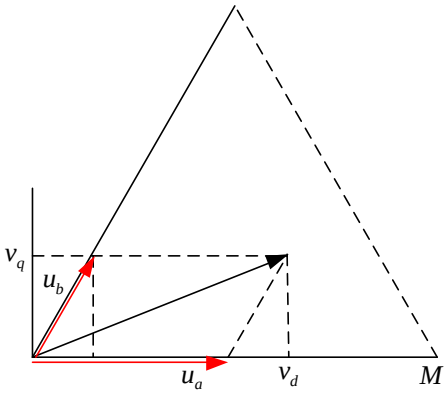

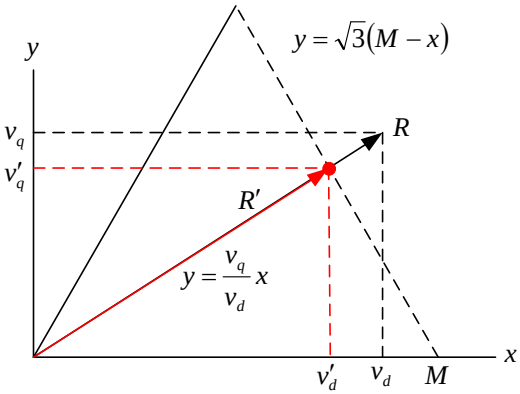

$$u_a = v_d - \frac{1}{\sqrt{3}}v_q$$

$$u_b = \frac{2}{\sqrt{3}}v_q$$

$$u_c = M - u_a - u_b$$

$$\sqrt{3}(M - v'_d) = \frac{v_q}{v_d}v'_d$$

$$\sqrt{3}M - \sqrt{3}v'_d = \frac{v_q}{v_d}v'_d$$

$$v'_d = \frac{\sqrt{3}Mv_d}{(v_q + \sqrt{3}v_d)}$$

$$v'_q = \sqrt{3}(M - v'_d)$$

When reference vector extends beyond the hexagon, the intersection with the boundary is used as the adjusted vector. This results is the angle remaining the same but the magnitude being reduced

SVM code tested in volume.c

$$M = 15000 \times 0.9871 = 14806$$

$$vd = 14806,\ vq = 0 \quad => \quad ma = 14903,\ mb = 97,\ mc = 97$$

$$R = \frac{\sqrt{3}}{2}M = \frac{\sqrt{3}}{2} \times 14806 = 12822$$

Figure 5.5 SVM design

5.1.4. Rotor-side converter control

The rotor-side converter employs cascaded power and current control loops. Its vector controller uses measurements of the rotor currents, stator currents, stator voltages and rotor shaft position to control the active and reactive stator power. The rotating *d-q* excitation frame is aligned to the synchronously rotating stator voltage vector.

5.1.4.1. Methods of Control

According to the diagram in Figure 5.1, the stator field orientation will cause:

$$\begin{cases} {u_{sd}}^e = u_s \\ {u_{sq}}^e = 0 \end{cases} \tag{5.1}$$

Then we will have:

$$\begin{cases} {u_{sd}}^e = R_s {i_{sd}}^e + \dfrac{d{\varphi_{sd}}^e}{dt} - \omega_s {\varphi_{sq}}^e = u_s \\ {u_{sq}}^e = R_s {i_{sq}}^e + \dfrac{d{\varphi_{sq}}^e}{dt} + \omega_s {\varphi_{sd}}^e = 0 \end{cases} \tag{5.2}$$

Taking account the steady state situation ($\frac{d}{dt} = 0$):

$$\begin{cases} {u_{sd}}^e = R_s {i_{sd}}^e - \omega_s {\varphi_{sq}}^e = u_s \\ {u_{sq}}^e = R_s {i_{sq}}^e + \omega_s {\varphi_{sd}}^e = 0 \end{cases} \tag{5.3}$$

When the stator resistance R_s is small enough to be ignored:

$$\begin{cases} {\varphi_{sq}}^e = \dfrac{R_s {i_{sd}}^e - u_s}{\omega_s} \approx \dfrac{-u_s}{\omega_s} \\ {\varphi_{sd}}^e = \dfrac{-R_s {i_{sq}}^e}{\omega_s} \approx 0 \end{cases} \tag{5.4}$$

This indicates that the stator flux must be maintained orthogonal to the stator voltage vector. Besides we also have:

$$\begin{cases} \varphi_{sd}{}^{e} = L_s i_{sd}{}^{e} + L_m i_{rd}{}^{e} = 0 \\ \varphi_{sq}{}^{e} = L_s i_{sq}{}^{e} + L_m i_{rq}{}^{e} = \varphi_s = L_m i_m \end{cases} \tag{5.5}$$

$$\begin{cases} i_{sd}{}^{e} = -\dfrac{L_m}{L_s} i_{rd}{}^{e} \\ i_{sq}{}^{e} = \dfrac{L_m}{L_s}\left(i_m - i_{rq}{}^{e}\right) \end{cases} \tag{5.6}$$

It is obvious that the stator and rotor current have linear relationship.

The stator is connected to the grid directly and the line resistance is small enough to ignore, thus if the grid voltage amplitude and frequency are assumed that they maintain to be constant, the stator flux magnitude will also be constant. The component of the generalized excited current i_m is unchanged as well. Then the active and reactive power P_s and Q_s have the relationship with stator current shown in Equation (5.7):

$$\begin{cases} P_s = 1.5 \times u_{sd}{}^{e} i_{sd}{}^{e} = 1.5 \times u_s i_{sd}{}^{e} = -1.5 \times \omega_s \varphi_{sq}{}^{e} i_{sd}{}^{e} \\ \qquad = -1.5 \times \omega_s \varphi_s i_{sd}{}^{e} = -1.5 \times \omega_s L_m i_m i_{sd}{}^{e} \\ Q_s = -1.5 \times u_{sd}{}^{e} i_{sq}{}^{e} = -1.5 \times u_s i_{sq}{}^{e} = 1.5 \times \omega_s \varphi_{sq}{}^{e} i_{sq}{}^{e} \\ \qquad = 1.5 \times \omega_s \varphi_s i_{sq}{}^{e} = 1.5 \times \omega_s L_m i_m i_{sq}{}^{e} \end{cases} \tag{5.7}$$

Due to Equation (5.7), P_s and Q_s can be also expressed as:

$$\begin{aligned} P_s = 1.5 \times u_s i_{sd}{}^{e} &= -1.5 \times \omega_s \varphi_s i_{sd}{}^{e} = 1.5 \times \frac{L_m}{L_s} \omega_s \varphi_s i_{rd}{}^{e} \\ &= -1.5 \times \frac{L_m}{L_s} u_s i_{rd}{}^{e} \end{aligned} \tag{5.8}$$

$$\begin{aligned} Q_s = 1.5 \times u_s i_{sq}{}^{e} &= -1.5 \times \omega_s \varphi_s i_{sq}{}^{e} = -1.5 \times \frac{L_m}{L_s} \omega_s \varphi_s \left(i_m - i_{rq}{}^{e}\right) \\ &= 1.5 \times \frac{L_m}{L_s} u_s \left(i_m - i_{rq}{}^{e}\right) = 1.5 \times \frac{\varphi_s}{L_s} u_s - \frac{L_m}{L_s} u_s i_{rq}{}^{e} \end{aligned} \tag{5.9}$$

It is clear that the stator active and reactive power can be expressed by the rotor current *d-q* component.

5.1.4.2. Control Loop Design

After defining a constant $\sigma = 1 - \frac{L_m^2}{L_s L_r}$, the rotor flux and voltage can be expressed by the rotor current and constant i_m. (Superscripts *e* are omitted in this development as the vector control scheme is designed and analysed in excitation reference frame.)

$$\begin{cases} \varphi_{rd} = L_r i_{rd} + L_m i_{sd} = \left(L_r - \frac{L_m^2}{L_s}\right) i_{rd} = \sigma L_r i_{rd} \\ \varphi_{rq} = L_r i_{rq} + L_m i_{sq} = \frac{L_m^2}{L_s} i_m + \left(L_r - \frac{L_m^2}{L_s}\right) i_{rq} = \frac{L_m^2}{L_s} i_m + \sigma L_r i_{rq} \end{cases} \tag{5.10}$$

$$\begin{cases} u_{rd} = R_r i_{rd} + \frac{d\varphi_{rd}}{dt} - \omega_{slip}\varphi_{rq} = R_r i_{rd} + \sigma L_r \frac{di_{rd}}{dt} - \omega_{slip}\left(\frac{L_m^2}{L_s} i_m + \sigma L_r i_{rq}\right) \\ u_{rq} = R_r i_{rq} + \frac{d\varphi_{rq}}{dt} + \omega_{slip}\varphi_{rd} = R_r i_{rq} + \sigma L_r \frac{di_{rq}}{dt} + \omega_{slip}\sigma L_r i_{rd} \end{cases} \tag{5.11}$$

Order $u' = R_r i + \sigma L_r \frac{di}{dt}$, then it is found that

$$\begin{cases} u_{rd}^* = u'_{rd} - \omega_{slip} \frac{L_m^2}{L_s} i_m - \omega_{slip}\sigma L_r i_{rq} \\ u_{rq}^* = u'_{rq} + \omega_{slip}\sigma L_r i_{rd} \end{cases} \tag{5.12}$$

Based on $u' = R_r i + \sigma L_r \frac{di}{dt}$, the plant for current loops is given by:

$$F_{ir(s)} = \frac{i_{rq\,(s)}}{u'_{rd\,(s)}} = \frac{i_{rd\,(s)}}{u'_{rq\,(s)}} = \frac{1}{\sigma L_r s + R_r} \tag{5.13}$$

Which can be written in the z-domain as:

$$F_{ir(z)} = \frac{(1-A)/R_r}{z-A} \qquad A = e^{-(R_r/\sigma L_r)T} \tag{5.14}$$

Where T is the sample time (*0.2ms*). That indicates that the converter switching frequency is *5kHz*. The standard design techniques are applied and the control schematic is shown in Figure 5.6.

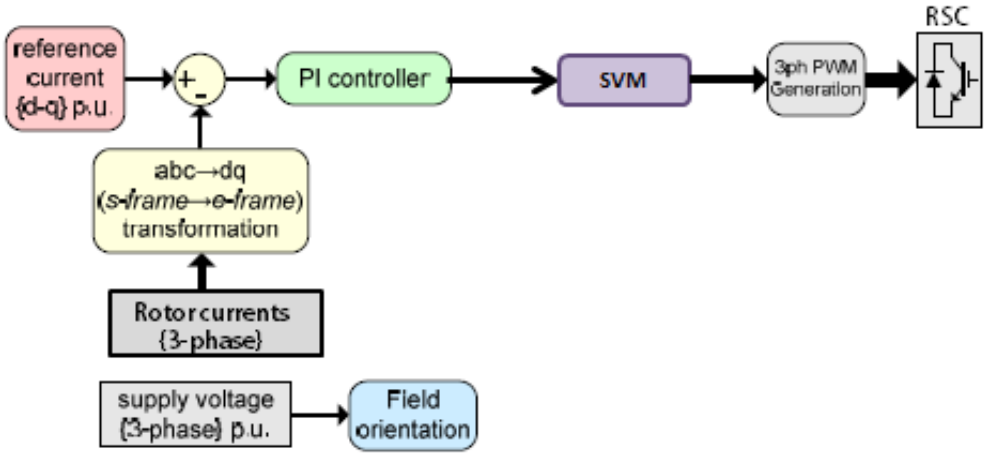

Figure 5.6 Rotor-side converter current control diagram

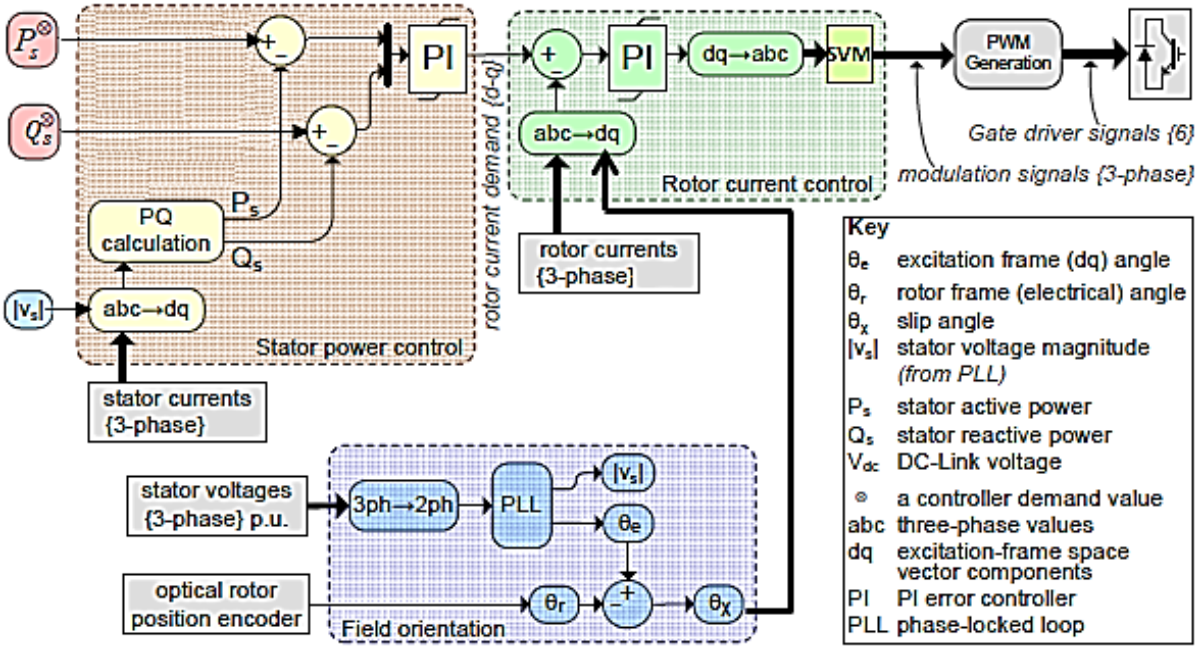

Figure 5.7 Rotor-side converter vector control scheme.

The stator real and reactive power can be controlled the rotor *d*, *q* current components respectively. The plant could be shown in equation (5.16) when we define that

$$\begin{cases} P_s^* = -1.5 \times \dfrac{L_m}{L_s} u_s i_{rd} = P_s' \\ Q_s^* = -1.5 \times \left(\dfrac{\varphi_s}{L_s} u_s - \dfrac{L_m}{L_s} u_s i_{rq} \right) = Q_s^{'} - \dfrac{\varphi_s}{L_s} u_s \end{cases} \tag{5.15}$$

$$F_{PQ(s)} = \frac{P_{s\,(s)}^{'}}{i_{rd\,(s)}} = \frac{Q_{s\,(s)}^{'}}{i_{rq\,(s)}} = -\frac{L_m u_s}{L_s} \tag{5.16}$$

Then the total rotor-side converter control system can be arranged as revealed in Figure 5.7.

For the rotor-side converter, the main vector control scheme is used for independent control of real and reactive power P_s and Q_s. This scheme is based on the stator voltage orientation principle, and defined in the synchronous *d-q* reference frame. The rotor current is separated into *2* parts representing P_s and Q_s respectively. The inner control loop is achieved by controlling the two rotor current components through PI controllers. The outer loop is for the control of P_s and Q_s adjusted by PI controller gains and provides the inner loop reference rotor current values.

5.1.5. Line-side converter control

The line-side converter transmits rotor circuit power to or from the grid connection. Its primary function is to manage the DC-link voltage, indirectly balancing power in or out from the rotor-side converter.

Similar to the rotor-side converter's control, the grid side converter uses the stator voltage orientation method. The vector controller uses measurements of the DC-link voltage, currents flowing on the lines and supply voltages to control the DC-link voltage and satisfy the requirements the reactive power exchanged between the

converter and the grid. Through the PI controller, the voltage into the grid-side converter is controlled by the line current. The main target of grid-side converter's control is to maintain the constant DC-link capacitor voltage and to minimize the reactive power.

5.1.5.1. Control Method

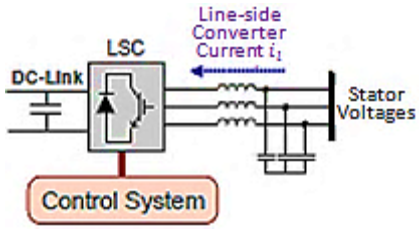

Figure 5.8 Line-side converter schematic

The line-side converter system is illustrated in Figure 5.8 above.

For the purposes of the simplifying the mathematical development, it is assumed that the line-side filter can be represented by a simple *L* configuration.

$$\begin{cases} u_d = Ri_d + L\dfrac{di_d}{dt} - \omega_s L i_q + u_{d1} \\ u_q = Ri_q + L\dfrac{di_q}{dt} + \omega_s L i_d + u_{q1} \end{cases} \tag{5.17}$$

Where u_{d1} and u_{q1} are the *d-q* components of the voltages injected to the converter. u_d, u_q, i_d and i_q stand for the main supply voltage and line current *d-q* components respectively. At the steady-state condition, the equation changes to:

$$\begin{cases} u_d = Ri_d - \omega_s L i_q + u_{d1} \\ u_q = Ri_q + \omega_s L i_d + u_{q1} \end{cases} \tag{5.18}$$

Then based on the reference frame of rotor-side converter control, we have $\overrightarrow{u_{dq}} = u_d + j0$. Assume $\overrightarrow{u_{dq1}} = u_{d1} + ju_{q1}$, Then the current of flowing between the grid and the converter can be obtained by

$$\overrightarrow{i_{dq}} = \frac{\overrightarrow{u_{dq}} - \overrightarrow{u_{dq1}}}{R + jX} = \frac{(u_d - u_{d1}) + j(-u_{q1})}{R + jX}$$

$$= \frac{u_d R - u_{d1} R - u_{q1} X - j(u_{q1} R + u_d X - u_{d1} X)}{R^2 + X^2} \tag{5.19}$$

Where the *X* represent combined the line and filter reactance.

The relationship between the active and reactive power absorbed from the grid (considered as positive) and the converter injected voltage is shown as follows:

$$\overrightarrow{S_g} = P_g + jQ_g = \overrightarrow{u_{dq}}\overrightarrow{i^*_{dq}} \tag{5.20}$$

$$P_g = u_d i_d + u_q i_q = u_d i_d = u_d \frac{u_d R - u_{d1} R - u_{q1} X}{R^2 + X^2} \tag{5.21}$$

$$Q_g = u_d i_q + u_q i_d = u_d i_q = u_d \frac{u_{q1} R + u_d X - u_{d1} X}{R^2 + X^2} \tag{5.22}$$

Therefore the power absorbed by the grid-side converter is:

$$P_{conv} = P_g - P_{fl} = P_g - \left|\overrightarrow{i^2_{dq}}\right| R$$

$$= u_d \frac{u_d R - u_{d1} R - u_{q1} X}{R^2 + X^2} - R \frac{\left(u_d R - u_{d1} R - u_{q1} X\right)^2 + \left(u_{q1} R + u_d X - u_{d1} X\right)^2}{(R^2 + X^2)^2}$$

$$= \frac{u_d u_{q1} X - u_d u_{d1} R - u_{d1}^2 R}{R^2 + X^2} \tag{5.23}$$

In which P_{fl} is the loss power of the filter. Normally, P_{conv}, the real power absorbed from grid through the grid-side converter would be kept equalling to the rotor real power injected to the rotor-side converter, when the converter losses are ignored. Actually, balancing these two active powers, $\frac{u_d u_{q1} X - u_d u_{d1} R - u_{d1}^2 R}{R^2 + X^2} = P_r$ is one requirement of $\overrightarrow{u_{dq1}}$ solution. Besides, minimizing the resultant reactive power sending to the grid ($Q_g - Q_s = u_q \frac{u_q X - u_{q1} X - u_{d1} R}{R^2 + X^2} - Q_s$) and the values satisfying the equation $u_{conv} = \sqrt{\frac{u_{d1}^2 + u_{q1}^2}{3}} \leq \frac{u_{dc-max}}{2\sqrt{2}}$ are another two requirements of $\overrightarrow{u_{dq1}}$.

5.1.5.2. Control Loop Design

Based on (5.18), the plant for current loop could be expressed as:

$$F_{i(s)} = \frac{u_{d\,(s)}^{'}}{i_{d\,(s)}} = \frac{u_{q\,(s)}^{'}}{i_{q\,(s)}} = \frac{1}{Ls + R} \tag{5.24}$$

When it is defined that

$$\begin{cases} u_{d1}^{*} = -u_{d}^{'} + \omega_s L i_q + u_d \\ u_{q1}^{*} = -u_{q}^{'} - \omega_s L i_d + u_q \end{cases} \tag{5.25}$$

The equation (5.24) can be written in the z-domain as:

$$F_{ir(z)} = \frac{{}^{(1-B)}/_{R}}{z - B} \qquad B = e^{-({}^{R}/_{L})T} \tag{5.26}$$

Where T is the sample time and has the same as the rotor-side converter's sampling time (*0.2ms*). Then, the current control loop could be designed as Figure 5.9.

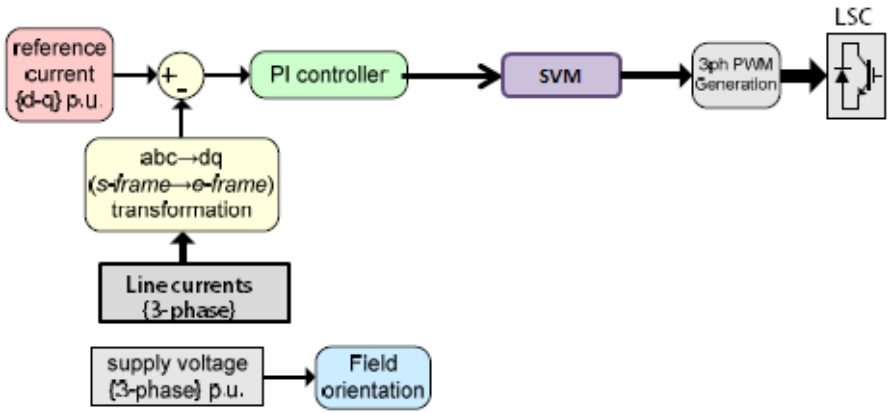

Figure 5.9 Grid-side converter current control diagram

In order to obtain the minimal reactive power of grid, the *q*-axis current is set to zero corresponding to unity power factor operation. The grid side voltage V_g, the converter

side voltage V_c and the current flowing in the line between the converter and the grid I_l has the relations diagrammatically presented in Figure 5.10.

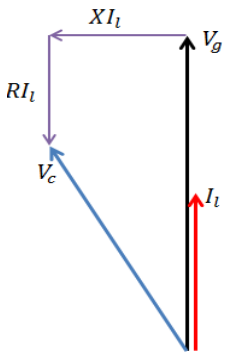

Figure 5.10 Diagram of grid side voltage V_g, converter side voltage V_c and the line current flowing between the converter and the grid I_l

How is the *d*-axis line current reference value set? It could be obtained by another control loop. In order to maintain the constant DC-link capacitor voltage, the *d* component of the line current is adjusted by outer loop PI controller. A typical cascade control arrangement for the line-side converter is shown schematically in Figure 5.11.

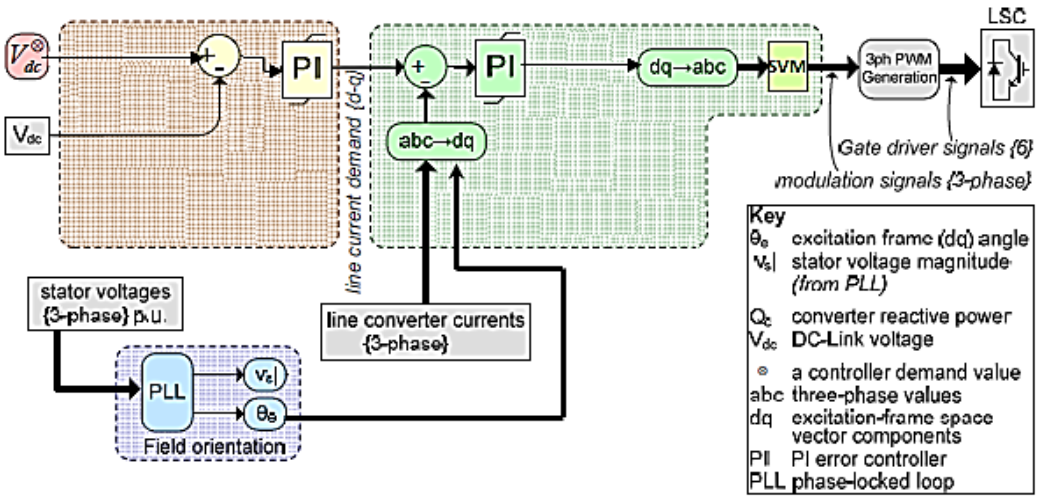

Figure 5.11 Line-side converter vector control scheme.

The line-side filter enables the fast-acting current controller to respond to current errors in milliseconds whilst maintaining a stable controlled output. The line-side converter controller can be tuned to respond faster than the rotor-converter's controller, which therefore permits good control of the DC-link voltage.

The overall line-side converter controller bears a similar structure to the rotor side converter (Figure 5.7). The line-side and rotor-side controllers are implemented independently, but may save computational effort by sharing information such as the PLL phase and the DC-link voltage measurement.

5.2. Comparative analysis of vector control response for DFIG and BDFRG

Both systems have the same power lever (*5kW*), pole number (*8* poles) and PWM switching frequency (*5kHz*). The test Rig and controller hardware are similar for both schemes. As they may be thought to have the same mathematic model, the parameters of BDFRG primary stator can be compared with DFIG stator's and secondary stator of BDFRG is conceivable to equal the rotor of DFIG. In the thesis, the subscripts *'p' 'c' 's'* and *'r'* represent the primary, secondary stator of BDFRG and DFIG's stator and rotor respectively. It is therefore of possibility to compare these two generators by the comparison of the relevant vector components with subscripts *'p'* and *'s'* or with *'c'* and *'r'*.

Both generators are expected to be controlled with a unity power factor. It means that the reactive power Q_s (DFIG) and Q_p (BDFRG) need be controlled to zero. However, due to the design problem of DFIG's main structure — the second-hand induction machine, when Q_s is set to zero, the rotor current will exceed the rated value. Hence, in order to protect the machine and compare the two generators at the same power, the reactive power Q_s (DFIG) and Q_p (BDFRG) are both controlled at

3000Vr while the active power P_s (DFIG) and P_p (BDFRG) have the step from *0W* to *-2000W* or from *-1000W* to *-3000W*

Altivar 71 cannot consume the torque, which results in that the machine can only be controlled under generator mode with mechanical power flowing from converter to the rotor or secondary stator. However, both DFIG and BDFRG could produce the power under both sub- and super- synchronous speed. As the synchronous speed of both DFIG and BDFRG is *750rpm*, *660rpm* and *840rpm* are selected as the sub- and super- synchronous mode with ± 0.12 slip to be implemented in the below experiments.

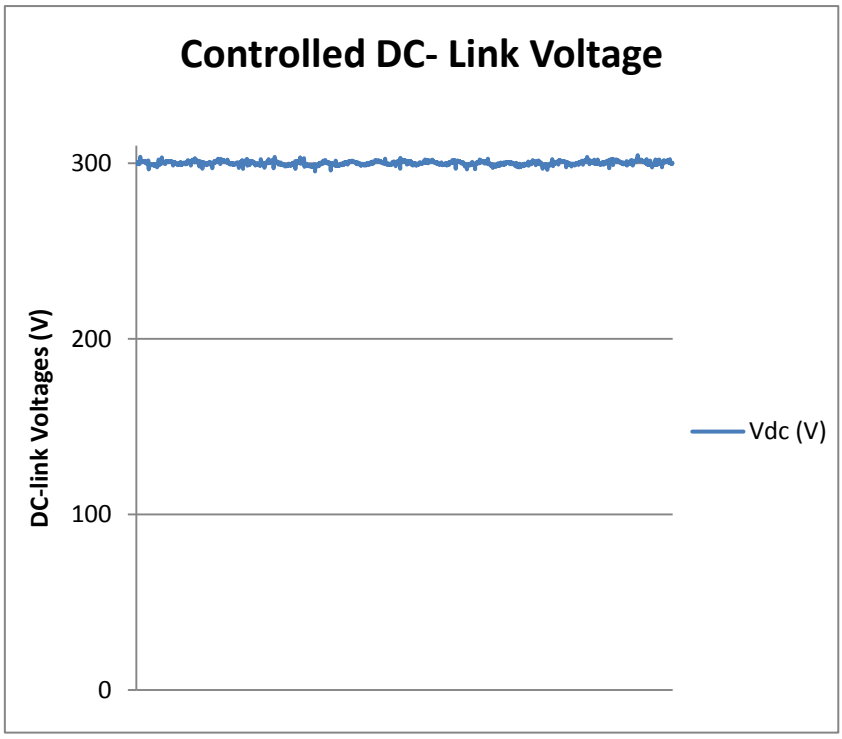

Figure 5.12 Experiment result of controlled DC-link voltage

In the expectation, both stator (primary stator) and the grid-side converter would be supplied by the rated *380V* line to line voltage and DC voltage would reach *600V*. But in fact, EMI would spark the PWM fault signal LED lights of *eZdsp* board and cause the sudden stop of the controller. Hence, the voltage passed across the IGBT of power modules has to be restricted. In the experiments, *100%* voltage is supplied to

the stator of DFIG or the primary stator of BDFRG and *50%* voltage has been provided to the grid side converter to support *300V* DC voltage. Figure 5.12 displays the experiment DC voltage when the grid side converter is fully controlled.

5.2.1. Test results of inner current loop control for two generators

First of all, both generators are controlled with the inner current loop as shown in Figure 5.6. Figure 5.13 and Figure 5.14 demonstrated two generators performance when a step is given to the reference rotor current components. The left graphs show the DFIG parameters and the right pictures explain BDFRG corresponding vectors in each page.

In Figure 5.13, both generators are experimented under the speed of *840rpm*. The *q*-component of DFIG rotor currents and BDFRG secondary stator currents are kept at *-5A*, while the *d*-component has a step from *3A* to *5A*. The *d-q* current response of the DFIG rotor and stator and BDFRG primary and secondary stator are graphically represented respectively in picture (a) to (d). The active and reactive power of two generators and phase currents of the DFIG rotor and BDFRG secondary stator are demonstrated respectively in figure (e) to (h).

The experimental results at *660rpm* speed with the constant *5A d*-component and a *-3A* to *-5A* step *q*-component of rotor currents (secondary currents) are illustrated in the pictures of Figure 5.14. Similar to Figure 5.13, the *d-q* component currents of the rotor (secondary stator) and the stator (primary stator), the active and reactive power and rotor (secondary stator) phase currents of two generators are shown separately from Figure 5.13 (a) to Figure 5.13 (h). Two pairs of pictures are displayed in each page. The left two graphs show the DFIG response and right two are BDFRG results.

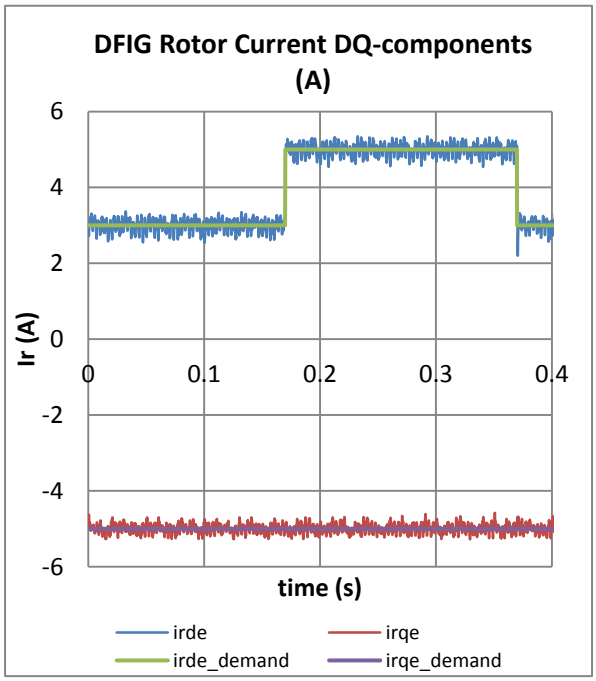

(a)

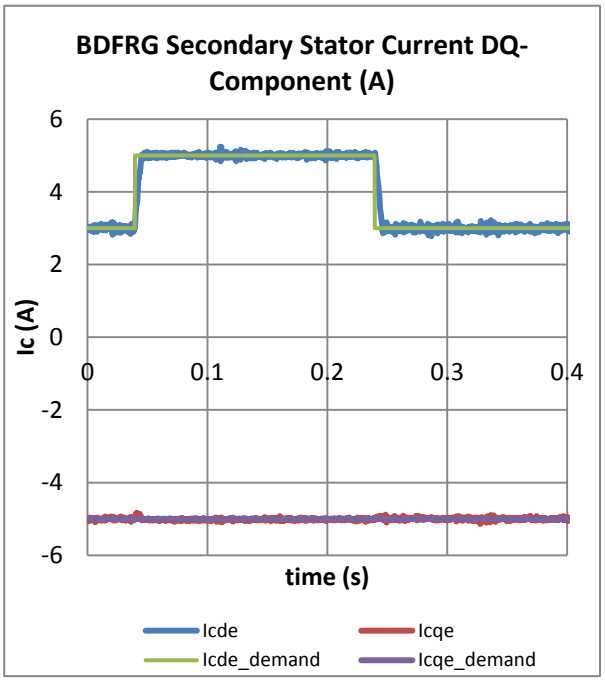

(c)

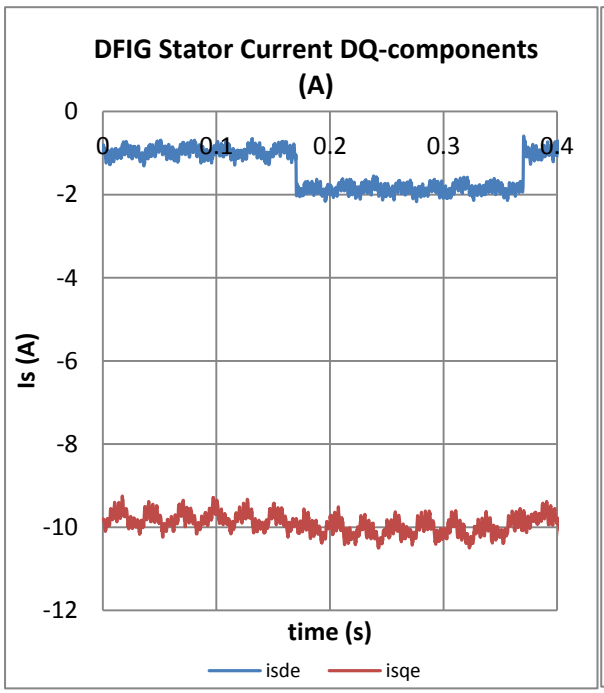

(b)

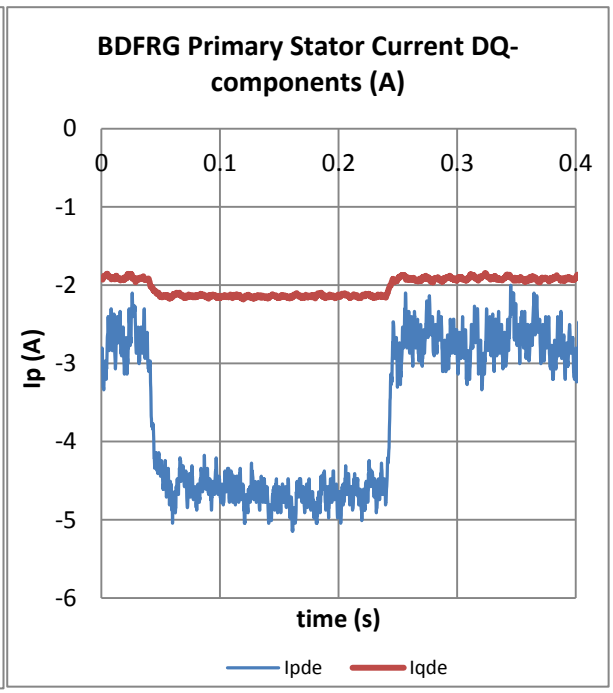

(d)

Figure 5.13 Step response under the condition that *d*-component of rotor current has a step reference at *840rpm* (a) DFIG rotor DQ-component currents (b) DFIG stator DQ-component currents (c) BDFRG secondary stator DQ-component currents (d) BDFRG primary stator DQ-component currents

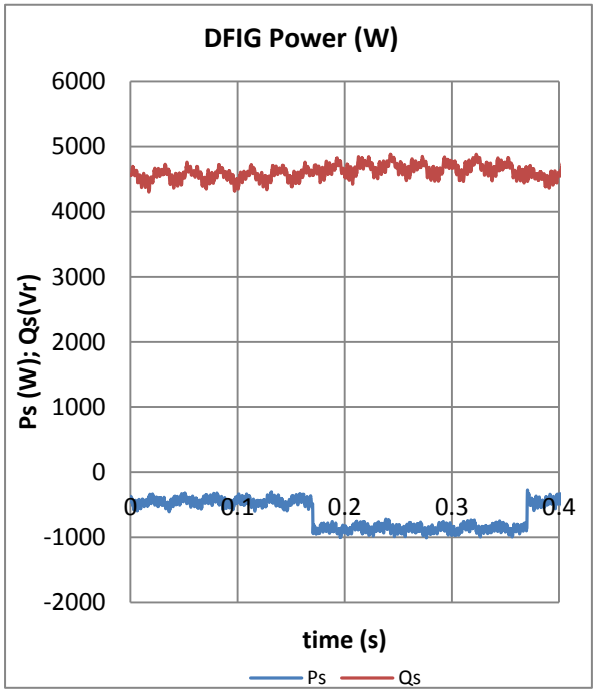

(e)

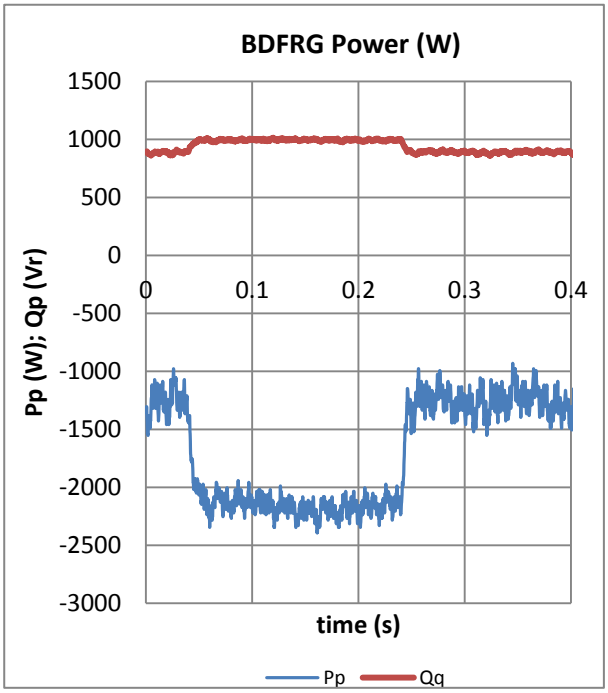

(g)

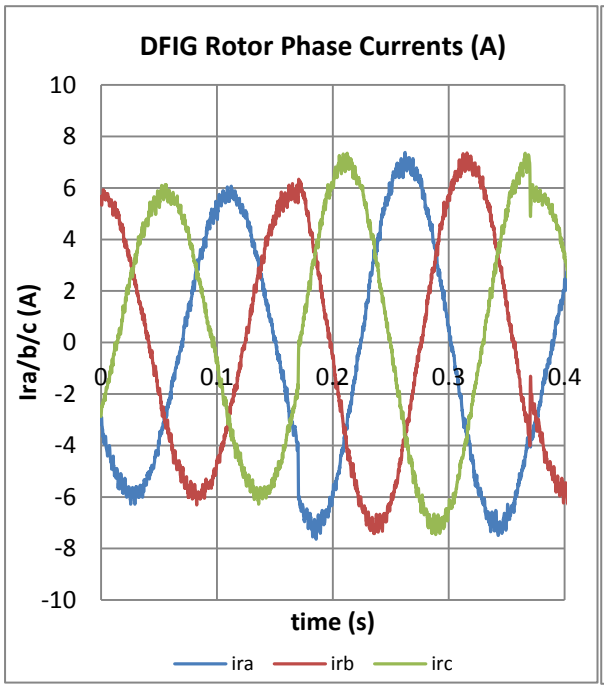

(f)

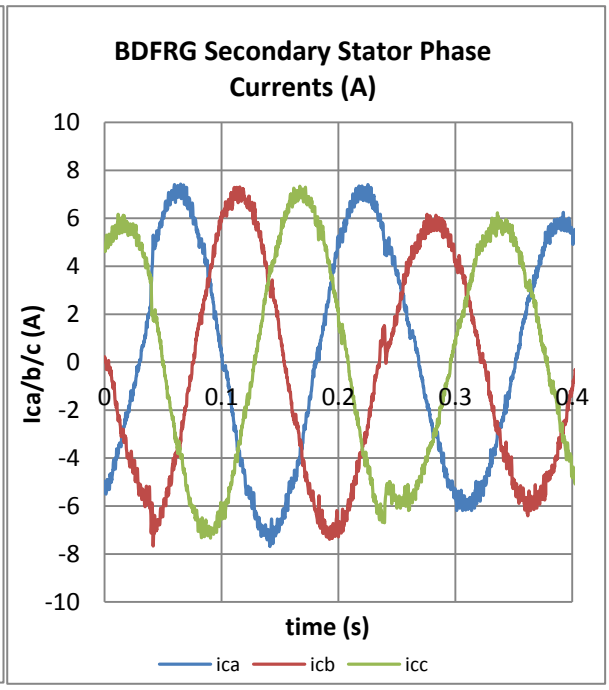

(h)

Figure 5.13 Step response under the condition that *d*-component of rotor current has a step reference at *840rpm* (e) DFIG active and reactive power (f) DFIG rotor phase currents (g) BDFRG active and reactive power (h) BDFRG secondary stator phase currents

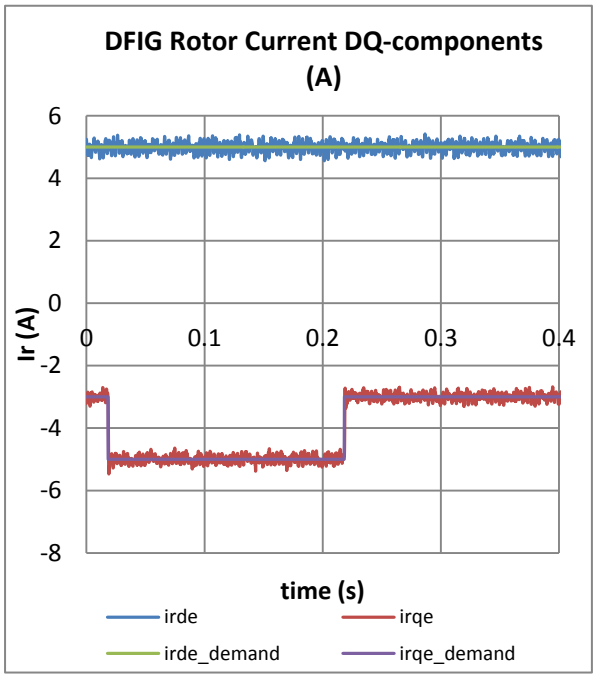

(a)

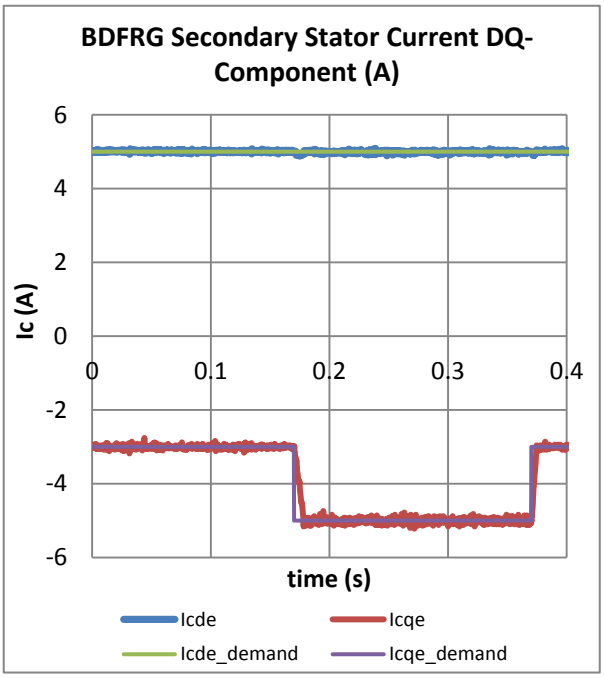

(c)

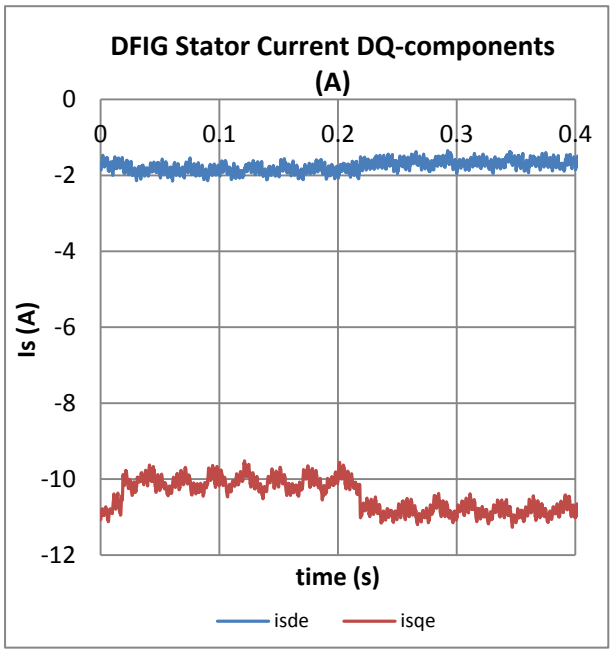

(b)

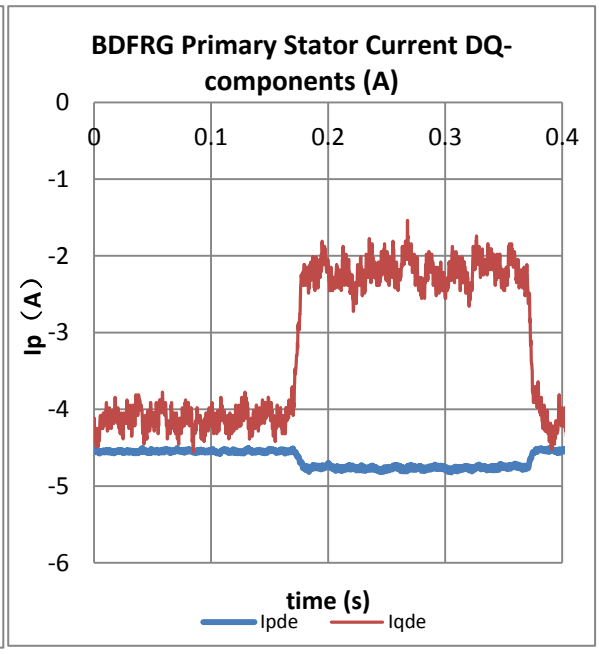

(d)

Figure 5.14 Step response under the condition that *q*-component of rotor current has a step reference at *660rpm* (a) DFIG rotor DQ-component currents (b) DFIG stator DQ-component currents (c) BDFRG secondary stator DQ-component currents (d) BDFRG primary stator DQ-component currents

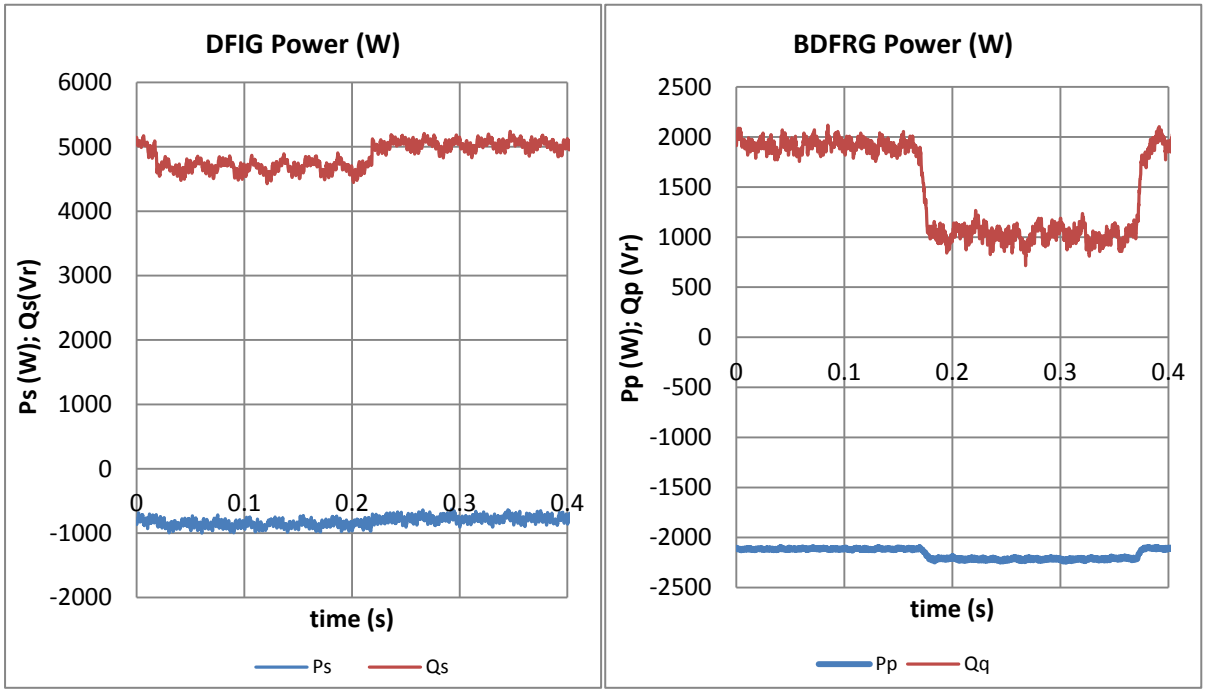

(e)

(g)

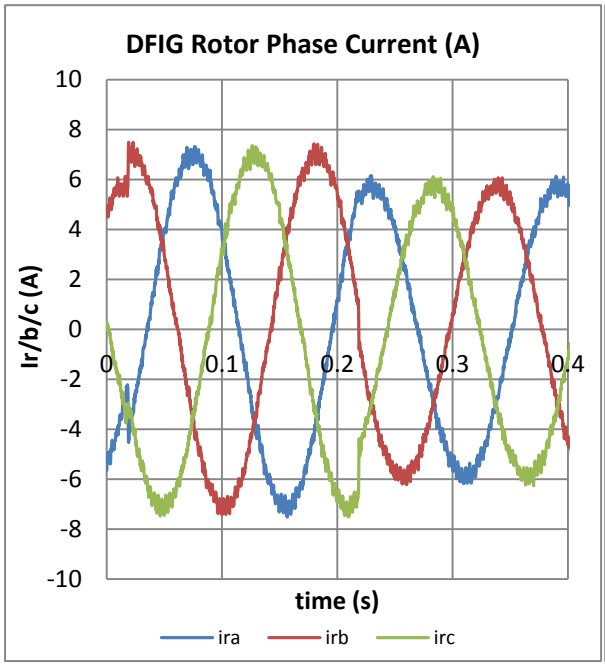

(f)

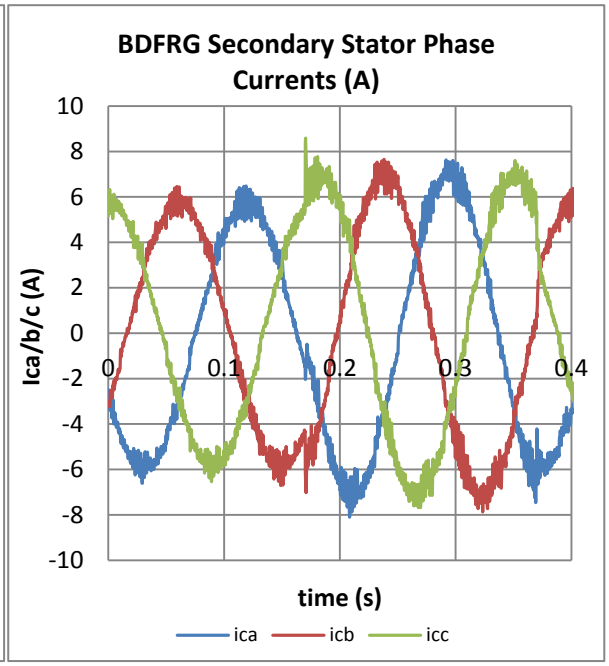

(h)

Figure 5.14 Step response under the condition that *q*-component of rotor current has a step reference at *660rpm* (e) DFIG active and reactive power (f) DFIG rotor phase currents (g) BDFRG active and reactive power (h) BDFRG secondary stator phase currents

5.2.2. Current control response analysis and discussion

All the vectors shown in the inner current control loop response graphs are expressed in excitation frame which aligns its *d*-axis to the input voltage vector. Taking the DFIG as example, we will have the following mathematical equations:

$$\overrightarrow{u_s{}^e} = R_s\overrightarrow{\imath_s{}^e} + \frac{d\overrightarrow{\varphi_s{}^e}}{dt} + j\omega_s\overrightarrow{\varphi_s{}^e} \tag{5.27}$$

$$\overrightarrow{u_r{}^e} = R_r\overrightarrow{\imath_r{}^e} + \frac{d\overrightarrow{\varphi_r{}^e}}{dt} + j\omega_{slip}\overrightarrow{\varphi_r{}^e} \tag{5.28}$$

Taking account to the steady state, the voltage equations change to:

$$\overrightarrow{u_s{}^e} = R_s\overrightarrow{\imath_s{}^e} + j\omega_s\overrightarrow{\varphi_s{}^e} \tag{5.29}$$

$$\overrightarrow{u_r{}^e} = R_r\overrightarrow{\imath_r{}^e} + j\omega_{slip}\overrightarrow{\varphi_r{}^e} \tag{5.30}$$

Adding the flux linkage equations

$$\overrightarrow{\varphi_s{}^e} = L_s\overrightarrow{\imath_s{}^e} + L_m\overrightarrow{\imath_r{}^e} \tag{5.31}$$

$$\overrightarrow{\varphi_r{}^e} = L_m\overrightarrow{\imath_s{}^e} + L_r\overrightarrow{\imath_r{}^e} \tag{5.32}$$

to the voltages, we will have:

$$\overrightarrow{u_s{}^e} = R_s\overrightarrow{\imath_s{}^e} + j\omega_s\left(\, L_s\overrightarrow{\imath_s{}^e} + L_m\overrightarrow{\imath_r{}^e}\,\right) \tag{5.33}$$

$$\overrightarrow{u_r{}^e} = R_r\overrightarrow{\imath_r{}^e} + j\omega_{slip}\left(L_m\overrightarrow{\imath_s{}^e} + L_r\overrightarrow{\imath_r{}^e}\right) \tag{5.34}$$

Expanding the formula to *d*-*q* components:

$$u_{sd}^e = R_s i_{sd}^e - \omega_s\left(\, L_s i_{sq}^e + L_m i_{rq}^e\,\right) \tag{5.35}$$

$$u_{sq}^{e} = R_s i_{sq}^{e} + \omega_s (L_s i_{sd}^{e} + L_m i_{rd}^{e}) \quad (5.36)$$

$$u_{rd}^{e} = R_r i_{rd}^{e} - \omega_{slip} \left(L_r i_{rq}^{e} + L_m i_{sq}^{e} \right) \quad (5.35)$$

$$u_{rq}^{e} = R_r i_{rq}^{e} + \omega_{slip} (L_r i_{rd}^{e} + L_m i_{sd}^{e}) \quad (5.36)$$

If i_{rd}^{e} decreases and i_{rq}^{e} keep constant, then we will have:

$$\Delta i_{rd}^{e} < 0, \ \ \Delta i_{rq}^{e} = 0 \quad (5.37, 5.38)$$

Besides, the input voltage and speed always keep constant, thus we know that:

$$\Delta u_{sd}^{e} = 0, \ \ \Delta u_{sq}^{e} = 0, \quad (5.39, 5.40)$$

$$R_s \Delta i_{sd}^{e} - \omega_s \left(L_s \Delta i_{sq}^{e} + L_m \Delta i_{rq}^{e} \right) = 0 \quad (5.41)$$

$$R_s \Delta i_{sq}^{e} + \omega_s (L_s \Delta i_{sd}^{e} + L_m \Delta i_{rd}^{e}) = 0 \quad (5.42)$$

$$\because \Delta i_{rq}^{e} = 0, \qquad \therefore R_s \Delta i_{sd}^{e} - \omega_s L_s \Delta i_{sq}^{e} = 0 \quad (5.43)$$

$$\because \Delta i_{rd}^{e} > 0, \qquad \therefore R_s \Delta i_{sq}^{e} + \omega_s L_s \Delta i_{sd}^{e} < 0 \quad (5.44)$$

From equation 5.43,

$$\Delta i_{sd}^{e} = \frac{\omega_s L_s}{R_s} \Delta i_{sq}^{e} \quad (5.45)$$

Substituting this equation to 5.44

$$R_s \Delta i_{sq}^{e} + \omega_s L_s \frac{\omega_s L_s}{R_s} \Delta i_{sq}^{e} = \frac{{R_s}^2 + (\omega_s L_s)^2}{R_s} \Delta i_{sq}^{e} < 0 \quad (5.46)$$

$$\because \frac{{R_s}^2 + (\omega_s L_s)^2}{R_s} < 0, \quad \therefore \Delta i_{sq}^{e} < 0 \quad (5.47)$$

$$\therefore \Delta i_{sd}^{e} = \frac{\omega_s L_s}{R_s} \Delta i_{sq}^{e} < 0 \tag{5.48}$$

From this derivation, it can be seen that, if keeping the *q*-component of rotor currents or secondary winding currents constant, the increasing rotor or secondary stator *d*-axis currents will bring about the decrease of stator or primary stator *d*-*q* currents whereas the decline of *d*-component of rotor or secondary stator currents will results in the uptrend of both *d* and *q* components of stator or primary winding currents.

This conclusion is validated in *d*-*q* current component curves of both DFIG and BDFRG in Figure 5.13. The *d*-component of the DFIG stator or BDFRG primary stator current varies obviously, whereas *q*-axis current does not change distinctly. Especially, the variation of *q*-component of DFIG stator current is so small that it is hardly visible to the naked eyes from the graph. The reason why the stator *q*-axis current varies so slightly is the DFIG stator resistance value is too small to impact the *q*-axis variations a lot. Considering the equation 5.43 and 5.44, if the stator resistance can be ignored, these two equations can be re-written to:

$$-\omega_s L_s \Delta i_{sq}^{e} = 0 \tag{5.49}$$

$$\omega_s L_s \Delta i_{sd}^{e} < 0 \tag{5.50}$$

Thus the change of *q*-axis stator current can be thought as zero, while *d*-axis stator current increases evidently. However, the small stator resistance does not equal to none. The *q*-component of stator current is still affected, although it is not palpable. Compared to DFIG rotor *q*-axis current, BDFRG secondary stator current *q*-component curve ascends. The major reason of this difference is BDFRG has bigger primary stator resistance value than DFIG stator resistance. Figure 5.13 (b) and (d) interprets this conclusion with abundant evidence.

Similarly, if i_{rq}^{e} declines and i_{rd}^{e} keep constant, then we will have:

$$\Delta i_{rd}^{e} = 0, \;\; \Delta i_{rq}^{e} < 0 \qquad (5.51, 5.52)$$

Equation 5.41 and 5.42 will change to

$$\because \Delta i_{rd}^{e} = 0, \qquad \therefore R_s \Delta i_{sq}^{e} + \omega_s L_s \Delta i_{sd}^{e} = 0 \qquad (5.53)$$

$$\because \Delta i_{rq}^{e} < 0, \qquad \therefore R_s \Delta i_{sd}^{e} - \omega_s L_s \Delta i_{sq}^{e} < 0 \qquad (5.54)$$

From 5.53

$$\Delta i_{sd}^{e} = -\frac{R_s}{\omega_s L_s} \Delta i_{sq}^{e} \qquad (5.55)$$

Substituting 5.55 to 5.54

$$R_s \Delta i_{sd}^{e} - \omega_s L_s \Delta i_{sq}^{e} = -\frac{{R_s}^2}{\omega_s L_s} \Delta i_{sq}^{e} - \omega_s L_s \Delta i_{sq}^{e} = -\frac{{R_s}^2 + (\omega_s L_s)^2}{\omega_s L_s} \Delta i_{sq}^{e} < 0 \qquad (5.56)$$

$$\because -\frac{{R_s}^2 + (\omega_s L_s)^2}{\omega_s L_s} < 0, \quad \therefore \Delta i_{sq}^{e} > 0 \qquad (5.57)$$

$$\therefore \Delta i_{sd}^{e} = -\frac{R_s}{\omega_s L_s} \Delta i_{sq}^{e} < 0 \qquad (5.58)$$

Hence, if keeping *d*-component of rotor or secondary stator currents constant and *q*-axis value descending, stator or primary stator *d*-axis current drops as well but *q*-components would climb and vice versa. It has been proved by the experimental results in Figure 5.14. In a similar way, the BDFRG's primary stator *d*-axis current has more visible variations than DFIG's stator current *d*-component. The reason has been analysed above.

A close-up focuses on the graphs of rotor and secondary stator current *d-q* components in both Figure 5.13 and Figure 5.14. It is evident that BDFRG secondary stator current shows a slower catch-up to reach the steady state on both d and *q* component step responses. It indicates BDFRG takes longer time to control the

secondary currents compared to DFIG rotor currents controller. In the other means, under a classical vector control, DFIG's controller speed is faster than BDFRG or BDFRG is harder to be controlled compared to DFIG.

The main reason for this significant difference between DFIG and BDFRG is the inductance of BDFRG is far larger than DFIG. As explained in Chapter 2, the reluctance rotor will bring about more saturation. More saturation would cause the flux-path block and flux density limitation. The restricted flux strength limits the MMF and current increase. Thus in order to obtain the same power level, BDFRG needs larger volume to accommodate more magnetic flux and results in the higher inductance value. But the inductance, as the factor of current-change-retardant, will block the current to catch up to the reference value. It causes the delay of the controller speed and of course postpones the primary stator currents and active and reactive power steady states.

Comparing the rotor and secondary phase currents graphs for both *840rpm* and *640rpm* experimental results, the following differences can be found. Firstly, the rotor and secondary currents have opposite sequence in *840rpm*'s results compared to *660rpm*'s. For *660rpm* results, the sequence of rotor phase currents in DFIG or corresponding position windings phase currents in BDFRG is 'red-yellow-blue', but in *840rpm* experiment, the sequence reverses to 'red-blue-yellow'. This difference is not hard to understand. The reversion of the rotor or secondary stator current phase sequence is because the slip changes from positive to negative. The generator operates in sub-synchronous speed mode with positive slip at *660rpm* and accelerates to super-synchronous speed situation as the slip declines to negative. However, the stator need keep same phase current sequence and generate the power out of the machine. Therefore, the rotor or secondary stator windings have to reverse the phase sequence to achieve this target at different speed mode. Secondly, all the phase current pictures explicate that BDFRG has more harmonics than DFIG. It is because of the BDFRG structures. The reluctance rotor produces more

harmonics specially the rotor with the flux barriers inserting used in the experiments and the position of the rotor brings about the variations of machine inductance as demonstrated in Chapter 2. The more harmonics may increase the difficulties of controlling a BDFRG. This point will be detailed in the power loop control results analysis.

According to the comparison of the experimental results of current loop vector control, there are some conclusions can be found:

①. BDFRG and DFIG have similar performance under the control.
②. DFIG's current controller speed is faster than BDFRG because of the smaller inductance of DFIG.
③. BDFRG produces more harmonics than DFIG due to the rotor structure and inductance variations.
④. BDFRG is more difficult to be controlled with the classical vector control method compared to DFIG according to above conclusion.

5.2.3. Test results of outer power loop control for two generators

Figure 5.15 and Figure 5.16 below give the power loop control results graphs at *660rpm* and *840rpm*. As explained above, the second-hand DFIG cannot be controlled under the unity power factor. Otherwise, the rotor current will exceed the rated value. Hence, in order to avoid the overcurrent and compare the two generators at the same power, the reactive power Q_s (DFIG) and Q_p (BDFRG) are both controlled to *3000Vr*. The active power P_s (DFIG) and P_p (BDFRG) have been experimented with a step reference from *0W* to *-2000W* at *660rpm* and from *-1000W* to *-3000W* at *840rpm*.

Figure 5.15 illustrates the step response with the active power stepping from 0W to *-2000W* at the speed of *660rpm*, while Figure 5.16 graphically describes the control results by giving a *-1000W* to *-3000W* step power reference at *840*rpm condition.

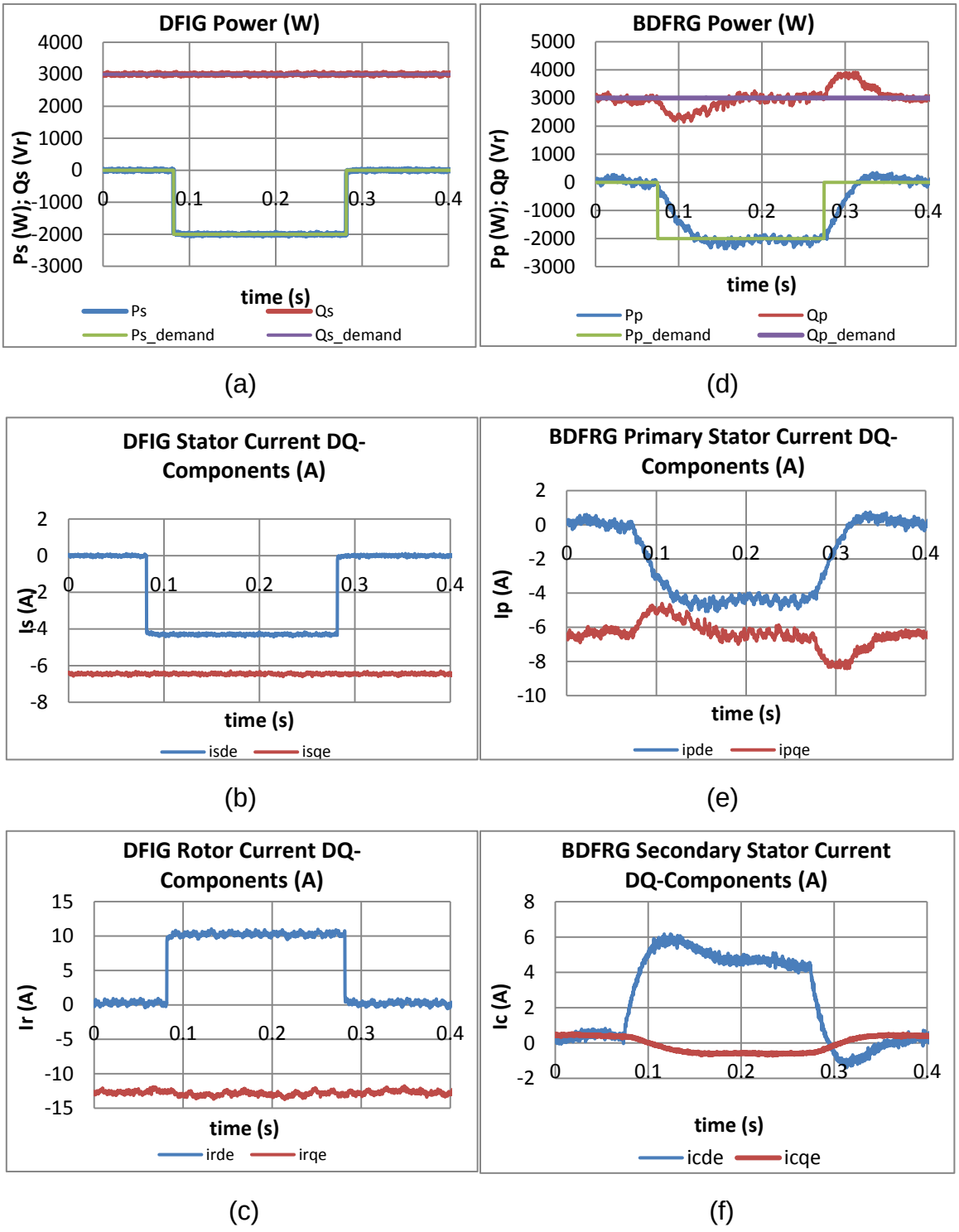

Figure 5.15 Step response under the condition that the active power has a step reference at *660rpm* (a) DFIG power (b) DFIG stator current DQ-components (c) DFIG rotor current DQ-components (d) BDFRG power (e) BDFRG primary stator current DQ-components (f) BDFRG secondary stator current DQ-components

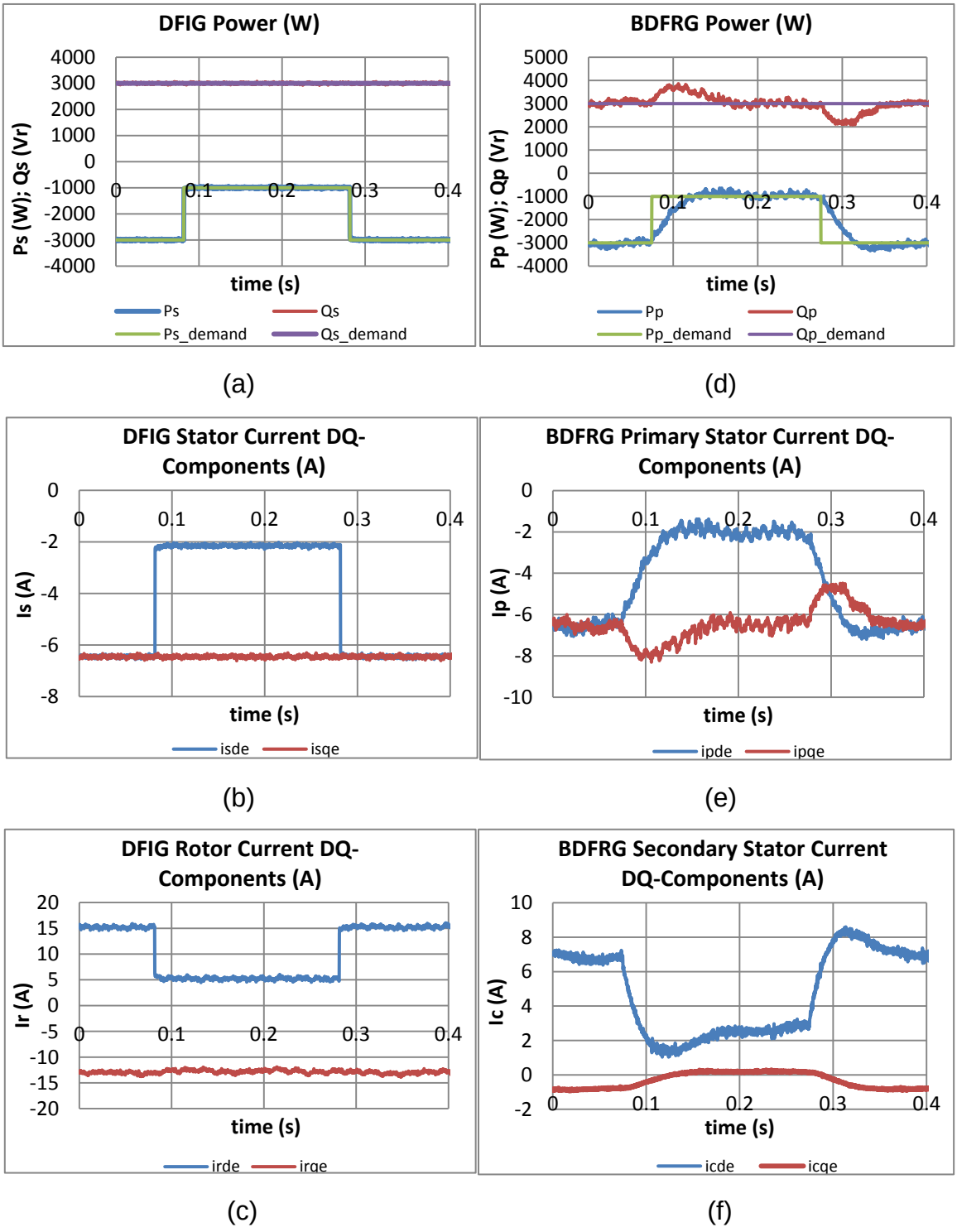

Figure 5.16 Step response under the condition that the active power has a step reference at *840rpm* (a) DFIG power (b) DFIG stator current DQ-components (c) DFIG rotor current DQ-components (d) BDFRG power (e) BDFRG primary stator current DQ-components (f) BDFRG secondary stator current DQ-components

For both Figure 5.15 and Figure 5.16, left side graphs demonstrate the DFIG experimental results and right group of the pictures display the BDFRG parameters.

5.2.4. Power control response analysis and discussion

According to the control method, the DFIG rotor *d*-axis current is proportional to the active power and *q*-component varies in direct proportion of reactive power. Similarly, BDFRG has the same proportional relation between secondary stator *d*-*q* current component and active and reactive power. This proportion indicates that when the active power keeps constant, the relative *q*-axis current does not change. The DFIG graph (c) in Figure 5.15 and Figure 5.16 almost faultlessly interprets this conclusion. However, the picture (f) in Figure 5.15 and Figure 5.16 demonstrates an entirely different situation for the BDFRG. The *q*-axis current ascends or descends followed the active power increasing or decreasing.

Why the experimental results give some different conclusions from the control method? The answer is the stator resistance. In the method, the stator resistance is considered small enough to be ignored. Thus the active and reactive power has the proportional relation to *d*-*q* axis rotor current. The resistor of DFIG in this thesis is qualified, but the BDFRG's is not.

When the primary resistor is too big to be neglected, normally, in order to achieve this decoupling target in the controller, people would subtract an iR potential in the control to avoid the primary stator resistance effects. At this time, the control accuracy depends on the parameters' correctness to a certain degree. However, the control scheme implemented in this thesis is independent on the parameters. The component which includes the primary stator resistance does not be subtracted. The experimental results are affected by the stator resistance. This explains why there is the ignorance of decoupling in vector control of BDFRG experimental results.

For the DFIG, although it seems that there is a decoupling its experimental results, in fact, there is still a slight variation of its active power curve when the step occurs. Compared to the palpable change in the BDFRG, DFIG result is not apparent. This differentia is because the BDFRG has a far larger primary stator resistance value than the DFIG stator resistance. Basically, the DFIG stator is small enough to be neglected which leads to the variations of DFIG active power curve is slight enough to be ignored as well. Therefore, the real and reactive power of DFIG can be thought as a decoupling situation.

Keeping the eyes focusing on the power graphs in both Figure 5.15 and Figure 5.16, a quite interesting phenomenon can be found. BDFRG not only illustrates a far slower speed of the power step response than DFIG response, but also has a coupling between the active power and reactive power compared to the decoupling of DFIG two powers.

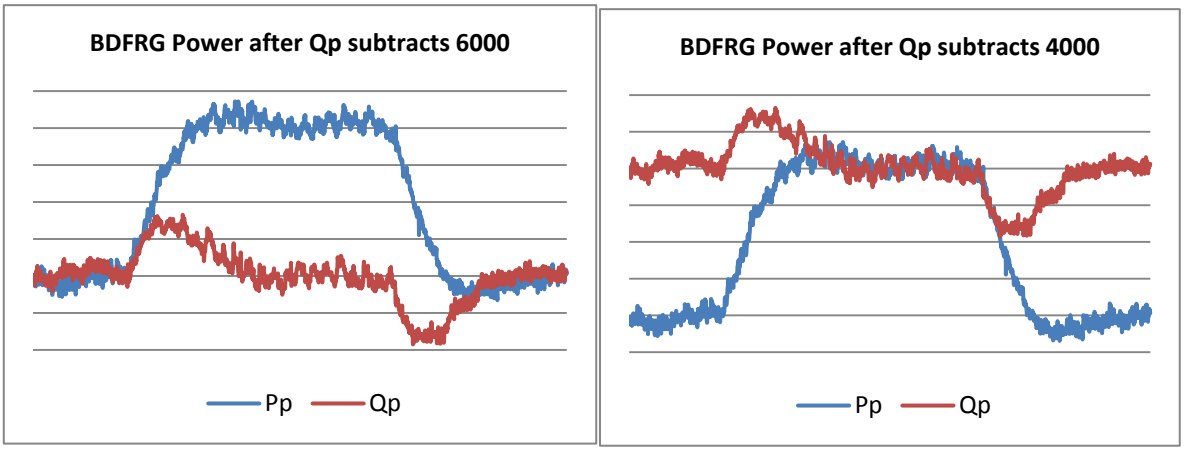

(a) (b)

Figure 5.17 The power after data processing

In order to analyse the whether the active and reactive power of BDFRG really have a coupling, the data in power graphs have been processed. If the reactive power Q_p in Figure 5.16 (d) subtracts *6000Vr*. Then the left side graph of Figure 5.17 could be produced. After increasing the *-3000Vr* Q_p to *-1000Vr*, the right picture can be obtained.

According to power equations:

$$P_p = 1.5\left(u_{sd}^e i_{sd}^e + u_{sq}^e i_{sq}^e\right) \tag{5.59}$$

$$Q_p = 1.5\left(u_{sq}^e i_{sd}^e - u_{sd}^e i_{sq}^e\right) \tag{5.60}$$

Because the proposed vector control is based on the stator voltage field orientation principle, thus u_{sq}^e has been set to zero through a PLL scheme. Then the power equations can be expressed by:

$$P_p = 1.5 u_{pd}^e i_{pd}^e \tag{5.61}$$

$$Q_p = -1.5 u_{pd}^e i_{pq}^e \tag{5.62}$$

The active power has the positive correlation of *d* components of primary stator currents while the reactive power is proportional to the *q*-axis value of the stator currents with a negative coefficient. Besides, P_p and Q_p have the same proportion ratio with i_{pd}^e and i_{pq}^e. It equals $1.5u_{pd}^e$ which is approximate *465* in the experiments.

From the pictures of Figure 5.17, the active and reactive power seems to have the same tendency at the initial point where the active power reference changes. The increase of active power P_p causes the reactive power Q_p climbing, whereas the drop of P_p induces the decrease of Q_p. Taking account of the relations of power and primary stator currents, the increment of i_{pd}^e would encourage the of reduction i_{pq}^e, and the diminution of i_{pd}^e could produce the augmentation of i_{pq}^e. Figure 5.16 (f) evidences this analysis. Considering the magnitude of *d-q* component of the primary stator current, the magnitude growing of i_{pd}^e will eliminate the absolute value of i_{pq}^e, while decline of the magnitude of i_{pd}^e could enhance the absolute value of i_{pq}^e.

Additionally, Figure 5.17 points out that the active and reactive power seems to have the same changed value as the coupling parts of two curves are approximately aligned. And P_p and Q_p have the same coefficient with i_{pd}^e and i_{pq}^e. Hence, in the coupling parts, i_{pd}^e and i_{pq}^e can be considered to have the similar changed magnitude. If i_{pd}^e and i_{pq}^e have similar but different direction of changes, it is of possibility to indicate the magnitude of primary stator currents $|\overrightarrow{i_p}|$ has almost no change like the demonstration in Figure 5.18.

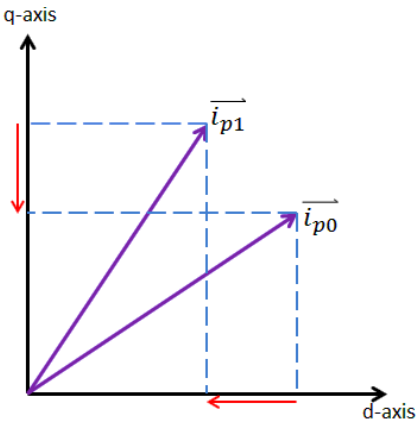

Figure 5.18 The effects of i_{pd}^e and i_{pq}^e changes

The analysis above may imply that the reason of the coupling of active and reactive power is $|\overrightarrow{i_p}|$ will maintain the magnitude for a while at the initial of which the controller starts to work. And the reason of this reservation may be because of the larger inductance. As we all know that the inductance is the factor to prevent the current changes. Thus the far larger inductance in BDFRG compared to DFIG will lead to the hold of the primary stator current changes, then cause the coupling of active and reactive power of BDFRG. On the contrary, DFIG's inductance is not big enough to persist the same amount of stator currents, therefore DFIG's active and reactive power exhibit a decoupling performance.

Looking closely at the current *d-q* component graphs, it is clear that the BDFRG currents emerge more ripples than DFIG. In order to prove this point, the active power of DFIG and BDFRG are examined in different level. Figure 5.19 gives the examples of active power for both DFIG and BDFRG at *-1000W*, *-2000W* and *-3000W* respectively.

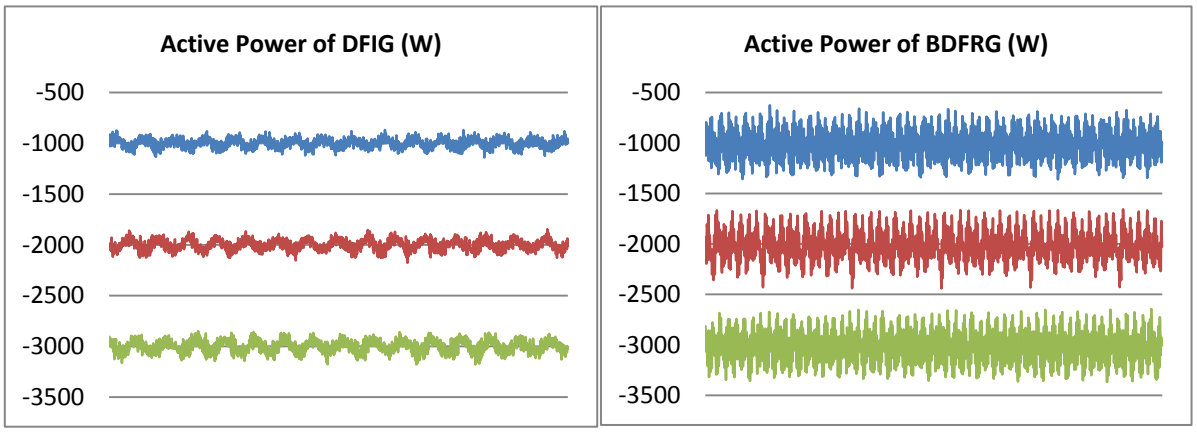

Figure 5.19 Active Power comparison (left) DFIG (right) BDFRG

Obviously, DFIG shows an approximate $\pm 150W$ oscillation and BDFRG has the $\pm 300W$ to $\pm 350W$ variations. DFIG has fewer ripples than BDFRG. This is mainly because the salient reluctance rotor produces more harmonics. The variable inductance as discussed in Chapter 2 is the partly reason for the current harmonics and causes the more power ripples. What is more, the rotor structure design with one barrier in each pole will impact the harmonics as well.

According to the analysis of the experimental results of power loop vector control, there are the following consequences can be found:

①. BDFRG's active and reactive powers display a coupling while DFIG's two powers present the decoupled performance owing to the larger inductance of BDFRG.

②. BDFRG's controller speed is tardy compared to DFIG's due to the larger inductance as well.

③. BDFRG produces more harmonics than DFIG because of the salient reluctance rotor and variable inductance.

④. BDFRG is more difficult to be controlled with the classical vector control method compared to DFIG mainly caused by the structure of the reluctance rotor.

5.2.5. Comparison of experiment and simulation results of vector control response for BDFRG

In this section, a BDFRG model in Matlab/Simulink has been further developed according to its mathematical model given in Section 2.3.2. And this model can be validated when its vector control simulation results are compared with the experimental results above. The correct model would be used in later section to simulate the fault ride through performance of BDFRG and to be compared with the DFIG's simulation results.

Figure 5.20 and Figure 5.21 illustrate the step response when the current loop control is applied to the BDFRG. Figure 5.20 shows the BDFRG performance when its secondary stator *d*-axis current was controlled to be increased from *3A* to *5A* and the rotor was rotating at *840rpm*. Figure 5.21 displays the machine response when the *q* component of the secondary stator current dropped from *-3A* to *-5A* and the generator operated at *660rpm*. In both figures, left graphs (a), (b) and (c) give the information of experimental results. And right pictures (d), (e) and (f) demonstrate the simulation results. Graphs (a) and (d) present the BDFRG secondary stator phase currents. (B) and (e) show the BDFRG primary stator *d*- and *q*- axis currents. (C) and (f) illustrate the BDFRG active and reactive power.

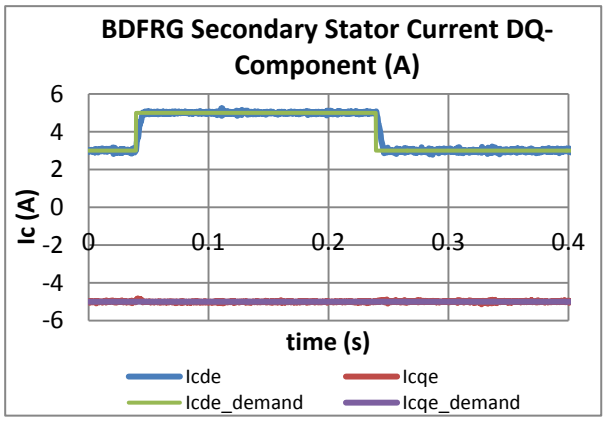

(a)

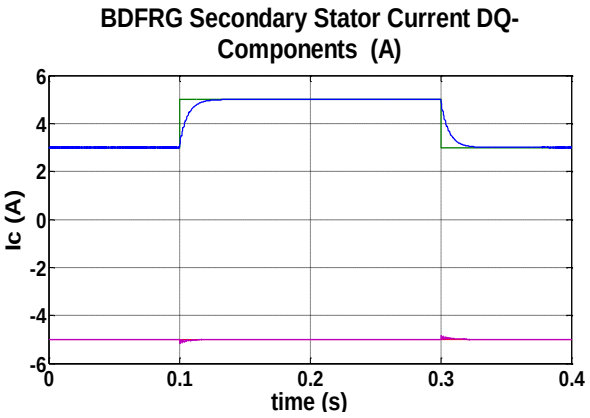

(d)

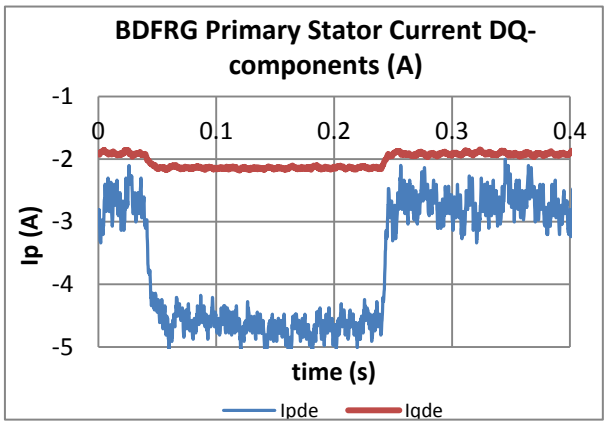

(b)

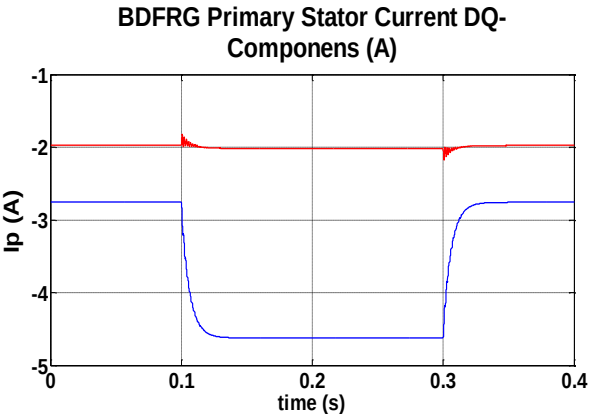

(e)

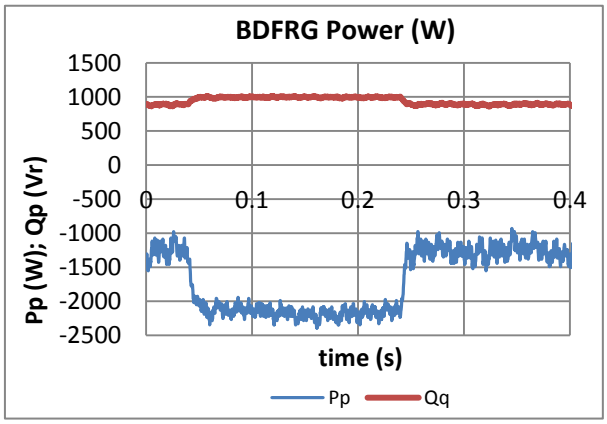

(c)

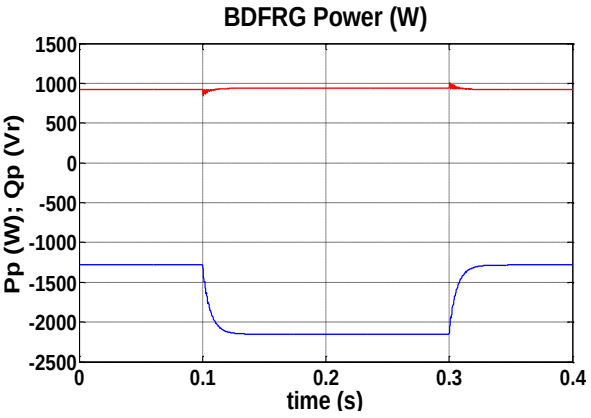

(f)

Figure 5.20 Step response under the condition that *d*-component of rotor current has a step reference at *840rpm* (left) experimental results (right) simulation results; (a) & (d) BDFRG secondary stator phase currents (b) & (e) BDFRG primary stator current DQ-components (c) & (f) BDFRG active and reactive power

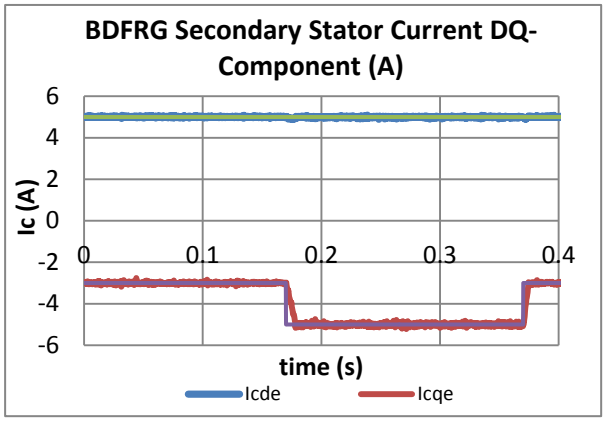

(a)

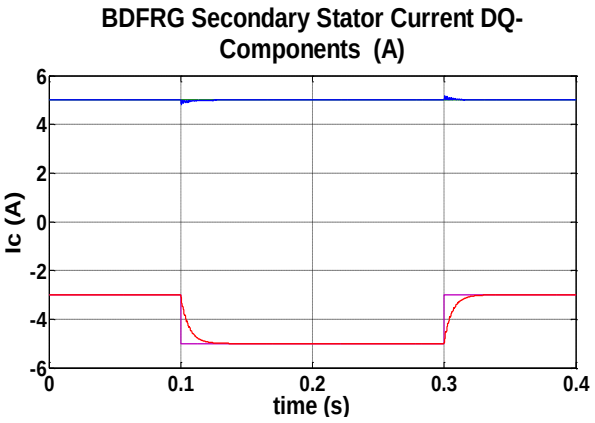

(d)

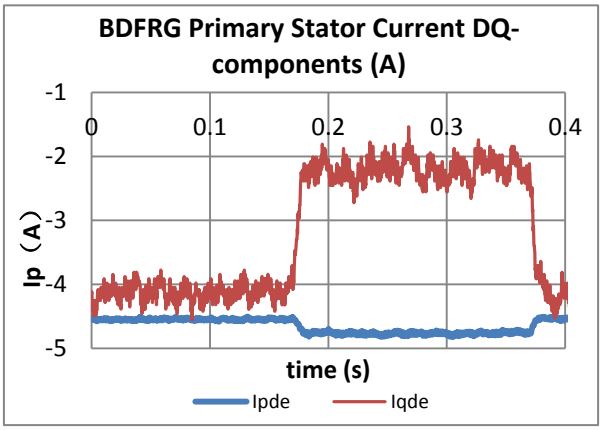

(b)

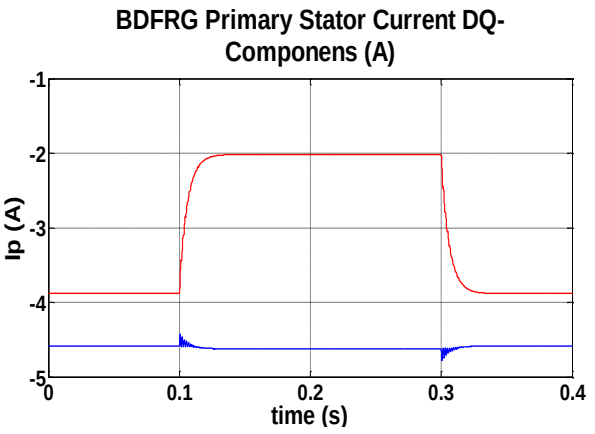

(e)

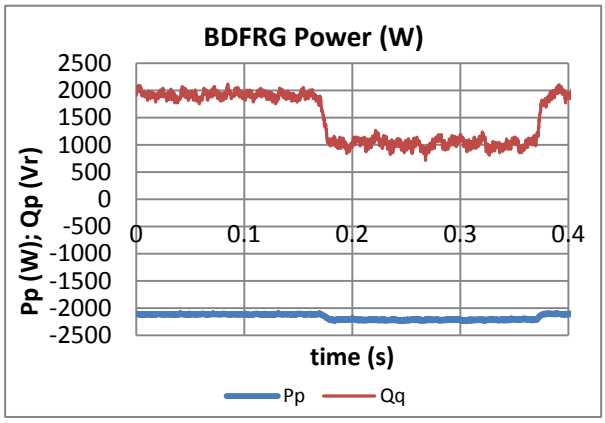

(c)

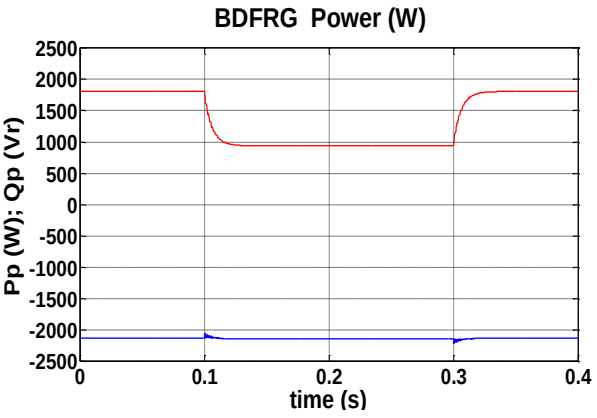

(f)

Figure 5.21 Step response under the condition that *q*-component of rotor current has a step reference at *660rpm* (left) experimental results (right) simulation results; (a) & (d) BDFRG secondary stator phase currents (b) & (e) BDFRG primary stator current DQ-components (c) & (f) BDFRG active and reactive power

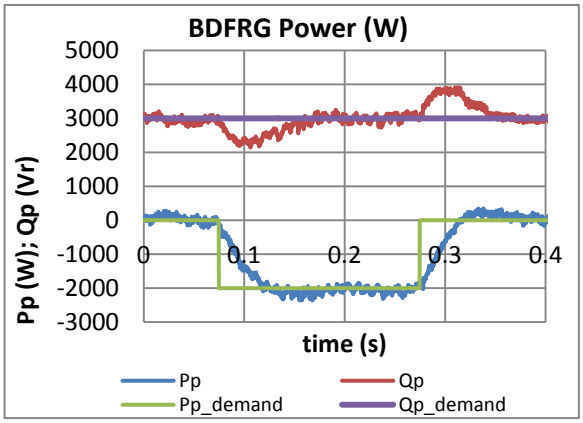

(a)

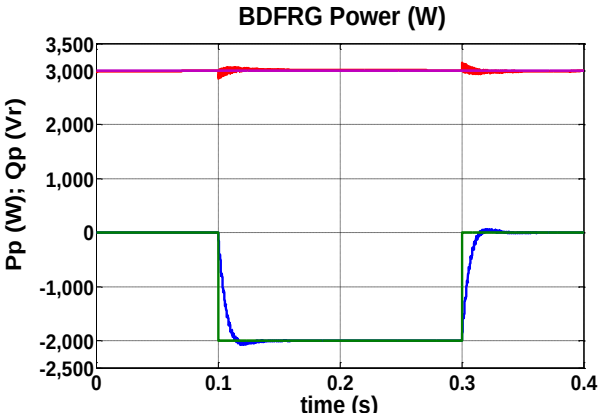

(d)

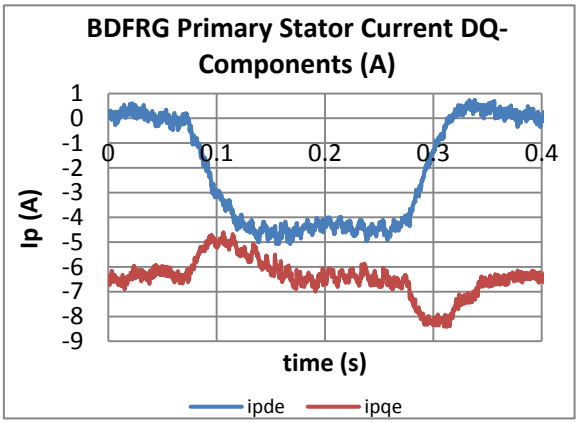

(b)

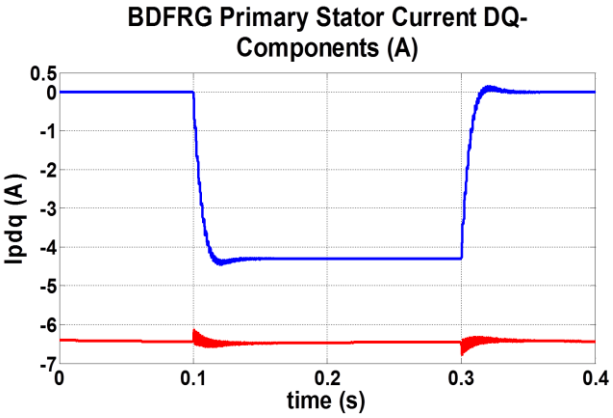

(e)

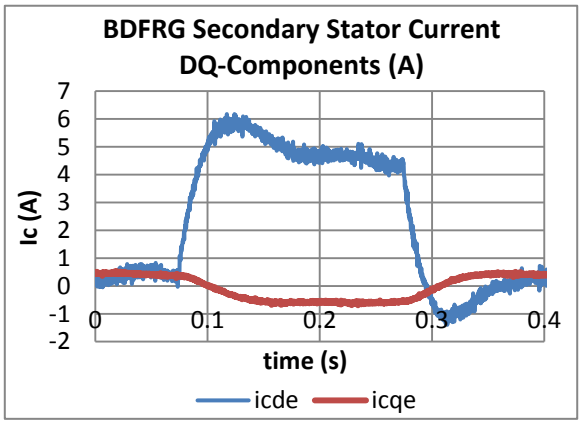

(c)

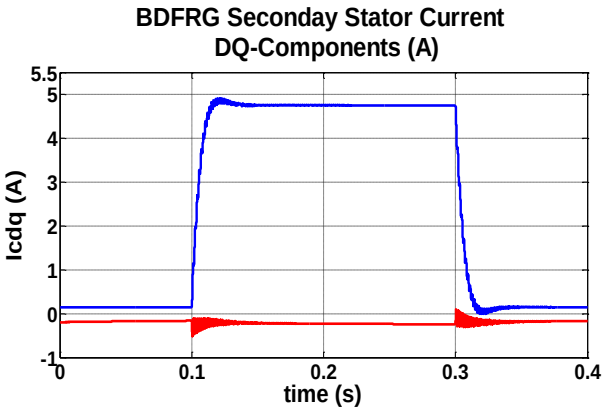

(f)

Figure 5.22 Step response under the condition that the active power has a step reference at *660rpm* (left) experimental results (right) simulation results; (a) & (d) BDFRG power (b) & (e) BDFRG primary stator current DQ-components (c) & (f) BDFRG secondary stator current DQ-components

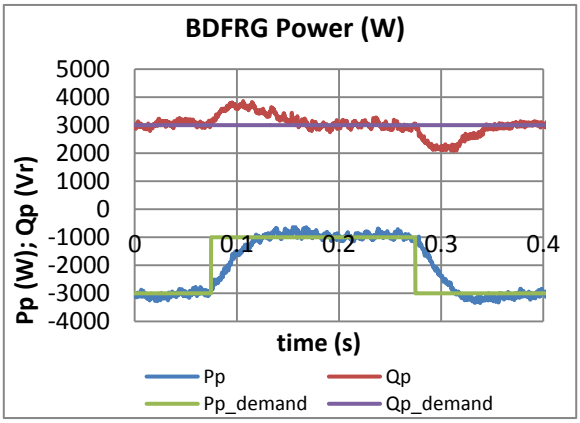

(a)

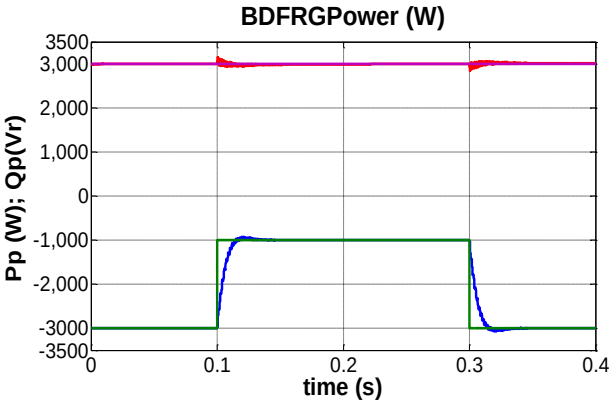

(d)

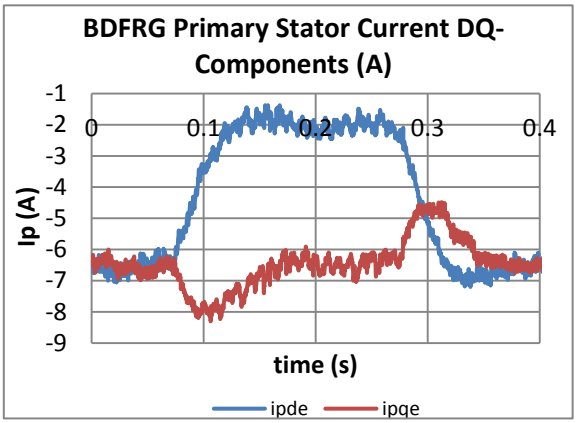

(b)

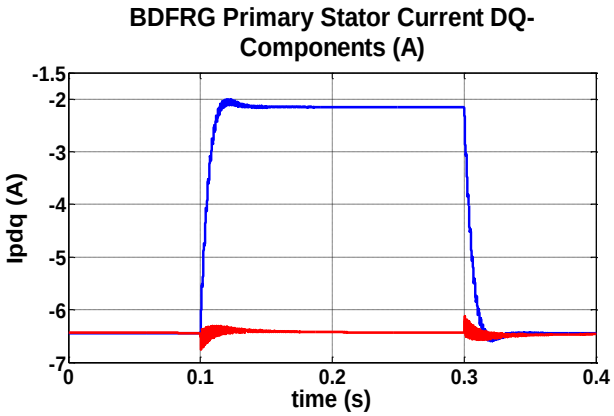

(e)

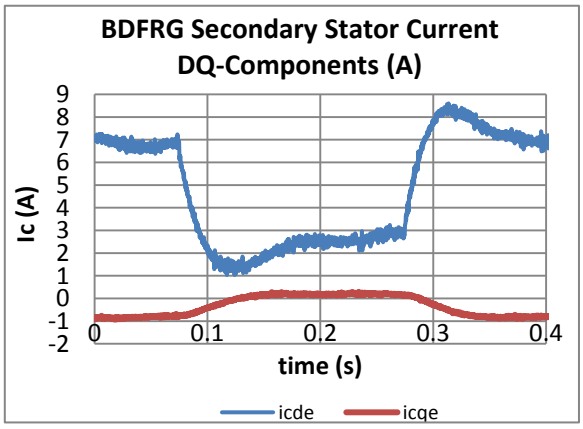

(c)

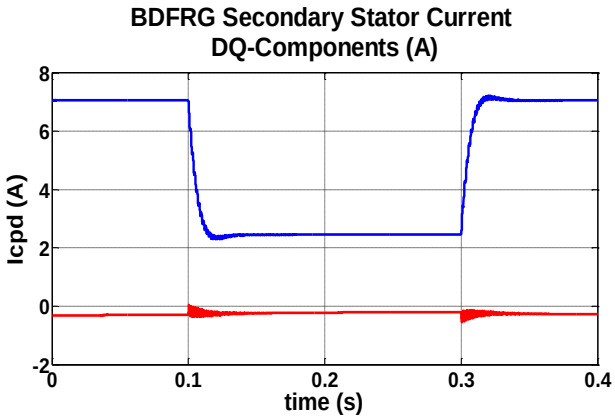

(f)

Figure 5.23 Step response under the condition that the active power has a step reference at *840rpm* (left) experimental results (right) simulation results; (a) & (d) BDFRG power (b) & (e) BDFRG primary stator current DQ-components (c) & (f) BDFRG secondary stator current DQ-components

Similarly, Figure 5.22 and Figure 5.23 show the active power step response when the power loop is used in the BDFRG control scheme. In two figures, the reactive power was kept at *3000Vr* and the active power was stepped from *0W* to *-2000W* and *-3000W* to *-1000W*. The graphs in the left and right columns illustrate the experimental and simulation results respectively. Picture (a) and (d) give the information of the BDFRG active and reactive power response. (B) and (e) display the BDFRG primary stator current *d* and *q* components. (C) and (f) present the BDFRG secondary stator *d*- and *q*- axis currents.

Comparing the right graphs with the relative left pictures, it is obvious that the simulation results have basic agreements with the experimental results in current loop control and power loop control. Both results present the BDFRG has a slow vector control speed.

However, the simulation graphs display less harmonic than the test results. The possibility reason might be caused by the input voltage. The three-phase primary stator voltages are pure sinusoid waveforms in simulation but brought the harmonics to the machine in the practical. And another possible explanation may be the reluctance rotor was not simulated in the BDFRG model because it has not the electrical equations.

Besides, Figure 5.22 (d) and Figure 5.23 (d) demonstrate a coupling between the active and reactive power. But compared with the experimental power graph (a), the coupling is less visible. The major reason may be caused by the exactitude of the rotor structure simulation and the accuracy of the inductance value. First of all, the reluctance rotor is quite hard to be simulated. In the all papers, a BDFRG is simply simulated by its electrical equations with the ignorance of its rotor structure. The rotor structure impacts cannot be reflected by the simulation results. This kind of model can give approximate rather than accurate results to us. Besides, as introduced in Section 2.3.1.2, the test generator was designed by Prof. Wang. In order to balance the

machine size and the output power, the flux barriers were inserted in the reluctance rotor. Thus this complex reluctance rotor would have the more distortions of the fluxes and the unevener distributions of the flux densities. This could result in the less agreement in details between the BDFRG simulation results and experimental results when the more complex reluctance rotor structure effects are not simulated. Additionally, the distorted fluxes would bring in the more special variations of the inductance in a narrow angle. However, in the parameter test in Section 4.2.2, some points were selected rather than all. The tested inductance thereby is not accurate enough. All the reasons above influence the accuracy of the BDFRG simulation model and further impact the simulation results. Therefore, although the simulation results have some difference from the experimental results, they could be accepted.

In sum, the simulation results have good match for the experimental results with some tolerable difference. Hence this simulation model can be considered as a valid model to simulate the performance of the BDFRG.

5.3. Prediction of BDFRG fault response and the crowbar performance

According to the conclusion above, it is obvious that the structure of the reluctance rotor of BDFRG brings about lots of differences between DFIG and BDFRG performance. The flux saturation causes the limitation of flux and MMF and restricts the increase of the machine currents. The current increase limitation requires larger volume to accommodate more magnetic flux and results in the higher inductance value to support the power level. The large inductance value will create the sluggishness of the transient current changes then result in the coupling performance of active and reactive power and deceleration of control speed. Besides, the saliency rotor structure leads to the inductance determination is dependent on the rotor position. Aligned, unaligned and intermediate rotor positions issue in the variations of

machine inductance. Then the reluctance rotor inserted by the flux barriers and variable inductance will lead to more oscillation of generator output.

These factors would influence BDFRG's fault response as well. When the voltage dips, the overcurrent is likely to cause machine damage. But compared to DFIG, the same rating BDFRG has a larger inductance which will restrict the level of fault current. The BDFRG's inductances are almost several times of DFIG's. Although the large fault currents would cause more saturation and the applicable magnetic saturation maybe accounted for a reduction of the relevant inductance [16], the effect of BDFRG inductance decrease cannot offset the difference between DFIG and BDFRG. In prediction, the large inductance in BDFRG would cause the slower current increase or even less overcurrent compared to DFIG fault response. Overall, the BDFRG may have better fault current compared to same power DFIG.

If adding a crowbar to BDFRG for protection purpose, the crowbar resistor value could be smaller because of the larger inductance and less overcurrent. But, because BDFRG are harder to be controlled than DFIG, the control scheme of crowbar method needs to be considered carefully. According to a timer action crowbar control scheme described in Section 3.3.3, when the crowbar is released, rotor-side converter and the inner rotor current PI control are immediately resumed. Outer control loop is resumed after a specified delay to allow the current controllers to settle. This delay would be longer in BDFRG than a DFIG's as BDFRG's controller speed is tardy compared to DFIG's.

Therefore, slow control speed is the restriction of BDFRG FRT implementation. If the controller difficulty could be overcome, BDFRG will have better fault response and fault ride through performance compared to DFIG. But this prediction needs to be proved in the future work.

5.3.1. DFIG and BDFRG fault response simulation results comparison

In this section, the DFIG model created in Chapter 3 and BDFRG model validated in above section have been used. The parameters tested in Chapter 4 are applied to two models respectively.

In order to obtain two generators' fault response, DFIG rotor and BDFRG secondary stator were both short circuit. Thus the machine slip had been calculated by using the equation 3.43. The BDFRG can only produce less than *0.15 p.u.* primary stator *d*-axis current, otherwise the slip would have the imaginaries. Thus both machines were setup to generate *0.15 p.u.* active power with a slip of *-0.009* for DFIG and *-0.0132* for BDFRG prior to the fault. As the rated power of both generators is *7.5kW* and speed is *750rpm*, the power was set to *1125W*, and the speed was set to *756.75rpm* and *759.9rpm* for DFIG and BDFRG respectively. In the simulation, after *1.0s* healthy operation, the input voltage was dropped to zero. Figure 5.24 shows the simulated fault response of both DFIG and BDFRG under a zero voltage fault.

Figure 5.24 (a) and (b) illustrate the DFIG stator and rotor currents under zero voltage fault condition. Both fault currents are less than *8 p.u.* Graphs (c) and (d) demonstrate the relative BDFRG primary and secondary stator phase currents respectively. However, the fault primary stator currents of BDFRG peak at *1.25 p.u*, while the fault secondary currents are less than *1 p.u*. The reason why the BDFRG has a far less peak current than the DFIG might be because it owns much higher machine inductance values.

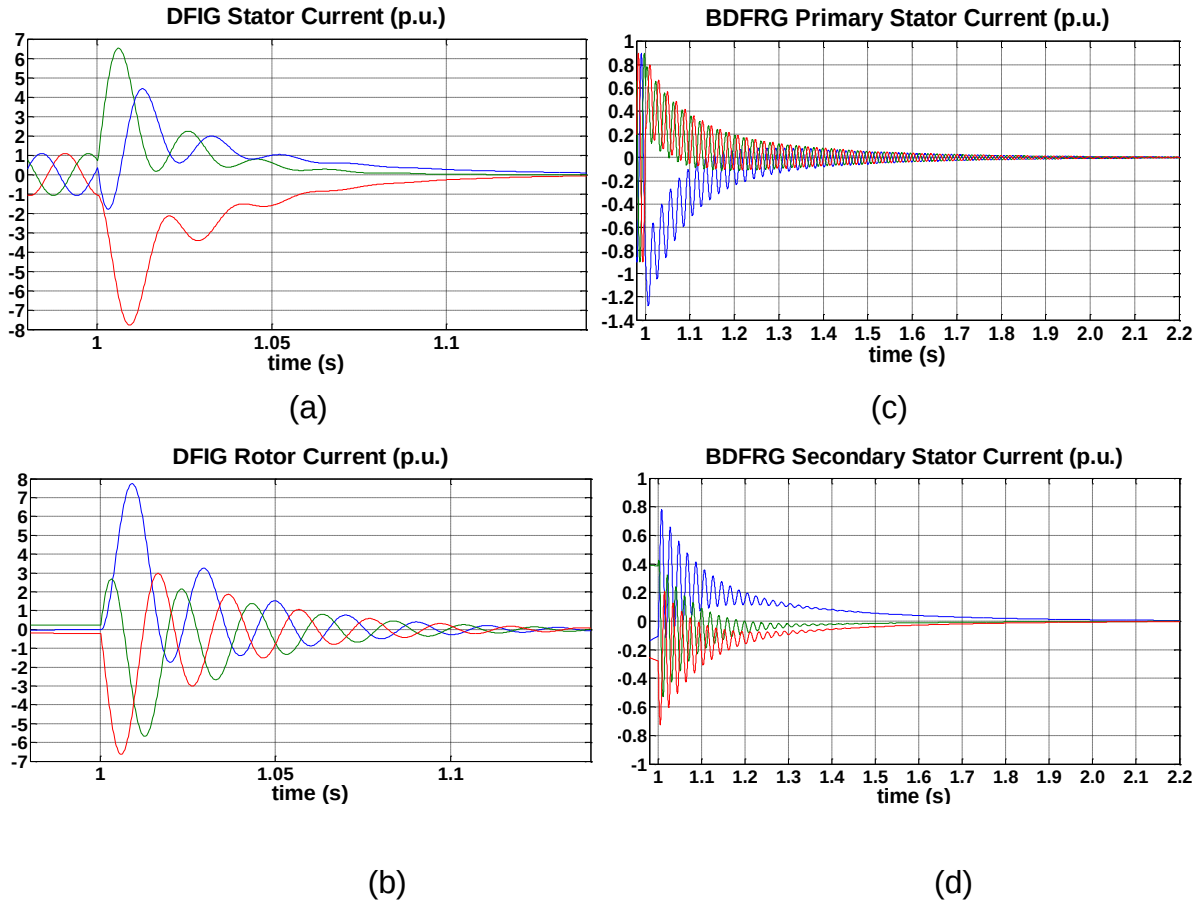

Figure 5.24 The simulation results of fault response for DFIG and BDFRG (a) fault DFIG stator phase currents (b) fault DFIG rotor phase currents (c) fault BDFRG primary stator phase currents (d) fault BDFRG secondary stator phase currents

The BDFRG peak fault current value indicates this BDFRG can ride through the fault with adding a zero value crowbar resistor when the machine current tolerance is higher than *1.25 p.u.* That means that the function of the crowbar used in this BDFRG is to simply short the secondary stator windings and isolate the back-to-back PWM converter only. After short-circuiting the secondary stator, the BDFRG can pass the fault by itself. Hence, in later timer action crowbar simulation, the BDFRG short-circuit its secondary stator and isolate the PWM converter rather than employ an additional resistor in the crowbar period.

However, the over-currents in DFIG fault response graphs suggest a crowbar circuit with the resistors is needed in order to ride through the fault. But how can the crowbar

resistance value be decided? In order to solve this question, we have to discuss the effect of changing the crowbar resistance. This impact with respect to DFIG fault response is best illustrated in Figure 5.25. This depicts the circuit path options for rotor currents faced with a PWM-disabled rotor converter and an active crowbar, flowing between two arbitrary rotor phases.

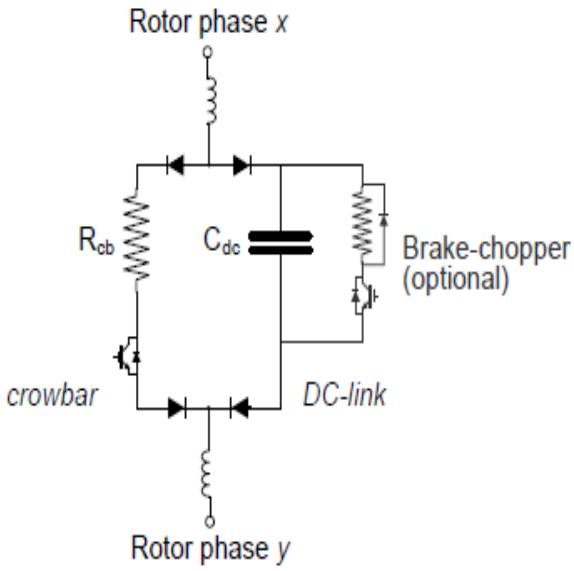

Figure 5.25 Short-circuit paths for transient rotor currents.

With zero or very low resistance, the crowbar simply shorts the rotor windings. The rotor converter's diodes are fully blocked and there is no current flow onto the DC-link. As the crowbar resistance is increased, the rotor time constant is reduced; the crowbar accepts the shortened periods of over-current while the DC-link remains blocked. At greater than twice the rotor winding resistance or more, the crowbar starts to dominate the rotor circuit, sinking the majority of the rotor magnetisation energy after a severe grid fault. Above a certain resistance, the IR potential across the crowbar indicates sufficient phase-to-phase rotor voltage to drive current through the rotor-converter diodes and through the DC-link capacitance. At successively higher crowbar resistance the share of current is increasingly taken by the DC-link capacitor and the DC-link voltage is forced higher. The action of a brake chopper helps to limit

the DC-link voltage rise, but does not directly influence the nature of the rotor flux decay.

In order to prevent a DC-over-voltage event, the crowbar resistance should be limited to prevent or at least minimise conduction through to the converter's DC-link; a restriction described by equation 5.63

$$i_{cb}R_{cb} < V_{dc} \tag{5.63}$$

Recognising the average value of rectified current from equation 3.43:

$$i_{cb} = \left(\frac{3\sqrt{2}}{\pi}\right) i_r = \frac{V_{dc}}{R_{cb}} = \left(\frac{3\sqrt{2}}{\pi}\right) \frac{\sqrt{3}V_{r,\ ph}}{R_{cb}} \tag{3.43}$$

$$R_{cb} < \frac{V_{dc}}{i_{cb}} = \frac{V_{dc}}{1.35 i_r} \tag{5.64}$$

The crowbar resistance should be maximised to improve its relative ability to hasten the decay of rotor flux, but should remain safely below the maximum limit imposed by equation 5.64.

Figure 5.25 (b) establishes the maximum transient rotor currents of roughly *8 p.u.* An approximation of the limit in equation 5.64 is therefore:

$$R_{cb} < \frac{V_{dc}}{10.8 i_{r,base}} \tag{5.65}$$

Using the operational DC-link voltage of *600V* dc and the base rotor current of *24.2715A* suggests a maximum crowbar resistance of *2.289* Ω. In later simulation, a *2* Ω resistor is selected.

5.3.2. DFIG and BDFRG timer action crowbar simulation comparison

The timer action crowbar employed in this simulation has the same structure and the same control method as the crowbar used in section 3.3.3. This crowbar is activated when the DFIG rotor or BDFRG secondary stator current exceeds a threshold value, and keep connection with windings for *0.12s*. DFIG's crowbar has a $2\,\Omega$ resistor whereas BDFRG's crowbar resistor is $0\,\Omega$.

The DFIG stator voltage and BDFRG primary stator voltage is *220V* per-phase initially and dropped to *15%* of healthy voltage *1.0s* after data-recording started. The fault voltage would keep a short fixed period before the fault recovery.

Figure 5.26 illustrates a comparison of the DFIG and BDFRG fault ride through performance under a timer action crowbar. In the simulation, the *15%* fault voltage existed for *0.5s* and the crowbar activated when the rotor or secondary stator current magnitude was over *2.0 p.u.* value. That indicates if the DFIG rotor current exceeded *48.543V* or the BDFRG secondary stator current was bigger than *22.79V*, the crowbar would be connected to the machine rotor or secondary stator windings. The crowbar would keep activation after *0.12s* and re-engaged when the current met the next limitation.

Figure 5.26 demonstrates both DFIG and BDFRG's simulation results. The left three graphs (a) (b) and (c) show the DFIG power, rotor phase currents and magnitude respectively, while the right pictures (d) (e) and (f) display the BDFRG corresponding results.

From Figure 5.26, the DFIG experiences twice crowbar periods during the fault and once in the fault recovery, but the BDFRG does not employ the crowbar to ride through the fault. Graph (f) gives the evidence of the crowbar's unemployment. The

fault period is not long enough to let the BDFRG secondary stator current magnitude exceeding the trigger threshold value *2.0 p.u.* This results in the crowbar disengagement of the BDFRG in the fault period. It is explicit that the BDFRG could withstand the fault by itself if one of two conditions is met. One is the trigger threshold value of the crowbar activation is big enough, the other is the voltage fault period is not too long. On the contract, if the voltage fault persists a long time to let the BDFRG secondary stator current increasing to a high value or the system over-current tolerance is low, the BDFRG may need the crowbar engagement.

Figure 5.27 attests one of the above conclusions. It demonstrates the DFIG and BDFRG performance under the same crowbar method as Figure 5.26. The fault period was still *0.5s* and the fault voltage was *15%* of healthy voltage, but the trigger threshold value was lower to *1.5 p.u.* It illustrates vividly in the picture that the DFIG experiences four crowbar periods while the BDFRG's crowbar is activated once at the initial point of the fault. From this, it can be seen that the crowbar may be activated in the BDFRG system when the tolerance of the over-current is dropped. But compared to the DFIG, the BDFRG has less crowbar engagement frequency.

Similarly to the Figure 5.27, Figure 5.29 will prove another conclusion. If the fault time is long enough to allow the BDFRG secondary stator current climbing to a high level, the crowbar may be employed in the BDFRG system during the fault. Thus compared to Figure 5.26, all the parameters in simulation did not change except the fault duration time. As shown in Figure 5.28, the BDFRG would take *1.6246s* to make the secondary stator current magnitude reach *2.0 p.u.* under *15%* fault voltage. Hence a *2.0s 15%* fault voltage was applied to the system in Figure 5.29.

Figure 5.29 (b) and (c) illustrates clearly that the BDFRG secondary stator currents increase gradually and reach *2.0 p.u.* The crowbar is engaged three times after approximate *1.6s*. Compared to Figure 5.26, these results explain that the BDFRG can withstand a longer fault period than the DFIG.

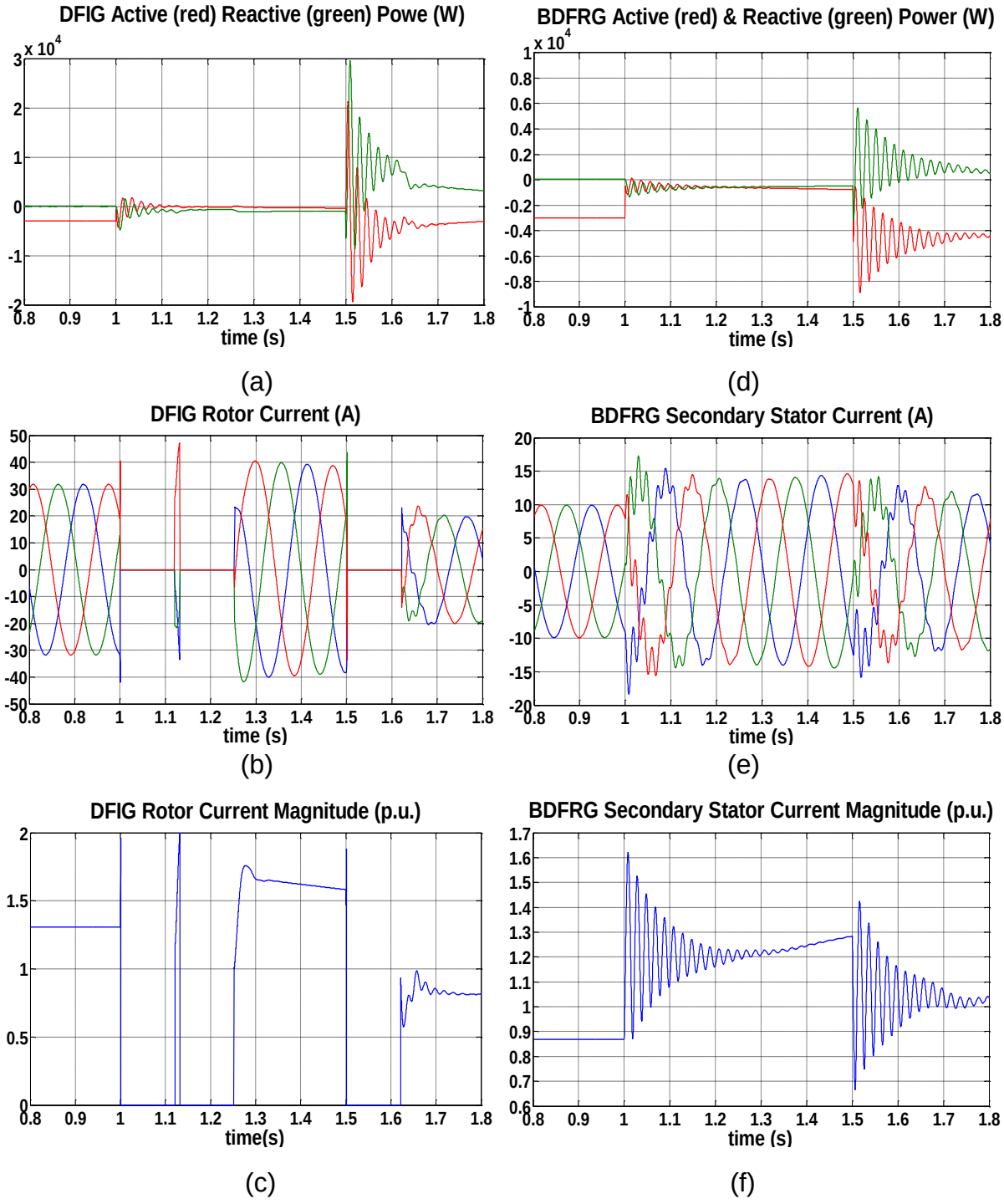

Figure 5.26 DFIG and BDFRG timer action crowbar simulation results with *0.5s 15%* fault voltage and *2.0 p.u.* rotor and secondary stator current limitation (a) DFIG active and reactive power (b) DFIG rotor *3*-phase currents (c) DFIG rotor current magnitude (d) BDFRG active and reactive power (e) BDFRG secondary stator *3*-phase currents (f) BDFRG secondary stator current magnitude

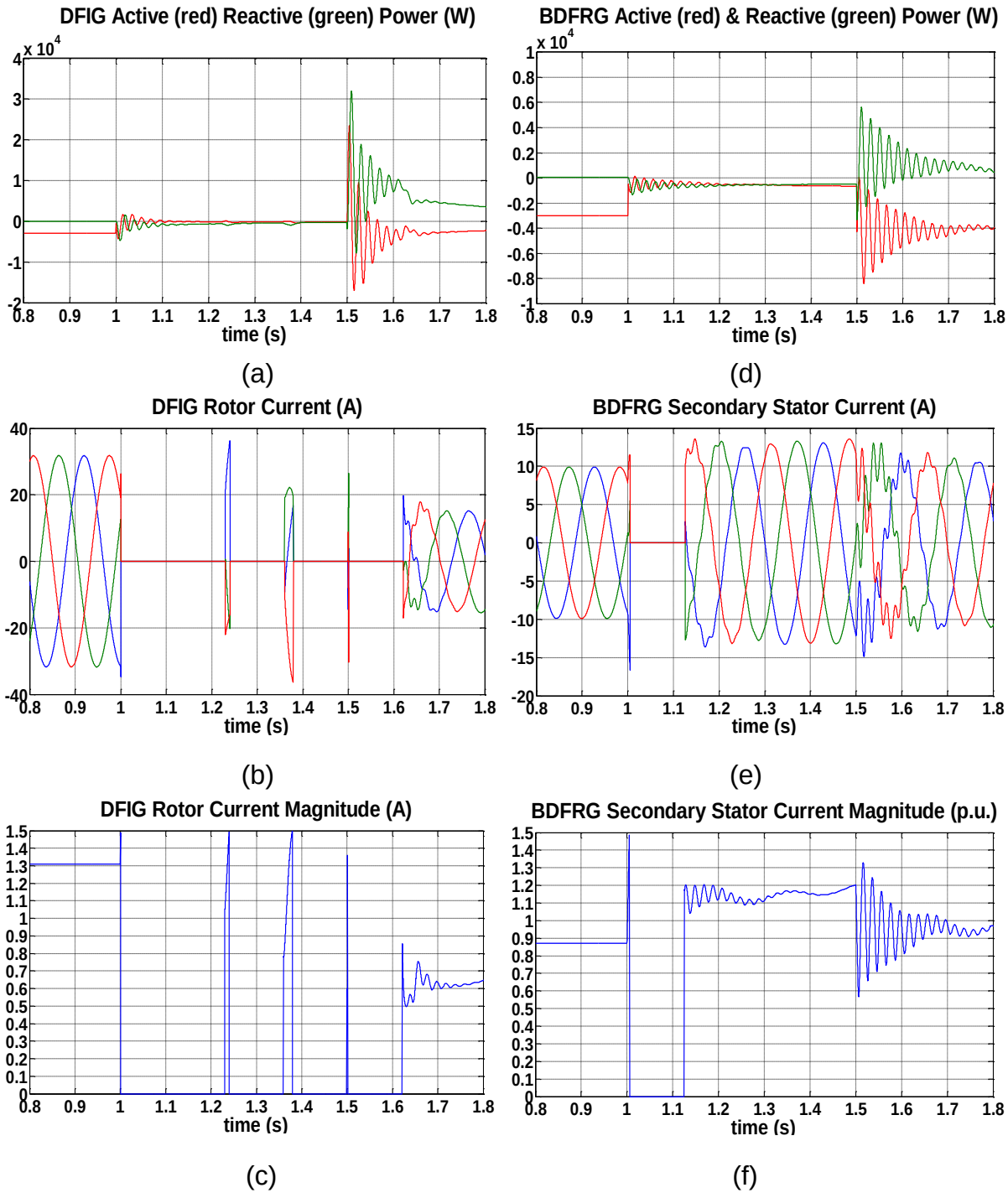

Figure 5.27 DFIG and BDFRG timer action crowbar simulation results with *0.5s 15%* fault voltage and *1.5 p.u.* rotor and secondary stator current limitation (a) DFIG active and reactive power (b) DFIG rotor *3*-phase currents (c) DFIG rotor current magnitude (d) BDFRG active and reactive power (e) BDFRG secondary stator *3*-phase currents (f) BDFRG secondary stator current magnitude

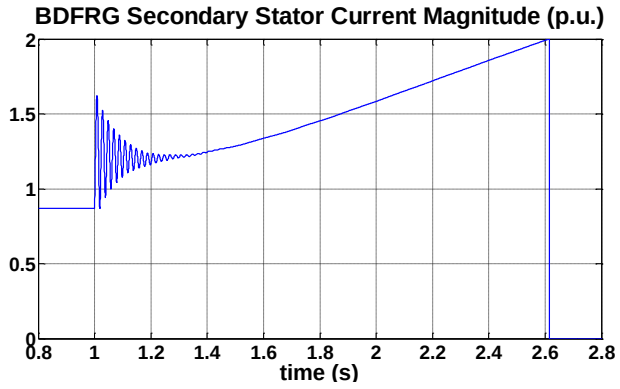

Figure 5.28 BDFRG secondary stator current magnitude when a 15% fault voltage is applied

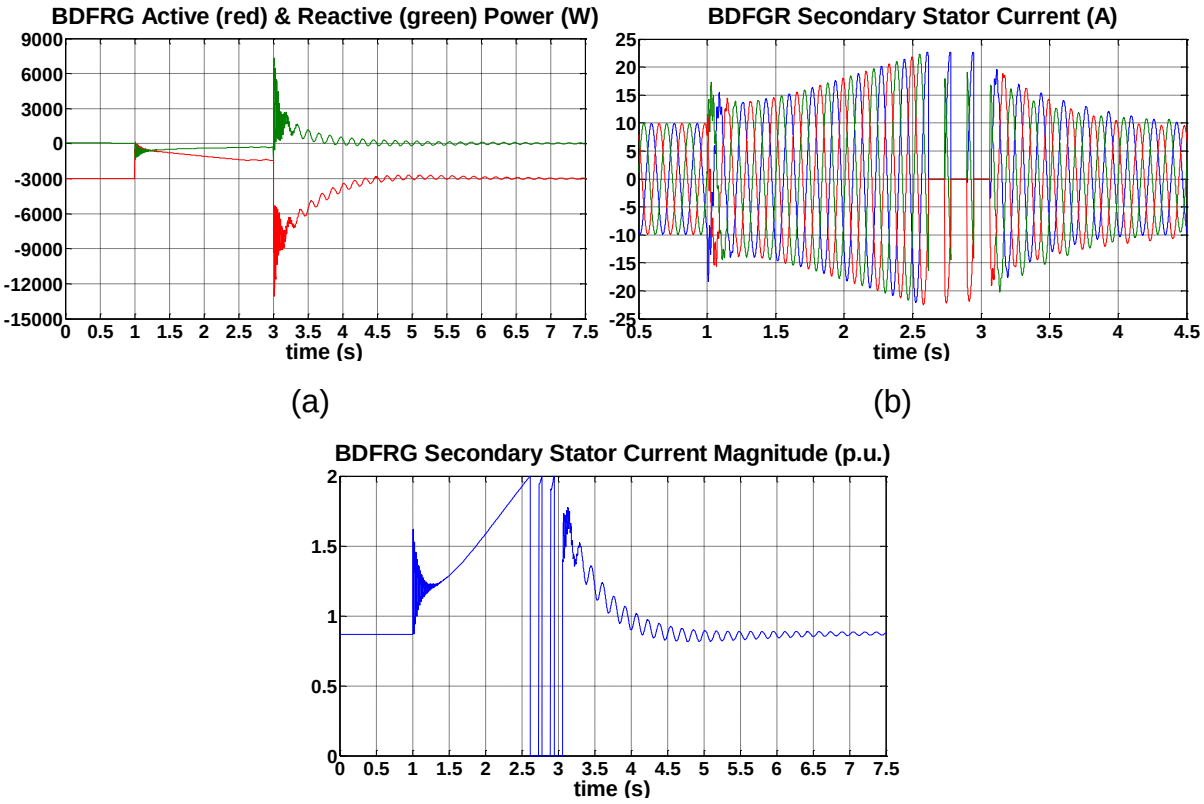

Figure 5.29 BDFRG timer action crowbar simulation results with 2.0s 15% fault voltage and 2.0 p.u. secondary stator current limitation (a) BDFRG active and reactive power (b) BDFRG secondary stator 3-phase currents (c) BDFRG secondary stator current magnitude

From all the results above, we can get the consequences as follows:

① The BDFRG can withstand a longer fault duration than the DFIG.

② In the same time, the BDFRG would activate the crowbar less times compared to the DFIG.

③ Even the BDFRG can ride through the fault without the crowbar when the fault persists for a short period and the trigger current threshold is big.

In summary, the BDFRG has the higher tolerance of the fault and better performance of the timer action crowbar method than the DFIG. In the other words, the BDFRG may take place of the DFIG in the future due to its similar healthy operation and better fault ride through ability compared to the DFIG.

6. Direct Power Control (DPC) response for DFIG and BDFRG

Direct Power Control is a fast response control based on the measurement of the active and reactive power on grid side where voltages and currents are alternating at fixed frequency *50Hz*. The active and reactive powers are made to track references using hysteresis controllers [38].

This method eliminates the requisite for rotor position sensing and gives excellent dynamic performance. It is thus an attractive sensorless control for drive as well as generator applications.

Besides, the active power and reactive power calculations do not need the *d-q* components of each vector viewed in the excitation reference frame, and the excitation frame angle θ_e is not a necessity. The Phase Locked Loop scheme is therefore not required, which reduces the inconveniency compared to the vector control.

Direct Power Control Method is first introduced and implemented on a wound rotor induction machine by Rajib Datta and V.T.Ranganathan in reference [38]. My project collaborator, Hamza successfully actualized the DPC on a BDFRM in [74] and we have expanded the method to a new sensorless torque and reactive power control presented in [13]. This simple yet efficient controller has the same control principle of DPC demonstrated by Rajib, but replacing the active power by the torque. References [75]-[77] also have the same idea presented in this Chapter. But in this Chapter, the control reference maintains active and reactive power.

The target of this Chapter is to implement DPC to both DFIG and BDFRG, and then have a comparison. BDFRG can be controlled under *10kHz* sampling frequency. But due to higher sampling frequency requirement of DPC and the limitation to *10kHz* of

Infineon *IFS100V12PT4* IGBT power module, the implementation of DPC to DFIG is not successful. Thus a DFIG DPC simulation is operated depending on the machine model used in Chapter 3. The generator performance at *5kHz*, *10kHz* and *20kHz* switching frequency is compared.

6.1. Direct Power Control Method

The general principle of Direct Power Control is shown in Figure 6.1.

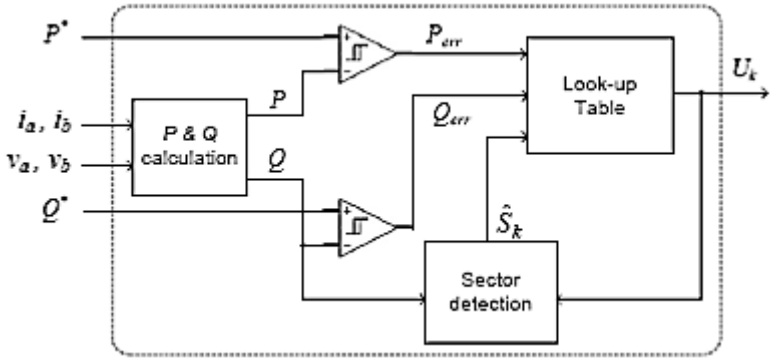

Figure 6.1 Schematic diagram of DPC

Based on the schematic diagram, the main task is to solve the look-up table and sector detection selection. As presented by Rajib Datta and V.T.Ranganathan in reference [38], taking DFIG as the example, the look-up table can be obtained by the analysis below.

The DPC analysis is based on the stator voltage field orientation reference frame as well. In the conventional space vector field oriented control strategy demonstrated in Chapter 5, the stator current component i_{sd} has to be controlled to control the stator active power P_s and i_{sq} has to be controlled to control the stator reactive power Q_s. This is achieved in turn by controlling the rotor currents i_{rd} and i_{rq}, respectively.

The variation of the rotor flux with change in the active and reactive power demand is shown in Figure 6.2. In the left graph, i_{rq} is set to zero, if i_{rd} is varied from 0 to full

load, the locus of φ_r changes along A to B. This implies a predominant change in angle δ_p between the stator flux φ_s and the rotor flux φ_r, whereas the magnitude of φ_r does not vary appreciably. In other words, a change in the angle δ_p would definitely lead to a change in the stator active power. In the right graph of Figure 6.2, the stator active power demand remains the same so that i_{rd} maintains constant and i_{rq} is altered from 0 to the rated value. The locus of φ_r varies along C to D, causing a predominant change in magnitude of φ_r, whereas the variation of δ_p is small. Therefore, the stator reactive power can be reduced by increasing the magnitude of the rotor flux and vice-versa.

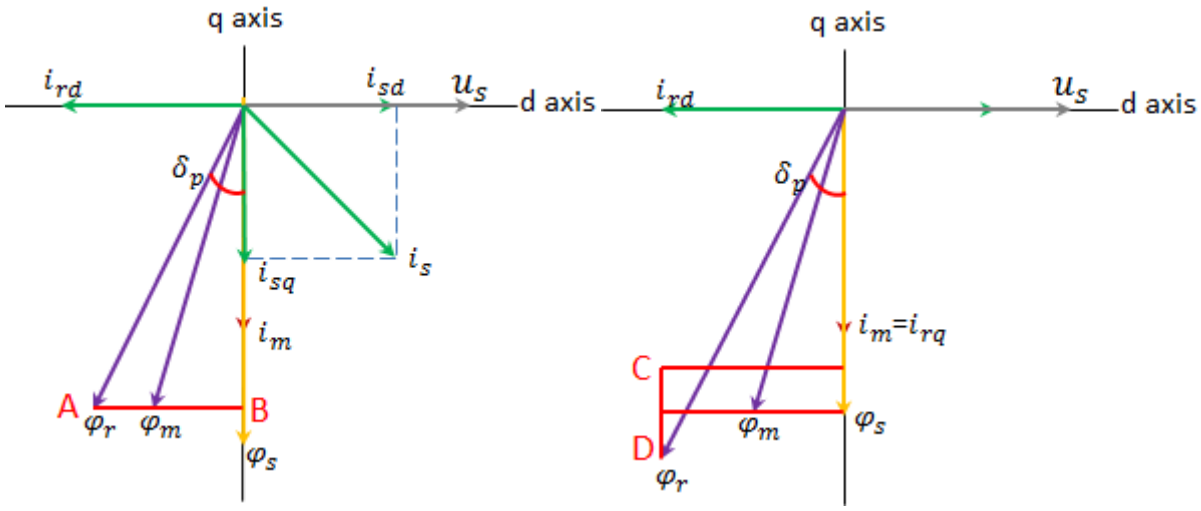

Figure 6.2 Phasor diagram showing variations in rotor flux with variations in active and reactive power.

It can be concluded from the above discussion that the stator active power can be controlled by controlling the angular position of the rotor flux vector and the stator reactive power can be controlled by controlling the magnitude of the rotor flux vector [38].

6.1.1. Voltage vector and their effects

In order to make an appropriate selection of the voltage vector, the space phasor plane is first subdivided into six 60° *sectors 1, 2…6* graphically displayed in Figure 6.3. There are six voltage space vectors *U1, U2……U6* lying in six sectors with each vector existing in each sector. These six voltage space vectors *U1, U2……U6* make up to another six 60° sextants with 30° difference from the sector sextant and are corresponding to six switching states *S1, S2……S6* respectively.

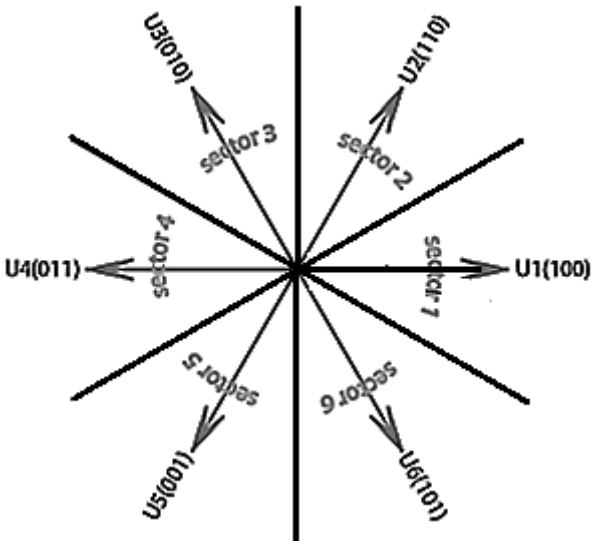

Figure 6.3 voltage space phasors

The instantaneous rotor flux magnitude and angular velocity can be controlled by selecting a particular voltage vector depending on its present location [38]. In the following description, the rotor flux is assumed to be initially positioned in *Sector 1* for the simplification of the discussion.

6.1.2. The vector effects on active power

Considering anti-clockwise direction of the flux vectors' rotation in the rotor reference frame to be positive, φ_s is ahead of φ_r in motoring mode of operation and behind φ_r in generating mode as shown in Figure 6.4. In the rotor reference frame the flux

vectors rotate in the negative direction (clockwise direction) at super-synchronous speeds, remain stationary at synchronous speed and start rotating in the positive direction (anti-clockwise direction) at sub-synchronous speeds.

Assuming that the rotor flux φ_r is placed in *Sector 1*, application of voltage space vectors *U2* and *U3* would accelerate φ_r in the anti-clockwise direction. In the motoring operation mode, the rotor flux acceleration decreases the angular separation between the two fluxes which brings about a drop of stator active power. This indicates the different power between the new and past value is less than zero ($\Delta P < 0$). On the contrary, in the generating mode of operation, application of vectors *U2* and *U3* causes an increase in angular separation between the two fluxes and thereby a growth in the active power. If power drawn by the stator being taken as positive and power generated being considered as negative, P_s is negative for generation. Thus, application of *U2* and *U3* will result in a decline of positive active power in both generator and motor operation modes. Similarly, it can be found that the effect of *U5* and *U6* on the active power would be exactly opposite to that of *U2* and *U3* in both the motoring and generating modes.

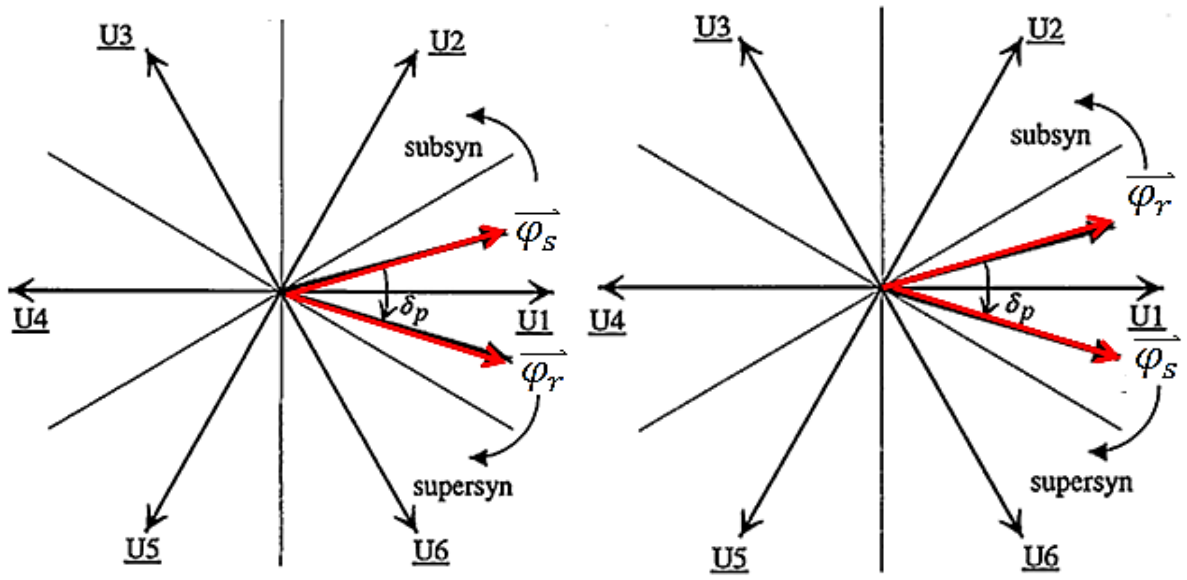

Figure 6.4 Flux vectors in (left) motoring mode (right) generating mode

The zero vectors effect on P_s is to stall the rotor flux without affecting its magnitude. This leads to an opposite effect on the stator active power in sub-synchronous and super-synchronous speed. Below the synchronous speed in motoring, application of a zero vector increases δ_p as φ_s maintains rotating in the anti-clockwise direction at slip speed. In super-synchronous speed, φ_s rotates in the negative direction and thereby induces the decrease of δ_p. Hence the application of the zero vectors can make P_s increase at sub-synchronous speed and decrease in super-synchronous operation mode because of the variations of δ_p affected by the rotating direction of φ_s. As the active power is negative in generator, the same conclusion holds true for the generating modes as well.

As a generalization, it can therefore, be said that, if the rotor flux φ_r is in the kth sector, where $k = 1,2,3, \dots 6,$ application of voltage space vectors $\underline{U(k+1)}$ and $\underline{U(k+2)}$ would result in a reduction in the stator active power P_s and application of vectors $\underline{U(k-1)}$ and $\underline{U(k-2)}$ would result in an increase in P_s [38]. The application of the zero vector increases P_s at sub-synchronous speed and reduces it in super-synchronous operation.

6.1.3. Vector effects on reactive power

From the phasor diagrams of Figure 6.2, the stator reactive power is dependent upon the component of φ_r along φ_s. It is φ_{rq} in stator voltage field orientation controller. The angle δ_p between φ_s and φ_r being small, the magnitude of φ_r is approximately equal to φ_{rq}. Therefore, when the rotor flux vector is located in *Sector 1*, the magnitude of φ_r increases under voltage vectors *U1*, *U2* and *U6*, whereas *U3*, *U4* and *U5* result in the reduction of it. This holds well irrespective of whether the machine is operating in either motor or generator operation mode. An increase in magnitude of φ_r implies a rising amount of the rotor side reactive power, and hence a reduction in the stator reactive power which amounts to an improved stator power

factor. A decrease in magnitude of φ_r results in a poor the stator power factor. It indicates the difference between the new and previous reactive power is negative ($\Delta Q < 0$) in the application of voltage vectors *U1*, *U2* and *U6* and positive ($\Delta Q > 0$) in the application of vectors *U3*, *U4* and *U5*.

As a zero vector does not change the magnitude of φ_r, its effect on Q_s is rather small. Nevertheless, Q_s still has some minor variation. This small change depends on whether the angle δ_p between the stator and rotor fluxes increases or reduces due to the application of a zero vector. The change of δ_p will cause the variation of φ_{rq} and hence result in the change of Q_s. For example, an increase of angular separation between the two fluxes decreases φ_{rq}. The rotor flux reduction leads to an increase of Q_s. The converse holds true when δ_p drops.

Speed	Motoring	Generating
Sub-synchronous	$\delta_p \uparrow \Rightarrow \varphi_{rq} \downarrow \Rightarrow Q_s \uparrow$	$\delta_p \downarrow \Rightarrow \varphi_{rq} \uparrow \Rightarrow Q_s \downarrow$
Super-synchronous	$\delta_p \downarrow \Rightarrow \varphi_{rq} \uparrow \Rightarrow Q_s \downarrow$	$\delta_p \uparrow \Rightarrow \varphi_{rq} \downarrow \Rightarrow Q_s \uparrow$

Table 6.1 Effect of zero vertor on active and reactive power

It is observed that the change in Q_s due to the application of the zero vector is different in all the 4 modes of operation. This is summarized in Table 6.1.

It may therefore, be concluded that, if the rotor flux resides in the kth sector, switching vectors $\underline{U(k)}$, $\underline{U(k+1)}$ and $\underline{U(k-1)}$ decrease the stator reactive power Q_s and $\underline{U(k+2)}$, $\underline{U(k-2)}$ and $\underline{U(k+3)}$ could increase Q_s [38]. The application of the zero vector brings about an increment of Q_s in either sub-synchronous motoring mode or super-synchronous generating mode, and a reduction of it at sub-synchronous speed as a generator or at super-synchronous speed as a motor.

6.1.4. The power band definition

The stator active and reactive powers can be directly calculated from the stator current and stator voltages after transferring the three-phase current and voltage to $\alpha - \beta$ components by following transformation:

$$V_{s\alpha} = \frac{2}{3}V_{sa} + \frac{1}{3}V_{sb} + \frac{1}{3}V_{sc} \tag{6.1}$$

$$V_{s\beta} = \frac{\sqrt{3}}{3}V_{sb} - \frac{\sqrt{3}}{3}V_{sc} \tag{6.2}$$

The active and reactive power then can be expressed as:

$$P_s = 1.5\left(u_{s\alpha}i_{s\alpha} + u_{s\beta}i_{s\beta}\right) \tag{6.3}$$

$$Q_s = 1.5\left(u_{s\beta}i_{s\alpha} - u_{s\alpha}i_{s\beta}\right) \tag{6.4}$$

In DPC method, the PLL and excitation frame angle are not necessary. But a band for reference power is needed as illustrated in Figure 6.5.

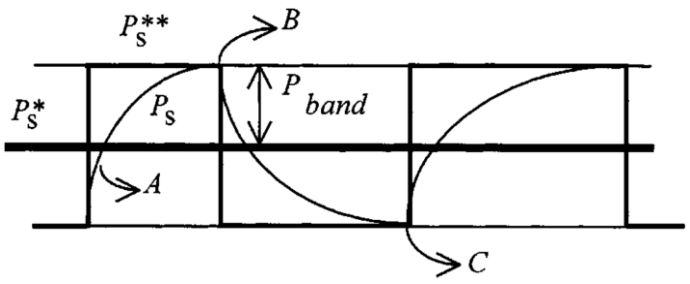

Figure 6.5 Hysteresis control of active power

P_s^* is the reference for the stator active power. The actual power P_s is to be controlled to stay within a band of width P_{band} about P_s^*. This is achieved by defining an auxiliary reference P_s^{**} and switching as per the following logic:

$$P_{error} = P_s^{**} - P_s$$

$$\text{if } (P_{error} > 0) \qquad P_s^{**} = P_s^* + P_{band}$$

$$\text{else} \qquad P_s^{**} = P_s^* - P_{band}$$

In a similar manner, the error and reference for reactive power can be written as:

$$Q_{error} = Q_s^{**} - Q_s$$

$$\text{if } (Q_{error} > 0) \qquad Q_s^{**} = Q_s^* + Q_{band}$$

$$\text{else} \qquad Q_s^{**} = Q_s^* - Q_{band}$$

The band plays a role of the 'toleration' of the power aberration. The machine noise, and harmonics effects and the power variations during one sampling frequency would impact the selection of the power band.

6.1.5. Switching vector selection

For the purpose of the appropriate switching vector determination at any instant of time, the errors of P_s and Q_s, and the sector in which the rotor flux vector is presently residing are taken into consideration [38]. Thus the switching table (Table 6.2) for active vector selection can be generated.

Error		Sector					
P_{error}	Q_{error}	1	2	3	4	5	6
<=	>	S3	S4	S5	S6	S1	S2
<=	<=	S2	S3	S4	S5	S6	S1
>	>	S5	S6	S1	S2	S3	S4
>	<=	S6	S1	S2	S3	S4	S5

Table 6.2 Selection of active switching state

If the rotor side converter is switched in accordance to the switch states in Table 6.2, it is of possibility to control the stator active and reactive powers within the desired error bands. But the use of active vectors alone would result in non-optimal switching of the converter and also a higher switching frequency.

Speed	Motoring	Generating
Sub-synchronous	$P_{error} \geq 0$ & $Q_{error} \geq 0$	$P_{error} \geq 0$ & $Q_{error} < 0$
Super-synchronous	$P_{error} < 0$ & $Q_{error} < 0$	$P_{error} < 0$ & $Q_{error} \geq 0$

Table 6.3 Condition for selection of zero vector

By considering the effect of the zero vector on active and reactive powers, the logic for how to select the zero vector can be summarized as in Table 6.3. Taking the sub-synchronous motoring mode of operation as an example, the application of a zero vector will increase Q_s as seen from Table 6.1. Since δ_p enlarges, P_s also increases. Therefore, when the errors in P_s and Q_s are positive, a zero vector is applied to effect an increase in both the P_s and Q_s and thereby bring down the errors. The zero vector effect under other modes in the table can be worked out in a similar manner.

It is conclusive that the effect of the zero vector on P_s is opposite in the sub-synchronous and super-synchronous operation but remains same action both as a motor and a generator, whereas the effect on Q_s is contrary in the motoring and generating modes but maintains same behaviour in both sub- and super-synchronous speed.

6.1.6. Sector Identification of rotor flux

In order to implement the switching algorithm, the present sector of the rotor flux has to be identified. The exact position of the rotor flux space phasor within the sector is not of importance as far as the selection of the switching vectors is concerned.

The proposed method of sector identification is based on the direction of change in Q_s when a particular switching vector is applied. Suppose that the present position of φ_r is in *Sector 1* and it is moving in the anti-clockwise direction (corresponding to Sub-synchronous operation). Application of switching states *S2* and *S6* lead to a reduction of Q_s and application of *S3* and *S5* result in an increase of Q_s. When the rotor flux vector φ_r crosses over to *Sector 2*, the effect of states *S3* and *S6* on Q_s would reverse. The voltage space vector *U3* would now act to decrease Q_s instead of increasing it. Similarly the effect of vector *U6* on Q_s would also be opposite. These reversals in the direction of change of Q_s can be detected and used for a decision of sector change, when a particular vector is applied. Similarly, if the flux vector is rotating in the negative direction (super-synchronous operation) the effect of states *S2* and *S5* on Q_s would reverse when φ_r crosses over from *Sector 1* to *Sector 6*. Thus in any particular direction of rotation, there are two vectors which can provide the information for a change in sector. Since the rotor flux vector cannot jump through sectors, the change will always be by one sector, either preceding or succeeding. In this method, even though the accurate position of the flux is unknown, the sector information can be updated just by observing the changes in Q_s due to the applied vectors.

	S1	S2	S3	S4	S5	S6
Sector 1	X	-	+	X	+	-
Sector 2	-	X	-	+	X	+
Sector 3	+	-	X	-	+	X
Sector 4	X	+	-	X	-	+
Sector 5	+	X	+	-	X	-
Sector 6	-	+	X	+	-	X

Table 6.4 Expected direction of change in Q_s

The expected direction of change in Q_s due to the application of any switching state in the different sectors can be summarised in Table 6.4. However it may be noted that in a particular sector not all vectors will be applied. For example, in sector k, vectors U_k and U_{k+3} will never be applied. These vectors would have predominant effect on the reactive power, but their effect on the active power would depend on the actual position of the rotor flux vector in the sector. In most applications, there is hardly any requirement for fast transient changes in reactive power; so it is not necessary to apply the strongest vector to effect any change in Q_s. In the switching logic, therefore, only those vectors are selected which have uniform effects on P_s and Q_s in terms of their direction of change irrespective of the position of the rotor flux in a particular sector.

	S1	S2	S3	S4	S5	S6
Sector 1	0	-1	+1	0	-1	+1
Sector 2	+1	0	-1	+1	0	-1
Sector 3	-1	+1	0	-1	+1	0
Sector 4	0	-1	+1	0	-1	+1
Sector 5	+1	0	-1	+1	0	-1
Sector 6	-1	+1	0	-1	+1	0

Table 6.5 Inferred change of sector position

For any given vector applied in a particular sector, the expected direction of change in Q_s can be found from Table 6.4. The actual direction of change can be computed from the present value of Q_s and its previous value. If the actual direction of change is opposite to the expected direction of change then a decision on change of sector is taken. This information is stored in another lookup table (Table 6.5).

From the Table 6.5, the sector changes principle is clear. For example, taking account of *sector* k, actual Q_s has the different changes compared to the

expectation in $S\,(k-2)$ and $S\,(k+1)$ will cause the sector number reducing *1* to *sector* $(k-1)$, and the difference change of actual and expected Q_s in $S\,(k+2)$ and $S\,(k-1)$ will encourage the sector number adding *1* to sector $(k+1)$.

6.2. Experimental results of DPC for BDFRG

Comparing the direct power control to vector control method, DPC needs higher sampling frequency. The explanation can be clear demonstrated in Figure 6.6. In one sampling frequency, the modulation index generates from the vector control can cut the carriers, and produces the signals to IGBT switches. In this condition, the vector control can have maximum 6 switch states in each sampling frequency. But the DPC can only present one switch state per sampling frequency. Thus the DPC requires the far higher converter switching frequency than vector control method.

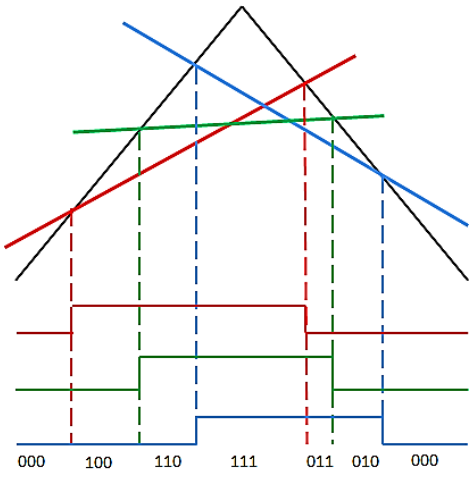

Figure 6.6 The example of the modulation index cutting the carrier

In the experiment above, the vector control uses *5kHz* converter frequency to sample. But when *5kHz* frequency is tried on DPC, both DFIG and BDFRG are failed to be controlled.

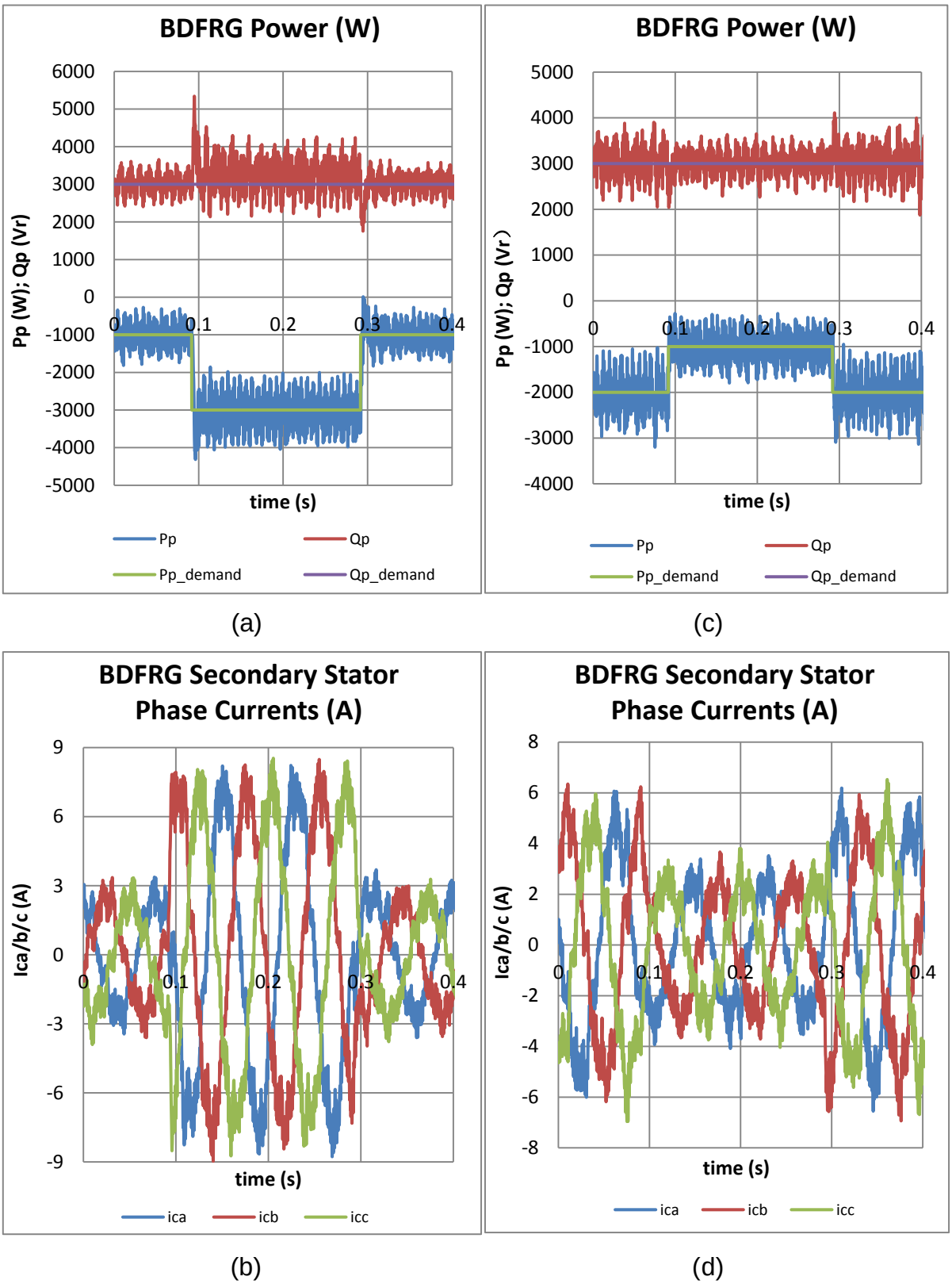

Figure 6.7 BDFRG experimental results under DPC (a) & (c) BDFRG active and reactive power (b) & (d) BDFRG secondary stator phase currents

After increase the sampling frequency to *10kHz*, DFIG remains unsuccessful, but BDFRG has the results presented in Figure 6.7. The left four graphs demonstrate the BDFRG performance when the primary stator active power dropped from *-1000W* to -3000W, while the corresponding right pictures illustrate the experimental results as the active power increased from *-2000W* to *0W*. And in all the tests, the primary stator reactive power was always kept at *3000Vr*.

From pictures (a) and (c), the BDFRG powers are oscillate within a band of $\pm 1000W(Vr)$. The graphs (b) and (d) show there are many distortions in both primary stator currents and secondary stator currents. Although the controller performance of BDFRG is not as good as vector control's with high power variations and current distortions, the generator definitely can be said 'under control'.

It seems that DPC is more effectual to be implemented in BDFRG than DFIG under lower sampling frequency. The possible reason may be caused by the larger inductance. As section 6.1.4 explained, a band is selected to 'tolerate' the effects of machine harmonics and the power changes during one sampling frequency. Although BDFRG has more harmonics than DFIG, its power change in specific period is much smaller than DFIG as its current would be hold for a while due to the large inductance. But this conclusion is made for the machine in the experiments. If this consequence want to be promoted, more different rotor structure and different power level BDFRGs need to be examined.

6.3. DPC simulation results comparison for DFIG and BDFRG

DFIG cannot be controlled with the converter frequency of *10kHz*, but the sampling frequency cannot be enhanced as Infineon *IFS100V12PT4* IGBT module has the limitation of converter frequency to *10kHz*. Thus, in order to make the two generators'

comparison clearly, the performances of both DFIG and BDFRG under DPC have been simulated.

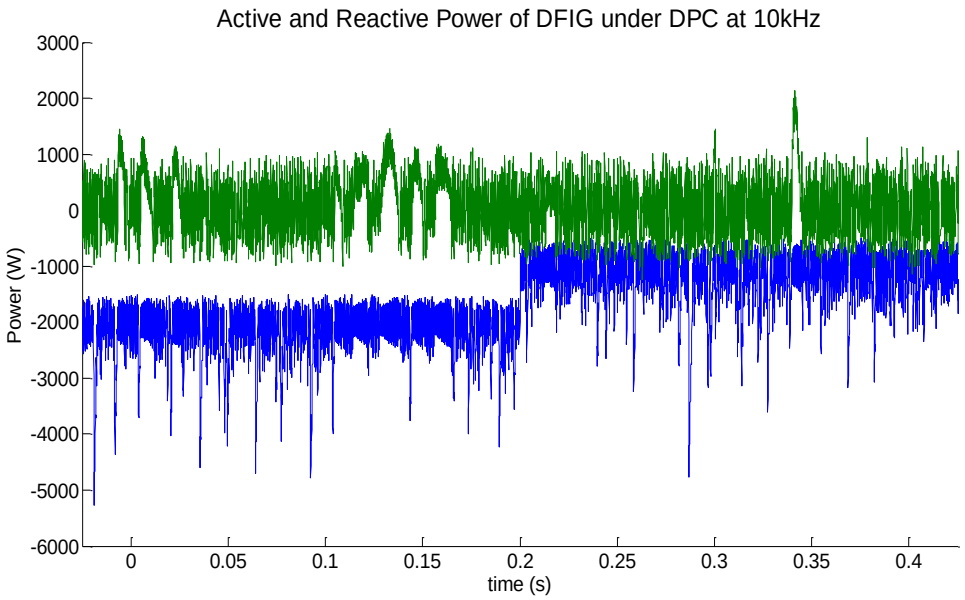

(a)

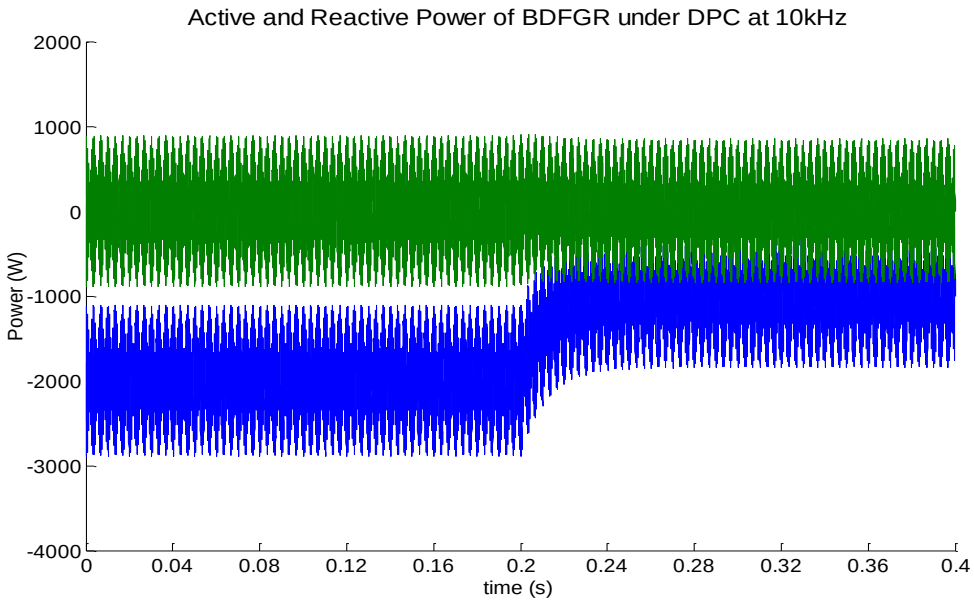

(b)

Figure 6.8 (a) Active (blue) and Reactive (green) Power of DFIG under DPC at *10kHz* (b) Active (blue) and Reactive (green) Power of BDFGR under DPC at *10kHz*

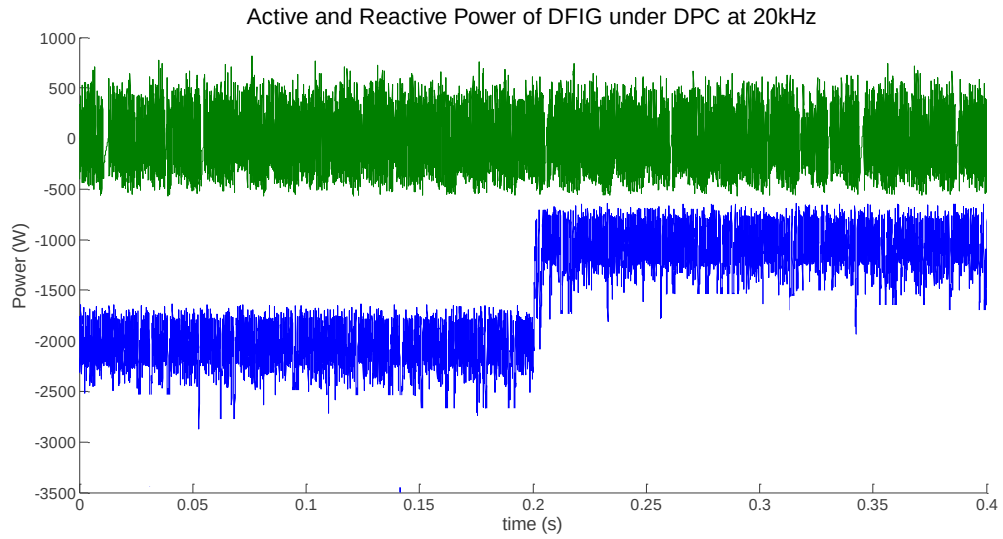

(a)

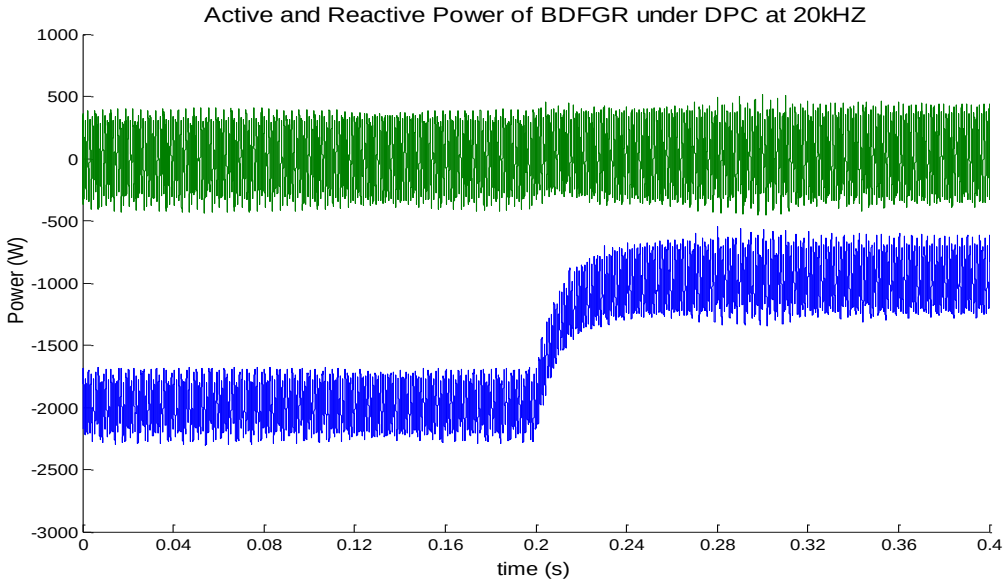

(b)

Figure 6.9 (a) Active (blue) and Reactive (green) Power of DFIG under DPC at *20kHz* (b) Active (blue) and Reactive (green) Power of BDFRG under DPC at *20kHz*

Figure 6.8 and Figure 6.9 graphically demonstrate the responses of two generators at *10kHz* and *20kHz* when a step change is given to the active power respectively. It is vivid that for both generator models, the machine performance in *20kHz* is far better

than the simulation results in *10kHz*. The comparisons of the same machine performance under different switching frequency give the evidences.

DFIG powers working at *10kHz* sampling frequency have many points out of control. Some extra lower or higher points will cause the overcurrent in the machine and rotor-side converter. The overcurrent would stop the converter switches working and open all the relays owe to the system protection scheme. The control would failed at this situation. That may be the major reason why the DPC cannot be successfully implemented at *10kHz* for the DFIG. However *20kHz* sampling frequency makes the curves of the DFIG powers much smoother. It seems that this DFIG could be operated by DPC under *20kHz*, which cannot be implemented by the existing test apparatus due to the IGBT module frequency limitation. Hopefully, this conclusion could be proved in the future work.

For the BDFRG, the powers vary in a band of $\pm$*900W(Vr)* when the controller switching frequency is set to *10kHz*, while the $\pm$*400W(Vr)* power variations are appeared at *20kHz*. It implies that the high sampling frequency can improve the DPC effects. In addition, comparing the vector control results, the DPC power graphs have the large power variation band and the visible coupling of real and reactive power. That may because the vector control can produce more switch states in each sampling frequency than DPC. Hence the DPC need bigger variation band to tolerant the power changes during on sampling frequency. Additionally, two powers in DPC figures have the same coupling relationships compared to the vector control curves, but more variations with larger band cause the coupling not very visible.

Besides, compared the graphs (a) and (b) in Figure 6.8 and Figure 6.9, it can be seen that the DPC works more effectually in BDFRG than DFIG when the same switching frequency is set to both machines. The major reason might be the BDFRG's current changes less during the same period compared to the DFIG due to its high inductance value. Considering both vector control and DPC results, the BDFRG can

be controlled by both vector control and DPC whereas DFIG is better to be controlled by the vector control if the switching frequency is not very high.

Consequently, although DPC is an effective sensorless, none PLL requirement and fast response control method. But the sampling frequency is the major restriction factor of its implementation. Additionally, the DPC might be more applicable to the BDFRG, especially under the lower sampling frequency. But this conclusion is made for the machine used in this thesis. Considering the distinctiveness of the BDFRG designed by Prof. Wang, if this consequence wants to be promoted, more different rotor structure and different power level BDFRGs need to be examined and compared with the corresponding DFIG.

7. Conclusion

7.1. DFIG and BDFRG difference reviews

The main aim of this thesis is to compare two generators: DFIG and BDFRG. The differences between them presented in this thesis are concluded below.

7.1.1. Machine structures comparison

BDFRG has eliminated the brushes and slip rings, which may increase the reliability and reduce maintenance. But, the BDFRG will be larger than the DFIG for the same power or will produce less output when the machines have the same size.

DFIG's stator and rotor have the same pole number, but BDFRG's secondary stator normally has a lower pole number than the primary stator. This structure makes the stator slot size of BDFRG far larger than the stator slots of the DFIG when BDFRG primary stator has the same pole number as DFIG stator. The slots of the BDFRG will be deep compared to DFIG's for the same width of stator tooth.

The yoke height of stator core is inversely proportional to the pole number. Hence the BDFRG has much greater stator core yoke height compared to the DFIG with the same pole number, as the flux of the control winding needs large yoke area to pass through.

The heights both of the slot and core yoke for the BDFRG are larger than DFIG's. The inner diameter of stator core for the BDFRG will be much smaller than the DFIG's. As a result, the power output of the BDFRG will be decreased due to the reduced rotor diameter for the same rotor speed in comparison with the DFIG.

Besides, the BDFRG has a symmetrical structure. If we 'see' this reluctance machine from one side of stator and neglected the other, it is quite similar to a switch reluctance machine. Thus this generator may be considered as superposition of two

switch reluctance machine. The BDFRG has more saturation and would cause the flux-path block and flux density limitation. The restricted flux strength limits the MMF and current increase. The current increase limitation requires larger volume to accommodate more magnetic flux and results in the higher inductance value to support the power level.

From above, it is explicit that the output power of the BDFRG will be much less than that of the DFIG in the same size. The BDFRG has larger volume and therefore is more expensive than DFIG in the same power level. This is a weakness of BDFGR compared to DFIG.

As the BDFRG normally produces less output than the DFIG of the same size, in order to design a BDFRG which has the same size and the same power compared to the existing DFIG, Prof. Wang, the collaborator in Shenyang University of Technology, designed the BDFRG used in this thesis with the flux barriers inserting into the rotor within reasonable cost. The details can be found in Section 2.3.1.2. This structure brings about larger flux density and more saturation in the BDFRG. The higher flux density will lead to the higher flux and cause the larger inductance in the same power level.

7.1.2. Inductance comparison

An idealised three phase AC machine has the constant inductance. However, the linking flux strength varies around the rotor surface in a saliency machine. This leads to the variations of the inductance values [17]. But, a poly-phase winding distribution is able to eliminate the saliency effect due to its multiple slots per phase and the narrow and identical airgap width. Even if the small, ripple-like deviations happen occasionally as the slots align and mis-align in, these ‘slot effects’ do not seriously impact. Inductance values, therefore, may ignore its variations with position and be considered as an approximate constant.

All wind turbine DFIGs are poly-phase induction machines. Typically, for the sake of maximum efficiency, DFIG is designed with a large number of slots and windings, and narrow smooth airgap [20]. Thus, DFIG has minimal saliency and it can be assumed that the machine inductances are independent of rotor position. This important conclusion provides us the support of considering the DFIG inductances as constant when viewed in a stator, rotor or synchronously-rotating reference frame.

But for a BDFRG, as it can be considered as the superposition of two switched reluctance machines, the BDFRG's inductances are quite like that of the switching reluctance machine. A switching reluctance machine's inductance determination has been demonstrated in Appendix A. The inductance peaks at the aligning rotor position and drops to lowest value at the un-aligning rotor position. The 'Inductance vs. rotor position' graph of the switched reluctance machine reveals the triangular wave if ignore the saturation effects.

The BDFRG's inductance changes following the position change of the rotational rotor. However, the superposition makes the machine flux density much higher even to the peak at the saturation. This leads to the smoother highest and lowest values in 'Inductance vs. rotor position' graph. Thus the BDFRG's 'Inductance vs. rotor position' graph looks like a sinusoidal waveform.

In addition, according to the conclusion in Section 7.1.1, either the larger size BDFRG in common or the same size design used in this thesis has the larger inductance than the DFIG which has the same power level.

In conclusion, it will be evidenced by the experimental results in Section 4.2.1 and Section 4.2.2 that the same size BDFRG has the sinusoidal inductance variations and far larger inductance than DFIG.

7.1.3. Inductance test comparison

DC resistance test can experiment the both stator and rotor resistances of DFIG. This test can be used to obtain BDFRG primary and secondary stator resistances value as well. But the inductance tests for DFIG and BDFRG are different.

DFIG's inductance can be obtained by using Locked rotor test, Synchronous speed test, as the DFIG is operated at a merely synchronous speed when the stator is applied with a rated symmetrical three-phase AC voltage source with the short-circuit rotor. But, the BDFRG would start asynchronously and operate like the same pole number induction machine, if the primary stator is supplied with an AC voltage source, and the secondary winding is short circuited [7]. Thus the Synchronous Speed Test, the way to obtain inductance value of the induction machine, is not suitable for the BDFRG.

For the BDFRG, if the secondary winding is open-circuited and the primary winding is supplied with symmetrical three-phase AC voltage, none current would flow through the secondary side windings. The primary stator inductance and mutual inductance can be obtained. Similarly, if taking account to exchange the position of the main stator and auxiliary stator and doing the same procedure as above test, the secondary stator inductance and mutual inductance can be got. Therefore, the self-inductance and mutual inductance of the BDFRG can be determined experimentally in standstill condition of the machine.

Section 4.2.1 and Section 4.2.2 give the examples that how the DFIG and BDFRG's parameters are tested.

7.1.4. Control performance comparison under vector control

According to the comparison of the experimental results of the vector control, BDFRG and DFIG have similar performance under the vector control. But there are some difference found:

①. BDFRG's controller speed is tardy compared to DFIG's. The inductance, as the factor of current-change-retardant, will block the current to catch up to the reference value. The larger inductance in BDFRG causes the delay of the BDFRG control speed and of course postpones the primary stator currents and active and reactive power steady states.

②. BDFRG's active and reactive powers display a coupling while DFIG's two powers present the decoupled performance. The reason of the BDFRG's active and reactive power coupling is its primary stator current maintains the magnitude for a while at the initial of which the controller starts to work. And the reason of this reservation may be because of the larger inductance. As we all know that the inductance is the factor to prevent the current changes. Thus the far larger inductance in BDFRG compared to DFIG will lead to the hold of the primary stator current changes, then cause the coupling of active and reactive power of BDFRG. On the contrary, DFIG's inductance is not big enough to persist the same amount of stator currents, therefore DFIG's active and reactive power exhibit a decoupling performance.

③. BDFRG produces more harmonics than DFIG. This is mainly because the salient reluctance rotor produces more harmonics. The variable inductance as discussed in Chapter 2 is partly the reason for the current harmonics and causes the more power ripples. What is more, the rotor structure design with one barrier in each pole will impact the harmonics as well.

Conclusively, the large inductance value will create the sluggishness of the transient current changes then result in the coupling performance of active and reactive power

and deceleration of control speed. Besides, the saliency rotor structure of BDFRG leads to the variations of machine inductance. Then the inserted-flux-barriers reluctance rotor and variable inductance will lead to more oscillation of generator output. Therefore, it can be found as the conclusion that the BDFRG is more difficult to be controlled with the classical vector control method compared to DFIG.

7.1.5. Vector control method and direct power control method comparison

Compared to the vector control, Direct Power Control has many advantages. It eliminates the need for rotor position sensing. It is thus an attractive sensorless control for drive as well as generator applications. Besides, the active power and reactive power calculations do not need the *d-q* components of each vector viewed in the excitation reference frame, and the excitation frame angle θ_e is not a necessity. The Phase Locked Loop scheme is therefore not required, which reduce the inconveniency compared to the vector control.

Comparing the direct power control to vector control method, DPC needs higher sampling frequency. In one sampling frequency, the modulation index generates from the vector control can cut the carriers, and leads to more switch states in each sampling frequency. But the DPC can only present one switch state per sampling frequency. Thus the DPC requires the far higher converter switching frequency than vector control method.

7.1.6. Control performance comparison under Direct Power Control

Based on the experiments, both BDFRG and DFIG cannot be controlled under DPC when the switching frequency is *5kHz*, and BDFRG can be controlled under *10kHz* but DFIG cannot. From these results, the switching frequency is the restriction of the DPC and the DPC can be considered to be more effectual when it is implemented in

BDFRG, especially under lower sampling frequency. The possible reason may be caused by the larger inductance. As section 6.1.4 explained, a band is selected in DPC to ‘tolerate’ the effects of machine harmonics and the power changes during one sampling frequency. Although BDFRG has more harmonics than DFIG, its power change in specific period is much smaller than DFIG as its current would be hold for a while due to the large inductance. But this conclusion is made for the machine used in this thesis. If this consequence wants to be promoted, more different rotor structure and different power level BDFRGs need to be examined and compared with the corresponding DFIG.

7.1.7. Fault response and fault ride through capability prediction and comparison

The larger inductance of BDFRG would restrict the level of fault current in prediction. Although the large fault currents would cause more saturation and lead to a reduction of the relevant inductance, the effect of BDFRG inductance decrease cannot offset the difference between DFIG and BDFRG because the BDFRG’s inductances are almost several times of DFIG’s. In prediction, the large inductance in BDFRG will cause the slower current increase or even less overcurrent compared to DFIG fault response. Overall, the BDFRG may have better fault current compared to the same power DFIG.

If adding a crowbar to BDFRG for protection purpose, the crowbar resistor value could be smaller because of the less overcurrent. But, because BDFRG are harder to be controlled than DFIG, the control scheme of the crowbar method needs to be considered carefully. According to a timer action crowbar control scheme described in Section 3.3.3, when the crowbar is released, rotor-side converter and the inner rotor current PI control are immediately resumed. Outer control loop is resumed after a

specified delay to allow the current controllers to settle. This delay would be longer in BDFRG than a DFIG's as BDFRG's controller speed is tardy compared to DFIG's.

Therefore, slow control speed is the restriction of BDFRG FRT implementation. If the controller difficulty could be overcome, BDFRG will have better fault response and fault ride through performance compared to DFIG.

This prediction has been proved in the simulation work in section 5.3.1 and section 5.3.2. From the results of the simulation, the conclusion below has been found:

① The BDFRG can withstand a longer fault duration than the DFIG.

② In the same time, the BDFRG would activate the crowbar less times compared to the DFIG.

③ Even the BDFRG can ride through the fault without the crowbar when the fault persists for a short period and the trigger current threshold is big.

In summary, the BDFRG has the higher tolerance of the fault and better performance of the crowbar method than the DFIG.

7.2. Suggestions for further work

From all the experimental and simulation results above, we may have a conclusion that the BDFRG may take place of the DFIG in the wind generation of the future due to its reasonable cost of manufacture, the similar healthy operation to the DFIG, the good controller response for both vector control and DPC, the higher fault tolerance and the better fault ride through ability compared to the DFIG. This conclusion is the main contribution of my PhD degree.

In the future, still many works can be done. For example:

① Direct Power Control experimental implementation for DFIG and BDFRG and their experimental results comparison

② FRT technologies experimental implementation for DFIG and BDFRG and comparison of the FRT experimental response for two generators

③ Comparing the different rotor structure BDFRGs' and DFIG from control response and FRT performance point of view

④ Direct Power Control experimental implementation for BDFIG

⑤ DFIG, BDFRG and BDFIG control response comparison under both classical vector control and DPC

⑥ DFIG, BDFRG and BDFIG FRT performance comparison

The last three works is hopefully to collaborate with Dr. Long Teng who has researched the comparison of DFIG and BDFIG in Cambridge University.

Reference

[1]. Yazhou Lei; Mullane, A.; Lightbody, G.; Yacamini, R.; “Modeling of the wind turbine with a doubly fed induction generator for grid integration studies”, Energy Conversion, IEEE Transaction on Volume 21, Issue 1, March 2006 Page(s):257 - 264 Digital Object Identifier 10.1109/TEC.2005.847958

[2]. R. David Richardson, and Gerald m. Mcnemey, "Wind Energy Systems", proceedings of the IEEE Vol.81, No. 3, March 1993.

[3]. World Wind Energy Association, "Worldwide wind energy boom in 2005: 58,982MW capacity installed", http://www.wwindea.org/default.html, 7 March 2006.

[4]. R. Grunbaun, P. Halvarsson, D. Larsson, P.R.Jones, “Conditioning of Power Grids Serving Offshore Wind Farms Based on Asynchronous Generators”, 2004 ABB power Technologies.

[5]. Muller, S.; Deicke, M.; De Doncker, R.W.; “Doubly fed induction generator systems for wind turbines”, Industry Applications Magazine, IEEE Volume 8, Issue 3, May-June 2002 Page(s):26 - 33 Digital Object Identifier 10.1109/2943.999610

[6]. Shuhui Li; Haskew, T.A.; “Analysis of Decoupled d-q Vector Control in DFIG Back-to-Back PWM Converter”, Power Engineering Society General Meeting, 2007. IEEE 24-28 June 2007 Page(s):1 - 7 Digital Object Identifier 10.1109/PES.2007.385461

[7]. Fengxiang Wang, Fengge Zhang, and Longya Xu, “Parameter and Performance Comparison of Doubly Fed Brushless Machine With Cage and Reluctance Rotors” IEEE TRANSACTIONS ON INDUSTRY APPLICATIONS, VOL. 38, NO. 5, SEPTEMBER/OCTOBER 2002

[8]. R.E.Betz and M.Jovanovic, “The Brushless Doubly Fed and the Synchronous Reluctance Machine – a comparison”, IEEE Transactions on Industry Applications, Vol. 36, No. 4, pp.1103-1110, July/Aug 2000.

[9]. E. M. Schulz and R. E. Betz, “Optimal torque per amp for brushless doubly fed reluctance machines,” in Proc. IEEE-IAS Annu. Meeting, Hong Kong, pp. 1749–1753, Oct. 2005.

[10]. R.Li, R.Spee, A.K.Wallace, G.C.Alexander, “Synchronous drive performance of brushless doubly-fed motors”, IEEE Transactions on Industry Applications, vol. 30, no. 4, 1994, pp. 963-970.

[11]. Pannell, Graham Steven. “Grid fault ride through for wind turbine doubly-fed induction generators” University of Newcastle upon Tyne.Theses. Eng. D. 2008.

[12]. WenJun Chen; Atkinson, David; Chaal, H.; Jovanovic, M., "Experimental and Simulation Comparison for Timer Action Crowbar of Doubly-Fed Induction Generator," Power and Energy Engineering Conference (APPEEC), 2011 Asia-Pacific , vol., no., pp.1,5, 25-28 March 2011 doi: 10.1109/APPEEC.2011.5748822

[13]. Chaal, H.; Jovanovic, M.; Atkinson, D.; Wenjun Chen, "A simple yet efficient doubly-fed drive/generator controller," Power Electronics and Applications (EPE 2011), Proceedings of the 2011-14th European Conference on , vol., no., pp.1,6, Aug. 30 2011-Sept. 1 2011

[14]. P. Vas, “Vector control of AC machines”: Oxford University Press, 1990

[15]. D.D. Li, “Analysis of Short-circuit Current of Wind Turbine – Doubly Fed Induction Generator”, 1st IEEE Conference on Industrial Electronics and Applications, 2006

[16]. P. Kundur, “Power System Stability and Control”: McGraw-Hill, 1994.

[17]. D. O’Kelly and S. Simmons, “Introduction to Generalized Electrical Machine Theory”: McGraw-Hill, 1968.

[18]. B. Rabelo, W. Hofmann, J.L. Silva, R.G. Oliveira and S.R. Silva, “Reactive Power Control in Doubly-Fed Induction Generators for Wind Turbines” Power Electronics Specialists Conference, 2008. PESC 2008. IEEE 15-19 June 2008 Page(s):106 - 112 Digital

[19]. Gonzalo Abad, Jesus Lopez, Miguel Rodrigues, Luis Marroyo, Grezegorz Iwanski, “Doubly Fed Induction Machine: Modeling and Control for Wind Energy Generation”, Hoboken, NJ: IEEE Press/Wiley, 2011

[20]. A. E. Fitzgerald, C Kingsley Jr., S. D. Umans, “Electric Machinery, 6 ed.”: McGraw-Hill, 2003

[21]. I. Boldea and S.A. Nasar, “Electric Machine Dynamics”: New York, Macmillan, 1986.

[22]. M.G. Say, “Alternating Current Machines, 5 ed.”: Longman Scientific and Technical, 1983.

[23]. P. Vas, “Sensorless Vector and Direct Torque Control”: Oxford University Press: Clarendon, 1998.

[24]. Lie Xu and Phillip Cartwright, “Direct Active and Reactive Power Control of DFIG FOR Wind Energy Generation,” IEEE Transactions ON Energy Conversion, Vol. 21, No. 3, Sept 2006, pp. 750-758.

[25]. Pena, R.; Clare, J.C.; Asher, G.M.; “Doubly fed induction generator using back-to-back PWM converters and its application to variable-speed wind-energy generation”, Electric Power Applications, IEE Proceedings -Volume 143, Issue 3, May 1996 Page(s):231 - 241

[26]. B. Hopfensperger, D. J. Atkinson “Performance Comparison of Traditional and Emerging Doubly-Fed Generator Topologies for Grid-Connected Wind Power Application”

[27]. B. Hopfensperger, “Fault-Ride-Through of Doubly-Fed Induction Generator”

[28]. Z. Liu, O.A. Mohammed, and S. Liu, “A Novel Direct Torque Control of Doubly-Fed Induction Generator Used for Variable Speed Wind Power Generation” Power Engineering Society General Meeting, 2007. IEEE
24-28 June 2007 Page(s):1 - 6 Digital Object Identifier 10.1109/PES.2007.386253

[29]. Rajib Datta and V. T. Ranganathan, “Variable-Speed Wind Power Generation Using Doubly-fed Wound Rotor Induction Machine—A Comparison With Alternative Schemes,” IEEE Transactions ON Energy Conversion, Vol. 17, No. 3, Sept 2002, pp. 414-421.

[30]. T. Burton, D. Sharpe, N. Jenkins, E. Bossanyi, “Wind Energy Handbook”: John Wiley & Sons, 2001.

[31]. B. Hopfensperger, D.J. Atkinson, “Doubly-fed a.c. machines: classification and comparison”

[32]. L. Xu and W. Cheng, “Torque and reactive power control of a doubly-fed induction machine by position sensorless scheme,” IEEE Trans. Ind. Appl., vol. 31, no. 3, pp. 636–641, May/Jun. 1995.

[33]. M. Godoy Simoes. Felix A. Farret, “Alternative Energy Systems, 2 Ed”: Boca Raton: CRC Press, 2008

[34]. Shuhui Li; Haskew, T.A.; Jackson, J.; “Power generation characteristic study of integrated DFIG and its frequency converter” Power and Energy Society General Meeting - Conversion and Delivery of Electrical Energy in the 21st Century, 2008 IEEE 20-24 July 2008 Page(s):1 - 9 Digital Object Identifier 10.1109/PES.2008.4596058

[35]. Feng Wu; Xiao-Ping Zhang; Godfrey, K.; Ping Ju; “Modeling and Control of Wind Turbine with Doubly Fed Induction Generator”; Power Systems Conference and Exposition, 2006. PSCE '06. 2006 IEEE PES Oct. 29 2006-Nov. 1 2006 Page(s):1404 – 1409 Digital Object Identifier 10.1109/PSCE.2006.296507

[36]. Kretschmann, J.; Wrede, H.; Mueller-Engelhardt, S.; Erlich, I.; “Enhanced Reduced Order Model of Wind Turbines with DFIG for Power System Stability Studies”; Power and Energy Conference, 2006. PECon '06. IEEE International 28-29 Nov. 2006 Page(s):303 - 311 Digital Object Identifier 10.1109/PECON.2006.346667

[37]. 谢桦；张德宏 “双馈风力发电机组最大风能捕获控制方法研究”

[38]. Rajib Datta, V. T. Ranganathan, “Direct Power Control of Grid-Connected Wound Rotor Induction Machine without Rotor Position” Power Electronics, IEEE Transactions on Volume 16, Issue 3, May 2001 Page(s):390 - 399 Digital Object Identifier 10.1109/63.923772

[39]. P.Tiitinen, P.Pohjalainen and J.Lalu, “The next generation motor control method: Direct Torque Control (DTC)”, EPE Journal, vol. 5, no. 1, pp. 14-18, 1995.

[40]. I.Takahashi, T.Noguchi, “A new quick-response and high-efficiency control strategy of an induction motor”, IEEE Transactions on Industry Applications, vol. IA-22, no. 5, pp. 820-827, 1986.

[41]. Dawei Zhi, Lie Xu, John Morrow, “Improved Direct Power Control of Doubly-Fed Induction Generator Based Wind Energy System” Electric Machines & Drives Conference, 2007. IEMDC '07. IEEE International Volume 1, 3-5 May 2007 Page(s):436 - 441 Digital Object Identifier 10.1109/IEMDC.2007.382707

[42]. R. Cárdenas, R. Peña, J. Proboste, G. Asher, and J. Clare, “MRAS observer for sensorless control of stand-alone doubly-fed induction generators,” IEEE Trans. Energy Conversion, vol. 20, no. 4, pp. 710–718, Dec. 2005.

[43]. Roberto Cárdenas, Rubén Peña, José Proboste, Greg Asher, and Jon Clare, “MRAS Observers for Sensorless Control of Doubly-Fed Induction Generators” Power Electronics, IEEE Transactions on Volume 23, Issue 3, May 2008 Page(s):1075 - 1084 Digital Object Identifier 10.1109/TPEL.2008.921189

[44]. M. Abolhassani, P. Niazi, H. Toliyat, and P. Enjeti, “A sensorless integrated doubly-fed electric alternator/active filter (IDEA) for variable speed wind energy system,” in Proc. 38th IAS Annu. Meeting, Oct. 2003, vol. 1, pp. 507–514.

[45]. R. Datta, V. T. Ranganathan, “A simple position-sensorless algorithm for rotor-side field-oriented control of wound-rotor induction machine,” IEEE Trans. Ind. Electron., vol. 48, no. 4, pp. 786–793, Aug. 2001

[46]. L. Morel, H. Godfroid, A. Mirzaian, and J. M. Kauffmann, “Double-fed induction machine: Converter optimization and field oriented control without position sensor,” Proc. Inst. Elect. Eng., vol. 145, no. 4, pp. 360–368, Jul. 1998.

[47]. B. Hopfensperger, D. J. Atkinson, and R. A. Lakin, “Stator-flux oriented control of a doubly-fed induction machine without position encoder,” Proc. Inst. Elect. Eng., vol. 147, no. 4, pp. 241–250, Jul. 2000.

[48]. U. Rädel, D. Navarro, G. Berger, and S. Berg, “Sensorless field-oriented control of a slipring induction generator for a 2.5MWwind power plant from Nordex Energy GMBH,” in Proc. Eur. Power Electron. Conf., Graz, Austria, 2001.

[49]. E. Bogalecka and Z. Krzeminski, “Sensorless control of a double-fed machine for wind power generators,” in Proc. Eur. Power Electron. Conf.-Power Electron., Machines Control, Dubrovnik and Cavtat, Slovenia, 2002.

[50]. S. Carmeli, F. C. Dezza, and R. Perini, “Double fed induction machine drive: Proposal of a speed sensorless control based on a MRAS,” in Proc. IEEE Int. Conf. Elect. Mach. Drives, May 2005, pp. 404–410.

[51]. O. A. Mohammed, Z. Liu, and S. Liu, “A novel sensorless control strategy of doubly fed induction motor and its examination with the physical modeling of machines,” IEEE Trans. Magnetics, vol. 41, no. 3, pp. 1852–1855, May 2005.

[52]. O. A. Mohammed, Z. Liu, and S. Liu, “A novel sensorless control strategy of doubly-fed induction machines,” in Proc. IEEE Int. Conf. Elect. Mach. Drives, May 2005, pp. 315–319.

[53]. Dawei Zhi, and Lie Xu, “Direct Power Control of DFIG With Constant Switching Frequency and Improved Transient Performance” Energy Conversion, IEEE Transaction on Volume 22, Issue 1, March 2007 Page(s):110 - 118 Digital Object Identifier 10.1109/TEC.2006.889549

[54]. G. S. Buja and M. P. Kazmierkowski, “Direct torque control of PWM inverter-fed AC motors—A survey,” IEEE Trans. Ind. Electron., vol. 51, no. 4, pp. 744–757, Aug. 2004.

[55]. M. P. Kazmierkowski and A. Kasprowicz, “Improved direct torque and flux vector control of PWM inverter-fed induction motor drives,” IEEE Trans. Ind. Electron., vol. 42, no. 4, pp. 344–350, Aug. 1995.

[56]. U. Baader, M. Depenbrock, and G. Gierse, “Direct self control (DSC) of inverter-fed induction machine—A basis for speed control without speed measurement,” IEEE Trans. Ind. Appl., vol. 28, no. 3, pp. 581–588, May–Jun. 1992

[57]. D. Casadei, G. Grandi, G. Serra, and A. Tani, “Effects of flux and torque hysteresis band amplitude in direct torque control of induction machines,” in Proc. 20th Int. Conf. Ind. Electron., Control Instrum., 1994, pp. 299– 304.

[58]. T. G. Habetler, F. Profumo, M. Pastorelli, and L. M. Tolbert, “Direct torque control of induction machines using space vector modulation,” IEEE Trans. Ind. Appl., vol. 28, no. 5, pp. 1045–1053, Sep. 1992.

[59]. Y. S. Lai and J. H. Chen, “A new approach to direct torque control of induction motor drives for constant inverter switching frequency and torque ripple reduction,” IEEE Trans. Energy Convers., vol. 16, no. 3, pp. 220– 227, Sep. 2001.

[60]. N. R. N. Idris and A. H. M. Yatim, “Direct torque control of induction machines with constant switching frequency and reduced torque ripple,” IEEE Trans. Ind. Electron., vol. 51, no. 4, pp. 758–767, Aug. 2004.

[61]. J. Kang and S. Sul, “New direct torque control of induction motor for minimum torque ripple and constant switching frequency,” IEEE Trans. Ind. Appl., vol. 35, no. 5, pp. 1076–1082, Sep./Oct. 1999.

[62]. K. P. Gokhale, D. W. Karraker, and S. J. Heikkila, "Controller for a wound rotor slip ring induction machine" US patent, 6448735B1, Jul.22, 2002.

[63]. Osama S. Ebrahim, Praveen K. Jain, Goel Nishith “New Direct Power Control for the Wind-Driven DFIG with Improved Performance” Telecommunications Energy Conference, 2007. INTELEC 2007. 29th International Sept. 30 2007-Oct. 4 2007 Page(s):550 - 556 Digital Object Identifier 10.1109/INTLEC.2007.4448840

[64]. Osama S. Ebrahim, Mohamed M. Negm and Mohamed Z. Youssef, “An Improved DTC scheme for The AC Drives Based on Optimal Preview Control Technique” ISIE2006, Jul. 2006.

[65]. Prof. Wang Presentation in Newcastle University

[66]. Prof. Wang ‘Design Report for BDFRG’

[67]. M.Jovanovic and R.E.Betz, “Control Strategies for Brushless Doubly Fed Reluctance Machines”, Transactions of IEE-J, Vol.121-D, No. 2, pp. 272-278, Feb 2001.

[68]. M.Jovanovic, R.E.Betz and J.Yu, “The use of doubly fed reluctance machines for large pumps and wind turbines”, IEEE Transactions on Industry Applications, Vol.38, No.6, pp. 1508-1516, Nov/Dec 2002.

[69]. L.Xu, L.Zhen, E.H.Kim, “Field-orientation control of a doubly-excited brushless reluctance machine”, IEEE Transactions on Industry Applications, vol. 34, no. 1, 1998, pp. 148-155.

[70]. L.Xu, Y.Tang, “A novel wind-power generating system using field orientation controlled doubly-excited brushless reluctance machine”, IEEE-IAS Annual Meeting, Houston, Texas, 1992, pp. 408-413.

[71]. Y.Liao, C.Sun, “A novel position sensorless control scheme for doubly fed reluctance motor drives”, IEEE Transaction on Industry Applications, vol. 30, no. 5, 1994, pp. 1210-1218.

[72]. M.Jovanovic, “Control of Brushless Doubly-Fed Reluctance Motors”, to appear in IEEE Transactions on Industrial Electronics (in press).

[73]. M.Jovanovic, J.Yu, E.Levi, “Encoder-less direct torque controller for limited speed range applications of brushless doublyfed reluctance motors”, IEEE Transactions on Industry Applications, Vol. 42, No. 3, 712-721, May/June 2006.

[74]. Chaal, Hamza; Jovanovic, M., "Direct Power Control of Brushless Doubly-Fed Reluctance Machines," Power Electronics, Machines and Drives (PEMD 2010), 5th IET International Conference on , vol., no., pp.1,6, 19-21 April 2010 doi: 10.1049/cp.2010.0148

[75]. Chaal, H.; Jovanovic, M., "Practical Implementation of Sensorless Torque and Reactive Power Control of Doubly Fed Machines," Industrial Electronics, IEEE Transactions on, vol.59, no.6, pp.2645,2653, June 2012 doi: 10.1109/TIE.2011.2161065

[76]. Chaal, H.; Jovanovic, M., "Toward a Generic Torque and Reactive Power Controller for Doubly Fed Machines," Power Electronics, IEEE Transactions on , vol.27, no.1, pp.113,121, Jan. 2012 doi: 10.1109/TPEL.2011.2160731

[77]. Chaal, H.; Jovanovic, M., "A new sensorless torque and reactive power controller for doubly-fed machines," Electrical Machines (ICEM), 2010 XIX International Conference on, vol., no., pp.1,6, 6-8 Sept. 2010 doi: 10.1109/ICELMACH.2010.5608111

[78]. CCTV1 News

[79]. ELTRA . Specifications for connecting wind farms to the transmission network[M]. Danmish, 2000

[80]. National grid electricity transmission Co.. The Grid Code Issue 3 Revision l3. 9th Jan. 20(I6. connection conditions 6. 3. 15

[81]. Dallachy J L, Tait I. "Guidance Note for the Connection of Wind Farms". Issue No. 2. 2. 2. SP Transmission and Distribution. Scottish Hydro-Electric. 2002

[82]. NIIR ANEN. "Voltage Ride Through of A Doubly Fed Generator Equipped With An Active Crow bar". EPE—PEM C Riga Latvia, 2004

[83]. MORREN J, DE HAAN S W H. "Ride Through of Wind Turbines With Doubly Fed Induction Generator During A Voltage Dip". IEEE Transactions on energy Conversion. 2005, 20(2): 435 441

[84]. T. Wildi, "Electrical Machines, Drives, and Power Systems: 4th Ed". Prentice Hall, 2000.

[85]. Y. Liao, L. Xu, and L. Zhen, "Design of a doubly fed reluctance motor for adjustable-speed drives," IEEE Trans. Ind. Applicat., vol. 32, pp. 1195–1203, Sept./Oct. 1996

[86]. W. Leonhard, "Control of Electric Drives, 3 Ed": Springer, 2001.

[87]. D. J. Atkinson, R. A. Lakin, and R. Jones, "A Vector-Controlled Doubly-Fed Induction Generator for a Variable-Speed Wind Turbine Application", IEEE Transactions of the Institute of Measurement and Control, vol. 19, 1997.

[88]. Paul. C. Krause, "Analysis of Electric Machinery": McGraw-Hill, 1986.

[89]. T. J. E. Miller, "Switched reluctance motors and their control", Hillsboro, OH: Magna Physics Pub. ; Oxford : Clarendon Press, 1993

[90]. R. Dorf, R. Bishop, Modern Control Systems, 9 Ed: Prentice Hall, 2001.

[91]. Rongxi Wang, Fei Lin, Ruixiang Hao, Xiaojie You, Trillion Q Zheng, "VSCF Doubly-Fed Induction Generator Control Strategy and Simulation Research" Industrial Electronics and Applications, 2008. ICIEA 2008. 3rd IEEE Conference on 3-5 June 2008 Page(s):2045 - 2050 Digital Object Identifier 10.1109/ICIEA.2008.4582880

[92]. Boldea, Tutelea L, Serban I, “Variable speed electric generators and their control：an emerging technology”. Journal of Electrical Engineering, 2002.(3): pp.60 ― 65.

[93]. B. Hopfensberger, Field Oriented Control of Single and Cascaded Doubly-Fed Induction Machines, PhD thesis, Department of Electrical and Electronic Engineering, Newcastle University, 1998.

[94]. Slemon, Gordon R, “Electric machines and drives”: Addison-Wesley, 1992

Appendices

A. Generalised Induction Machine Analysis

A.1. Reference frames and transformations

A.1.1. Reference frames

Consider a three-phase non-salient ac machine, with a symmetrical three-phase distribution of windings. The space vector is defined by:

$$\overrightarrow{V(t)} = V_a(t) + aV_b(t) + a^2V_c(t) \qquad (A.1)$$

Where

$$a = exp\left(-j\,{}^{2\pi}/_{3}\right) \qquad (A.2)$$

This applies to any instantaneous set of three-phase parameters, such as the voltages or currents. For the balanced winding, the instantaneous value is:

$$V_a + V_b + V_c = 0 \qquad (A.3)$$

A space vector in the radial machine plane can be defined against any set of orthogonal d-q axes. Particular axes have defined relationships with the machine, and are known as ‘reference frames’. Each vector parameter will appear to possess a different phase and relative velocity when ‘seen’ from different reference frames. Three common choices of reference frame are:

- A stationary reference frame, fixed against the stator windings: the ‘stator frame’

- A reference frame pinned to the space vector of supply voltage and hence rotating at system frequency with respect to the stationary reference frame: the ‘excitation frame’

• A reference frame pinned to the rotor windings (allowing for multiple magnetic poles), rotating at rotor speed (per pole-pair) with respect to the stationary reference frame: the ‘rotor frame’

A complete list of reference frames used in this work can be found in the glossary. An example of changing reference frames is shown in Figure A.1, where the stator current is given angle ξ with respect to the stator reference frame.

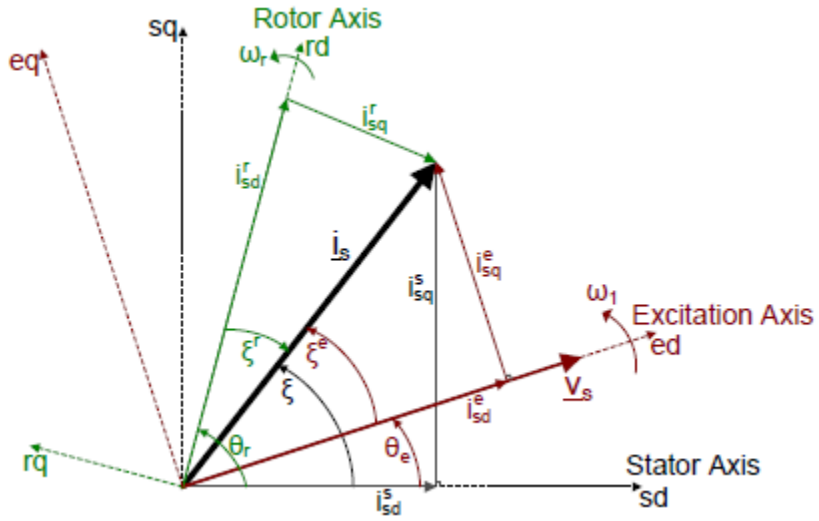

Figure A.1 Space vector of stator current in various reference frames

The stator current space vector appears with a different phase angle when viewed in each of the aforementioned reference frames. It may be seen to rotate at 50Hz in the stationary frame, appear pseudo-stationary in the excitation frame, and to rotate at slip frequency when viewed from the rotor frame.

$$\overrightarrow{i_s^s}(t) = |i_s| \exp(j\xi) = i_{sd}^s + j i_{sq}^s \qquad (A.4)$$

$$\overrightarrow{i_s^e}(t) = |i_s| \exp(j\xi^e) = |i_s| \exp(j\{\xi - \theta_e\}) = i_{sd}^e + j i_{sq}^e \qquad (A.5)$$

$$\overrightarrow{i_s^r}(t) = |i_s| \exp(j\xi^r) = |i_s| \exp(j\{\xi - \theta_r\}) = i_{sd}^r + j i_{sq}^r \qquad (A.6)$$

The d-q components are all scalar quantities by definition. The vector operator j is used to position the quadrature-axis components with respect to the direct-axis components.

A.1.2. Reference frame transformation

How does the reference frame transfers from one to the other? Figure A.2 gives the answer.

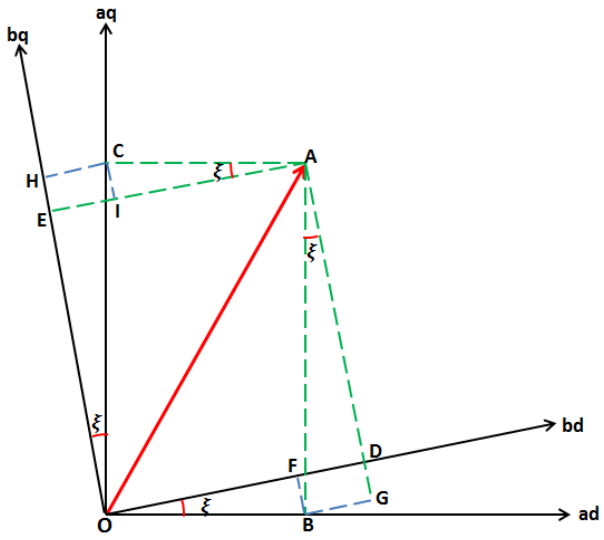

Figure A.2 The transformation of space vector in two reference frames

In the graph, OA represents a generalized space vector. For the convenient purpose, the current is taken as the example. Thus,

$$|\vec{\imath}| = OA \tag{A.7}$$

There are '*a*' and '*b*' two reference frames with their d and q axis named '*ad*', '*aq*' and '*bd*', '*bq*'. It can be clearly seen in the graphs that:

$$i_d^a = OB = AC \tag{A.8}$$

$$i_q^a = OC = AB \tag{A.9}$$

$$i_d^b = OD \tag{A.10}$$

$$i_q^b = OE \tag{A.11}$$

ξ is the angle between two reference frame. According to the parallel principle, we will have

$$\angle CAE = \angle BAD = \xi \tag{A.12}$$

Then the following relationship can be obtained:

$$OF = OB * \cos\xi = i_d^a * \cos\xi \tag{A.13}$$

$$FD = BD = AB * \sin\xi = OC * \sin\xi = i_q^a * \sin\xi \tag{A.14}$$

$$OH = OC * \cos\xi = i_q^a * \cos\xi \tag{A.15}$$

$$HE = CI = AC * \sin\xi = OB * \sin\xi = i_d^a * \sin\xi \tag{A.16}$$

Thus, the d-q components viewed by 'b' reference frame are:

$$i_d^b = OD = OF + FD = i_d^a * \cos\xi + i_q^a * \sin\xi \tag{A.17}$$

$$i_q^b = OE = OH - HE = i_q^a * \cos\xi - i_d^a * \sin\xi \tag{A.18}$$

Write the transformation equations to matrix:

$$\begin{bmatrix} i_d^b \\ i_q^b \end{bmatrix} = \begin{bmatrix} \cos\xi & \sin\xi \\ -\sin\xi & \cos\xi \end{bmatrix} \begin{bmatrix} i_d^a \\ i_q^a \end{bmatrix} \tag{A.19}$$

Similarly, the inverse transformation is:

$$\begin{bmatrix} i_d^a \\ i_q^a \end{bmatrix} = \begin{bmatrix} \cos\xi & -\sin\xi \\ \sin\xi & \cos\xi \end{bmatrix} \begin{bmatrix} i_d^b \\ i_q^b \end{bmatrix} \tag{A.20}$$

A.2. Generalised induction machine

A.2.1. Magnetic field distribution

To simplify the analysis, an idealised three-phase machine is considered. Stator and rotor consist of two concentric cylinders separated by a small uniform airgap with a symmetrical circumference, as demonstrated in Figure A.3Figu. Saliency effects will be discussed in later part.

As shown in the graph, the machine coils lie parallel along with the cylinder. r, h and l represent the rotor radius, airgap length and the cylinder length respectively. In the idea machine, the cylinder is long enough, such that the end effects may be negligible. The magnetic saturation is not considered as description in the above section.

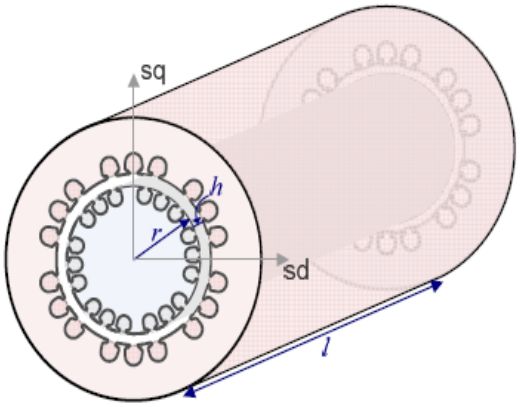

Figure A.3 Simplified stator and rotor

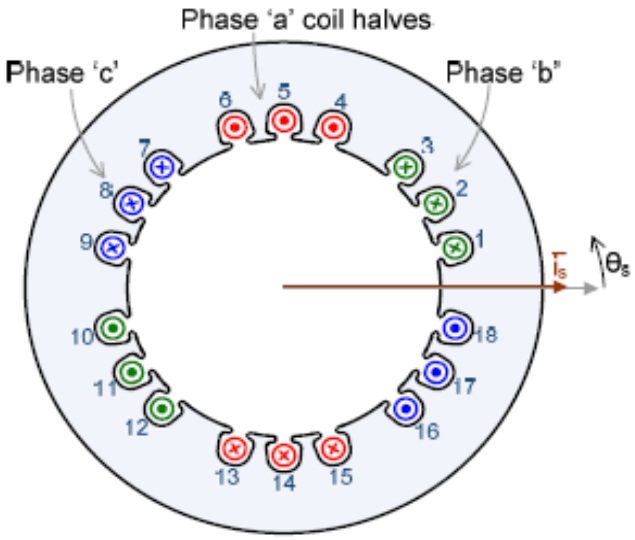

Figure A.4 Example of the cross section of the machine at a single moment

Taking account of the cross section of the machine at a single moment, the machine stator windings produce an approximately sinusoidal MMF around airgap when supplied with three balanced currents.[18][88] (Figure A.4 and Figure A.5)

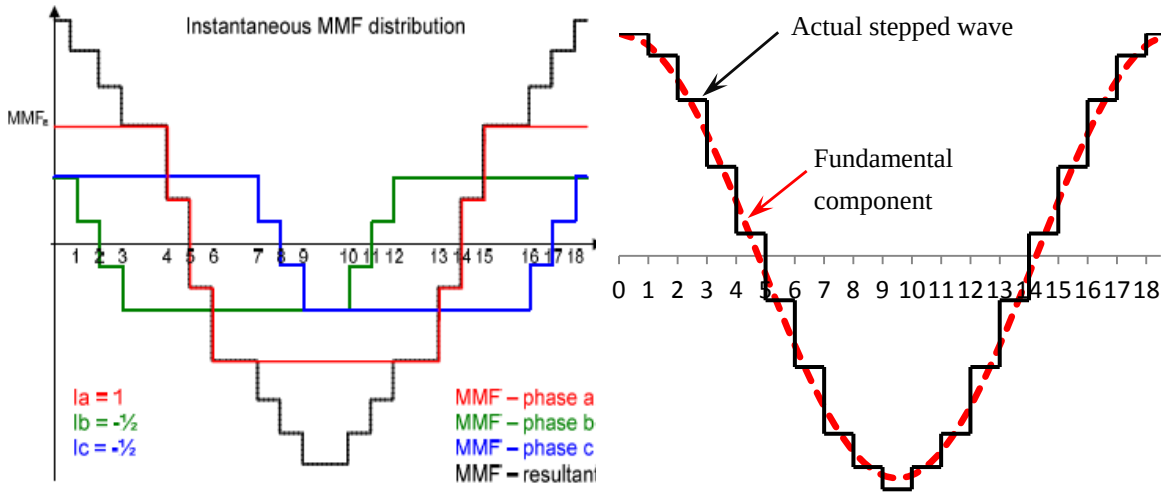

Figure A.5 (left) Example of stator MMF distribution based (right) Magnetomotive force for the left total MMF

The current of each phase contributes a stepped wave to MMF distribution. The three MMF of each phase add together to produce the total MMF shown as black polyline in

Figure A.5 left graph. Even in this very simple winding, the approximation to a sine wave is reasonably good as illustrated in the right picture of Figure A.5. The sinusoidal quality of MMF depends upon the number and geometric distribution of the windings. Thus with the larger number of slots that occur in most machines, the sine form can be more closely approximated, smooth and symmetrical [88].

The space vector of stator MMF is defined as the instantaneous peak of the resultant stator MMF distribution. According to the discussion above, the stator MMF space vector can be derived from: the actual number of coils of each stator phase winding, $N_{s,\ actual}$, the carrying stator current space vector, $\overrightarrow{\iota_s}$, and a coefficient describing the geometric distribution, $k(\theta_s)$:

$$\overrightarrow{\Theta_s} = k(\theta_s) N_{s,\ actual} \overrightarrow{\iota_s} \qquad (A.21)$$

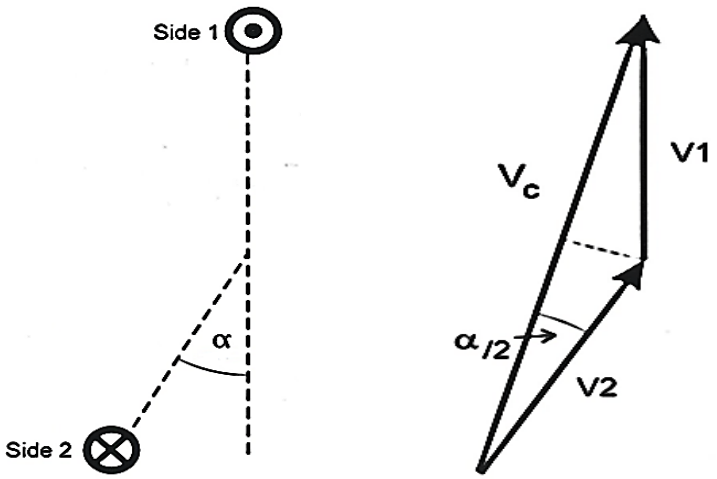

Figure A.6 (left) Short pitch coil (right) induced voltage pitch effect diagram

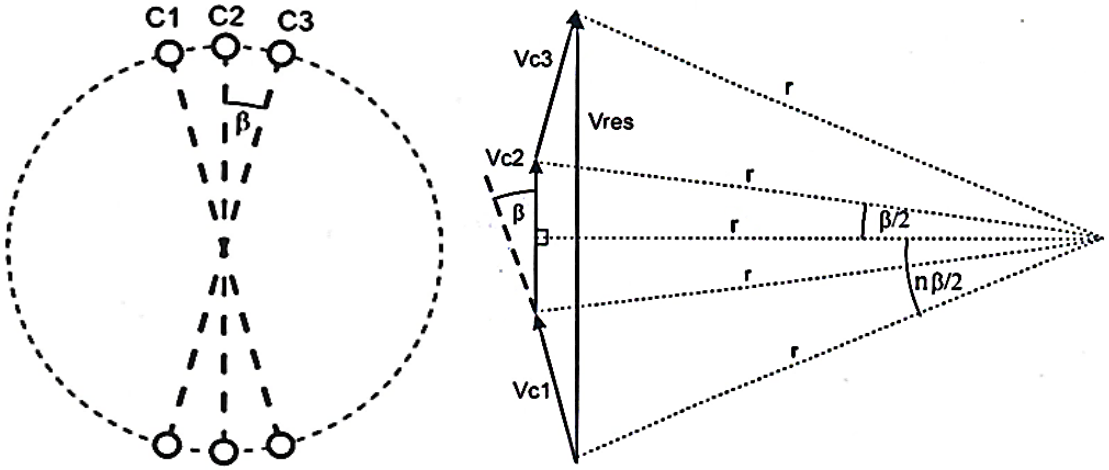

Figure A.7 (left) distributed coils (right) induced voltage distribution effect diagram

For a non-salient machine, the coefficient $k(\theta_s)$ remains constant around the airgap. An effective coil number which includes pitch and distribution factors is therefore generally instead of the actual coil number:

$$N_s = N_{s,\ effective} = k(\theta_s) N_{s,\ actual} \qquad (A.22)$$

Hence, the MMF expression can be shortened as:

$$\overrightarrow{\Theta_s} = N_s \overrightarrow{\iota_s} \qquad (A.23)$$

It is important to recognize that if the three phase currents are sinusoidal in time, the MMF will travel across the airgap and ‘leak’ to the rotor circumference. The locus of the stator MMF space vector will form a circle, as it rotates with the stator current space vector.

Similarly, a rotor MMF space vector may be provided with respect to the instantaneous peak of the rotor MMF distribution. Imitate the stator MMF equation, use the rotor current and effective turns’ number of rotor coils to replace the stator current and the effective stator turns, the rotor MMF is possible to be expressed by:

$$\overrightarrow{\Theta_r} = N_r \overrightarrow{\iota_r} \qquad (A.24)$$

The MMF plays a role of the source of a sinusoidal distributed magnetic flux across the airgap of the machine. Taking account of the stator flux, the reluctance and area of the airgap flux path, the magnetic flux flows with the flux density:

$$\overrightarrow{B_s} = \frac{1}{A}\frac{\overrightarrow{\Theta_s}}{\Re} \qquad (A.25)$$

Given the high relative permeability of iron, the magnetic reluctance path is dominated by the airgap, width h. Hence the stator magnetic field, neglecting saturation, is inversely proportional the airgap length:

$$\overrightarrow{B_s} = \frac{\mu_0 N_s}{2h}\overrightarrow{\imath_s} \qquad (A.26)$$

In order to simplify the analysis, the magnetic field around the airgap illustrated in Figure A.8-Figure A.10 is generated by a single coil on each of the stator and rotor. Left graphs describe the cross -section how the flux flows around the periphery of a symmetrical two-pole AC machine, while right sinusoidal wave is the stator and rotor self- or mutual- magnetic field.

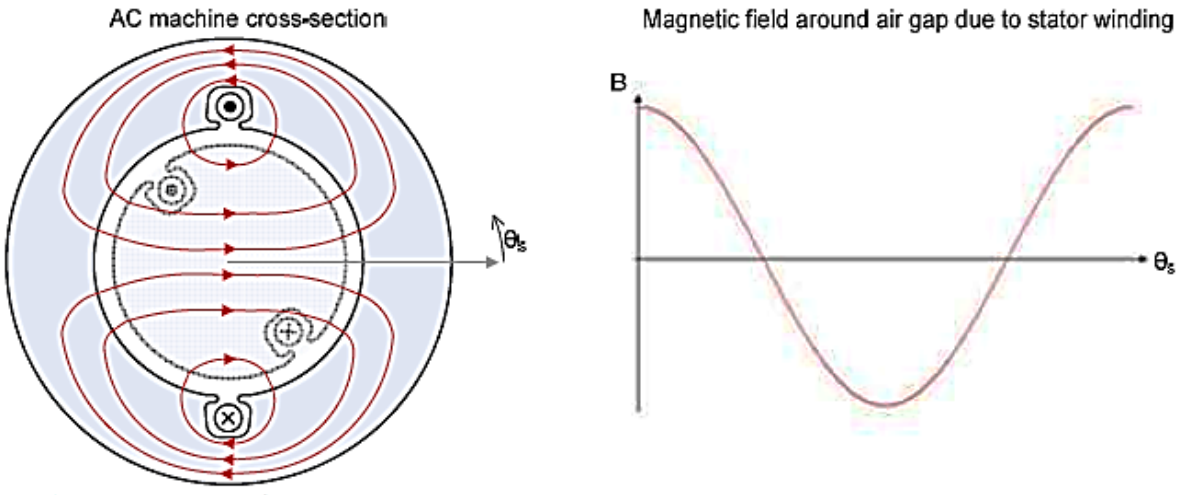

Figure A.8 (left) Stator contribution to magnetic flux around the circumference of a symmetrical two-pole AC machine cross-section (right) magnetic field around airgap due to the stator winding

Figure A.8 demonstrates the direction and relative strength of the stator component of magnetic field around the airgap of an idealised two-pole machine with one stator coil acting. A sinusoidal magnetic flux density is produced by this action as shown in right side.

A similar magnetic field is produced by the rotor circuit MMF, shown by Equation A.27 and Figure A.9. The rotor current pass through the single rotor coil induces the rotor MMF with the flux path shown in left graph and the flux density wave displayed in the right.

$$\overrightarrow{B_r} = \frac{\mu_0 N_r}{2h}\overrightarrow{\iota_r} \qquad (A.27)$$

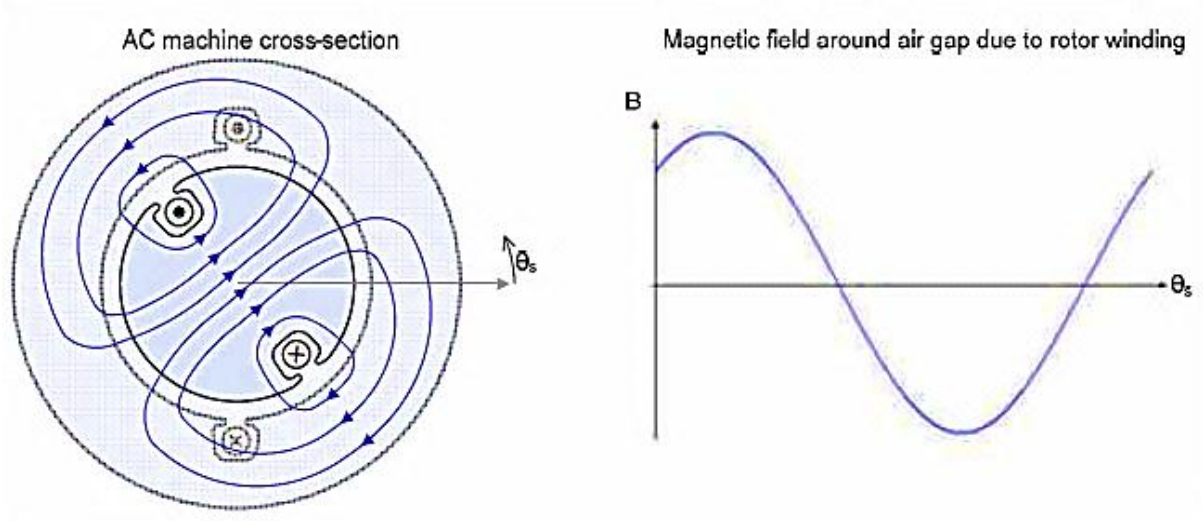

Figure A.9 (left) Rotor flux distribution of a symmetrical two-pole AC machine cross-section (right) magnetic field around airgap due to the rotor winding

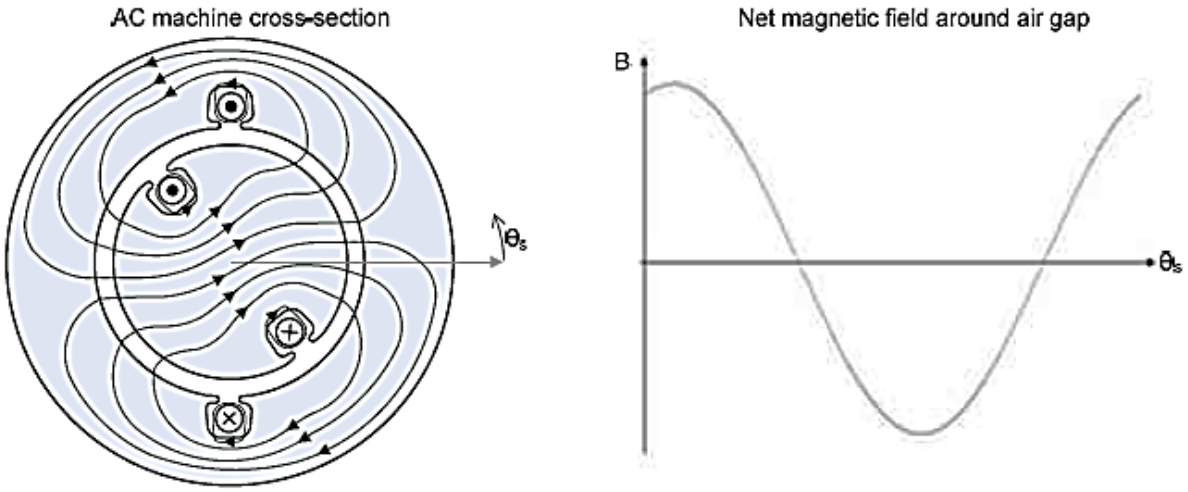

Figure A.10 (left) Net flux for an arbitrarily aligned position of a symmetrical two-pole AC machine cross-section (right) net magnetic field around airgap

The resultant flux distribution is an approximately linear combination of the both stator and rotor self-magnetic fields (Figure A.10). In the left graph, it is possible to find two kinds of flux paths. One threads stator or rotor only called ‘leakage’ flux path, the other crosses over both stator and rotor named ‘mutual’ flux path. It is significant to pay attention to that both the leakage and mutual flux paths comprise the net magnetic flux linkage.

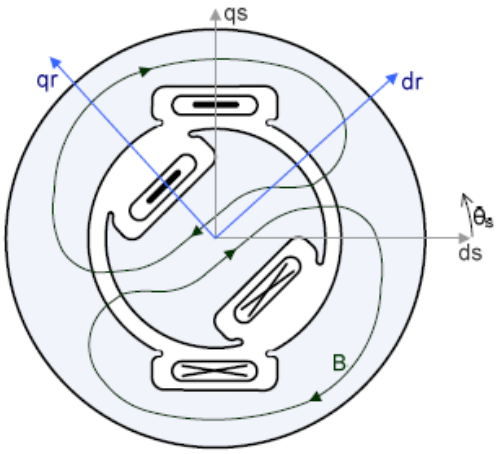

Figure A.11 Salient rotor-pole machine example.

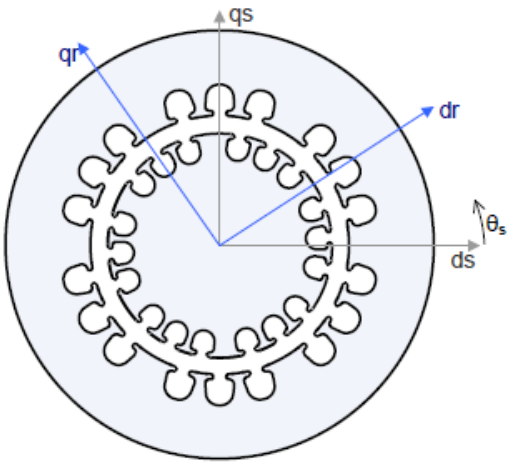

Figure A.12 Low-saliency machine.

In a salient wound rotor machine, the capability of linking flux varies around the rotor surface. The magnetic flux path reluctance $\Re$ is dominated by the effective airgap, which may lengthen across large or deep winding slots. As a result inductance values will vary with rotor alignment [17]. It will be discussed in later section.

A salient wound rotor machine cross-section example is illustrated in Figure A.11. In the graph, it is obvious that there is far less iron in the qr-axis path. The less iron compared to dr-axis will cause a far greater magnetic reluctance in the qr-axis path, and result in that the flux linkage along the flux path parallel to the qr-axis will be far less than the linkage parallel to the dr-axis.

For a polyphase winding distribution, with multiple slots per phase and a small, consistent airgap width, the aggregate effect of saliency is diminished, as can be seen from Figure A.12.

A.2.2. Torque generation

In an electrical machine, the misalignment between the stator and rotor rotating magnetic field encourages the torque generation. In a generator, the rotor field is effectively dragged ahead of the stator field by the mechanical input toque.

For a multi-pole machine, the multiple concentric dipoles can be divided by several pole pairs. The effects of the pole pairs can be considered as linear with omitting the saturation. It indicates that the influence of each pole pair can be superimposed. Hence, a single pair of poles can be considered instead of the multi-pairs then scale the results of the multi-poles. A single pole pair stator and rotor behave like two magnetic dipoles. The electromagnetic torque would depend on the strength of each field and separating phase sinusoidal wave. The books [23] and [86] document the derivations of the torque production.

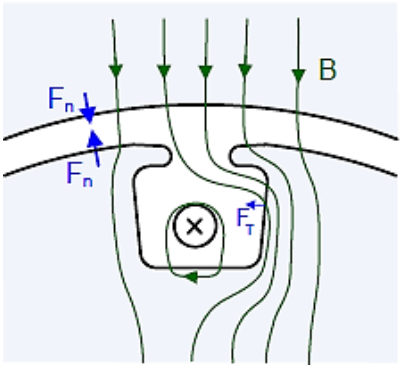

Figure A.13 Flux path near a rotor slot

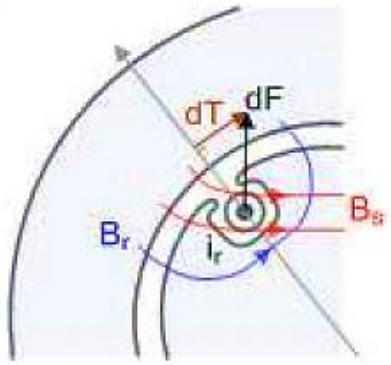

Figure A.14 Force elemet on a rotor conductor

Figure A. 13 illustrates the flux path near a rotor slots. It can be seen that largely radial flux flows across the airgap, and then is replaced by the leakage fields around the conductor in the slots. A strong alignment force F_n is produced to the rotor surface because of the radial flux, and does not force to the rotation. The skew flux at

the fringe fields brings a much smaller force F_T. This force is the tangency of the rotor surface at the slot edges and will generate the torque.

With assuming to place the rotor current artificially into an undisturbed stator magnetic field (or vice versa), the torque can be computed [20]. Figure A.14 demonstrates the force element on a single rotor conductor due to the stator field.

Applying the Lorentz Force Law to a line current in a magnetic field, the rotor current conductor experiences a force in the radial plane. For a current carrying element of length dl:

$$\overrightarrow{dF} = i_r \overrightarrow{dl} \times \overrightarrow{B_s} \qquad (A.28)$$

The magnetic field is perpendicular to the axial direction current element, hence:

$$dF = i_r dl \left|\overrightarrow{B_s}\right| \qquad (A.29)$$

A torque element is generated by the component of the force perpendicular to the radius, r, where θ is the angle between the stator field and rotor field.

$$dT = i_r dl \left|\overrightarrow{B_s}\right| r sin\theta \qquad (A.30)$$

This describes the torque for the single slots condition. Because of the linear characteristic of the pole pair effects, the total torque produced by all rotor conductors with p_A pole pairs is expressed below:

$$T = 2lrp_A \sum_{i=1}^{N_r} i_r \left|\overrightarrow{B_s}\right|_i sin\theta_i \qquad (A.31)$$

The rotor field is driven by the rotor MMF, and sinusoidally distributed around the airgap. The rotor current space vector places in the rotor field and similar to the rotor,

every stator field element keeps separating the phase from the rotor field. Thus the torque can be simplified as:

$$T = 2lrp_A \sum_{i=1}^{N_r} i_r \left|\overrightarrow{B_s}\right|_i sin\theta_i = (2N_r lrp_A)\overrightarrow{\imath_r} \Lambda \overrightarrow{B_s} \qquad (A.32)$$

Substituting the stator field flux density $\overrightarrow{B_s} = \frac{\mu_0 N_s}{2h}\overrightarrow{\imath_s}$:

$$T = p_A \left(\frac{N_s N_r lr\mu_0}{h}\right) \overrightarrow{\imath_r} \Lambda \overrightarrow{\imath_s} \qquad (A.33)$$

It is interesting that the bracketed coefficient in this torque equation is as the same as the definition of the mutual inductance of the machine, L_m. Hence, the torque equation can be shortened as:

$$T = p_A L_m \overrightarrow{\imath_r} \Lambda \overrightarrow{\imath_s} \qquad (A.34)$$

Where the cross product can be defined as $\overrightarrow{\imath_r} \Lambda \overrightarrow{\imath_s} = |\overrightarrow{\imath_r}||\overrightarrow{\imath_s}| \sin(\theta_s - \theta_r) = i_{rd} i_{sq} - i_{rq} i_{sd}$. Thus the influence factor of the cross product is the magnitude of both vectors and the sine of angle between them.

According to the torque equation $A.34$ and cross product determination, it is clear that the stator and rotor current space vector magnitude and the direction will affect the torque value. If the stator field position is aligned with the rotor field, the net force around the airgap is cancelled, which cause the zero torque. On the contrary, the torque is maximised while the rotor field is perpendicular to the stator field.

The per-pole-pair torque also can be derived by replacing the mutual inductance with the mutual flux linkage. Taking into account of the orthogonal nature of the vector cross product, we may have

$$T = \overrightarrow{\varphi_m} \Lambda \overrightarrow{\imath_s} = \overrightarrow{\imath_r} \Lambda \overrightarrow{\varphi_m} \qquad (A.35)$$

This expression shows that the torque is possible to be represented by the mutual flux linkage across the airgap and either stator or rotor current space vector. The stator and rotor currents are independent and impacted by the exclusive current experienced the mutual airgap flux.

A.2.3. Voltage equations

For the stator and rotor voltages, it is better to analyse them separately in different reference frame as the voltage can effectively find its own windings in its own frame. Thus the voltage applied to the stator windings in the stationary frame, only consist of two parts: one is the resistive drop of the stator current and the other is the back emf induced by the stator flux. Similarly, the rotor voltage has the same components under the rotor reference frame. The voltage equations are given below:

$$\overrightarrow{u_s^s} = R_s\overrightarrow{\imath_s^s} + \frac{d\overrightarrow{\varphi_s^s}}{dt} \qquad (A.36)$$

$$\overrightarrow{u_r^r} = R_r\overrightarrow{\imath_r^r} + \frac{d\overrightarrow{\varphi_r^r}}{dt} \qquad (A.37)$$

The stator voltage and rotor voltage viewed in themselves reference frame are not symmetrical rotation. Either the stator voltage viewed in the rotor frame or the rotor voltage referred to the stator reference frame, a rotational emf component would be included according to the Faraday's Law.

$$\overrightarrow{u_s^r} = R_s\overrightarrow{\imath_s^r} + \frac{d\overrightarrow{\varphi_s^r}}{dt} + j\omega_r\overrightarrow{\varphi_s^r} \qquad (A.38)$$

$$\overrightarrow{u_r^s} = R_r\overrightarrow{\imath_r^s} + \frac{d\overrightarrow{\varphi_r^s}}{dt} - j\omega_r\overrightarrow{\varphi_r^s} \qquad (A.39)$$

From the equation $A.38$ and $A.39$, it can be found that if the voltage is viewed in the reference frame rotating with respect to either circuit, in order to maintain the flux

linkage, a rotating voltage must be pursued (stator voltage viewed in rotor reference frame) or offset (opposite condition) by a rotor frequency flux linkage element.

Similarly, the voltages referred to the excitation reference frame are shown as follows:

$$\overrightarrow{u_s^e} = R_s\overrightarrow{\imath_s^e} + \frac{d\overrightarrow{\varphi_s^e}}{dt} + j\omega_e\overrightarrow{\varphi_s^e} \qquad (A.40)$$

$$\overrightarrow{u_r^e} = R_r\overrightarrow{\imath_r^e} + \frac{d\overrightarrow{\varphi_r^e}}{dt} + j\omega_{slip}\overrightarrow{\varphi_r^e} \qquad (A.41)$$

Explicitly, the voltage in any reference frame must include an emf dependent upon the relative motion of the reference frame while the rotational emf is not apparent only in the stationary frame with respect to the coil.

A.2.4. Generalised machine equations

Taking into account of the description above, a symmetric poly-phase induction machine may be described by the voltage and flux equations of both the stator and rotor adding the torque equation. They are (viewed in the excitation reference frame):

$$\overrightarrow{u_s^e} = R_s\overrightarrow{\imath_s^e} + \frac{d\overrightarrow{\varphi_s^e}}{dt} + j\omega_e\overrightarrow{\varphi_s^e} \qquad (> A.40)$$

$$\overrightarrow{u_r^e} = R_r\overrightarrow{\imath_r^e} + \frac{d\overrightarrow{\varphi_r^e}}{dt} + j\omega_{slip}\overrightarrow{\varphi_r^e} \qquad (> A.41)$$

$$\overrightarrow{\varphi_s^e} = L_s\overrightarrow{\imath_s^e} + L_m\overrightarrow{\imath_r^e} \qquad (A.42)$$

$$\overrightarrow{\varphi_r^e} = L_r\overrightarrow{\imath_r^e} + L_m\overrightarrow{\imath_s^e} \qquad (A.43)$$

$$T = p_A L_m\overrightarrow{\imath_r}\Lambda\overrightarrow{\imath_s} \qquad (> A.34)$$

These five equations can be used to simulate a ‘fifth order’ mathematical machine model and remain valid in transient situation [23]. Thus, they are named ‘generalised machine equation’ and applied widely in the electrical modelling of induction machine [86].

A.2.5. Transient timescales

Dynamic electromagnetic phenomena of electric machines with a constant rotor speed are governed by the transient timescales. Essentially, the transient time coefficient helps to describe the change rate of magnetic flux linkage in a given circuit. The book [17] and [21] demonstrates the derivation progress details, and will be simple introduced in following content.

First of all, the induction machine is considered with a short circuit of the rotor, then the rotor voltage equation changes as:

$$0 = R_r\overrightarrow{\imath_r^s} + \frac{d\overrightarrow{\varphi_r^s}}{dt} - j\omega_r\overrightarrow{\varphi_r^s} \qquad (A.44)$$

Substituting for the stator flux linkage $\overrightarrow{\varphi_r^s} = L_r\overrightarrow{\imath_r^s} + L_m\overrightarrow{\imath_s^s}$, the rotor voltage would be represented by:

$$0 = R_r\overrightarrow{\imath_r^s} + \frac{d\left(L_r\overrightarrow{\imath_r^s} + L_m\overrightarrow{\imath_s^s}\right)}{dt} - j\omega_r\left(L_r\overrightarrow{\imath_r^s} + L_m\overrightarrow{\imath_s^s}\right) \qquad (A.45)$$

$$0 = \left(R_r + L_r\frac{d}{dt} - j\omega_r L_r\right)\overrightarrow{\imath_r^s} + \left(L_m\frac{d}{dt} - j\omega_r L_m\right)\overrightarrow{\imath_s^s} \qquad (A.46)$$

Thus, the rotor current can be inferred:

$$\overrightarrow{\imath_r^s} = -\frac{L_m\left(\frac{d}{dt} - j\omega_r\right)}{\left(R_r + L_r\left(\frac{d}{dt} - j\omega_r\right)\right)}\overrightarrow{\imath_s^s} \qquad (A.47)$$

Substituting the rotor current expression to the stator flux equation $\overrightarrow{\varphi_s^s} = L_s\overrightarrow{\imath_s^s} + L_m\overrightarrow{\imath_r^s}$, we will have a new stator flux representation:

$$\overrightarrow{\varphi_s^s} = \overrightarrow{\imath_s^s}\left(L_s - \frac{L_m^2\left(\frac{d}{dt} - j\omega_r\right)}{\left(R_r + L_r\left(\frac{d}{dt} - j\omega_r\right)\right)}\right) \quad (A.48)$$

$$\overrightarrow{\varphi_s^s} = \overrightarrow{\imath_s^s}L_s\left(1 - \frac{L_m^2\left(\frac{d}{dt} - j\omega_r\right)}{\left(R_rL_s + L_rL_s\left(\frac{d}{dt} - j\omega_r\right)\right)}\right) \quad (A.49)$$

Define an operational inductance, L_s':

$$L_s' = L_s\left(1 - \frac{L_m^2\left(\frac{d}{dt} - j\omega_r\right)}{\left(R_rL_s + L_rL_s\left(\frac{d}{dt} - j\omega_r\right)\right)}\right) \quad (A.50)$$

Therefore the stator flux is re-arranged as:

$$\overrightarrow{\varphi_s^s} = \overrightarrow{\imath_s^s}L_s' \quad (A.51)$$

A timescale for the electromagnetic dynamic phenomena of machine stator can be defined as

$$\tau_{IM,stator} = \frac{L_s'}{R_s} \quad (A.52)$$

The transient operational inductance at the initial time can be derived by the limit;

$$L_{s,actual}' = \lim_{\frac{d}{dt}\to\infty} L_s' = \lim_{\frac{d}{dt}\to\infty} L_s\left(1 - \frac{L_m^2\left(\frac{d}{dt} - j\omega_r\right)}{\left(R_rL_s + L_rL_s\left(\frac{d}{dt} - j\omega_r\right)\right)}\right) = L_s\left(1 - \frac{L_m^2}{L_rL_s}\right) \quad (A.53)$$

The bracketed coefficient is as same as the leakage constant equation:

$$\sigma = 1 - \frac{L_m^2}{L_r L_s} \qquad (A.54)$$

Using the leakage constant to displace the bracketed expression, the actual transient stator inductance is:

$$L'_{s,actual} = \sigma L_s \qquad (A.55)$$

Thus the single dominate timescale for the stator circuit electrical response is represented by:

$$\tau_s = \frac{\sigma L_s}{R_s} \qquad (A.56)$$

Similarly, the transient time constant for the rotor circuit can be inferred by the same progress by short-circuited the stator and stated by

$$\tau_r = \frac{\sigma L_r}{R_r} \qquad (A.57)$$

Generally, if we use the per-unit parameters in a symmetrical wound-rotor induction machine, the inductance and resistance values on its stator and rotor circuits may be quite close. As a result, the transient timescale will be similar.

A.3. Reluctance Machine Principles

From the BDFRG windings picture, clearly, the machine looks like a symmetrical structure. If we ‘see’ this reluctance machine from one side of stator and neglected the other, it is quite similar to a switch reluctance machine. Thus this generator may be considered as superposition of two switch reluctance machine. The parameter test will use this characteristic in Chapter 4. For simplification purpose, the switch reluctance machine is analysed firstly in this section and the name is shorted for SRM.

A.3.1. Induction variation of SRM

Superficially, the switch reluctance machine may be the most uncomplicated of all drives. Lack of windings or magnets on the rotor makes the basic machine simple and all torque is ‘reluctance’ torque.

Figure A.15 shows a typical cross section of it with six stator poles and four rotor teeth, known as 6/4 SRM. Both the stator and the rotor are laminated and each stator tooth has a winding wound round it as illustrated in right graph of Figure A.15. Coils round opposite teeth are connected to form the N and S pole pair for one ‘phase’. The 6/4 machine can therefore be seen to be three phase. Many other combinations of the stator poles, rotor poles and phase number also exist. But a 6/4 motor is taken as an example.

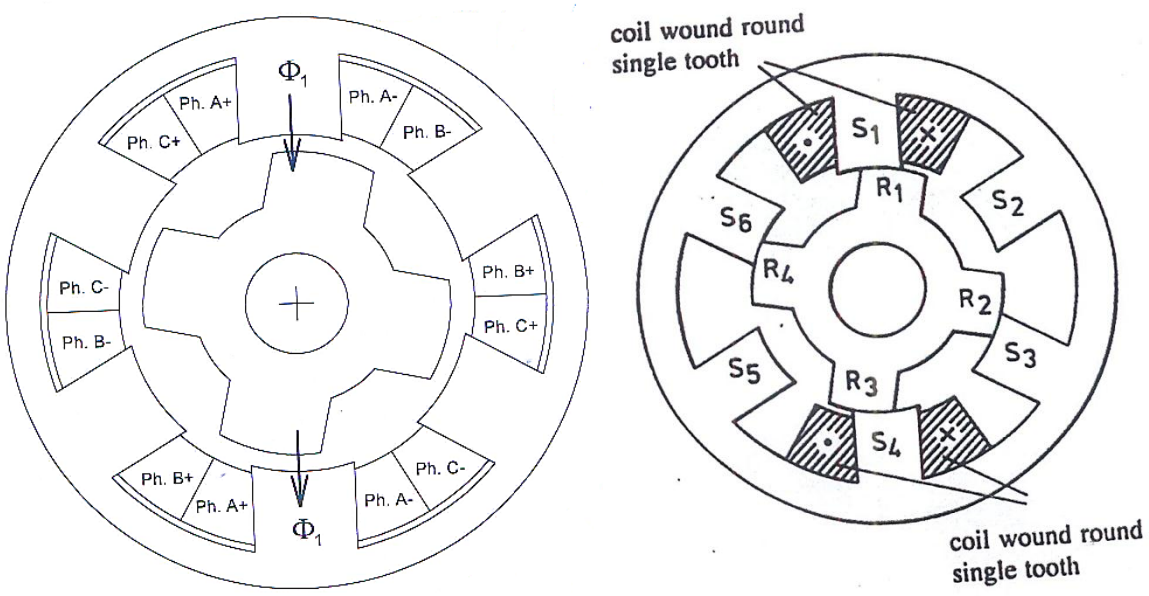

Figure A.15 (left) a typical cross section of a 6/4 SRM (right) typical geometry

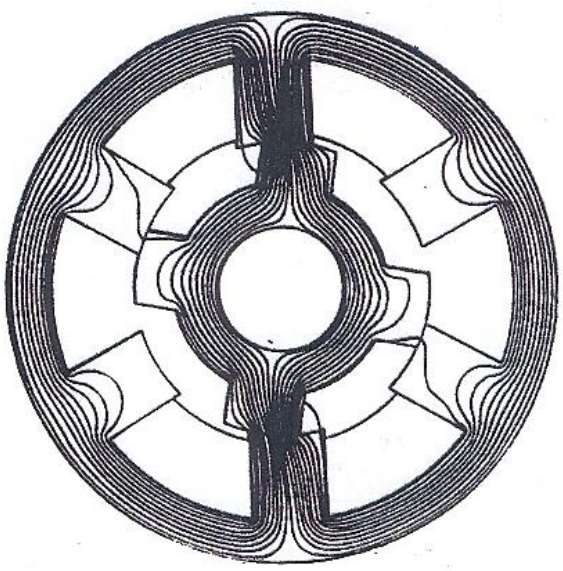

Figure A.16 Typical magnetic flux plot

Normally, the inductance determination depends on the magnetic flux and the carrying current. According to the flux path in Figure A.16, it is obvious that the flux density may have the relations to the rotor position. Hence, the machine inductance analysis can be researched by three situations: aligned, unaligned and intermediate rotor position. However, the flux path picture also shows that the saturation effects are enormous in the machine. It will be thought about later. Here, we assume the saturation of magnetic circuit to be unimportant.

The aligned position

When any pair of rotor poles is exactly aligned with the stator poles of phase 1, that phase is said to be in the aligned position. Figure A.17 illustrates the aligned position of phase 1 whose poles are on the horizontal axis [89].

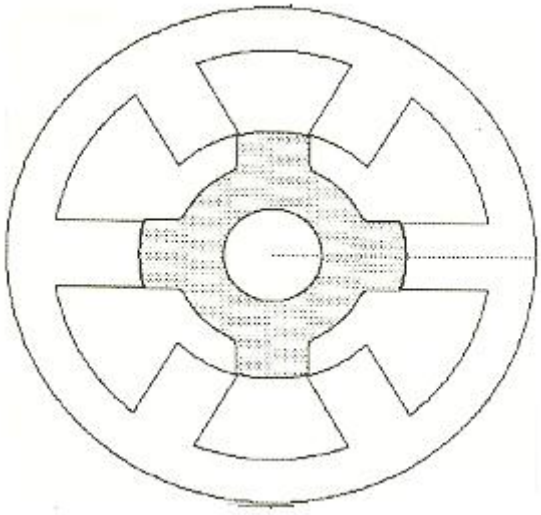

Figure A.17 Aligned position on phase 1 [89]

At this moment, the magnetic reluctance of flux path is at its lowest, so that the phase inductance peaks. Use L_{max} to represent inductance at this moment

The unaligned position

As the inter-polar axis of the rotor is aligned with the stator poles of phase 1.this phase is called in the unaligned position as shown in Figure A.18. The fluxes pass through the longest airgap. The reluctance of the airgap is much bigger than the steel parts, as the result, the phase inductance will minimize caused by the highest magnetic reluctance of the flux path. Here, the minimum inductance is expressed by L_{min}.

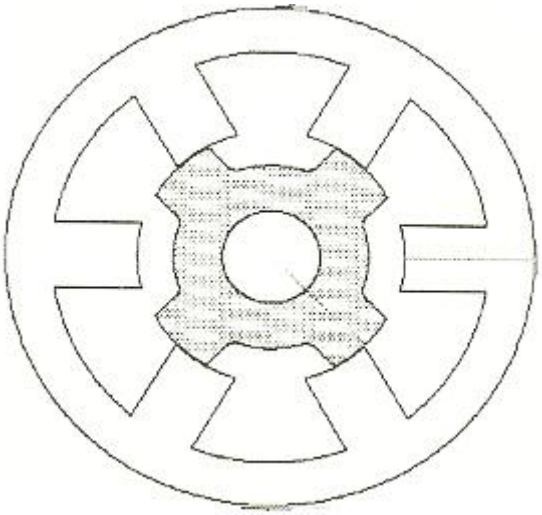

Figure A.18 Unaligned position on phase 1 [89]

Intermediate rotor position

At the intermediate rotor position, the rotor is in the position ‘between’ the aligned and unaligned with one side aligned and the other unaligned. It indicates the rotor poles have partial overlap with the stator poles of phase 1, lagging in the motoring mode (Figure A.19 left graph) and leading as a generator (Figure A.19 right picture).

The overlap part between rotor and stator poles becomes greater for the motoring mode and smaller in the generating mode. It leads to the reduction of reluctance and the increase of phase induction in the motor, while causes the rising reluctance and decreased induction in the generating mode. If the machine is rotated with a uniform speed, the growth and drop rates of the overlap area will be fixed. The phase inductance, therefore, descends or ascends linearly.

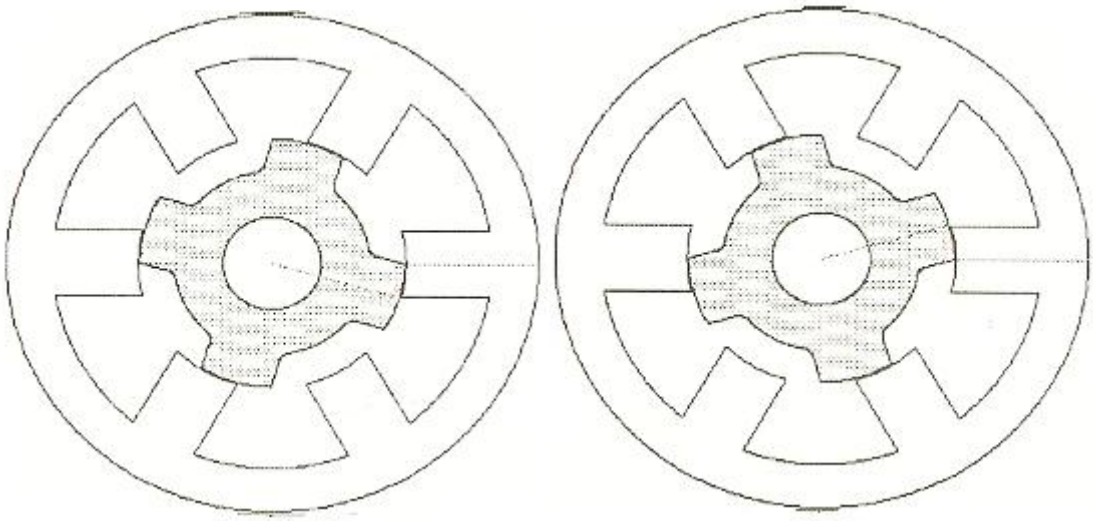

Figure A.19 Partial overlap position on phase 1 (left) while motoring in the counter-clockwise direction (right) while generating in anti-clockwise direction [89]

Inductance vs. rotor position

Based on the discussion above, we can have a conclusion that the phase inductance changes following the position change of the rotational rotor.

The relationship between the inductance and the rotor position in non-saturable motor is demonstrated in the Figure A.20. The inductance peaks at the rotor is in aligned position and jumps to the nadir when the rotor unaligned with the stator poles. It will grow linearly in motoring and shrink in generating mode. From the graph, it can be found that the phase current during the unaligned rotor position is none. Therefore, ‘as the rotor rotates, the phase flux-linkage should have a triangular or sawtooth waveform but not vary with current’ [89].

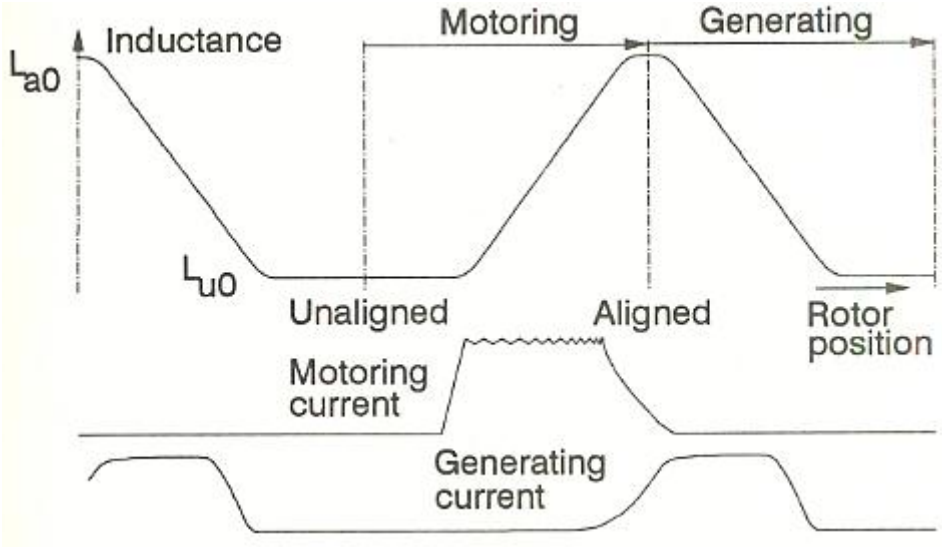

Figure A.20 Inductance vs. rotor position in non-saturable motor [89]

A.3.2. Instantaneous Torque of SRM

According to the discussion above, all torque is 'reluctance' torque. When the rotor poles are exactly aligned or unaligned with phase1 stator poles, there is no torque produced. However, in the intermediate rotor position, a torque is generated to minimise the reluctance by returning the rotor to the align position or attracting it towards the next aligned position.

In order to analyse the torque value, the energy is considered firstly. Because the torque is independent of the current direction, hence the unidirectional winding current may be used. Neglect the effect of the magnetic saturation, the power input to winding is:

$$W = i^2R + \frac{d}{dt}\left(\frac{1}{2}Li^2\right) + T\omega \qquad (A.58)$$

Where i^2R is the representation of the winding losses, while $\frac{1}{2}Li^2$ stands for the magnetic stored energy. The torque and the speed comprise the output power. Resolve the equation A.58, we will have:

$$W = i^2R + \frac{i^2}{2}\frac{dL}{dt} + Li\frac{di}{dt} + T\omega \qquad (A.59)$$

We also know the equation of the voltage applied to the winding:

$$V = iR + \frac{d\varphi}{dt} = iR + \frac{d(Li)}{dt} \qquad (A.60)$$

So

$$Vi = i^2R + i\frac{d(Li)}{dt} = i^2R + i^2\frac{dL}{dt} + Li\frac{di}{dt} \qquad (A.61)$$

$W = Vi$ is well known, thus equation $A.59$ and $A.61$ have same left side. Then we will have a new equation:

$$i^2R + \frac{i^2}{2}\frac{dL}{dt} + Li\frac{di}{dt} + T\omega = i^2R + i^2\frac{dL}{dt} + Li\frac{di}{dt} \qquad (A.62)$$

$$T\omega = \frac{i^2}{2}\frac{dL}{dt} = \frac{i^2}{2}\frac{dL}{d\theta}\frac{d\theta}{dt} = \frac{i^2}{2}\frac{dL}{d\theta}\omega \qquad (A.63)$$

$$T = \frac{i^2}{2}\frac{dL}{d\theta} \qquad (A.64)$$

This torque is calculated in the idealized condition. In practical, the situation is complicated by saturation.

Figure A.21 describes the energy conversion. The grey part is the energy during the phase on time. It is constituted by the stored magnetic field energy (the blue part) and the energy converter to the toque (the green area)

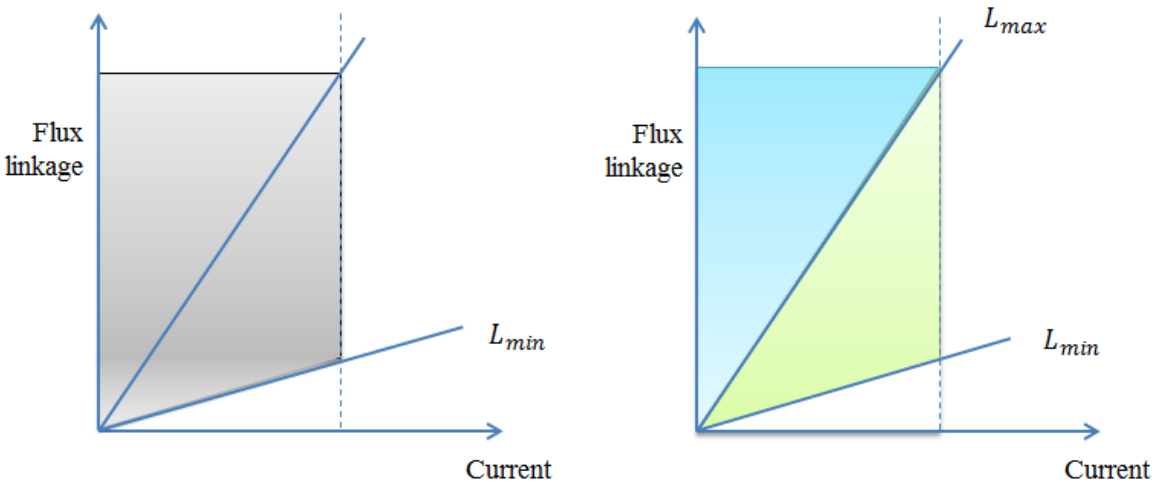

Figure A.21 Average torque, energy-conversion loop

A.3.3. Saturation effects of inductance and torque

So far we have assumed that the saturation of magnetic circuit is negligible. In fact, the actual machine has an enormous effect upon the characteristics. The unaligned magnetization is not as susceptible to saturation as the aligned [89], which causes the unaligned inductance does not saturate much but the aligned inductance affects strongly.

Figure A.22 and Figure A.23 give the inductance and energy with the effects of the saturation. Figure A.22 illustrates the inductance changes with the rotor rotation, and also shows the saturation influence as the current increase. Figure A.23 demonstrates the area change of the energy converted to the torque following the maximum inductance strongly impacted by the saturation.

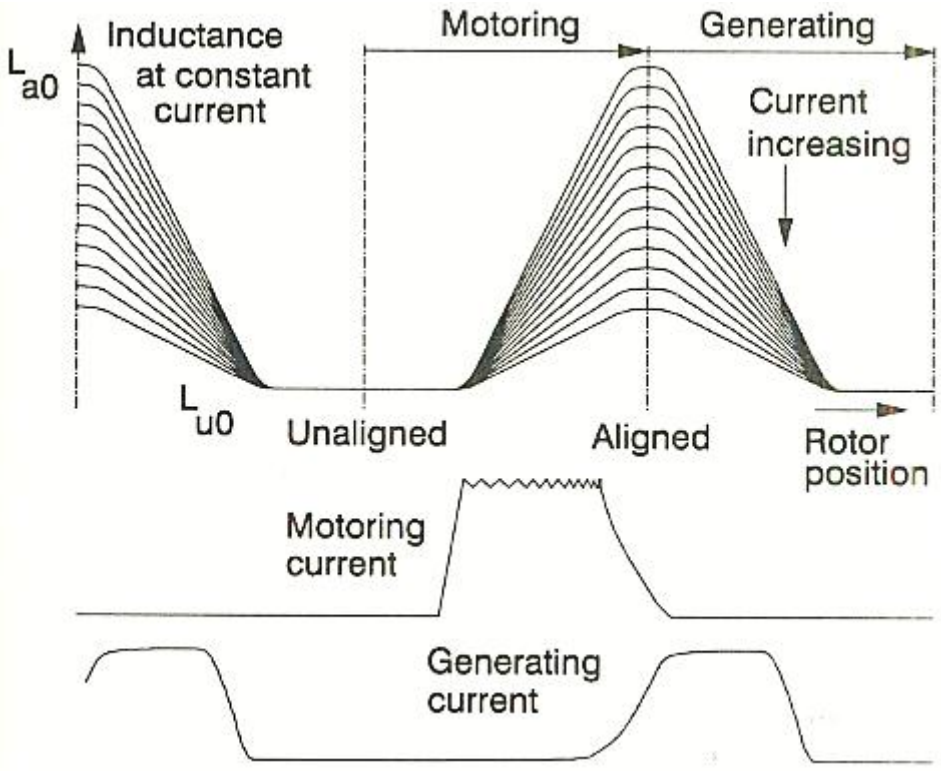

Figure A.22 Inductance vs. rotor position with the saturation [89]

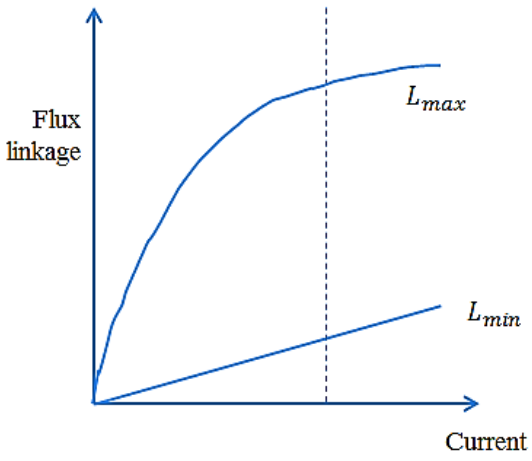

Figure A.23 The energy conversion loop

The saturation makes the inductance smoother at the peak of the phase inductance. The superposition of the phase inductance of two SRMs may make the BDFRG's inductance shape be closer to a sine wave. It will be witnessed in the BDFRG parameters tests.

A.4. Transformation from twin axis dynamic model to stator referred equivalent circuit

A.4.1. Twin axis dynamic model to stator referred equivalent circuit transformation

For performance prediction and analysis, it is quite useful to have an equivalent circuit for the induction machine. In many respects, the induction machine behaviors like a transformer. Thus the transformer equivalent circuit is a wise initial point. The graph below (Figure A.24) illustrates the equivalent circuit for the transformer and one phase of a balance induction machine.

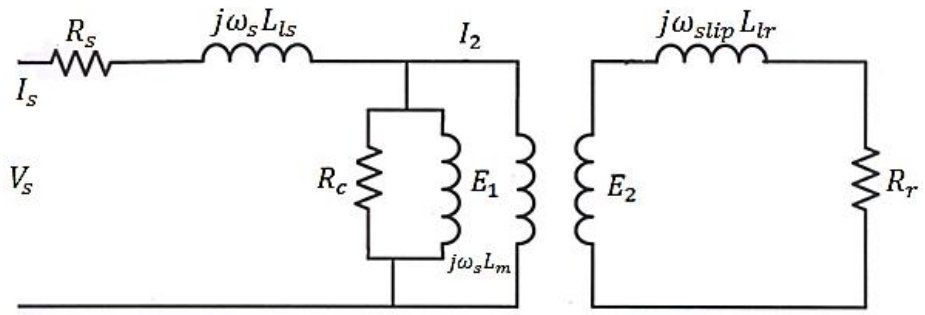

Figure A.24 the equivalent circuit for one phase of a balance induction machine

In the graph, each symbol represents the meaning below:

V_s : Applied stator phase voltage;

I_s : Stator phase current;

R_s : Stator phase resistance;

L_{ls} : Stator phase leakage inductance;

ω_s : Stator angular velocity ($^{rad}/_{s}$);

L_m : Mutual inductance;

R_c : Core loss resistance;

E_1 : EMF induced by resultant rotating magnet field;

E_2 : EMF induced at rotor side;

a: Stator/rotor turns ratio;

I_r : Actual rotor phase current;

R_r : Actual rotor phase resistance;

L_{lr} : Actual rotor phase leakage inductance;

ω_{slip} : Rotor circuit angular velocity ($^{rad}/_{s}$), also the slip angular velocity;

I_2 : Reflected rotor phase current;

Using basic AC circuit theory, the stator voltage and rotor circuit equations can be inferred from the picture Figure :

$$V_s = R_s I_s + j\omega_s L_{ls} I_s + E_1 \qquad (A.65)$$

$$E_2 = R_r I_r + j\omega_{slip} L_{lr} I_r \qquad (A.66)$$

Consider the 'ideal transformer' element, we can write:

$$E_2 = s\frac{E_1}{a} \qquad (A.67)$$

where s is the slip, which can be obtained from $\frac{\omega_{slip}}{\omega_s}$.

Combining to the equations $A.66$ and $A.67$, we can have:

$$E_1 = \frac{aR_r I_r}{s} + \frac{aj\omega_{slip} L_{lr} I_r}{s} \qquad (A.68)$$

Now consider the reflected rotor phase current I_2. As $sE_1I_2 = E_2I_r$ according to the equivalent circuit above, the equation $A.59$ can be inferred.

$$I_r = aI_2 \qquad (A.69)$$

Then $A.58$ can be re-written as:

$$E_1 = \frac{a^2R_r}{s}I_2 + \frac{j\omega_{slip}}{s}a^2L_{lr}I_2 \qquad (A.70)$$

also $\omega_{slip} = s\omega_s$, and therefore $\omega_s = \frac{\omega_{slip}}{s}$.

$$E_1 = \frac{a^2R_r}{s}I_2 + j\omega_s(a^2L_{lr})I_2 \qquad (A.71)$$

using

$I_2 = \frac{I_r}{a} =$ referred rotor phase current;

$R_2 = a^2R_r =$ referred rotor phase resistance;

$L_2 = a^2L_{lr} =$ referred rotor phase leakage inductance;

to take place the corresponding symbols, we can obtain:

$$E_1 = \frac{R_2}{s}I_2 + j\omega_sL_2I_2 \qquad (A.72)$$

Now the rotor can be represented by a simple branch circuit shown in Figure A.25.

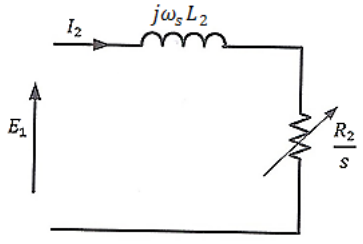

Figure A.25 Rotor simple branch circuit

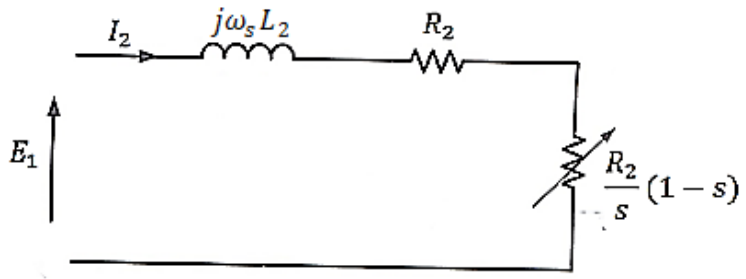

Figure A.26 Rotor simple branch circuit with split resistance

The term $\frac{R_2}{s}$ can be split into $R_2 + \frac{R_2(1-s)}{s}$, the Figure A.26 would be deduced instead of Figure A.25.

At this moment, the twin axis dynamic model of an induction machine shown in Figure A.24 can be transferred to a stator referred equivalent circuit (Figure A.27). Taking account to the symmetry of the circuit graph, all subscripts 's' of stator side symbols has been replaced by '1', where $X_1 = \omega_s L_{ls}$, $X_2 = \omega_s L_2$ and $X_m = \omega_s L_m$.

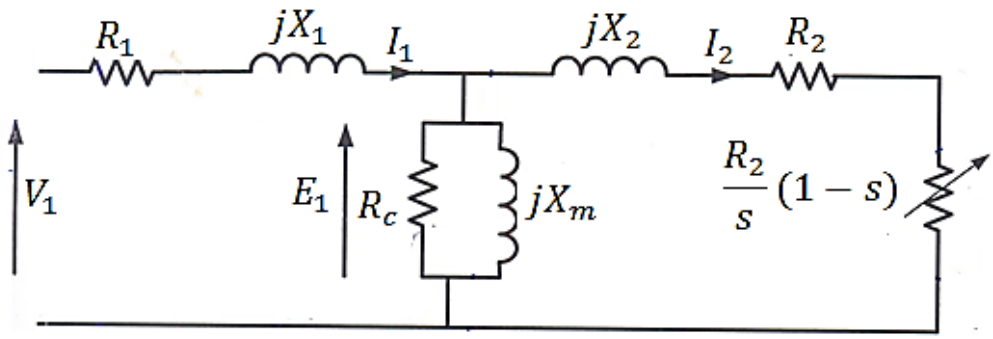

Figure A.27 Stator referred equivalent circuit for one phase of a balance induction machine

A.4.2. Power and torque in the induction machine

According to the Figure A.26, The power dissipated in each resistor can be inferred as $I_2^2 R_2$ is the power lost in the rotor resistance, called 'copper loss' P_c, while $I_2^2 \frac{R_2(1-s)}{s}$ is the power converted to the mechanical output, named 'mechanical power'

P_m. The per-phase power crossing air-gap is the sum of copper loss and mechanical output. Thus

$$P_g = I_2^2 \frac{R_2}{s}, \qquad sP_g = I_2^2 R_2 \qquad (A.73, A.74)$$

Therefore the per-phase mechanical power is

$$P_m = I_2^2 \frac{R_2(1-s)}{s} = (1-s)P_g \qquad (A.75)$$

The ratio of mechanical power to the power crossing the air-gap is known as the air-gap efficiency:

$$\frac{P_m}{P_g} = (1-s) \qquad (A.76)$$

But the actual overall efficiency of the machine is lower than this due to other losses.

The total mechanical power is

$$3 \times P_m = T\omega_r \qquad (A.77)$$

where T and ω_r stand for the torque and rotor shaft speed respectively. Therefore we have

$$\omega_r = \omega_s - \omega_{slip} = (1-s)\omega_s \qquad (A.78)$$

Taking account to equations $A.75$ and $A.78$, we would get:

$$\frac{P_m}{\omega_r} = \frac{(1-s)P_g}{(1-s)\omega_s} = \frac{P_g}{\omega_s} \qquad (A.79)$$

Consider this equation with combining to $A.77$. It is now possible to form an alternative torque equation below:

$$T = 3 \times \frac{P_m}{\omega_r} = 3 \times \frac{P_g}{\omega_s} = 3 \frac{I_2^2}{\omega_s} \frac{R_2}{s} \qquad (A.80)$$

B. PI Control

The reader is assumed to be familiar with PI control, of which is well-covered by a variety of undergraduate texts. This section provides C language code for the DFIG control techniques described in the body of this work.

B.1. Digital implementation of PI control

A standard feedback error 'PI' controller has following time domain form:

$$u(t) = k\left\{e(t) + \frac{1}{T_i}\int e(t)\,dt\right\} \qquad (B.1)$$

In the Laplace domain this becomes:

$$u(s) = k\left\{e(t) + \frac{1}{sT_i} + T_d s\right\} e(s) \qquad (B.2)$$

It is possible to converting to discrete time domain using an approximation for the discrete time operator [90]. Using Tustin's (bilinear) approximation:

$$z \approx \frac{1 + sT_s/2}{1 - sT_s/2} \qquad \therefore s \approx \frac{2}{T_s}\left(\frac{1 - z^{-1}}{1 + z^{-1}}\right) \qquad (B.3)$$

Hence;

$$U(z) = k\left\{1 + \frac{T_s}{2T_i}\left(\frac{1 + z^{-1}}{1 - z^{-1}}\right)\right\} E(z) \qquad (B.4)$$

$$U(z) = k\left\{\left(1 - \frac{T_s}{2T_i}\right) + \left(\frac{T_s}{T_i}\right)\frac{1}{1 - z^{-1}}\right\} E(z) \qquad (B.5)$$

The digital control constants become:

$$K_p = k\left(1 - \frac{T_s}{2T_i}\right) \qquad (B.6)$$

$$K_i = k\left(\frac{T_s}{T_i}\right) \qquad (B.7)$$

Such that the overall control equation simplifies to:

$$U(z) = k\left\{K_p + \frac{K_i}{1 - z^{-1}}\right\}E(z) \qquad (B.8)$$

Equation B.8 describes a digital PI controller. Equations B.6 and B.7 allow us to transform real-time controller gains into discrete-time controller gains.

In practical application we can break the discrete controller equation (B.8) down into separate proportional and integral components:

$$u[k] = u_p[k] + u_i[k] \qquad (B.9)$$

Proportional component:

$$u_p[k] = K_p e[k] \qquad (B.10)$$

Integral Component:

$$u_i[k] = K_i e[k] + u_i[k-1] \qquad (B.11)$$

This discrete PI controller can be described graphically in Figure B.1.

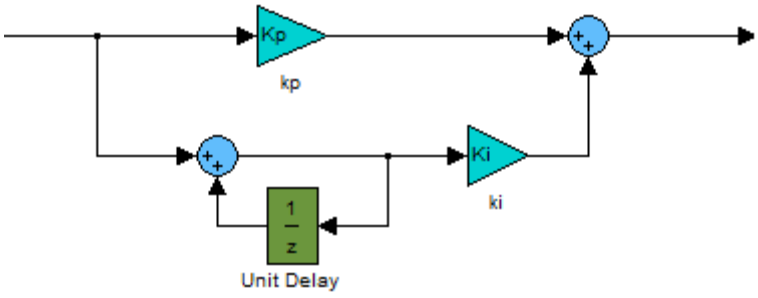

Figure B.1 Discrete PI controller

It is necessary to define an initial state for the integral component, normally zero. In order to prevent windup of the integral component, its value is limited in software to lie within a specific range.

B.2. Experimental Controller Code

```
P_error = (P_ref - P);
Q_error = (Q_ref - Q);

ird_demand = kp2*P_error+zd2;
if(release)
    zd2 = zd2 + ki2*P_error;

if(zd2 > CURRENT_LOOP_INT_CLAMP)
    zd2 = CURRENT_LOOP_INT_CLAMP;
if(zd2 < -CURRENT_LOOP_INT_CLAMP)
    zd2 = -CURRENT_LOOP_INT_CLAMP;

irq_demand = kp2*Q_error+zq2;
if(release)
    zq2 = zq2 + ki2*Q_error;

if(zq2 > CURRENT_LOOP_INT_CLAMP)
    zq2 = CURRENT_LOOP_INT_CLAMP;
if(zq2 < -CURRENT_LOOP_INT_CLAMP)
    zq2 = -CURRENT_LOOP_INT_CLAMP;

ird_error = (ird_demand - irde);
irq_error = (irq_demand - irqe);
```

```
vde1 = kp1*ird_error + zd1;
if(release)
    zd1 = zd1 + ki1*ird_error;
if(zd1 > CURRENT_LOOP_INT_CLAMP)
    zd1 = CURRENT_LOOP_INT_CLAMP;
if(zd1 < -CURRENT_LOOP_INT_CLAMP)
    zd1 = -CURRENT_LOOP_INT_CLAMP;

vqe1 = kp1*irq_error + zq1;
if(release)
zq1 = zq1 + ki1*irq_error;

if(zq1 > CURRENT_LOOP_INT_CLAMP)
    zq1 = CURRENT_LOOP_INT_CLAMP;
if(zq1 < -CURRENT_LOOP_INT_CLAMP)
    zq1 = -CURRENT_LOOP_INT_CLAMP;
```

C. Space Vector Modulation

C.1. Basic concept

Space vector modulation can be applied to each leg of a three-phase inverter. It is a form of pulse width modulation but it considers the collective effect on all three-phase rather than independent phase leg modulation. Details are shown below.

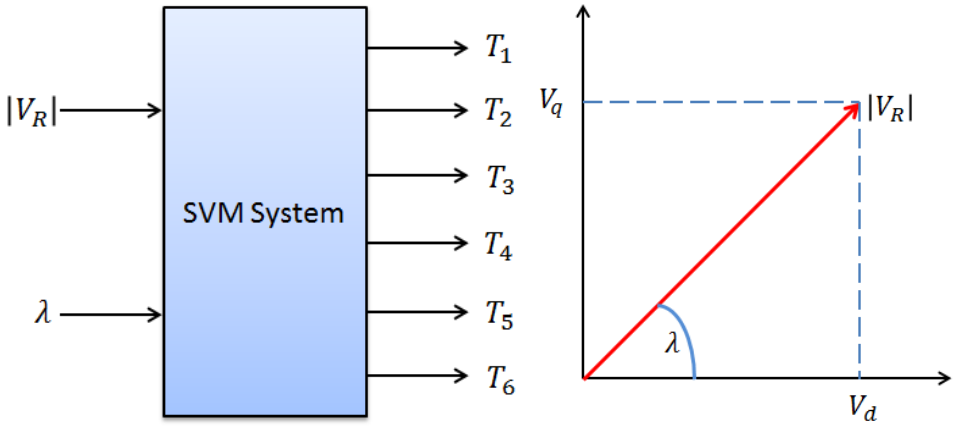

Figure C.1 (Left) Space vector modulator block (Right) input demand vector

The space vector modulator is shown in left graph of Figure C.1. The input signal to the modulator is the reference stator voltage $\overrightarrow{V_R}$ which can be given in either rectangular or polar form:

$$\overrightarrow{V_R} = |V_R| \exp(j\lambda) = V_d + jV_q \qquad (C.1)$$

The output signals T_1, $T_2 \cdots T_6$ are the switching signals for the six inverter switching devices. There are a limited number of the switching states associated with a six-transistor or IGBT inverter circuit. Referring to this circuit, 8 states can be identified as shown below. (Figure C.2)

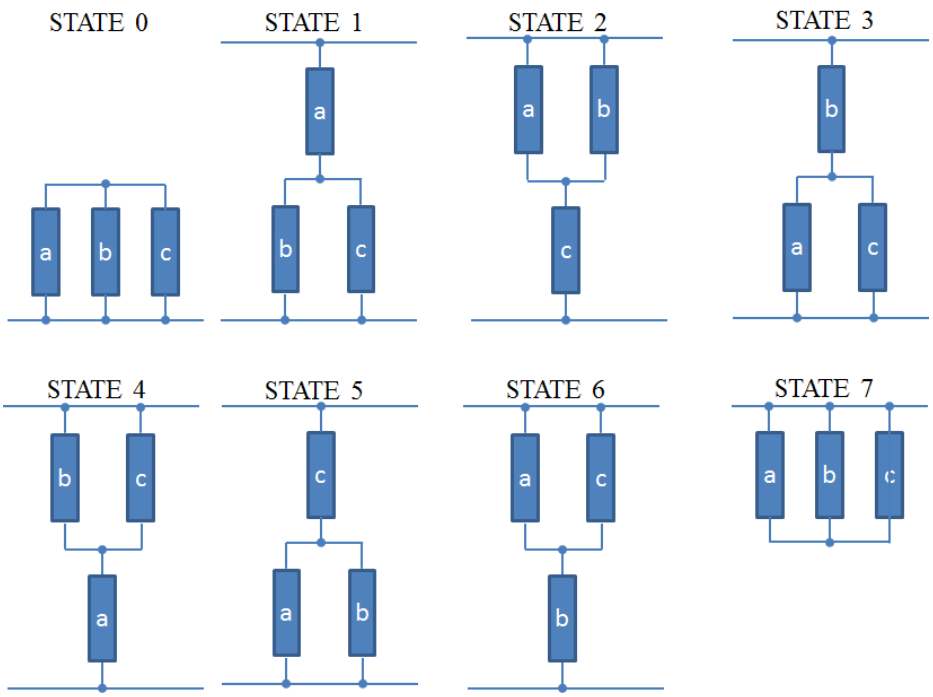

Figure C.2 Switching states of three-phase inverter

State	Vector	$\frac{V_{ab}}{V_{dc}}$	$\frac{V_{bc}}{V_{dc}}$	$\frac{V_{ca}}{V_{dc}}$	$\frac{V_{an}}{V_{dc}}$	$\frac{V_{bn}}{V_{dc}}$	$\frac{V_{cn}}{V_{dc}}$	$\frac{V_{d}}{V_{dc}}$	$\frac{V_{q}}{V_{dc}}$
000	$\overrightarrow{V_0}$	0	0	0	0	0	0	0	0
100	$\overrightarrow{V_1}$	1	0	-1	2/3	-1/3	-1/3	2/3	0
110	$\overrightarrow{V_2}$	0	1	-1	1/3	1/3	-2/3	1/3	$1/\sqrt{3}$
010	$\overrightarrow{V_3}$	-1	1	0	-1/3	2/3	-1/3	-1/3	$1/\sqrt{3}$
011	$\overrightarrow{V_4}$	-1	0	1	-2/3	1/3	1/3	-2/3	0
001	$\overrightarrow{V_5}$	0	-1	1	-1/3	-1/3	2/3	-1/3	$-1/\sqrt{3}$
101	$\overrightarrow{V_6}$	1	-1	0	1/3	-2/3	1/3	1/3	$-1/\sqrt{3}$
111	$\overrightarrow{V_7}$	0	0	0	0	0	0	0	0

Table C.1 The states corresponding voltages

The line and phase voltages corresponding to each state are given the table above (Table C.1). The idea of association a vector with each inverter state can be explained by considering the resulting static magnetic field direction if the inverter state was allowed to produce a DC current flow.

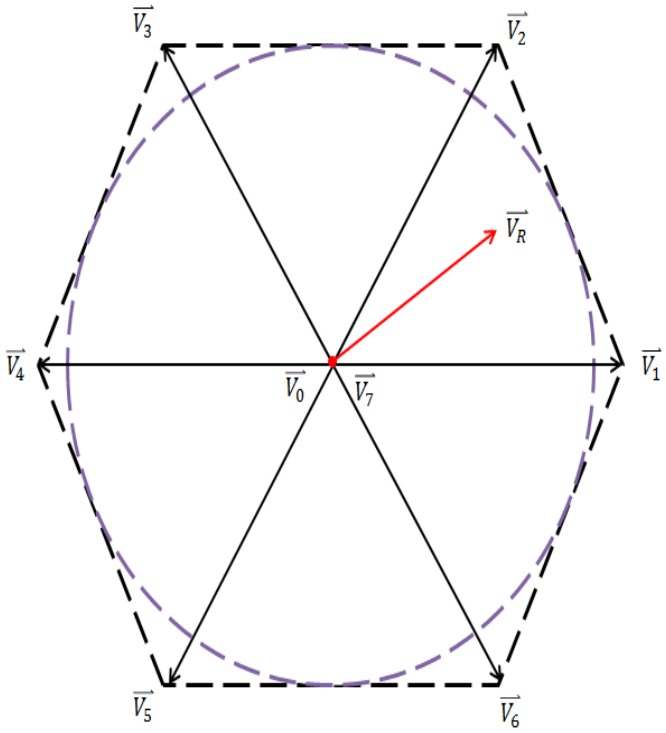

Figure C.3 Diagram of eight state vectors

Figure C.3 shows the voltage vectors corresponding to the eight inverter switching states. There are six 60° sextants which occupy the space between each pair of state vectors. For normal operation, the reference voltage vector $\overrightarrow{V_R}$ can lie anywhere within the hexagon. In the steady state operation this voltage vector would rotate with a constant magnitude and constant angular velocity. The direction in which the vector rotates determines the direction in which the motor turns. The inscribed circle indicates the maximum voltage vector trajectory for sinusoidal modulation. Application of over-modulation techniques where the circle extends beyond the hexagon boundaries can produce more output voltage from a given DC bus voltage.

More detail of first sextant is shown below. The reference voltage vector $\overrightarrow{V_R}$ has components U_a and U_b determine the amount of time that vectors $\overrightarrow{V_1}$ and $\overrightarrow{V_2}$ are applied during the PWM cycle.

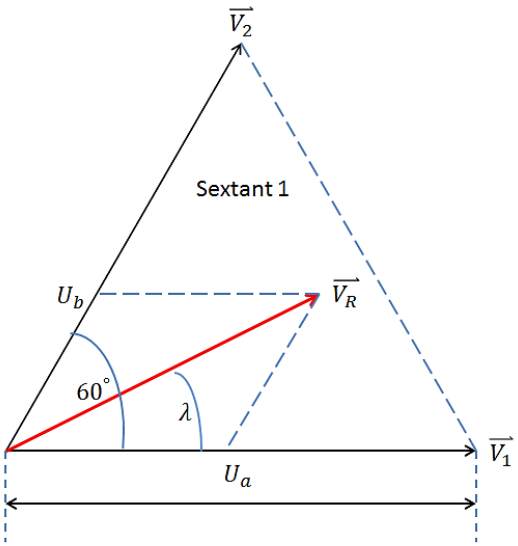

Figure C.4 Projections of the reference voltage vector onto two adjacent state vectors

Considering the mapping of $\overrightarrow{V_R}$ onto $\overrightarrow{V_1}$ and $\overrightarrow{V_2}$.

$$\left|\overrightarrow{V_R}\right| \sin\lambda = U_b \sin 60^\circ \qquad (C.2)$$

$$U_b = \left|\overrightarrow{V_R}\right| \frac{\sin\lambda}{\sin 60^\circ} = \frac{2}{\sqrt{3}} \left|\overrightarrow{V_R}\right| \sin\lambda \qquad (C.3)$$

$$U_a = \left|\overrightarrow{V_R}\right| \cos\lambda - U_b \cos 60^\circ = \left|\overrightarrow{V_R}\right| \cos\lambda - \frac{1}{\sqrt{3}} \left|\overrightarrow{V_R}\right| \sin\lambda = \frac{2}{\sqrt{3}} \left|\overrightarrow{V_R}\right| \left\{\frac{\sqrt{3}}{2}\cos\lambda - \frac{1}{2}\sin\lambda\right\}$$

$$= \frac{2}{\sqrt{3}} \left|\overrightarrow{V_R}\right| \sin(60^\circ - \lambda) \qquad (C.4)$$

Thus

$$U_a = \frac{2}{\sqrt{3}} \left|\overrightarrow{V_R}\right| \sin(60^\circ - \lambda), \qquad U_b = \frac{2}{\sqrt{3}} \left|\overrightarrow{V_R}\right| \sin\lambda \qquad (C.5, C.6)$$

The timing of the leg switching is based on the magnitude of the components U_a and U_b using the following expressions:

$$T_a = \frac{TU_a}{V_{dc}}, \qquad T_b = \frac{TU_a}{V_{dc}}, \qquad T_c = T - T_a - T_b \qquad (C.7, C.8, C.9)$$

Where $T = \frac{T_{PWM}}{2}$

The timing of a single PWM cycle is shown below. (Figure C.5)

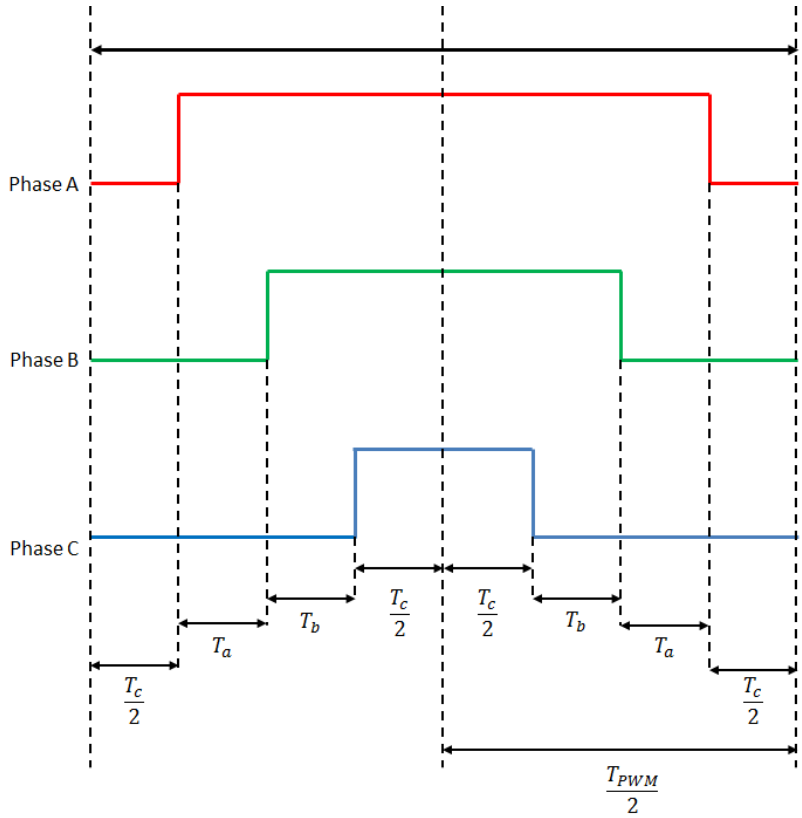

Figure C.5 Timing of inverter leg switching signals

The inverter phases are switched in accordance with this timing using digital counters. It is possible to use the standard centre-aligned (triangular carrier based) PWM logic described earlier and available within many standard microcontrollers to implement this timing.

When switching a phase leg, it is important to prevent the momentary condition where both devices are on at the same time. This condition is unknown as a shoot-through fault. To prevent this, a delay is inserted between turning off one device and turning of the power devices and other delay in the gate drive circuits. For IGBT devices it is likely to be of the order of 1 or 2 μs.

C.2. Experimental SVM Code

```
void svm(float vds, float vqs, Uint16 *mia, Uint16 *mib, Uint16 *mic)
{
    Uint16 flag;
    float ua,ub,uc;
    float v1,v2;
    Uint16 ma,mb,mc;
    extern Uint16 T0_count;

    flag = 0;
    if(vqs >= 0) flag = flag|4;
    if(vqs >= ROOT3*vds) flag = flag|2;
    if(vqs >= -ROOT3*vds) flag = flag|1;

    switch(flag)
    {
    case 0: /* sextant 5, rotate reference vector 240 deg clockwise */
        v1 = -0.5*vds - 0.8660254*vqs;
        v2 = 0.8660254*vds - 0.5*vqs;
        if(v2 > (INTERCEPT - ROOT3*v1))
            {
            v1 = INTERCEPT*v1/(v2 + ROOT3*v1);
```

```
            v2 = INTERCEPT - ROOT3*v1;
            }
        ua = v1 - 0.5773502*v2;
        ub = 1.1547005*v2;
        uc = MAX_MOD_INDEX - ua - ub;
        ma = (int)(ub + 0.5*uc);
        mb = (int)(0.5*uc);
        mc = (int)(ua + ub + 0.5*uc);
        break;

    case 1: /* sextant 6, do not rotate reference vector */
         v1 = vds;
        v2 = -vqs;
        if(v2 > (INTERCEPT - ROOT3*v1))
            {
            v1 = INTERCEPT*v1/(v2 + ROOT3*v1);
            v2 = INTERCEPT - ROOT3*v1;
            }
        ua = v1 - 0.5773502*v2;
        ub = 1.1547005*v2;
        uc = MAX_MOD_INDEX - ua - ub;
        ma = (int)(ua + ub + 0.5*uc);
        mb = (int)(0.5*uc);
        mc = (int)(ub + 0.5*uc);
        break;

    case 2: /* sextant 4, rotate reference vector 240 deg clockwise and flip horizontal
*/
        v1 =    -0.5*vds - 0.8660254*vqs;
```

```
        v2 =    -0.8660254*vds + 0.5*vqs;
        if(v2 > (INTERCEPT - ROOT3*v1))
            {
            v1 = INTERCEPT*v1/(v2 + ROOT3*v1);
            v2 = INTERCEPT - ROOT3*v1;
            }
        ua = v1 - 0.5773502*v2;
        ub = 1.1547005*v2;
        uc = MAX_MOD_INDEX - ua - ub;
        ma = (int)(0.5*uc);
        mb = (int)(ub + 0.5*uc);
        mc = (int)(ua + ub + 0.5*uc);
        break;

    case 3: break;

    case 4: break;

    case 5: /* sextant 1 do not rotate reference vector */
        v1 = vds;
        v2 = vqs;
        if(v2 > (INTERCEPT - ROOT3*v1))
            {
            v1 = INTERCEPT*v1/(v2 + ROOT3*v1);
            v2 = INTERCEPT - ROOT3*v1;
            }
        ua = v1 - 0.5773502*v2;
        ub = 1.1547005*v2;
        uc = MAX_MOD_INDEX - ua - ub;
```

```
        ma = (int)(ua + ub + 0.5*uc);
        mb = (int)(ub + 0.5*uc);
        mc = (int)(0.5*uc);
        break;

    case 6: /* sextant 3, rotate reference vector 120 deg clockwise */
        v1 = -0.5*vds + 0.8660254*vqs;
        v2 = -0.8660254*vds - 0.5*vqs;
        if(v2 > (INTERCEPT - ROOT3*v1))
            {
            v1 = INTERCEPT*v1/(v2 + ROOT3*v1);
            v2 = INTERCEPT - ROOT3*v1;
            }
        ua = v1 - 0.5773502*v2;
        ub = 1.1547005*v2;
        uc = MAX_MOD_INDEX - ua - ub;
        ma = (int)(0.5*uc);
        mb = (int)(ua + ub + 0.5*uc);
        mc = (int)(ub + 0.5*uc);
        break;

    case 7: /* sextant 2, rotate reference vector 120 deg clockwise and flip horizontal
*/
        v1 = -0.5*vds + 0.8660254*vqs;
        v2 = 0.8660254*vds + 0.5*vqs;
        if(v2 > (INTERCEPT - ROOT3*v1))
            {
            v1 = INTERCEPT*v1/(v2 + ROOT3*v1);
            v2 = INTERCEPT - ROOT3*v1;
```

```
            }
        ua = v1 - 0.5773502*v2;
        ub = 1.1547005*v2;
        uc = MAX_MOD_INDEX - ua - ub;
        ma = (int)(ub + 0.5*uc);
        mb = (int)(ua + ub + 0.5*uc);
        mc = (int)(0.5*uc);
        break;

    default: break;
    }

    *mia = MAX_MOD_INDEX - ma;
    *mib = MAX_MOD_INDEX - mb;
    *mic = MAX_MOD_INDEX - mc;
}
```

D. Induction Machine Parameters Test

In order to obtain the parameters in an induction machine, four fundamental tests are involved based on the induction machine performance and its equivalent circuit. The details are specified in IEEE Standard 112.

D.1. DC Resistance Test

When a DC voltage is supplied to the stator terminals, no any potential difference is applied across the inductance and no voltage is induced on the rotor. That indicates the per-phase circuit is reduced to the stator winding resistance and the stator side apparent works as an individual pure-resistor circuit. Depending upon the different connections of stator windings, the equivalent circuits are illustrated in Figure. D.1. Graph (a) shows the Star Connection circuit, while picture (b) reveals the machine stator windings are Delta connected. Considering the both figures below, it can be obvious that the stator resistance of induction machine will depend on the whether the stator windings are Star or Delta connection.

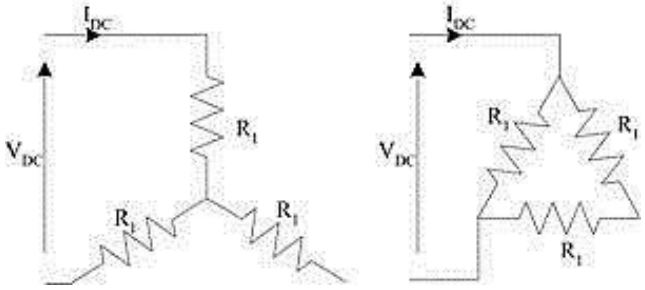

Figure D.1 Equivalent circuits of different stator winding connections (a) Star or Y connection; (b) Delta Connection under DC resistance test

If the stator is star connected like the Figure. D.1 (a), when the DC voltage is applied across two terminals, for example, Red and Yellow winding terminals, the DC current will be gone through red and yellow winding resistances. The entire apparent is a simple resistor series circuit. The total resistance value is the sum of red and yellow

resistance. Conjecturing the stator windings are balance, the red or yellow or blue winding resistance is the same as each other. Then the stator resistance value can be considered as anyone of three winding resistance. At this time, the stator resistance value R_s is computed as half of the test result. In order to minimise the error of test, normally, the resistance is better to be experimented three times. The DC voltage will be added to the red-yellow terminals, yellow-blue terminals, and blue-red terminals separately, and get the test value. The final stator value is obtained by averaging the half of three test results. In the entire experiments, the rated current has better to be reached and the measurements are better to be read after five minutes to avoid the effects of temperature.

For the Delta connection situation, if applying a DC voltage across two terminals of Delta connection stator, the DC current will be split into two paths based on the picture D.1 (b). One flows through a resistor, the other passes two series-connection resistors. Hence, according to the principle of parallel circuit, the stator resistance value exactly equals to three second of the test value. Experiment the different terminals respectively to the red, yellow and blue resistance value separately and receive the average to increase the accuracy.

To summary, the stator winding resistance can be obtained by the equations below:

$$R_s{}^{star} = \frac{1}{2}\frac{V_{dc}}{I_{dc}}, \quad R_s{}^{delta} = \frac{3}{2}\frac{V_{dc}}{I_{dc}} \qquad (D.1, D.2)$$

where V_{dc} and I_{dc} stand for the measurement values of supplied DC voltage and total DC current across to two terminals respectively. $R_s{}^{star}$ and $R_s{}^{delta}$ indicates the stator resistor value under Star connection and Delta connection separately.

Similar to the stator resistance experiment procedure, the rotor resistance can be obtained by the same tests. However, considering the impacts of brushes, slip rings or other contacted apparent, it is better to rotate the rotor shaft slowly to receive a constant measured current, when the experiment is being taken. Other procedures

are as same as stator resistance tests. Similarly, the rotor winding resistor value is got by the given equations D.3 or D.4:

$$R_r{}^{star} = \frac{1}{2}\frac{V_{dc}}{I_{dc}}, \quad R_r{}^{delta} = \frac{3}{2}\frac{V_{dc}}{I_{dc}} \qquad (D.3, D.4)$$

where $R_r{}^{star}$ and $R_r{}^{delta}$ are delegated to the rotor resistance of Star connection and Delta connection respectively.

D.2. Locked Rotor Test

In the locked rotor test, the rotor of machine is short-circuit and prevented from rotating. In the initial test, the supply voltage increases gradually to find the critical voltage that encourages the rotor starts to rotate. Then the entire tests might be done under this voltage. Normally, this critical voltage is approximately 25% to 30% rated voltage due to the impacts of the friction and the inertia of the rotor shaft. Thus the locked rotor test would be taken under a reduced voltage. However, accounting for the temperature effects and more accurately predict of the induction parameters under load condition, the current is better to reach the rated value.

For the induction machine, when the rotor is stationary, the slip $s = 1,$ and the induction machine equivalent circuit can be elliptically drawn as:

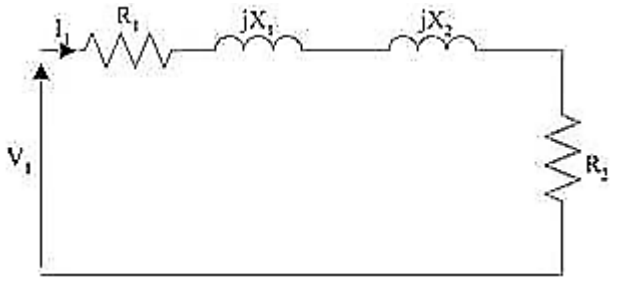

Figure D.2 Induction Machine model equivalent circuit under the locked rotor test

Analysing this circuit, V is the supplied per-phase voltage vector, and I is the measured per-phase current vector. R_1 and R_2, equally, stand for stator referred

stator resistance and rotor resistance respectively, while X_1 and X_2 represent the reactance relative to the stator and rotor when the induction machine model converts from the basic circuit to the equivalent circuit in Figure. D.2. Depending on the converted principle of induction machine, the stator referred stator value is as same as its original value whereas the stator referred rotor value is the real rotor value over the square of turns ratio a. Therefore, R_1 equals to the stator rotor R_s tested above while R_2 is a^2R_r. However, the relation between X_1 and X_s, or X_2 and X_r are a little complicate. It will describe in the later paragraph.

According to the circuit in the graph D.2,

$$V = IZ = I\big((R_1 + R_2) + j(X_1 + X_2)\big) \qquad (D.5)$$

where Z is total apparent impedance whose real part is all of resistances and the imaginary part is the entire leakage reactance. From the picture, it is clear that the induction machine model under the locked rotor test is an inductance-resistance (LR) series circuit. Hence, the total resistance is the sum of R_1 and R_2, while the whole reactance is X_1 pluses X_2.

Eq. D.5 could be inferred to the equations D.6and D.7below for the calculation purpose:

$$R_1 + R_2 = \frac{|V|}{|I|}|\cos\theta| \qquad (D.6)$$

$$X_1 + X_2 = \frac{|V|}{|I|}|\sin\theta| \qquad (D.7)$$

where $|V|$ and $|I|$ are the magnitudes of the voltage and current vector and θ is the phase shift between the voltage and the current.

With the value of stator resistance from the DC test, the rotor resistance referred to the stator can be found as the total resistance subtracts the stator resistance.

However, only the total leakage reactance is known. The relative values of stator leakage and stator referred rotor leakage must be obtained from experience. And for the wound rotor induction machines, X_1 and X_2 will occupy fifty per-cent of the total reactance. Hence:

$$R_2 = \frac{|V|}{|I|}|\cos\theta| - R_1 = \frac{|V|}{|I|}|\cos\theta| - R_s \qquad (D.8)$$

$$X_1 = X_2 = \frac{1}{2}\frac{|V|}{|I|}|\sin\theta| \qquad (D.9)$$

After the obtainment of the reactance, the inductance could be scaled to find the correct result due to $X = 2\pi f L$ $X = 2\pi f L$ where X represents the reactance and L stands for the inductance. f indicates the frequency which is 50Hz in common. This equation reveals the relationship of inductance and reactance. It is obvious that the inductance is proportional to the reactance and reversed proportional to the frequency. Thus, the relative inductance L_1 and L_2 can be got as:

$$L_1 = \frac{X_1}{2\pi f}, \quad L_2 = \frac{X_2}{2\pi f} \qquad (D.10, D.11)$$

Due to the relationship of the rotor resistance and stator referred rotor resistance, the turns ratio a can be obtained by:

$$a = \sqrt{R_2/R_r} \qquad (D.12)$$

However, the turns ratio could be validated in the open circuit test described in Section D.4.

D.3. Synchronous Speed Test

During the synchronous speed test, the machine is allowed to accelerate up to the synchronous speed with no load applied. Normally, when the rotor of induction

machine is short circuit and the rated voltage is applied to the stator terminals, the machine would performance at a No-load speed which is quite close to synchronous speed. Thus the no-load speed can be performed instead of synchronous speed. Similar to the locked rotor experiment, the rated current is better to be reached in the test. But, differently, the voltage of the synchronous speed test would be increased to the rated as well.

If the machine runs close to the synchronous speed the slip approaches zero. The rotor Current will fall to zero. The equivalent circuit of induction machine model can be simplified to Figure. D. 3.

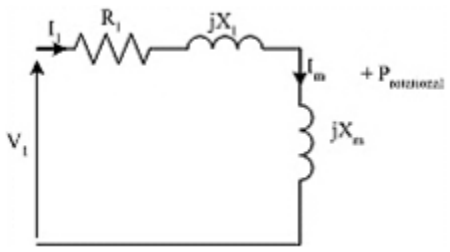

Figure D.3 Equivalent circuit of Induction Machine under the synchronous speed test

According to the equivalent circuit in Figure D.3, the equations below can be written:

$$V = IZ = I\big(R_1 + j(X_1 + X_m)\big) \qquad (D.13)$$

or alternatively:

$$X_1 + X_m = \frac{|V|}{|I|}|\sin\theta| \qquad (D.14)$$

where V and I are the applied voltage and measured current vector, while $|V|$ and $|I|$ are the magnitude of these voltage and current. θ is the phase shift angle between the voltage and current vector. X_m is the converted mutual reactance from standard induction machine model to the equivalent circuit of D.3. Normally is a proportional to the relative mutual inductance L_{mag} and frequency.

At this point, the mutual reactance can be found by Eq D.14 with X_1 knowing. Then the mutual inductance of correspondence to X_m can be calculated by equation D.15:

$$L_{mag} = \frac{X_m}{2\pi f} \qquad (D.15)$$

Based on the standard per-phase equivalent circuit as shown in figure D.4 and the twin axis dynamic model drawn in picture D.5, the relationship between the test value and the real machine parameters could be inferred as the equations below:

$$R_s = R_1 \qquad R_r = \frac{R_2}{a^2} \qquad (D.16, D.17)$$

$$L_m = \frac{L_{mag}}{a} = \frac{X_m}{2\pi f a} \qquad (D.18)$$

$$L_s = L_1 + L_{mag} = L_1 + aL_m \qquad (D.19)$$

$$L_r = \frac{L_2 + L_{mag}}{a^2} = \frac{L_2}{a^2} + \frac{L_{mag}}{a} \qquad (D.20)$$

D.4. Open circuit test

From the Equation D.16- D.20 above, it is easy to find the significance of the turns ratio a when the machine model is transferred from the twin to the standard equivalent circuit. Although the requirement of turns ratio can be satisfied by equation D.12, it is best to be measured with the procedure of open circuit test. Normally, $a = \sqrt{R_2/R_r}$ could be used to validate the veracity of the measured result.

Both the Locked Rotor Test and Synchronous Speed Test are short circuit tests. However, this Open Circuit Test, as the name suggests, is released the rotor as an open circuit. The equivalent circuit at this time is illustrated in graph D.6. It can be seen that the turns ratio is the division result of induced voltages E_1 and E_2 which can be simplified as the ratio between stator and rotor voltage. Thus, the open circuit

test method consists of applying a stator voltage V_1 and measuring the resulting rotor voltage V_2 at the open circuit slip rings. This voltage V_2 is then applied to the rotor and the stator voltage V_1 is measured. The effective turns ratio is then computed from the voltage ratio.

E. Test Rig

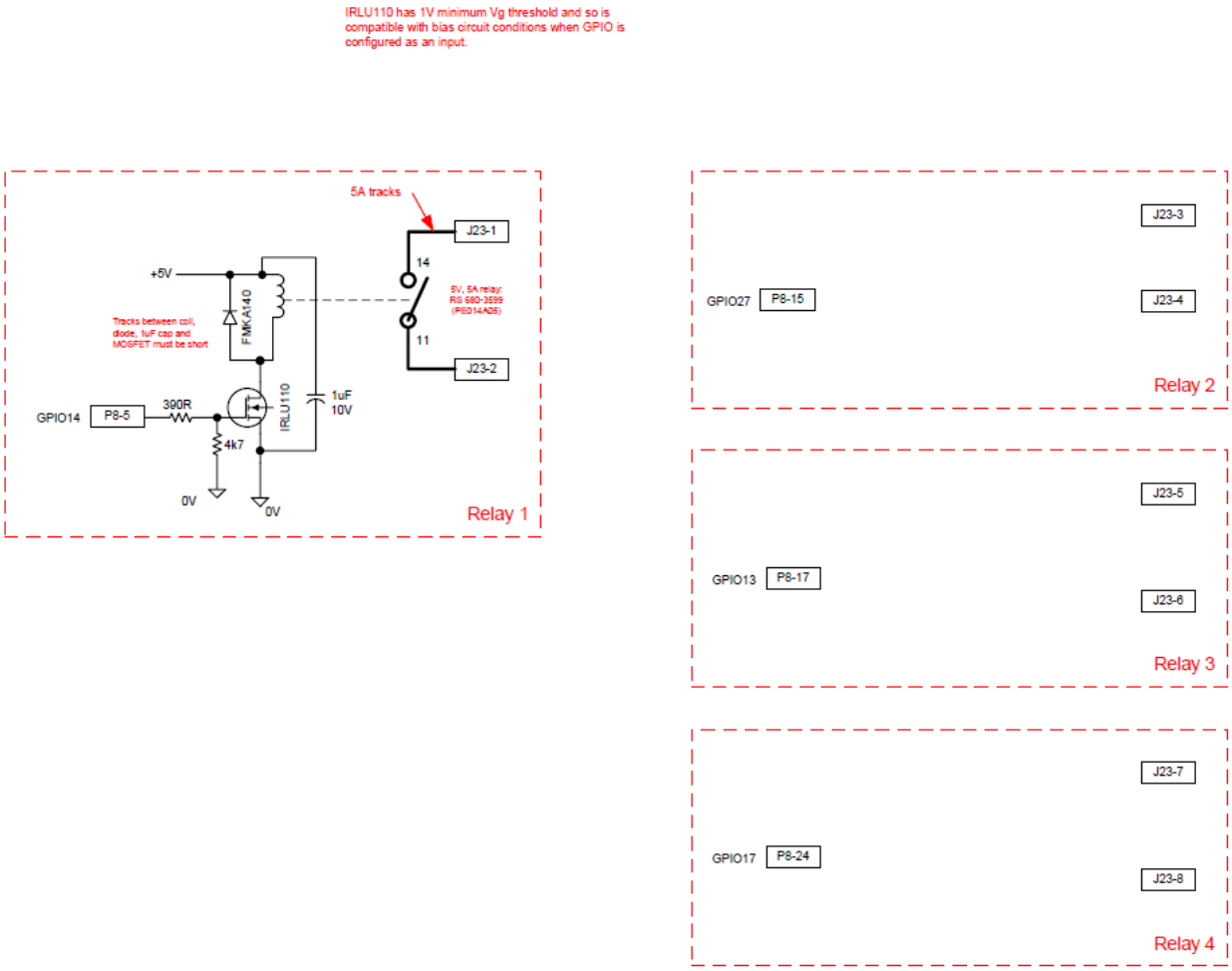

Figure E.1 F28335 Drive Basic Design—Relays

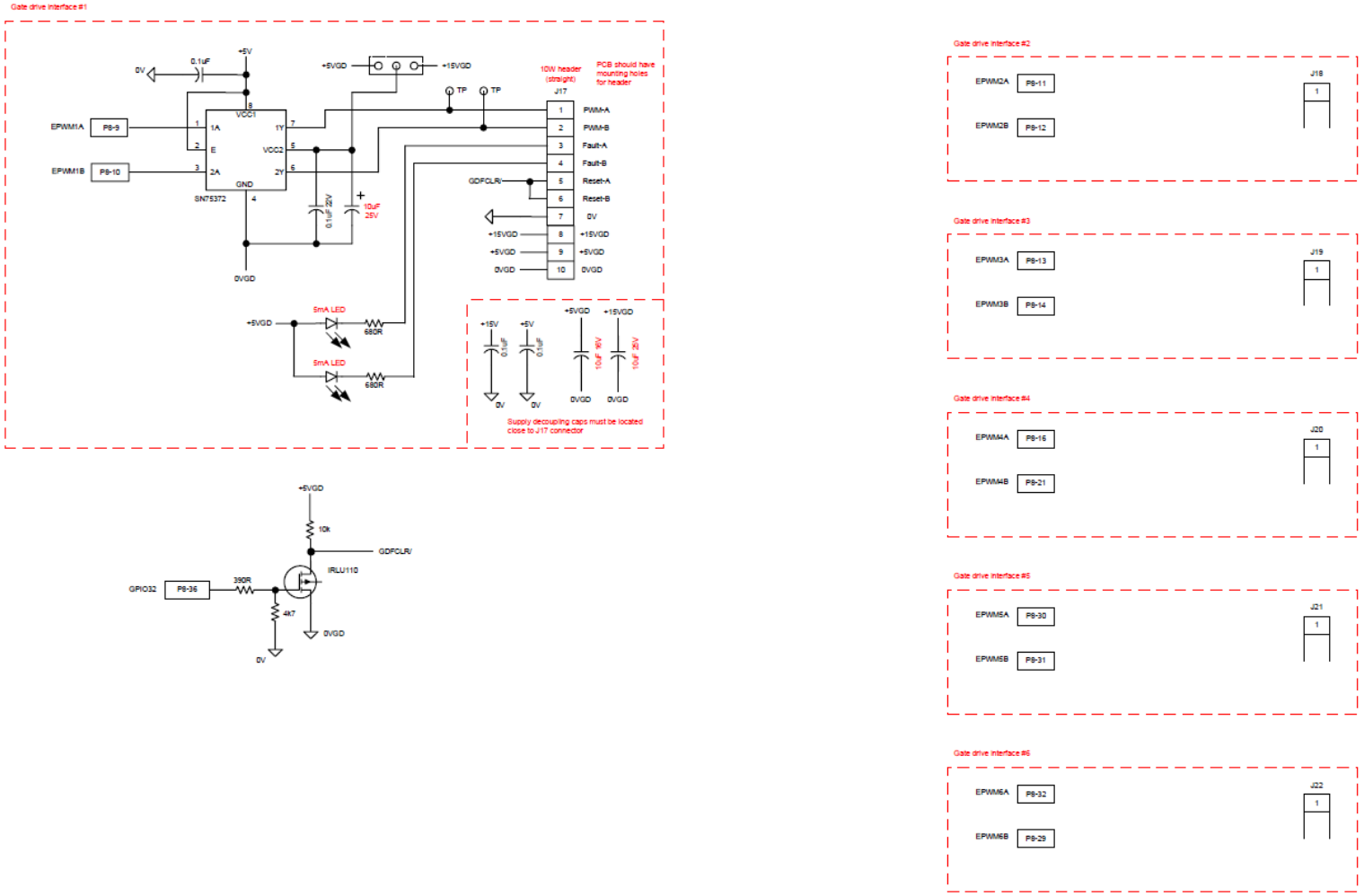

Figure E.2 F28335 Drive Basic Design—Gate Drive Interface

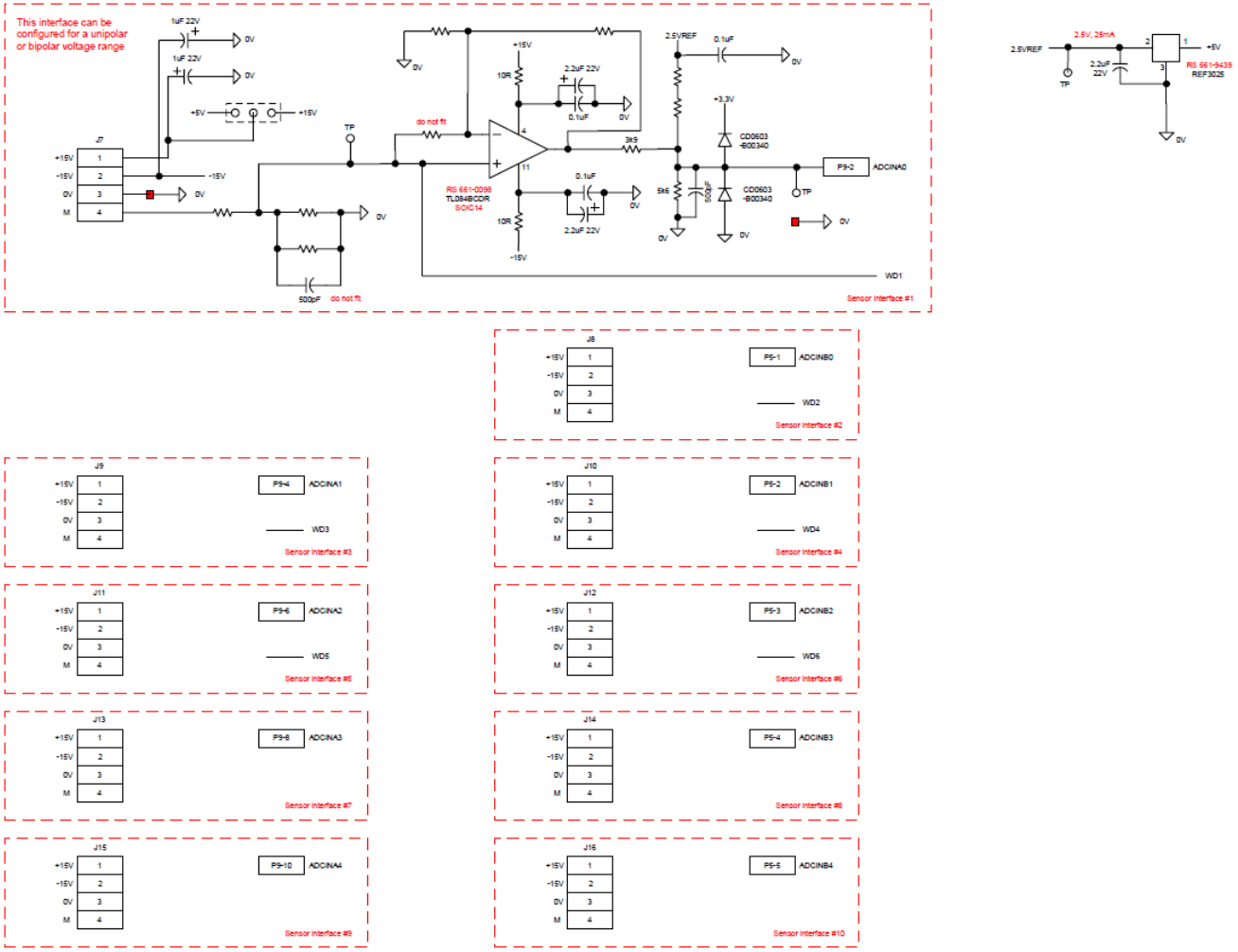

Figure E.3 F28335 Drive Basic Design—ADC

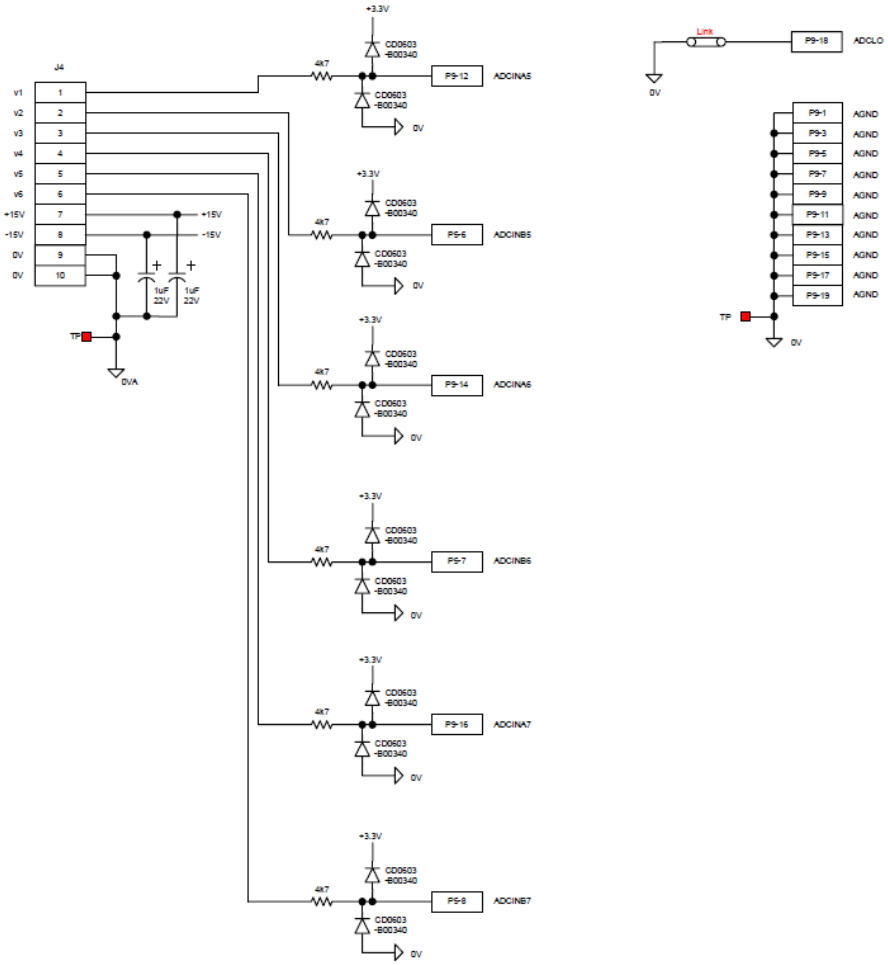

Figure E.4 F28335 Drive Basic Design—ADC Details

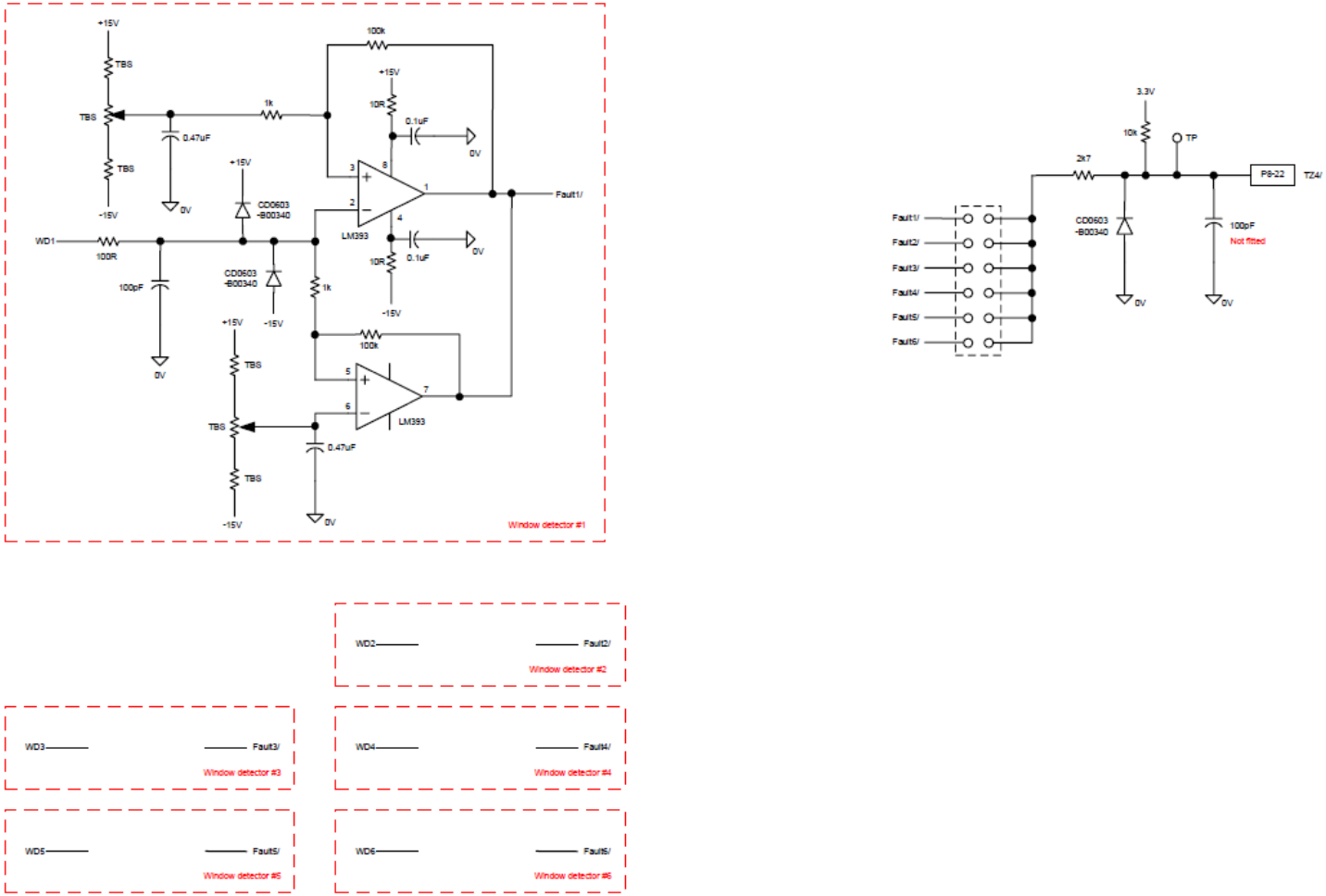

Figure E.5 F28335 Drive Basic Design—Window Detector

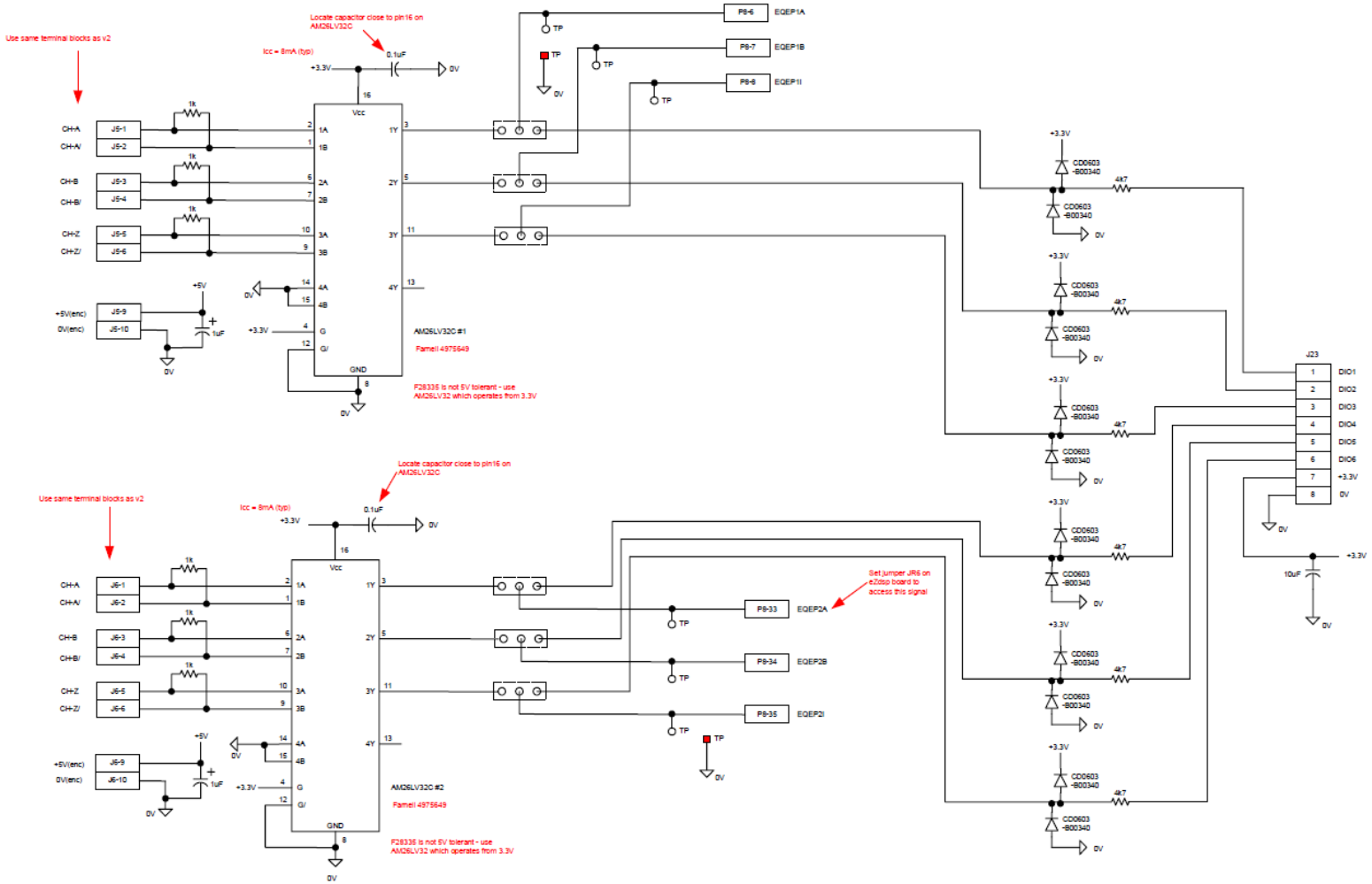

Figure E.6 F28335 Drive Basic Design—Encoder (EQEP)

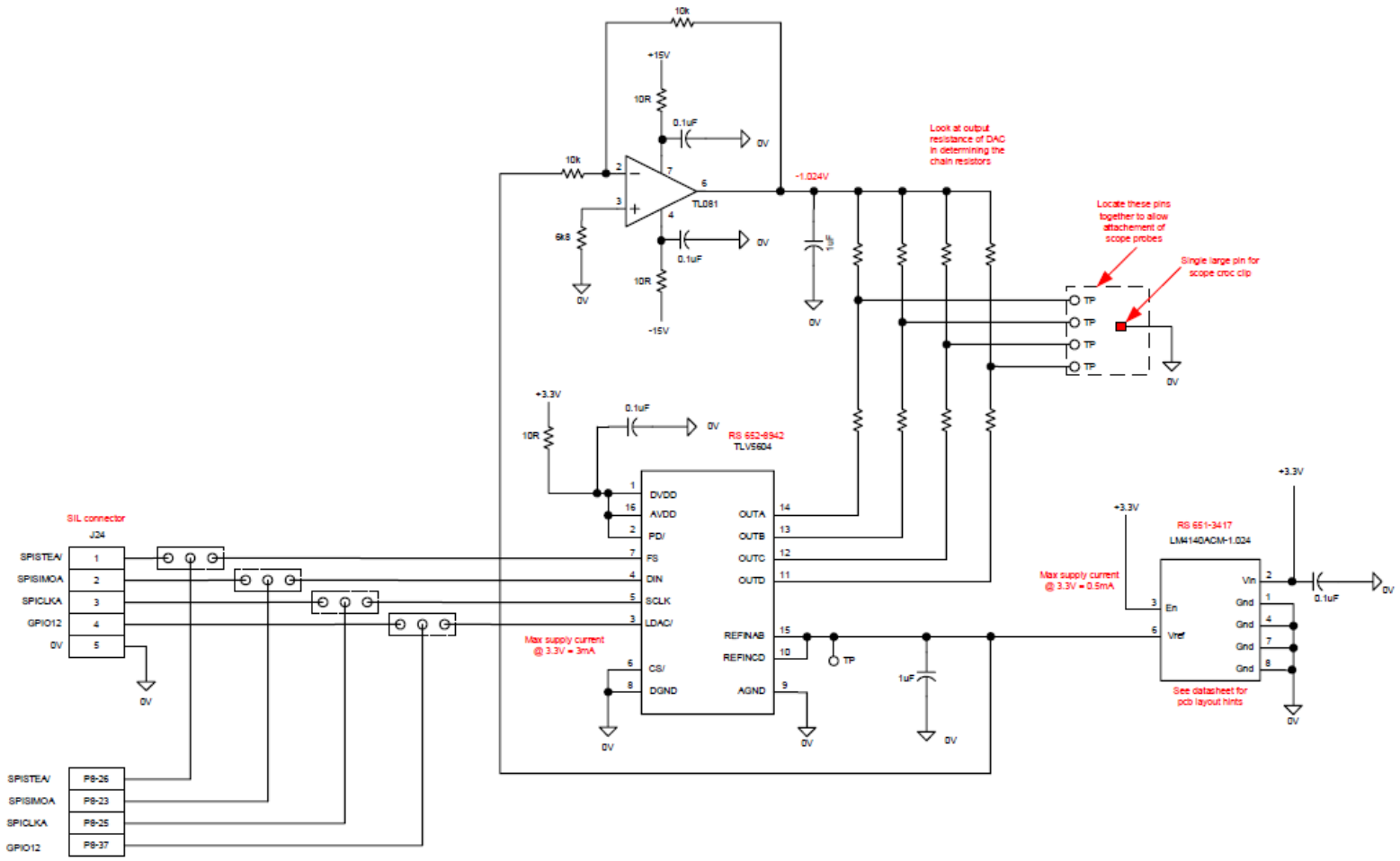

Figure E.7 F28335 Drive Basic Design—DAC

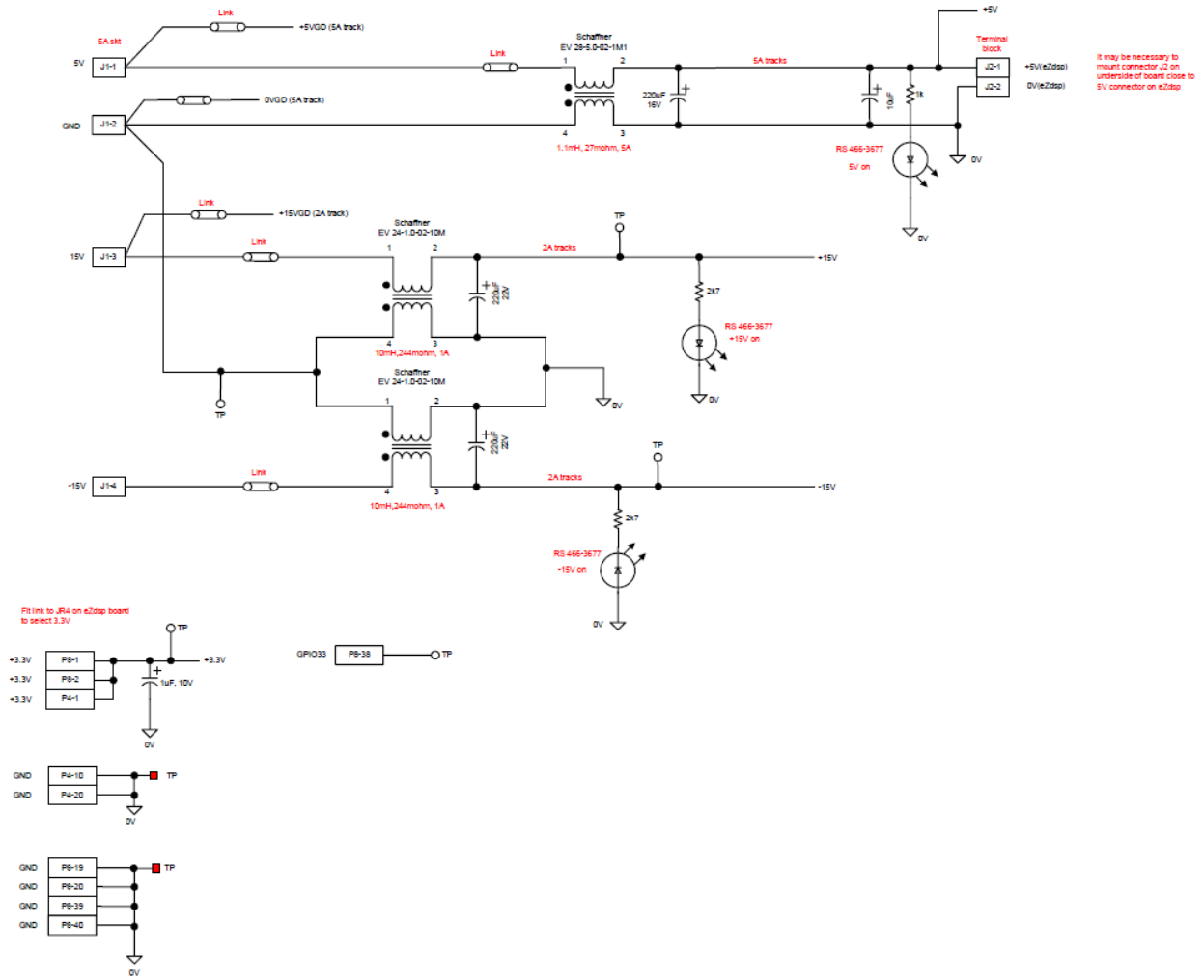

Figure E.8 F28335 Drive Basic Design—Power Supplier Unit (PSU)

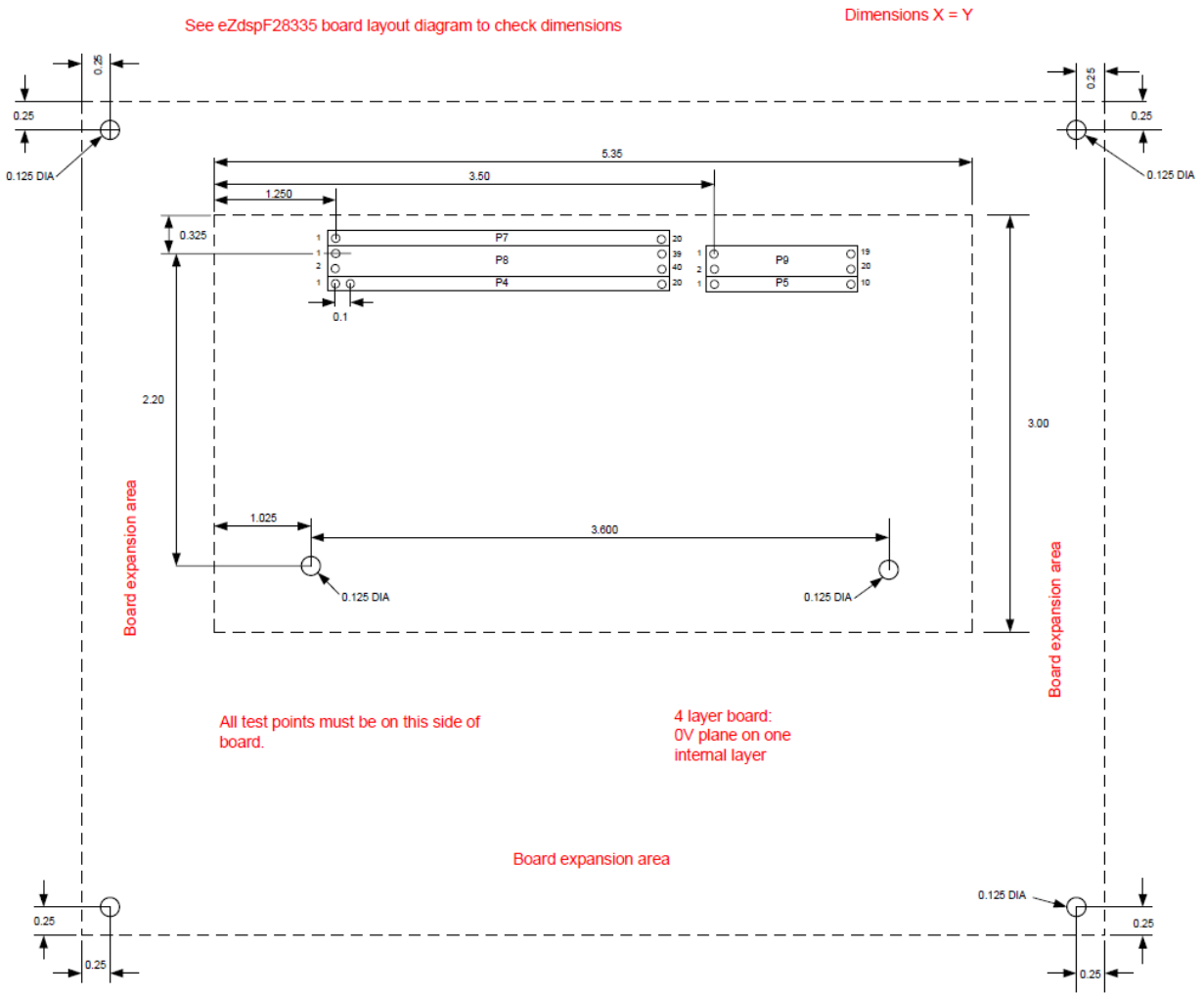

Figure E.9 F28335 Drive Basic Design— board layout diagram to check dimensions

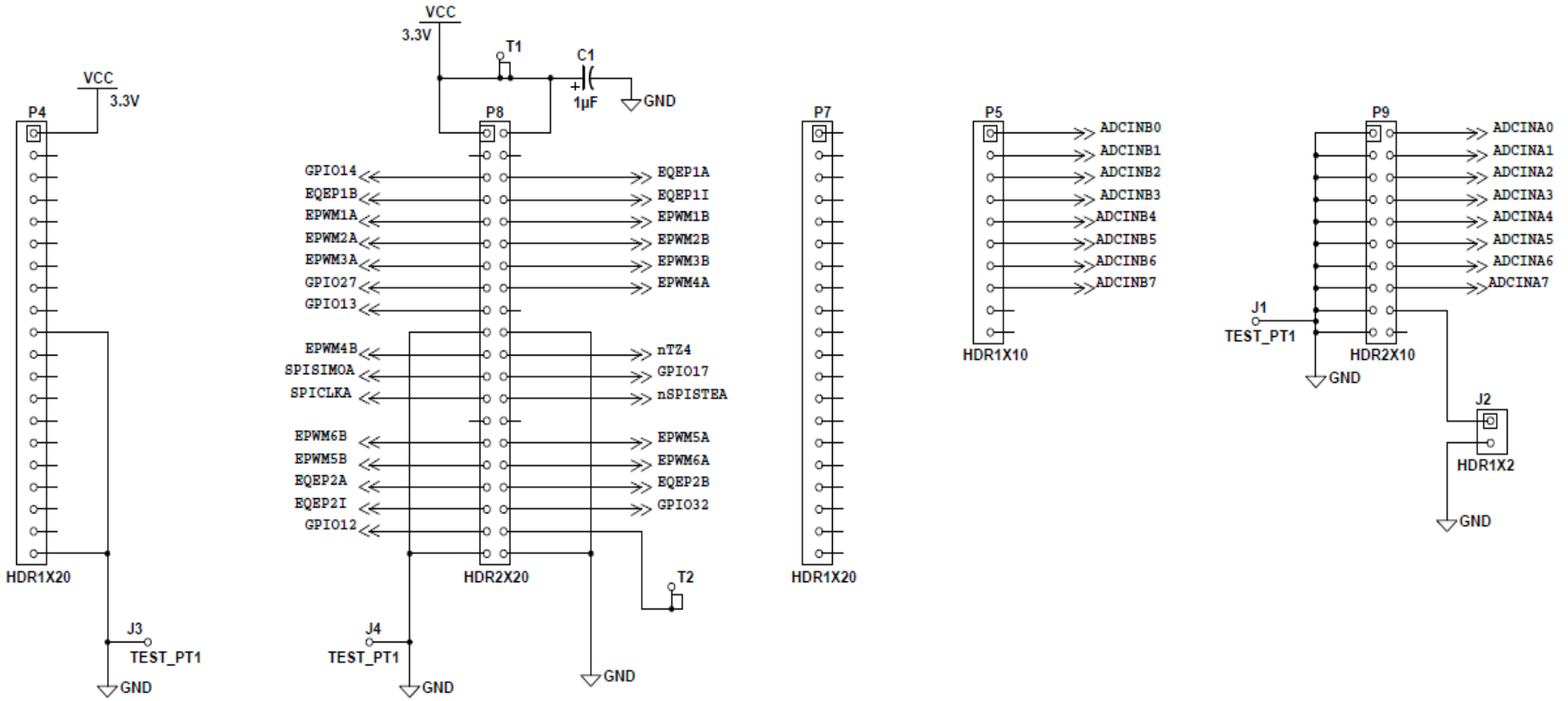

Figure E.10 Motor Drive Board Interface—Pin Connector

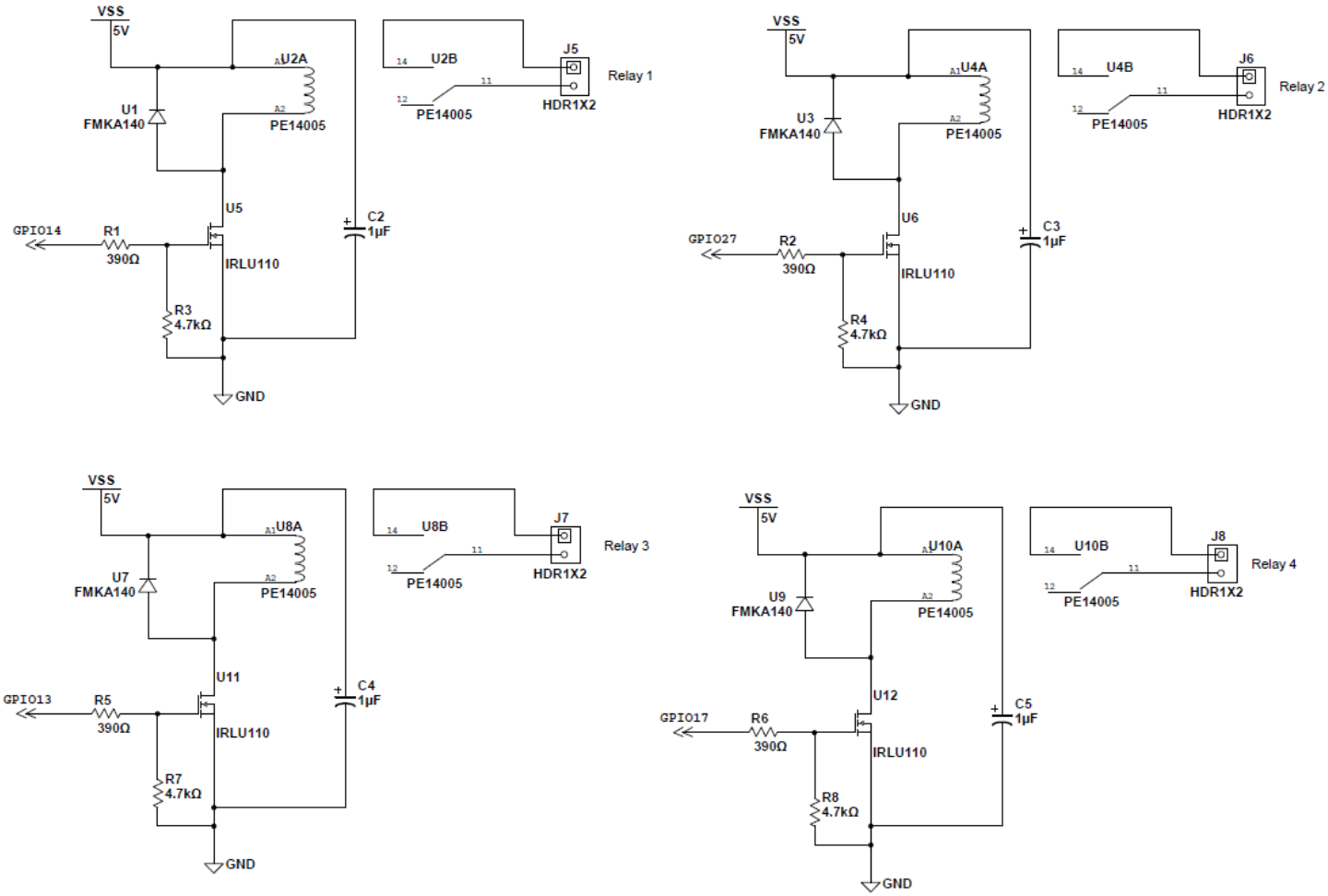

Figure E.11 Motor Drive Board Interface—Relays

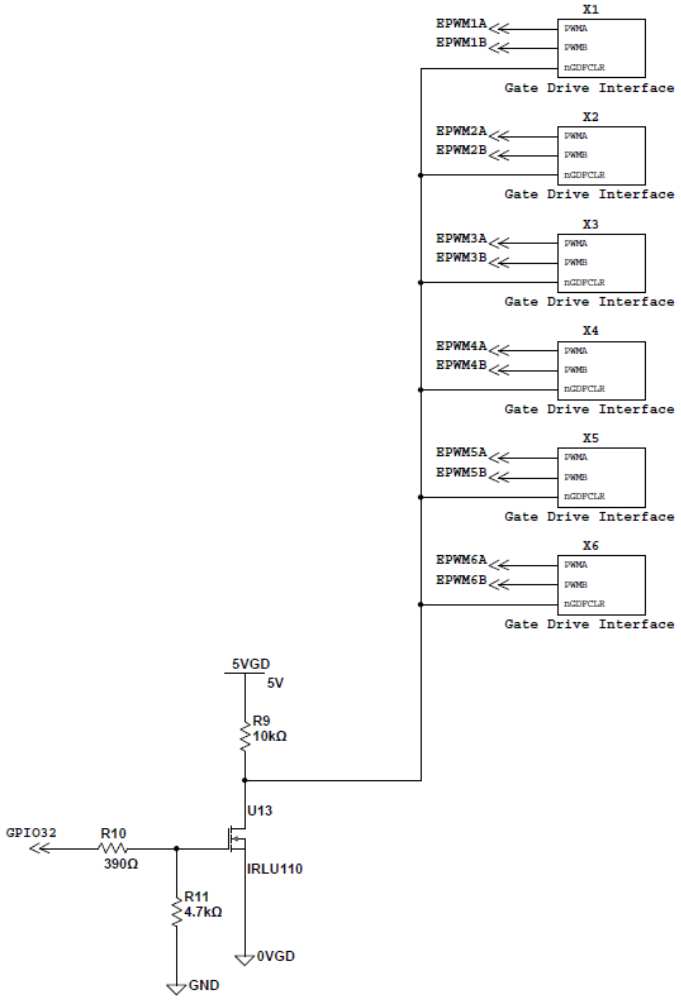

Figure E.12 Motor Drive Board Interface—Gate Drive Interface (EPWM)

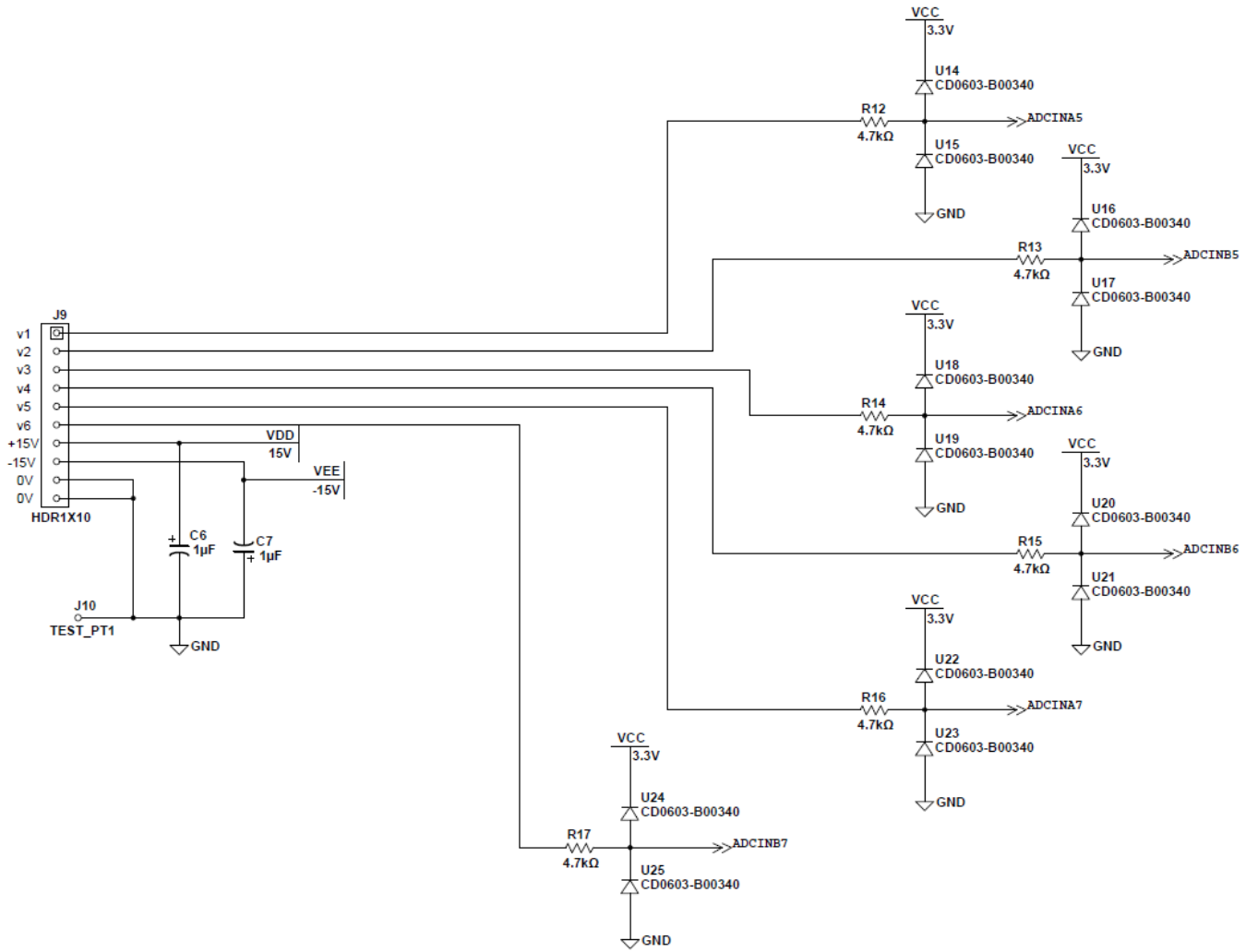

Figure E.13 Motor Drive Board Interface—Analogue Interface

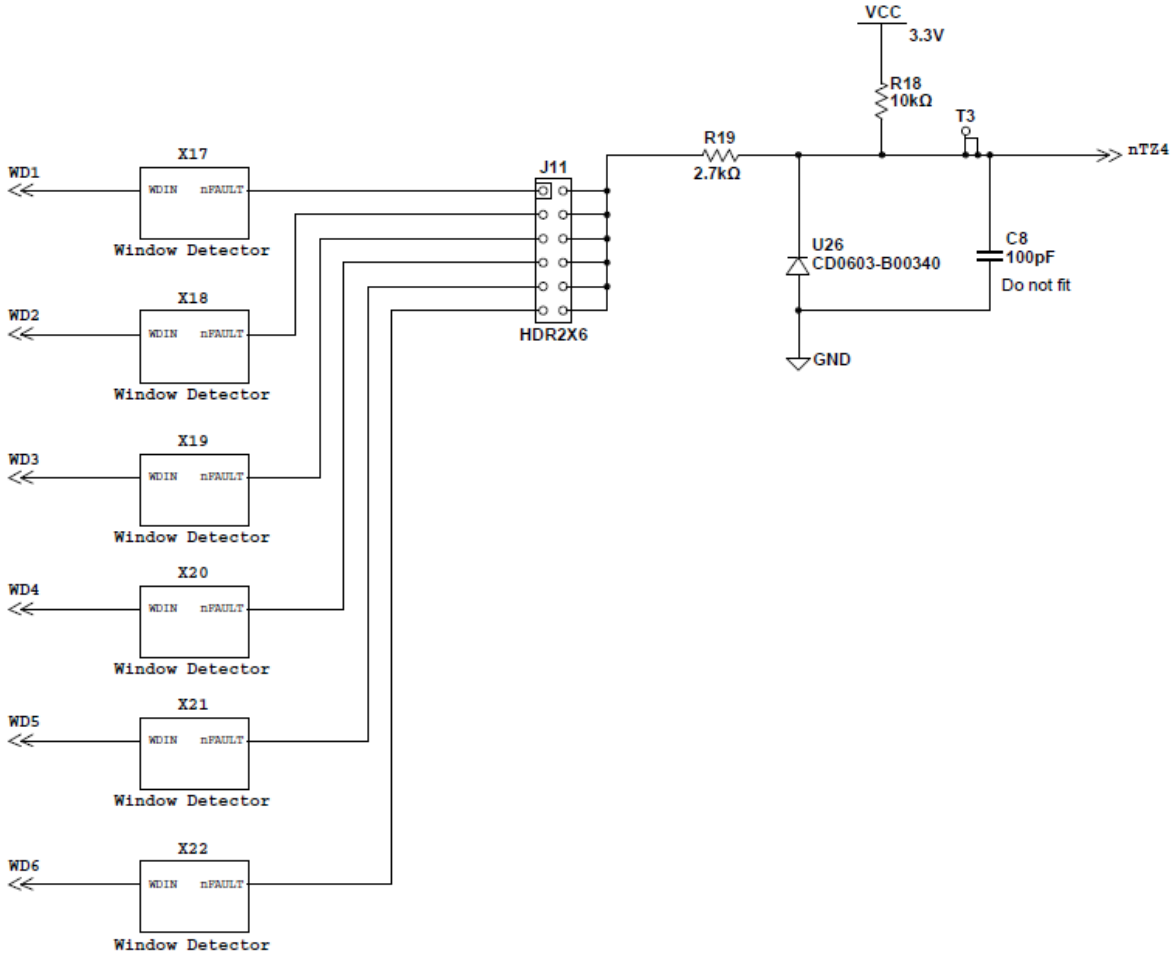

Figure E.14 Motor Drive Board Interface—Window Detector

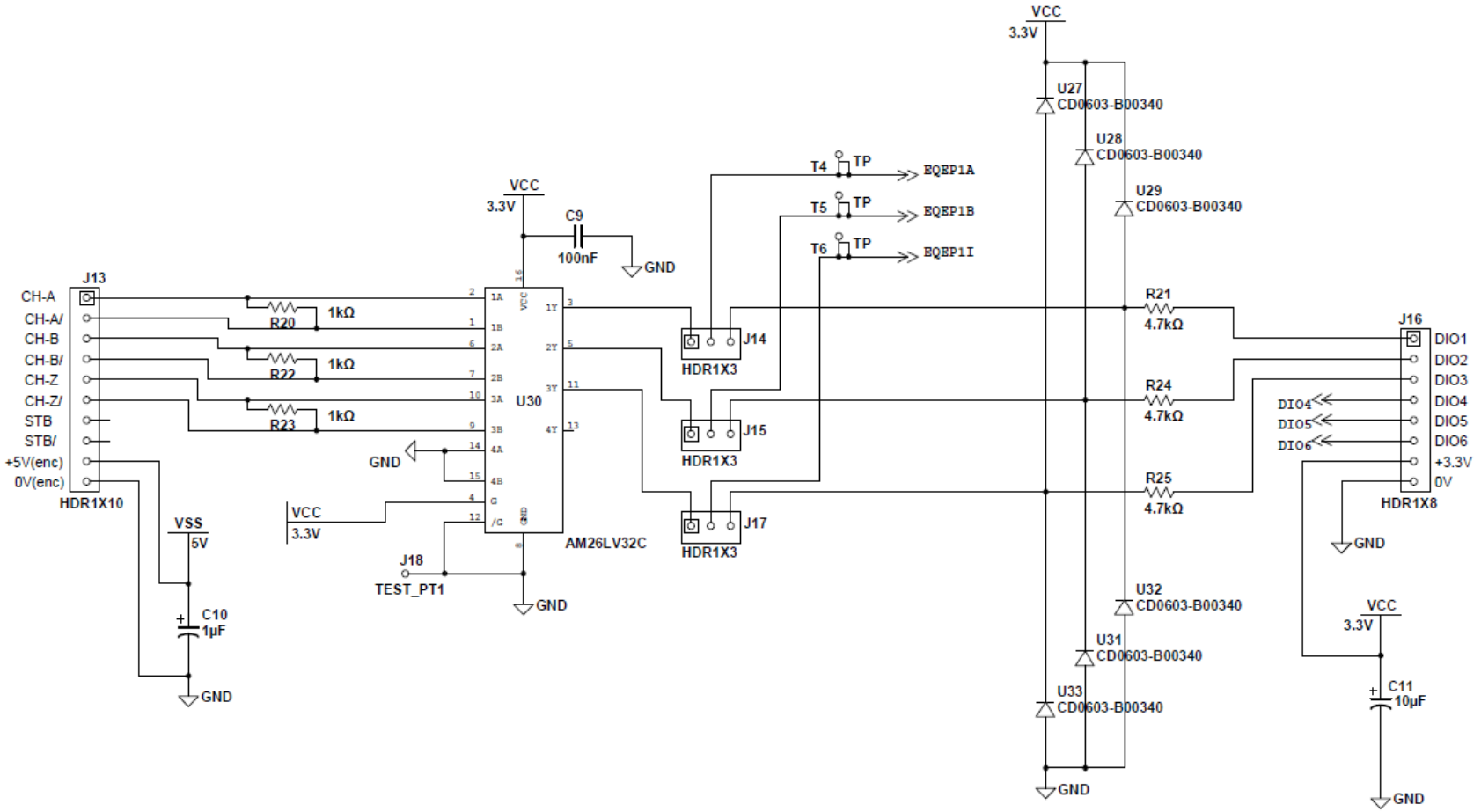

Figure E.15 Motor Drive Board Interface—Encoder Interface (EQEP 1)

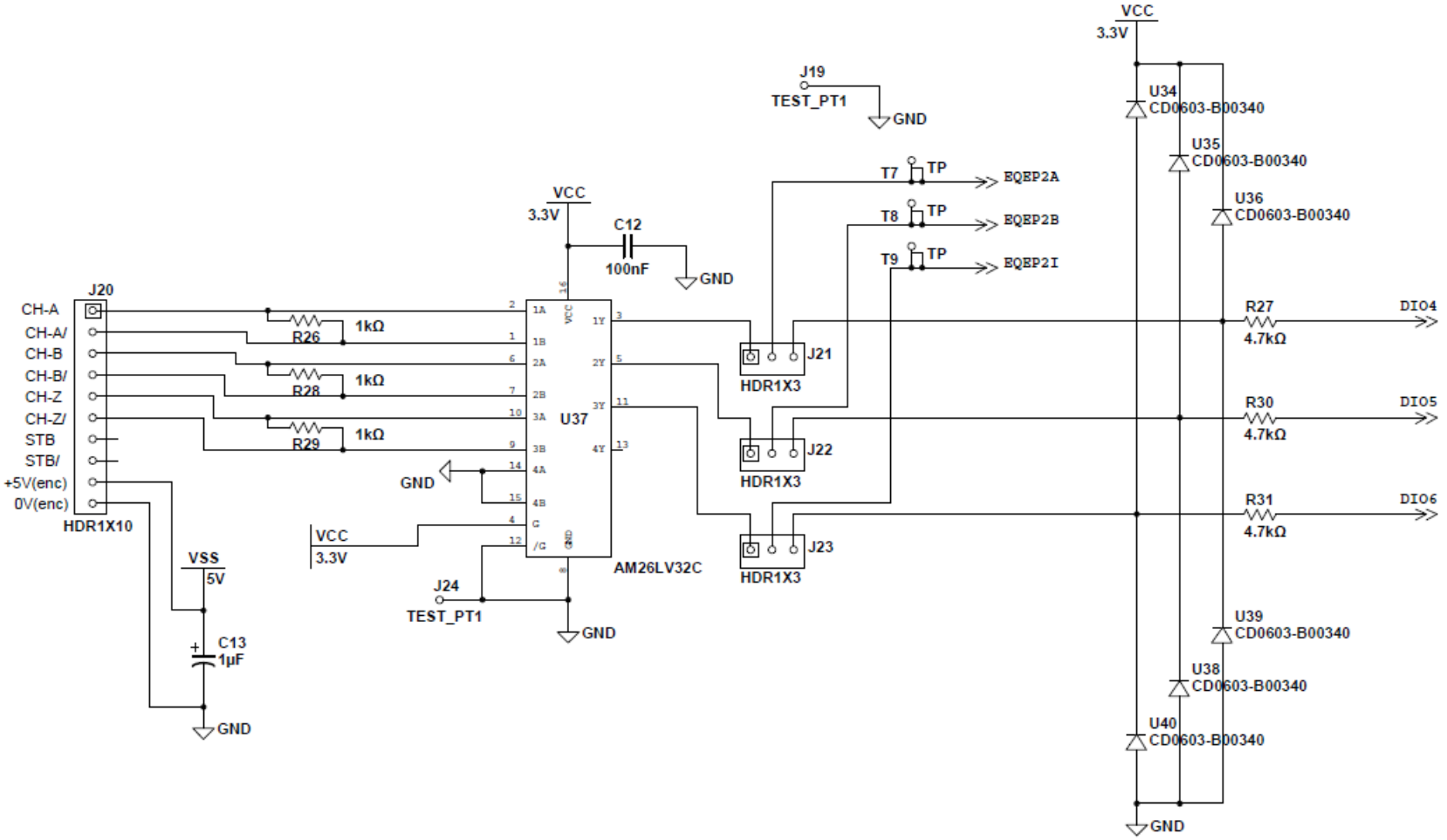

Figure E.16 Motor Drive Board Interface—Encoder Interface (EQEP 2)

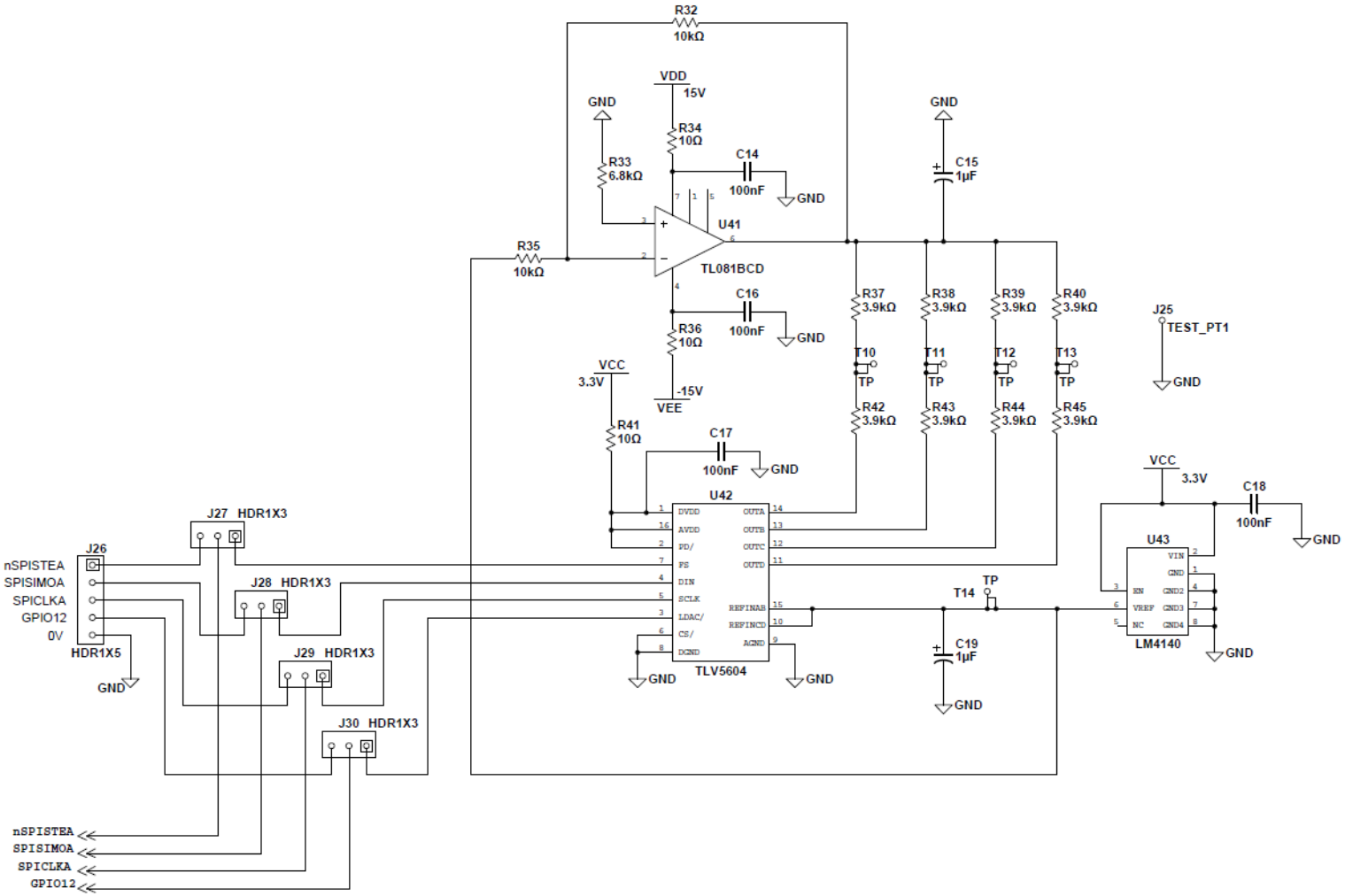

Figure E.17 Motor Drive Board Interface—DAC

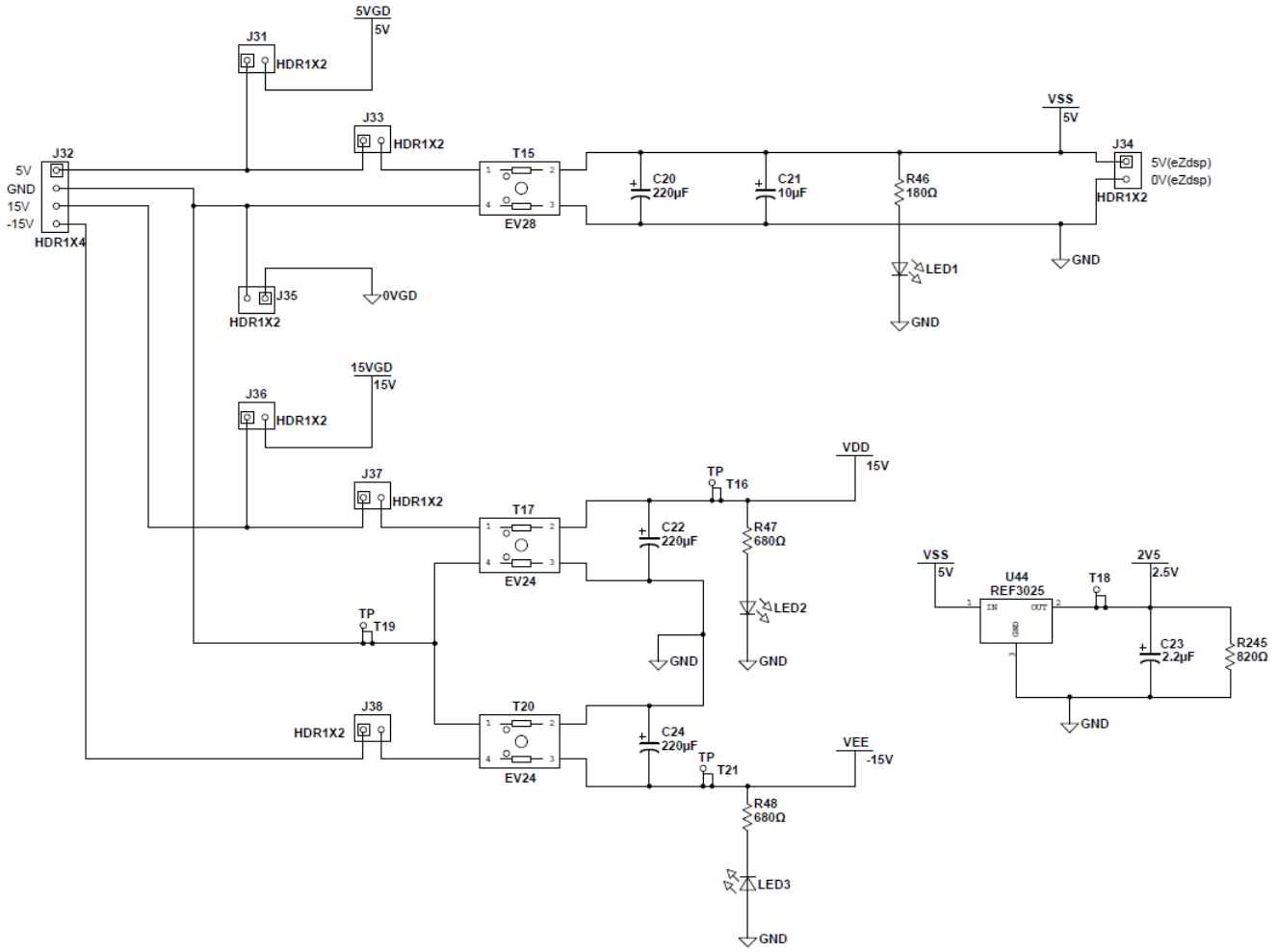

Figure E.18 Motor Drive Board Interface—Power Supplier Unit (PSU)

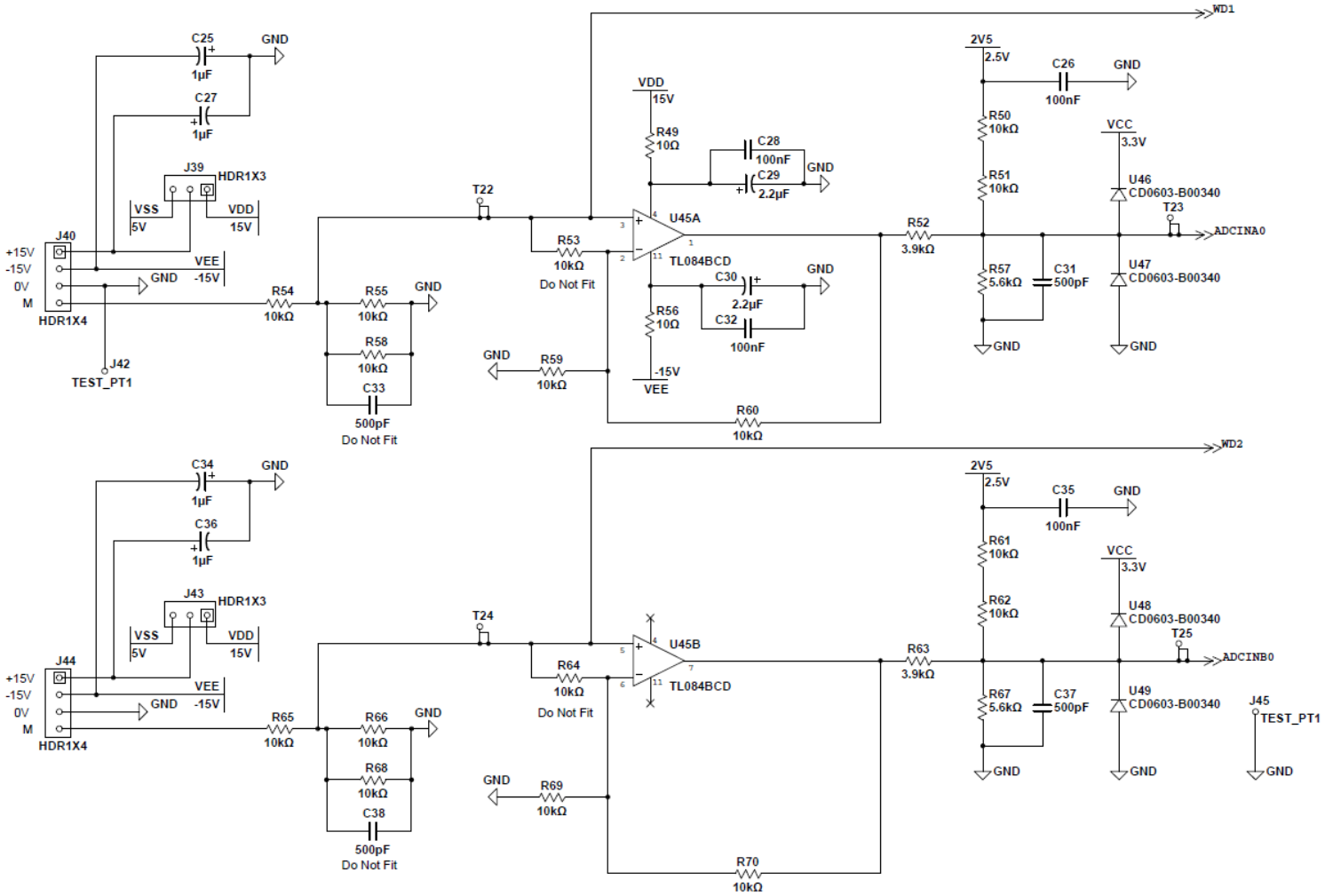

Figure E. 19 Motor Drive Board Interface—Sensor Interface 1

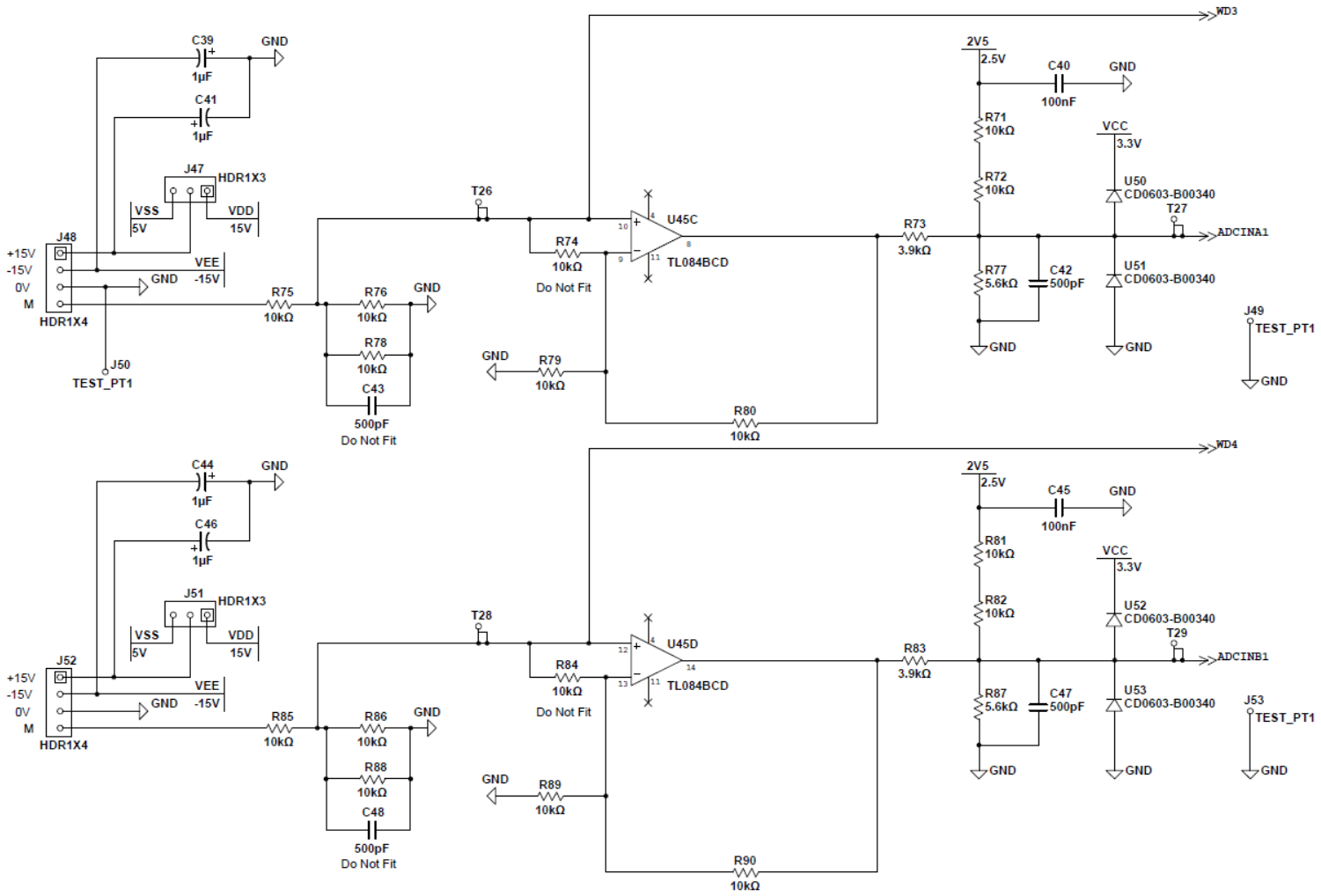

Figure E. 20 Motor Drive Board Interface—Sensor Interface 2

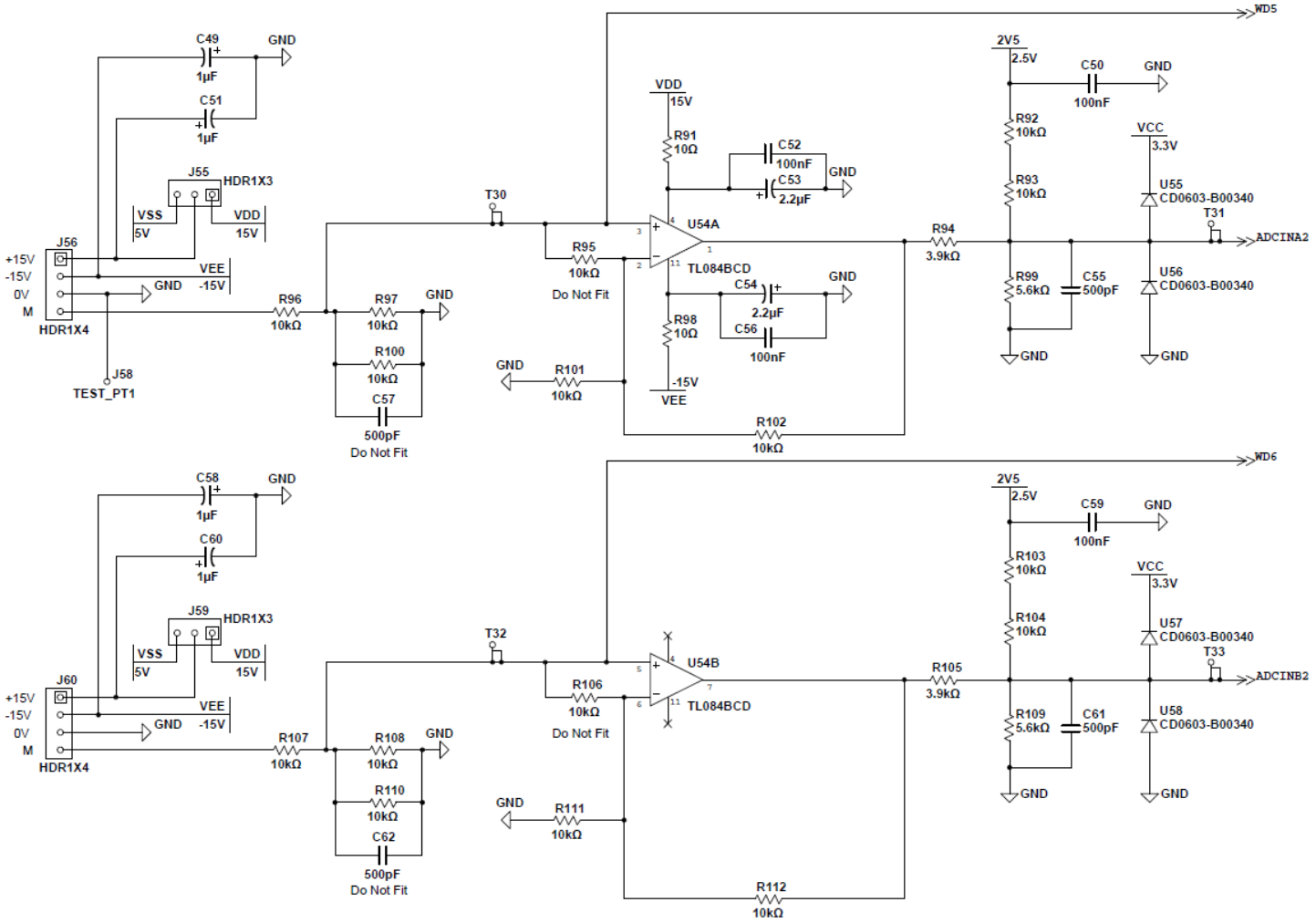

Figure E.21 Motor Drive Board Interface—Sensor Interface 3

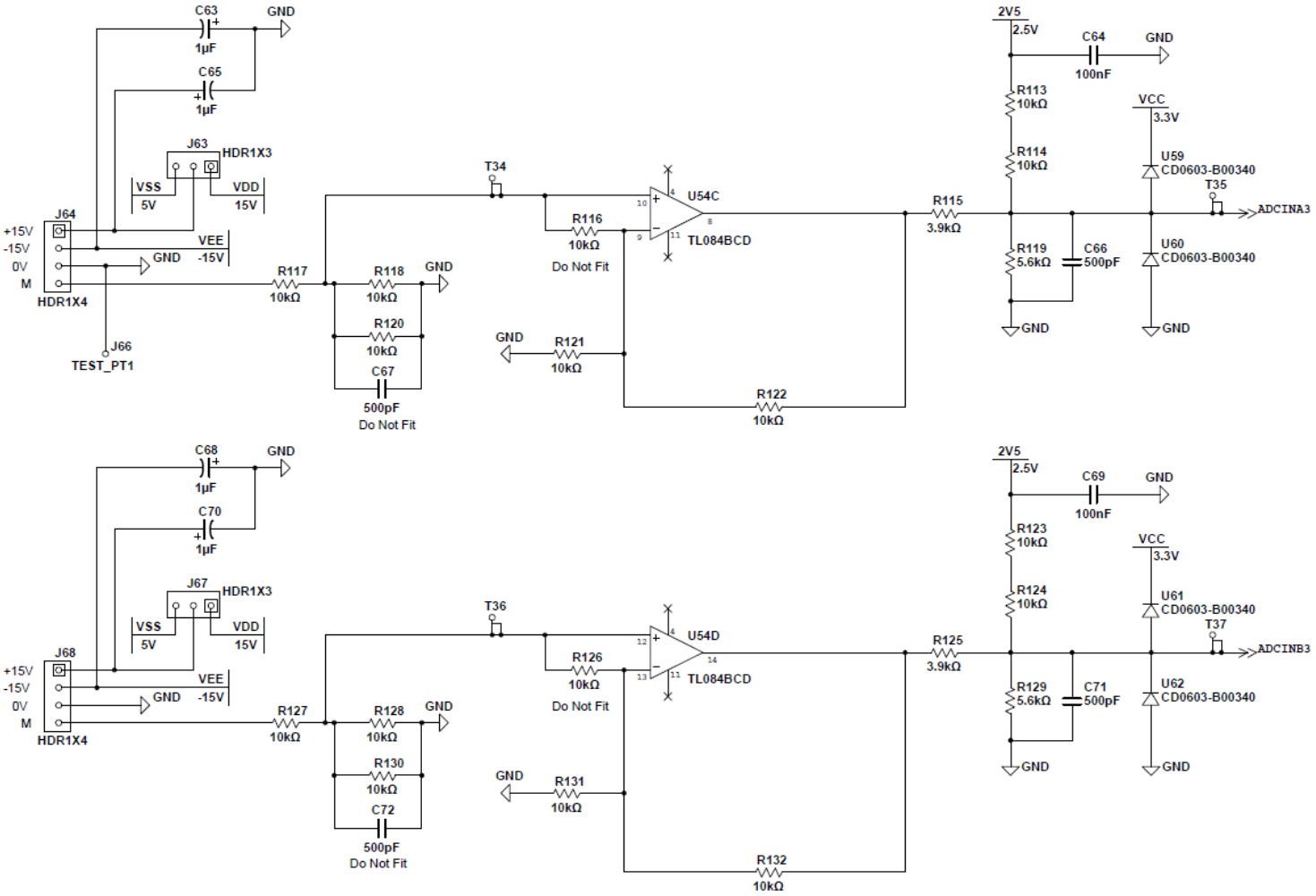

Figure E.22 Motor Drive Board Interface—Sensor Interface 4

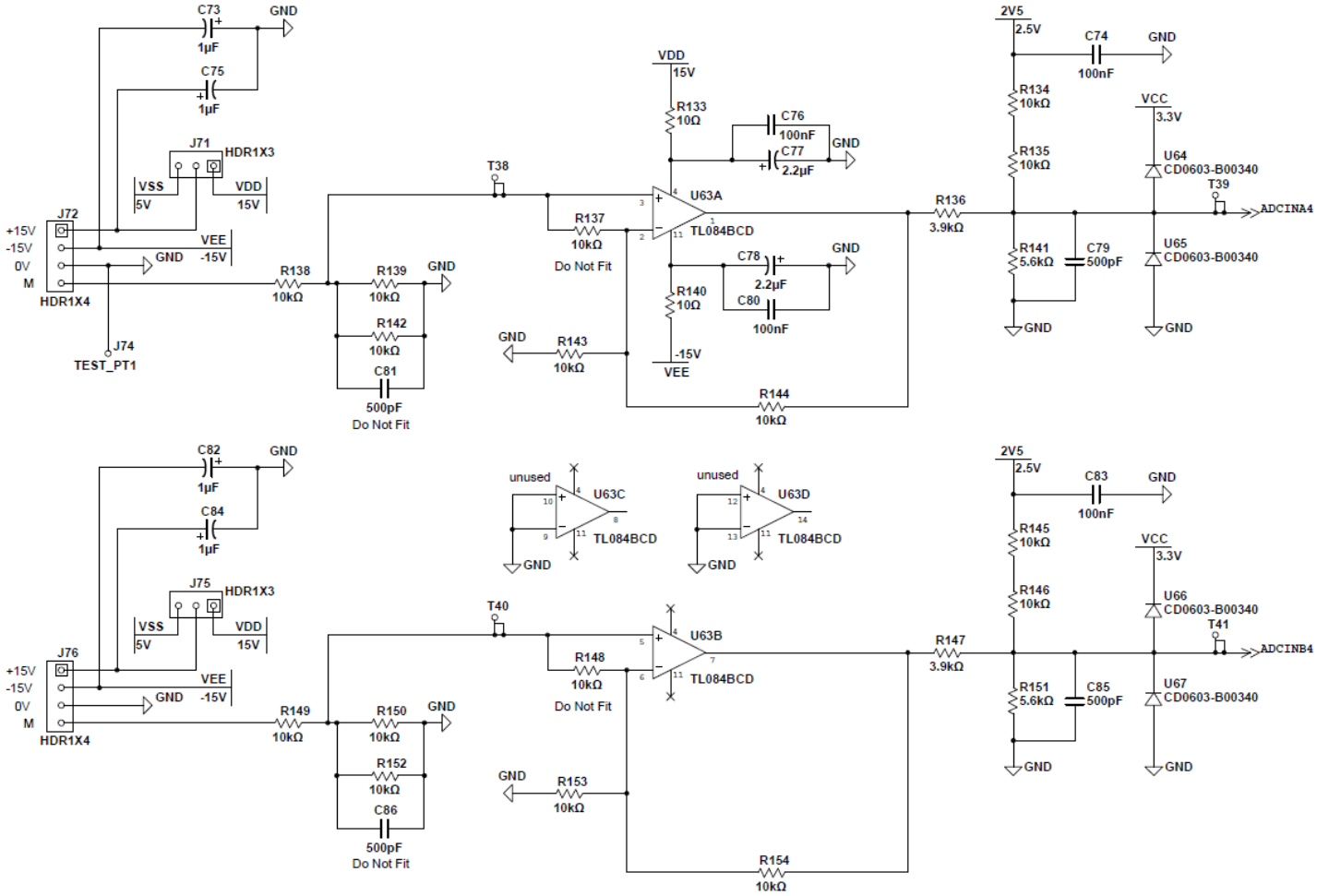

Figure E.23 Motor Drive Board Interface—Sensor Interface 5

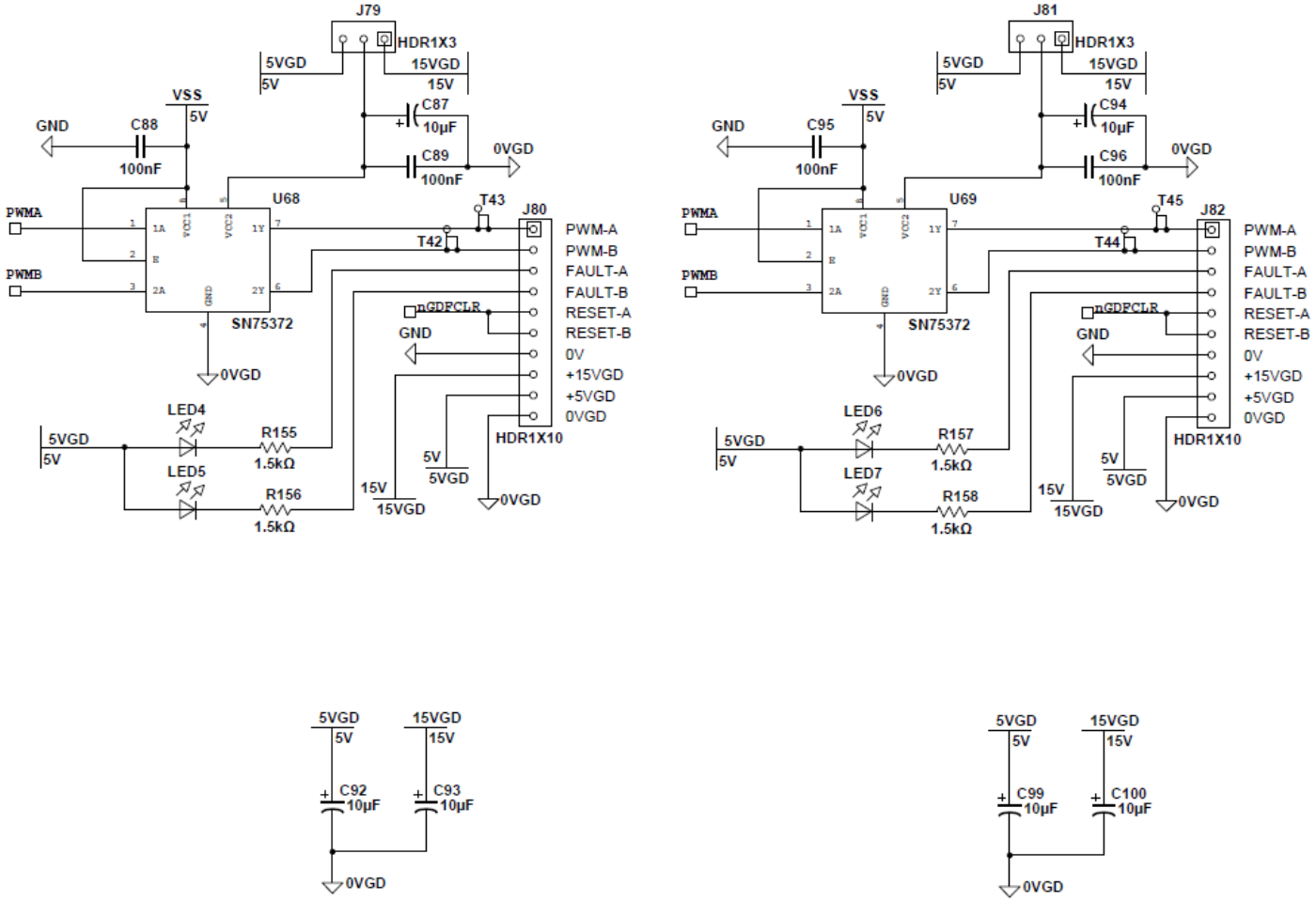

Figure E.24 Motor Drive Board Interface—Gate Drive Interface 1 (EPWM 1 & 2)

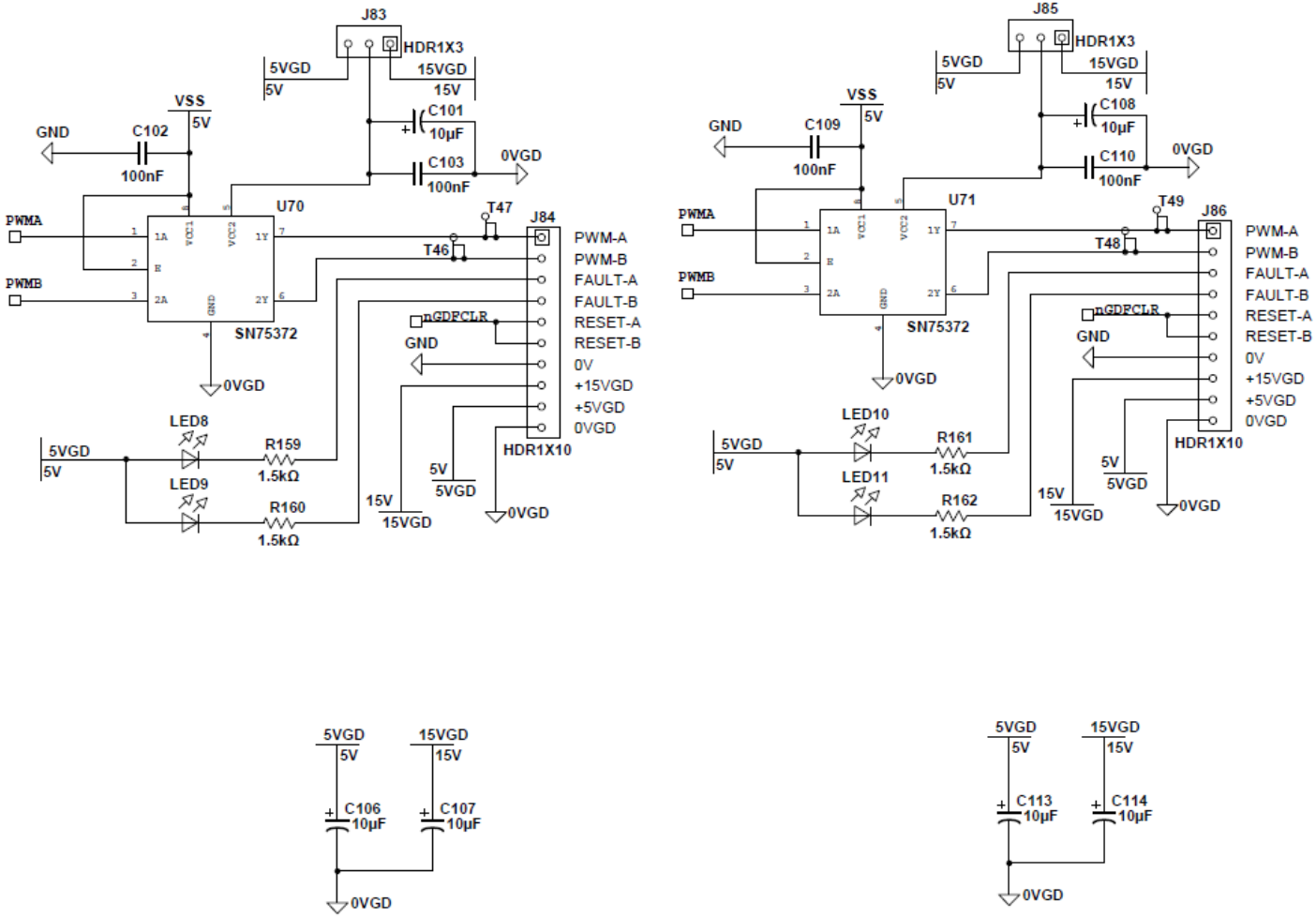

Figure E.25 Motor Drive Board Interface—Gate Drive Interface 2 (EPWM 3 & 4)

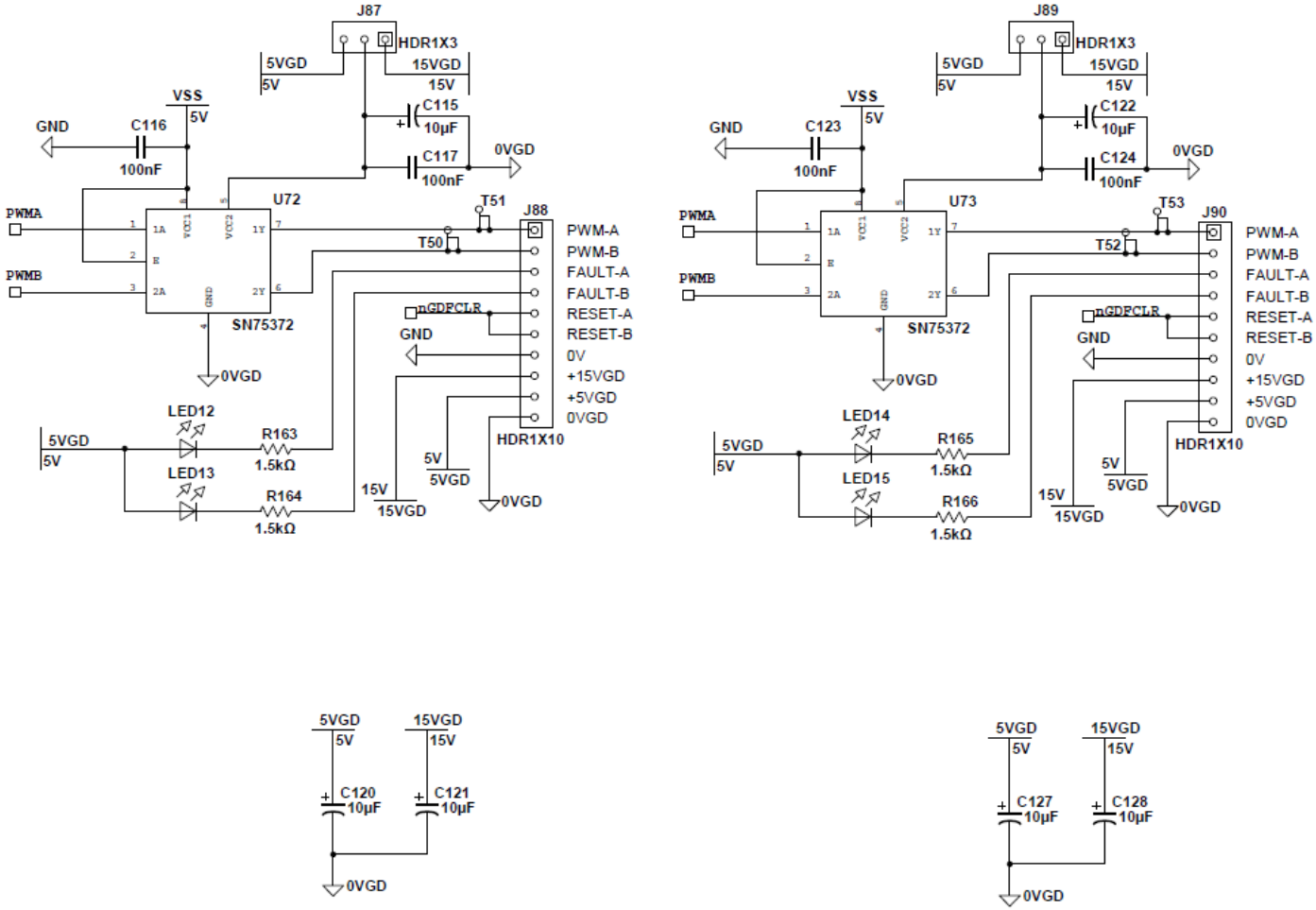

Figure E.26 Motor Drive Board Interface—Gate Drive Interface 3 (EPWM 5 & 6)

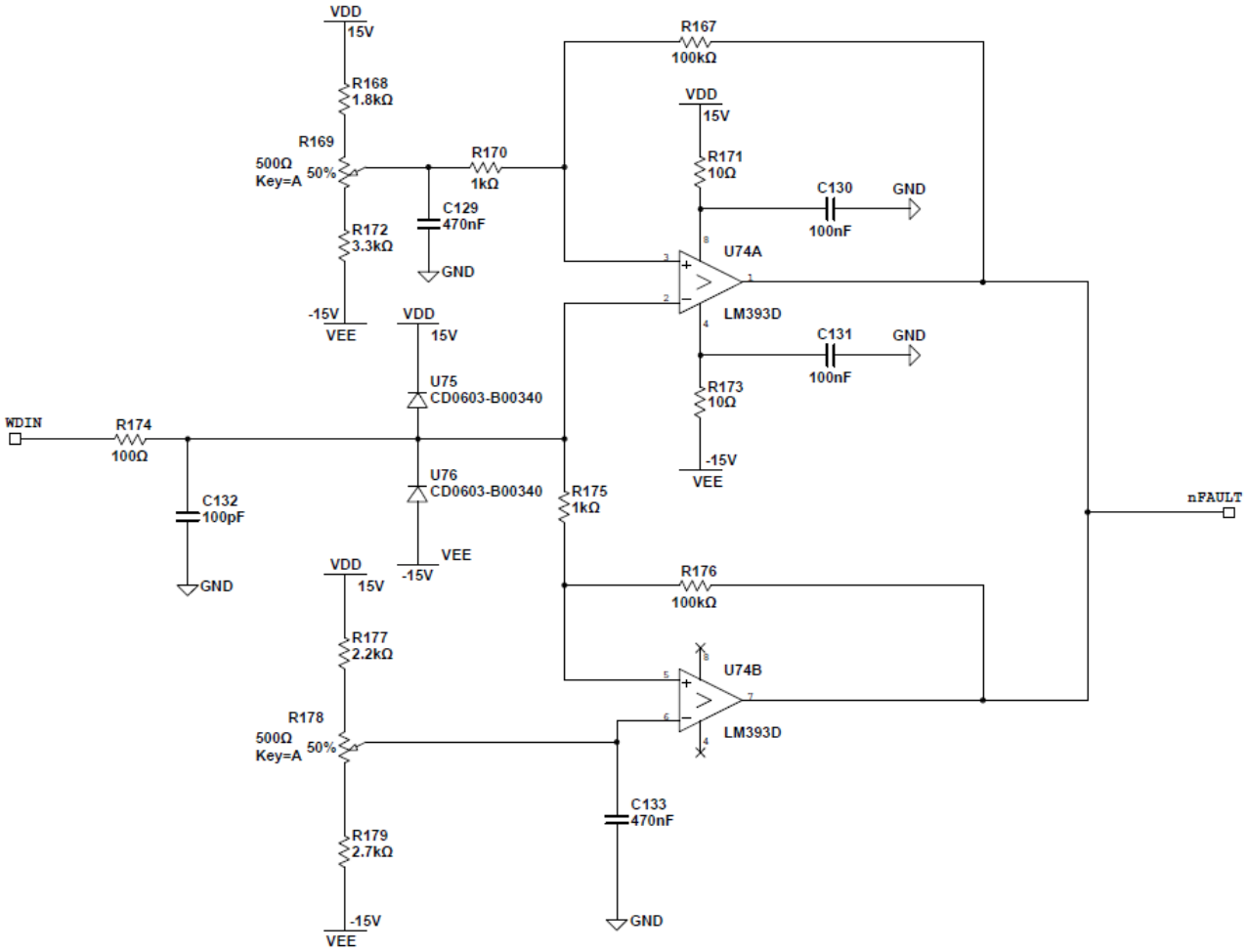

Figure E.27 Motor Drive Board Interface—Window Detector 1

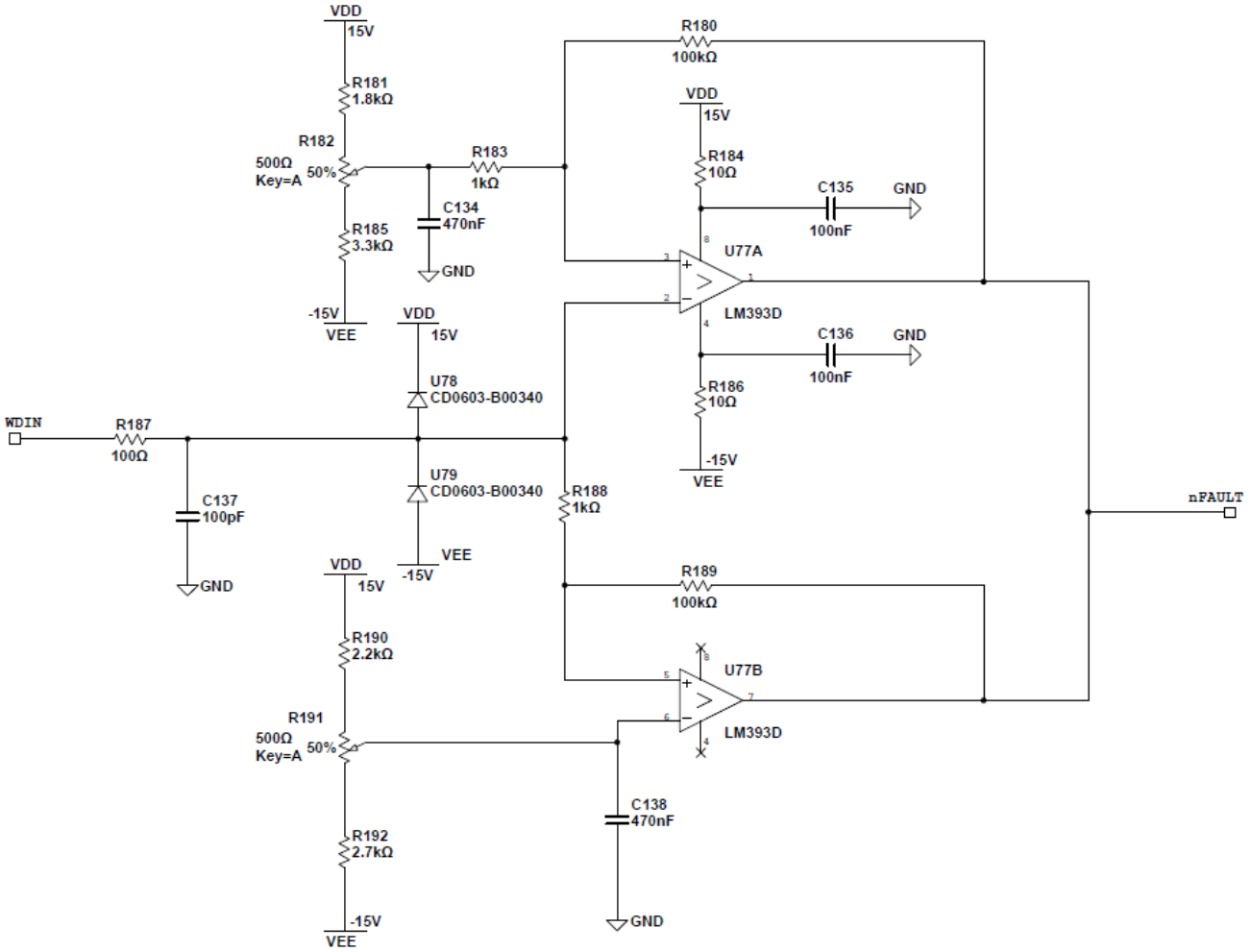

Figure E.28 Motor Drive Board Interface—Window Detector 2

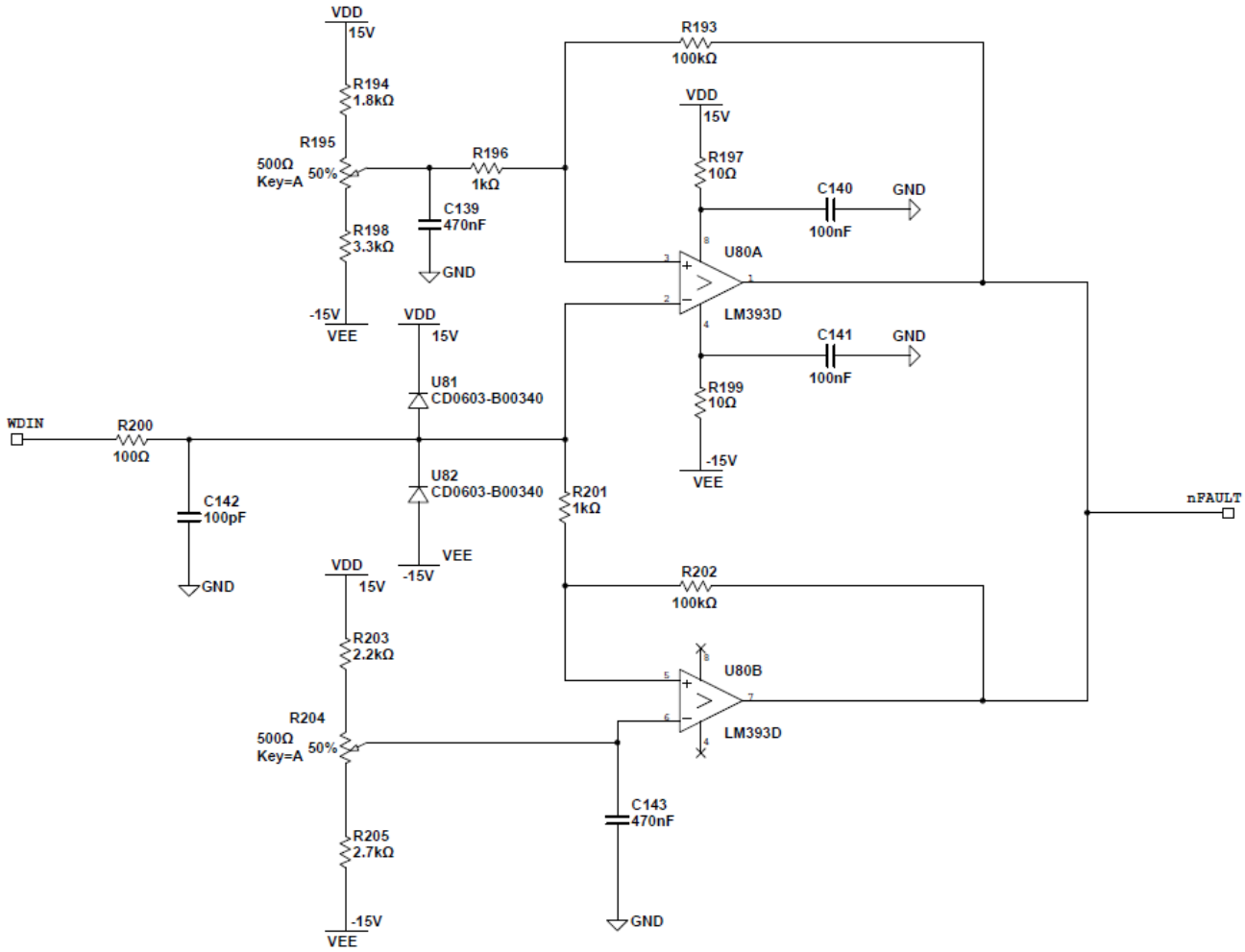

Figure E.29 Motor Drive Board Interface—Window Detector 3

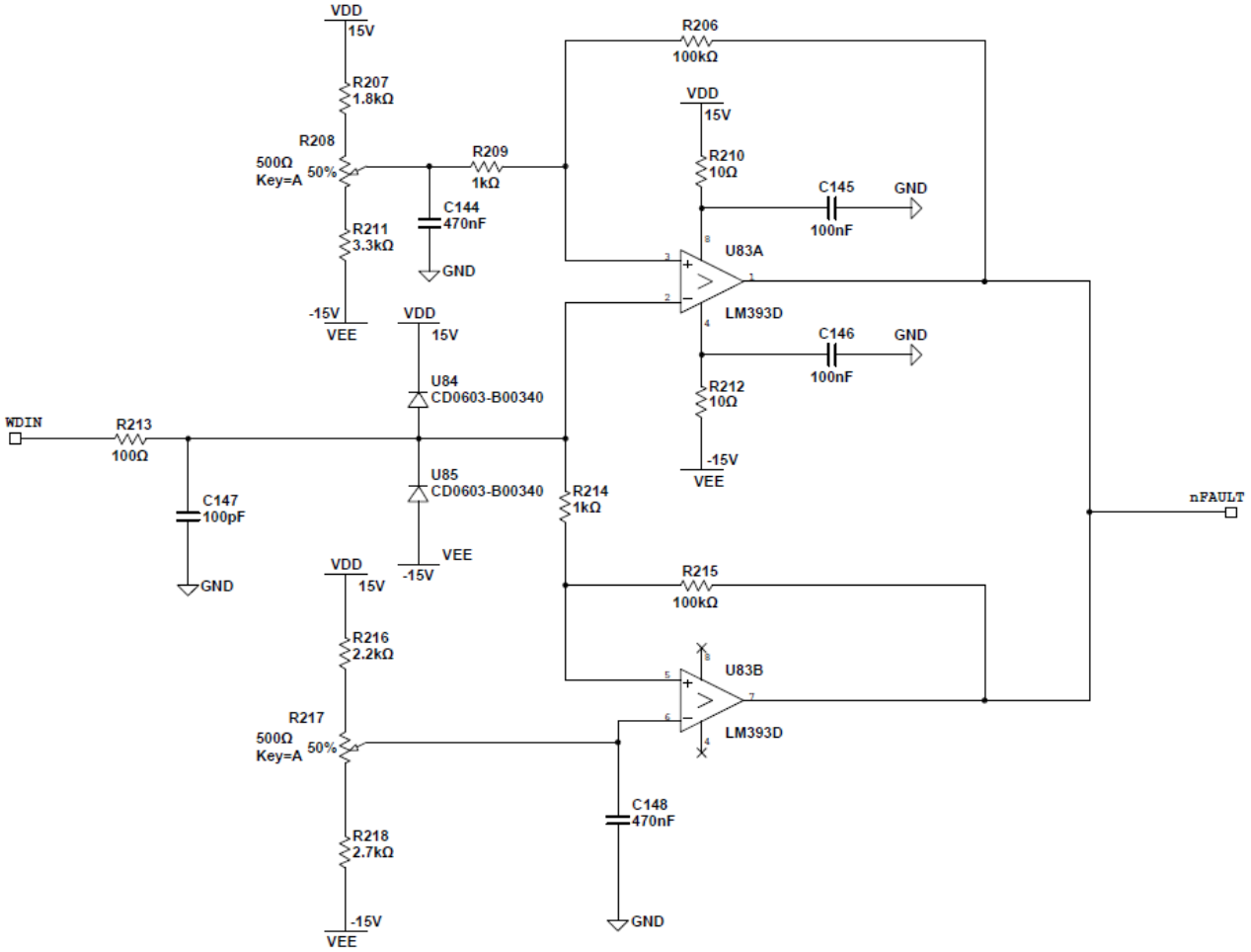

Figure E.30 Motor Drive Board Interface—Window Detector 4

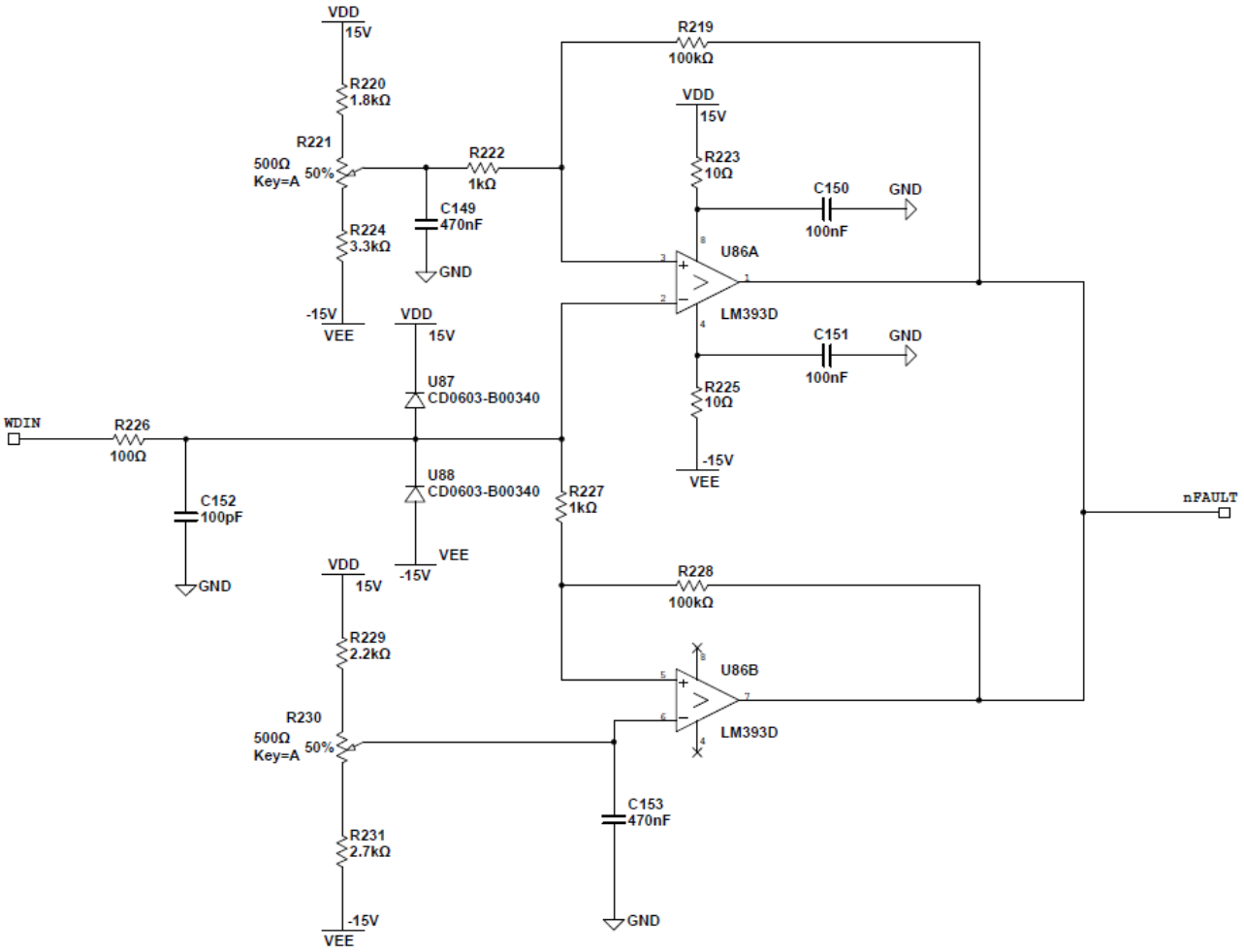

Figure E.31 Motor Drive Board Interface—Window Detector 5

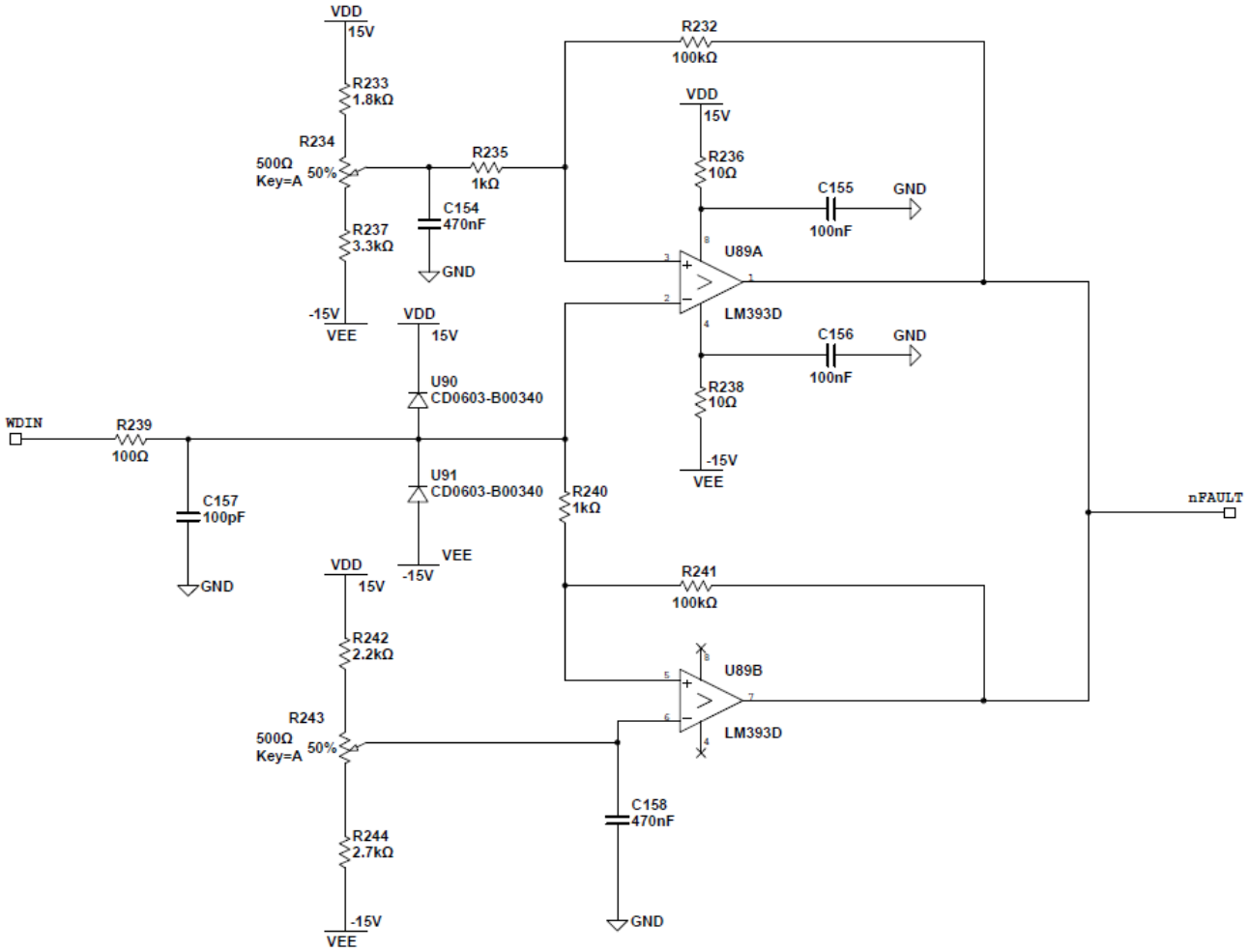

Figure E.32 Motor Drive Board Interface—Window Detector 6

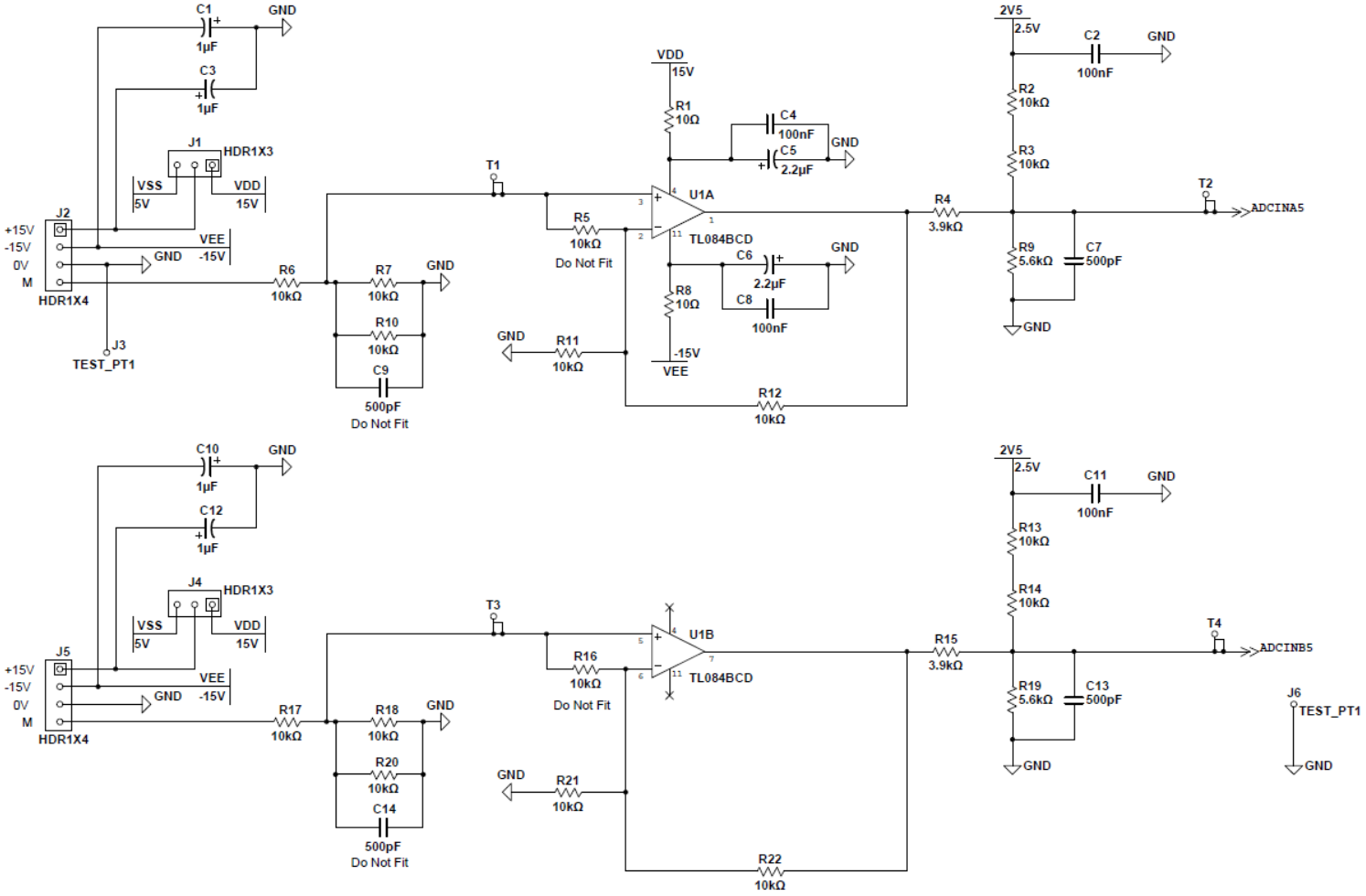

Figure E.33 Expansion Analogue Board Interface 1

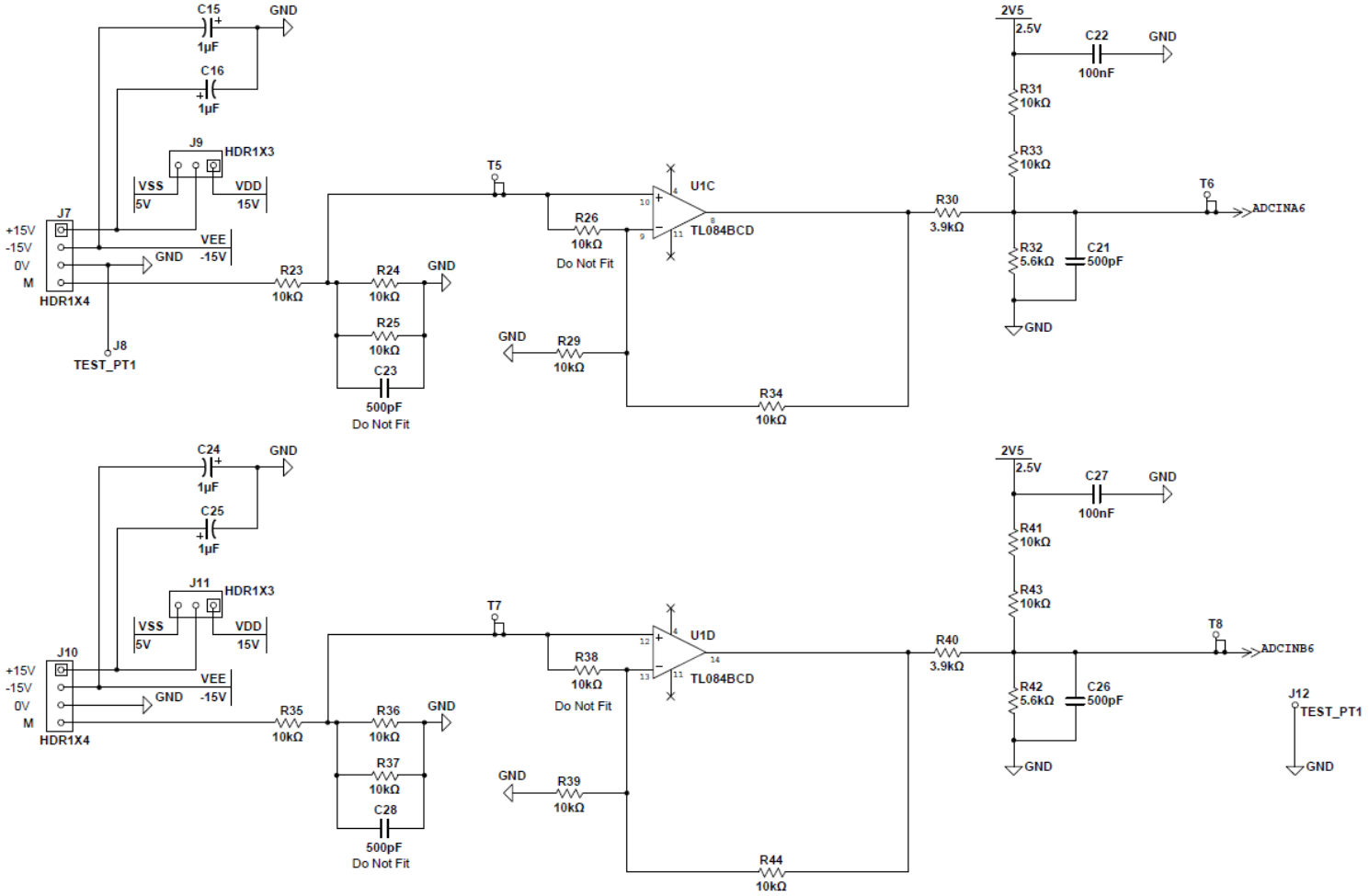

Figure E.34 Expansion Analogue Board Interface 2

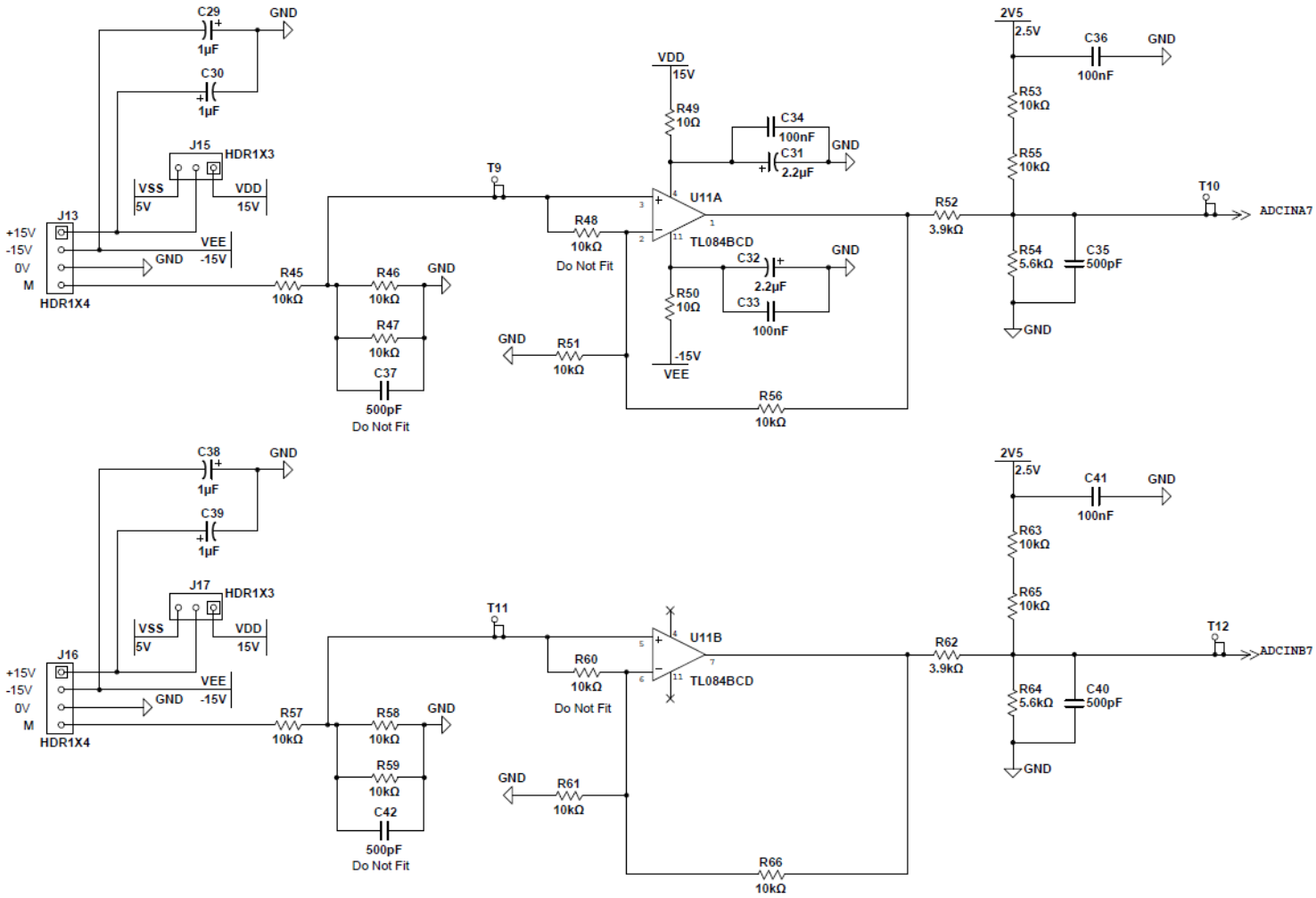

Figure E.35 Expansion Analogue Board Interface 3

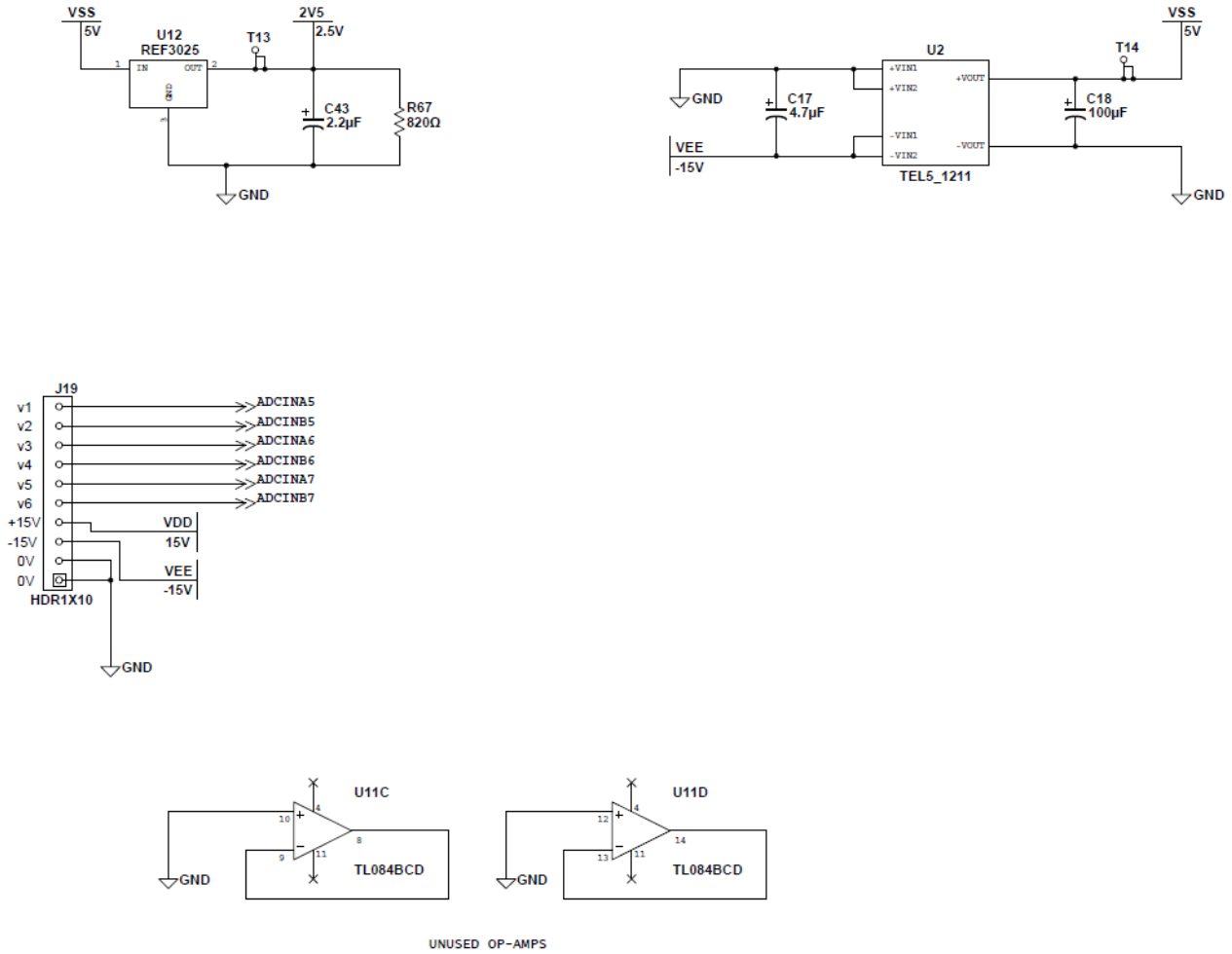

Figure E.36 Expansion Analogue Board Interface Power Supplier Unit

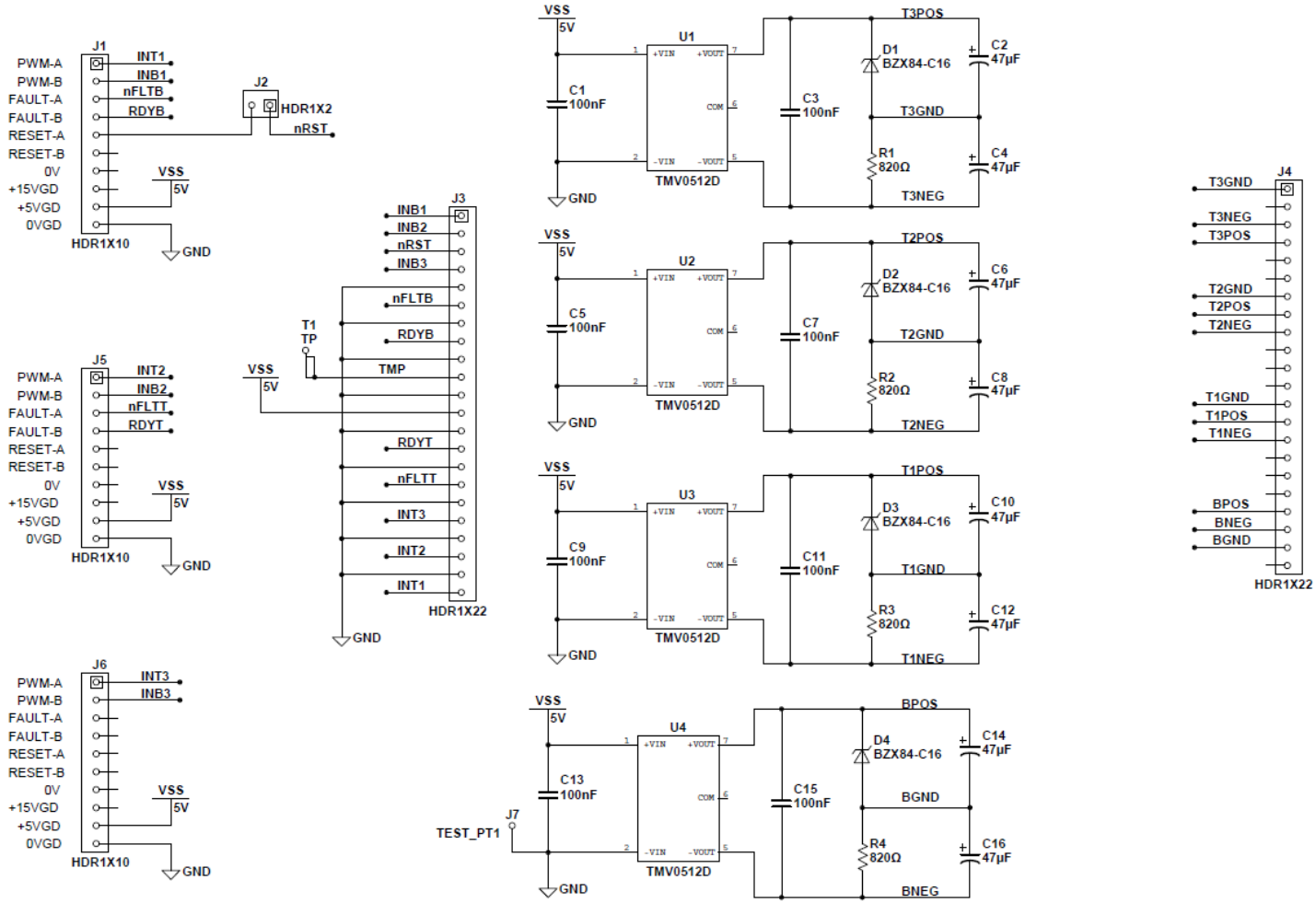

Figure E.37 Gate Drive Board Interface

F. Analytical Solution for Fault response

F.1. Analytical solution for a zero voltage fault

F.1.1. Generalised equations

Consider a non-salient DFIG with a small, uniform air-gap. The governing machine equations in space vector form are reproduced here, where all parameters have been referred to the stator reference frame. The equation (F.1) and (F.2) reveals the model analysis needed.

$$\begin{cases} \overrightarrow{u_s^s} = R_s\overrightarrow{\imath_s^s} + \dfrac{d\overrightarrow{\varphi_s^s}}{dt} & (a) \\ \overrightarrow{u_r^s} = R_s\overrightarrow{\imath_r^s} + \dfrac{d\overrightarrow{\varphi_r^s}}{dt} - j\omega_r\overrightarrow{\varphi_r^s} & (b) \end{cases} \qquad (F.1)$$

$$\begin{cases} \overrightarrow{\varphi_s^s} = L_s\overrightarrow{\imath_s^s} + L_m\overrightarrow{\imath_r^s} & (a) \\ \overrightarrow{\varphi_s^s} = L_m\overrightarrow{\imath_s^s} + L_r\overrightarrow{\imath_r^s} & (b) \end{cases} \qquad (F.2)$$

Equation (F.2) may be rearranged for stator current, using the leakage parameter, σ, as follows:

$$\sigma = 1 - \frac{L_m^2}{L_s L_r} \qquad (F.3)$$

$$\overrightarrow{\imath_s^s} = \frac{1}{\sigma L_s}\left(\overrightarrow{\varphi_s^s} - \frac{L_m}{L_r}\overrightarrow{\varphi_r^s}\right) \qquad (F.4)$$

Similarly, for rotor current:

$$\overrightarrow{\imath_r^s} = \frac{1}{\sigma L_r}\left(\overrightarrow{\varphi_r^s} - \frac{L_m}{L_s}\overrightarrow{\varphi_s^s}\right) \qquad (F.5)$$

Current equations (F.4, F.5) are substituted into the voltage equations (F.1), using transient time constants:

$$\tau_s = \frac{L'_s}{R_s} = \frac{\sigma L_s}{R_s}, \qquad \tau_r = \frac{L'_r}{R_r} = \frac{\sigma L_r}{R_r} \tag{F.6, F.7}$$

$$\overrightarrow{u_s^s} = \frac{1}{\tau_s}\left(\overrightarrow{\varphi_s^s} - \frac{L_m}{L_r}\overrightarrow{\varphi_r^s}\right) + \frac{d\overrightarrow{\varphi_s^s}}{dt} \tag{F.8}$$

$$\overrightarrow{u_r^s} = \frac{1}{\tau_r}\left(\overrightarrow{\varphi_r^s} - \frac{L_m}{L_s}\overrightarrow{\varphi_s^s}\right) + \frac{d\overrightarrow{\varphi_r^s}}{dt} - j\omega_r\overrightarrow{\varphi_r^s} \tag{F.9}$$

Voltage-flux equations of Eqs. F.8 and F.9 are useful in the proceeding derivations.

F.1.2. Laplace Transform solution for stator flux linkage

A solution to these first order differential equations (F.8, F.9) may be found using the Laplace transform. Now, consider the general Laplace transform and the Laplace transform of a time differential [90]:

$$F(v) = \int_{-\infty}^{+\infty} f(t)e^{-vt}dt = \Gamma\{f(t)\} \tag{F.10}$$

$$\Gamma\left\{\frac{df(t)}{dt}\right\} = vF(v) - f(0) \tag{F.11}$$

Note that the Laplace variable is chosen to be ‘v’ instead of the more common‘s’ to avoid confusion with induction machine slip. The linearity of the Laplace transform allows its application on complex numbers. The transformed parameters are defined with relevant capitalization (e.g. Eqs. F.12, F.13) and the initial conditions are defined with a zero in the subscript (e.g. Eqs. F.14, F.15).

$$\Gamma\{\vec{\varphi}(t)\} = \vec{\Psi}(v), \quad \Gamma\{\vec{u}(t)\} = \vec{U}(v) \tag{F.12, F.13}$$

$$\overrightarrow{\varphi_s^s}(\mathrm{t} = 0) = \overrightarrow{\varphi_{s0}^s}, \quad \overrightarrow{\varphi_r^s}(t = 0) = \overrightarrow{\varphi_{r0}^s} \tag{F.14, F.15}$$

Fault conditions are defined here as an instantaneous stator voltage drop to zero volts occurring at time zero. Given the relative mechanical and electromagnetic time constants, rotor speed changes will occur far slower than magnetic flux changes. Rotor speed is assumed roughly constant over the grid fault interval.

Taking zero stator voltage and using constant rotor speed, the Laplace transforms of Eqs. (F.8, F.9):

$$0 = \frac{1}{\tau_s}\left(\overrightarrow{\Psi_s^s} - \frac{L_m}{L_r}\overrightarrow{\Psi_r^s}\right) + \left(v\overrightarrow{\Psi_s^s} - \overrightarrow{\varphi_{s0}^s}\right) \qquad (F.16)$$

$$\overrightarrow{U_r^s}(v) = \frac{1}{\tau_r}\left(\overrightarrow{\Psi_r^s} - \frac{L_m}{L_s}\overrightarrow{\Psi_s^s}\right) + \left(v\overrightarrow{\Psi_r^s} - \overrightarrow{\varphi_{r0}^s}\right) - j\omega_r\overrightarrow{\Psi_r^s} \qquad (F.17)$$

Rearranging for stator flux in terms of the initial conditions and rotor voltage:

$$\frac{L_m}{\tau_s L_r}\left(\overrightarrow{U_r^s}(v) + \overrightarrow{\varphi_{r0}^s}\right) + \left(\frac{1}{\tau_r} - j\omega_r + v\right)\overrightarrow{\varphi_{s0}^s} = \left[\left(\frac{1}{\tau_r} - j\omega_r + v\right)\left(\frac{1}{\tau_s} + v\right) - \frac{(1-\sigma)}{\tau_s\tau_r}\right]\overrightarrow{\Psi_s^s}\,(v) \qquad (F.18)$$

$$\overrightarrow{\Psi_s^s}\,(v) = \frac{\left(\frac{1}{\tau_r} - j\omega_r + v\right)\overrightarrow{\varphi_{s0}^s} + \frac{L_m}{\tau_s L_r}\overrightarrow{\varphi_{r0}^s}}{\left[\left(\frac{1}{\tau_r} - j\omega_r + v\right)\left(\frac{1}{\tau_s} + v\right) - \frac{(1-\sigma)}{\tau_s\tau_r}\right]} + \frac{\frac{L_m}{\tau_s L_r}\overrightarrow{U_r^s}(v)}{\left[\left(\frac{1}{\tau_r} - j\omega_r + v\right)\left(\frac{1}{\tau_s} + v\right) - \frac{(1-\sigma)}{\tau_s\tau_r}\right]} \qquad (F.19)$$

This form can be simplified, defining certain numeric and complex constants (Eqs. F.20, F.21, F.22 and F.23):

$$\rho_s = \frac{1}{\tau_s}, \qquad \rho_r = \frac{1}{\tau_r} - j\omega_r, \qquad k_\sigma = \frac{(1-\sigma)}{\tau_s\tau_r}, \qquad k_r = \frac{L_m}{L_r} \qquad (F.20, F.21, F.22, F.23)$$

$$\overrightarrow{\Psi_s^s} = \frac{(\rho_r + v)\overrightarrow{\varphi_{s0}^s} + \left(k_r/\tau_s\right)\overrightarrow{\varphi_{r0}^s}}{[(\rho_r + v)(\rho_s + v) - k_\sigma]} \quad \ldots\ldots\ldots\ldots\ldots\ldots\ldots\ldots \textit{Natural Response}$$

$$+ \frac{\left(k_r/\tau_s\right)\overrightarrow{U_r^s}(v)}{[(\rho_r + v)(\rho_s + v) - k_\sigma]} \quad \ldots\ldots\ldots\ldots\ldots\ldots\ldots \textit{Forced Response} \qquad (F.24)$$

Eq. F.24 describes the stator flux linkage – consisting of a natural response (term containing the initial conditions) and a forced response (term containing the rotor voltage). The natural response contains the whole solution in a singly-fed machine or with a doubly-fed machine where the rotor circuit has been short-circuited.

F.1.3. Natural response solution for stator flux linkage

Inverse Laplace transform

Eq. F.24 showed the stator flux to comprise of a natural and forced response. By linear superposition, the real-time solution for stator flux linkage is the sum of the solutions for each independent response:

$$\overrightarrow{\varphi_s^s}(\mathrm{t}) = \Gamma^{-1}\left\{\overrightarrow{\Psi_s^s}\,(v)\right\}$$

$$= \Gamma^{-1}\left\{\frac{(\rho_r + v)\overrightarrow{\varphi_{s0}^s} + ({}^{k_r}/_{\tau_s})\overrightarrow{\varphi_{r0}^s}}{[(\rho_r + v)(\rho_s + v) - k_\sigma]}\right\} + \Gamma^{-1}\left\{\frac{({}^{k_r}/_{\tau_s})\overrightarrow{U_r^s}(v)}{[(\rho_r + v)(\rho_s + v) - k_\sigma]}\right\} \qquad (F.25)$$

Looking at the natural response alone, we see a first order numerator and a second order denominator. This form suggests a two-part exponential solution as shown by the following inverse-Laplace transform, where α, β, A, B may be complex:

$$\Gamma^{-1}\left\{\frac{k_1 v + k_2}{[(\alpha + v)(\beta + v)]}\right\} = \Gamma^{-1}\left\{\frac{A}{(\alpha + v)} + \frac{B}{(\beta + v)}\right\} = Ae^{-\alpha t} + Be^{-\beta t} \qquad (F.26)$$

Natural response roots

Equating Eq. F.26 with the natural response term from Eq.F. 25:

$$\frac{k_1 v + k_2}{[(\alpha + v)(\beta + v)]} = \frac{(\rho_r + v)\overrightarrow{\varphi_{s0}^s} + ({}^{k_r}/_{\tau_s})\overrightarrow{\varphi_{r0}^s}}{[(\rho_r + v)(\rho_s + v) - k_\sigma]} \qquad (F.27)$$

The denominators of Eq.(F.27) can be solved to find the roots α, β:

$$(\alpha + v)(\beta + v) = (\rho_r + v)(\rho_s + v) - k_\sigma \qquad (F.28)$$

$$0 = \alpha^2 - (\rho_r + \rho_s)\alpha + (\rho_r\rho_s - k_\sigma) \qquad (F.29)$$

$$\alpha = \frac{(\rho_r + \rho_s)}{2} \pm \frac{1}{2}(\rho_r - \rho_s)\sqrt{1 + \frac{4k_\sigma}{(\rho_r - \rho_s)^2}} \qquad (F.30)$$

Induction machine transient time constants are no smaller than tens of milliseconds, which equates to roughly 10 p.u. or more on this p.u. base ($1\,\text{p.u. of time} = (100 * \pi)^{-1}\text{seconds such that } \omega_e = 1\,\text{p.u.}$). As such we can make the general assumption:

$$\frac{1}{\tau_{s,r}{}^2} \ll \omega_r \approx 1 \qquad (F.31)$$

and hence:

$$|\rho_r - \rho_s| = \left|(\frac{1}{\tau_r} - \frac{1}{\tau_s}) - j\omega_r\right| \approx \omega_r \gg k_\sigma \qquad (F.32)$$

Therefore, using a Taylor Series expansion for the square root term:

$$\sqrt{(1+x)} = 1 + {}^1\!/_2\,(x) + \{f(x^{k>1}) \to 0\} \qquad (F.33)$$

$$\sqrt{1 + \frac{4k_\sigma}{(\rho_r - \rho_s)^2}} \approx 1 + \frac{2k_\sigma}{(\rho_r - \rho_s)^2} \qquad (F.34)$$

$$\alpha = \rho_s - \frac{k_\sigma}{(\rho_r - \rho_s)} \quad \beta = \rho_r + \frac{k_\sigma}{(\rho_r - \rho_s)} \qquad (F.35, F.36)$$

Complex frequency adjustment

We can define the complex frequency adjustment in terms of its real and imaginary parts:

$$\varsigma_f = \frac{k_\sigma}{(\rho_r - \rho_s)} = \kappa + j\delta \qquad (F.37)$$

where κ and δ are both real and small; κ vanishingly so if the two time constants are very close. Note also that the imaginary part δ is always positive. An expansion in terms of the transient time constants is given in Eq. F.40.

$$\varsigma_f = \frac{k_\sigma}{|\rho_r - \rho_s|}\angle -(\rho_r - \rho_s) = \frac{\frac{1-\sigma}{\tau_s\tau_r}}{\left|\left(\frac{1}{\tau_r} - \frac{1}{\tau_s}\right) - j\omega_r\right|}\angle \tan^{-1}\left\{\frac{\omega_r}{\frac{1}{\tau_r} - \frac{1}{\tau_s}}\right\} \qquad (F.38)$$

The frequency adjustment parameter helps to rewrite the roots of the stator flux linkage solution (from Eqs.F.35, F.36):

$$\alpha = \tau_s^{-1} - \varsigma_f \qquad \beta = \tau_r^{-1} - j\omega_r + \varsigma_f \qquad (F.39, F.40)$$

$$\alpha = (\tau_s^{-1} - \kappa) - j\delta \qquad \beta = (\tau_r^{-1} + \kappa) - j(\omega_r - \delta) \qquad (F.41, F.42)$$

The effective transient time constants take into account the fractional adjustment caused by the complex frequency adjustment term:

$$\tau_s'^{-1} = (\tau_s^{-1} - \kappa) \qquad \tau_r'^{-1} = (\tau_r^{-1} + \kappa) \qquad (F.43, F.44)$$

The effective decay frequencies (described in the main text as ‘near-dc’ and ‘near-rotor speed’) are closer in value as a result, remembering that δ is always positive:

$$f_{own\_circuit} = \delta \qquad f_{mutual} = (\omega_r - \delta) \qquad (F.45, F.46)$$

We can approximate the complex frequency adjustment in the case where the transient timescales for stator and rotor are similar. Here the adjustment parameter ς_f is almost purely imaginary. Using the approximation from Eq. F.32:

$$\varsigma_f = \frac{(1-\sigma)/\tau_s\tau_r}{\omega_r} \angle \left(90 - \tan^{-1} \left\{ \frac{\frac{1}{\tau_r} - \frac{1}{\tau_s}}{\omega_r} \right\} \right) \qquad (F.47)$$

$$\tau_s \approx \tau_r \gg 1 \qquad \therefore \frac{\frac{1}{\tau_r} - \frac{1}{\tau_s}}{\omega_r} \ll 1, \qquad (F.48)$$

$$\varsigma_f \approx \frac{(1-\sigma)}{{\omega_r}^2\tau_s\tau_r} \left(\left\{ \frac{\frac{1}{\tau_r} - \frac{1}{\tau_s}}{\omega_r} \right\} + j \right) \qquad (F.49)$$

Therefore, estimating the real and imaginary frequency-adjustment parameters:

$$\kappa \approx \frac{(1-\sigma)}{{\omega_r}^2\tau_s\tau_r} \left(\frac{1}{\tau_r} - \frac{1}{\tau_s} \right) \qquad \delta \approx \frac{(1-\sigma)}{\omega_r\tau_s\tau_r} \qquad (F.50, F.51)$$

The real part,κ, is of the order of τ_r^{-3} and therefore has negligible impact. Using the imaginary frequency adjustment from Eq. F.51 therefore, denominator roots approximate to:

$$\alpha \approx \tau_s^{-1} - j\frac{(1-\sigma)}{\omega_r\tau_s\tau_r}, \qquad \beta \approx \tau_r^{-1} - j\omega_r \left(1 - \frac{(1-\sigma)}{{\omega_r}^2\tau_s\tau_r} \right) \qquad (F.52, F.53)$$

Form of the solution

Substituting the denominator roots (Eqs. F.41, F.42) into the trial solution (Eq. F.26), we see these roots determining the characteristic time-evolution of the natural response of stator flux decay:

$$\overrightarrow{\varphi_s^s}(t) = Ae^{-\frac{t}{\tau_s'^{-1}}} e^{j\delta t} \quad \ldots\ldots\ldots\ldots\ldots\ldots\ldots\ldots\ldots\ldots Near - DC$$

$$+Be^{-t/\tau_r'^{-1}} e^{j(\omega_r - \delta)t} \quad \ldots\ldots\ldots\ldots\ldots\ldots Near - rotor\ speed \qquad (F.54)$$

In physical terms, we see two components of decaying stator flux. Firstly, unsupported flux decays from its pre-fault value on the stator circuit at near-dc frequency over the stator transient timescale. Secondly, unsupported flux decays on the rotor circuit at near-dc frequency over the rotor transient timescale. This rotor flux linkage decay induces a decaying emf on the stator circuit, acting to oppose the rotor flux decay. The emf appears from the stator windings to possess near-rotor-speed. This produces a near-rotor-frequency contribution to the stator flux, which decays over the rotor leakage timescale. This painfully verbose text is better illustrated by inspection of Eq. F.54.

The twin components make sense intuitively as the rotor windings “cut” the stator flux at rotor speed, and vice versa. If we first accept that each circuit in its own frame will see a dc collapse of unsupported flux (as would an isolated stationary inductive coil), the mutual coupling of rotor and stator will necessitate an induced ac component reflecting the other circuit’s dc decay.

The ac component is at near-rotor speed (electrical radians/s, accounting for the number of poles). Now, without the supply voltage neither the 50Hz excitation-frame nor machine-slip holds any physical meaning with respect to the short-circuited machine.

The complex frequency adjustment hints at an interaction between the fluxes linked by either set of windings. As explained in the section on torque generation, the tendency of two concentric magnetic dipoles is to align: the rotor flux’s rotation will be slowed by the stator field and the stator field accelerated by the passing rotor field. If time constants were near-infinite, implying minimal energy loss, eventually both sets of fluxes would align and rotate at a common velocity somewhere between zero and rotor speed.

$$f_{own\_circuit} > 0 \qquad f_{mutual} < \omega_r \qquad (F.55, F.56)$$

The magnitude of this dragging effect depends upon the relative speed of the two fields – i.e. the rotor speed. With high rotor speed the fields barely interact, whereas this alignment-force-drag will be more pronounced at lower speeds. This is evident in the inverse relation between the frequency adjustment parameter and rotor speed (Eq. F.51).

The effect on the effective flux-decay time constants is to increase the difference between them. Put mathematically:

$$|\tau_r' - \tau_s'| > |\tau_r - \tau_s| \qquad (F.57)$$

However, the percentage difference is of the order of $\delta \times (\tau_r^{-1} - \tau_s^{-1})$, well below 0.5% for a practical machine and as a result bearing little impact.

Stator flux solution

The coefficients of the trial solution (Eq. F.54) may be obtained from a partial fraction expansion of Eq. F.27:

$$\overrightarrow{\Psi_s^s}_{\,natural} = \frac{(\rho_r + v)\overrightarrow{\varphi_{s0}^s} + \left(k_r/\tau_s\right)\overrightarrow{\varphi_{r0}^s}}{[(\rho_r + v)(\rho_s + v) - k_\sigma]} = \frac{A}{(\alpha + v)} + \frac{B}{(\beta + v)} \qquad (F.58)$$

A convenient redefinition of constant A helps the trial solution as follows:

$$\frac{A}{(\alpha + v)} + \frac{B}{(\beta + v)} = \frac{\overrightarrow{\varphi_{s0}^s} + A_s^s}{(\alpha + v)} + \frac{B}{(\beta + v)} \qquad (F.59)$$

$$\left(\overrightarrow{\varphi_{s0}^s} + A_s^s\right)(\beta + v) + B(\alpha + v) = (\rho_r + v)\overrightarrow{\varphi_{s0}^s} + \left(k_r/\tau_s\right)\overrightarrow{\varphi_{r0}^s} \qquad (F.60)$$

Equating the first order terms in v:

$$\beta = -A_s^s \qquad (F.61)$$

Equating the zero order terms in v:

$$A_s^s = \frac{(\rho_r - \beta)\overrightarrow{\varphi_{s0}^s} + \left(k_r/\tau_s\right)\overrightarrow{\varphi_{r0}^s}}{(\beta - \alpha)} \qquad (F.62)$$

Using the frequency adjustment parameters with the root definitions (Eqs. F.41, F.42):

$$A_s^s = \frac{(\delta + j\kappa)\overrightarrow{\varphi_{s0}^s} + j\left(k_r/\tau_s\right)\overrightarrow{\varphi_{r0}^s}}{(\omega_r - 2\delta) + j(\tau_r'^{-1} - \tau_s'^{-1})} \qquad (F.63)$$

Note the addition of the superscript to the coefficient; the coefficient depends on initial conditions of flux linkage as measured in the stator reference frame. Initial conditions in their own reference frame must be transformed by the initial rotor frame angle at the instant of short-circuit, for example:

$$A_s^s = \frac{(\delta + j\kappa)\overrightarrow{\varphi_{s0}^s} + j\left(k_r/\tau_s\right)\left(\overrightarrow{\varphi_{r0}^r}e^{+j\theta_{r0}}\right)}{(\omega_r - 2\delta) + j(\tau_r'^{-1} - \tau_s'^{-1})} \qquad (F.64)$$

As previously discussed, the reciprocals of the transient machine timescales are far smaller than rotor speed. Using the approximation from Eq. F.32 therefore:

$$A_s^s \approx j\frac{k_r\overrightarrow{\varphi_{r0}^s}}{\omega_r\tau_s} \qquad (F.65)$$

The full expansion produces a description of the natural response of the stator flux linkage, with certain derived parameters repeated below for clarity:

$$\overrightarrow{\varphi_s^s}(t) = \left(\overrightarrow{\varphi_{s0}^s} + A_s^s\right) e^{-\frac{t}{\tau_s'^{-1}}} e^{j\delta t} \quad \ldots\ldots\ldots\ldots\ldots\ldots\ldots Near - DC$$

$$-A_s^s e^{-\frac{t}{\tau_r'^{-1}}} e^{j(\omega_r - \delta)t} \quad \ldots\ldots\ldots\ldots\ldots\ldots Near - rotor\ speed \qquad (F.66)$$

As a sanity check, the above solution (F.66) satisfies the initial conditions:

$$\overrightarrow{\varphi_s^s}(t=0) = \overrightarrow{\varphi_{s0}^s}$$

F.1.4. Stator current natural response

The stator circuit equation (Eq. F. 1) with zero stator voltage:

$$0 = R_s \overrightarrow{\imath_s^s} + \frac{d\overrightarrow{\varphi_s^s}}{dt} \qquad (F.67)$$

Using (F.67) and differentiating the stator flux derivation (F.66) therefore:

$$\overrightarrow{\imath^s}(t) = \frac{\left(\overrightarrow{\varphi_{s0}^s} + A_s^s\right)\alpha}{R_s} e^{-\alpha t} - \frac{A_s^s \beta}{R_s} e^{-\beta t} \qquad (F.68)$$

$$\overrightarrow{\imath_s^s}(t) = \frac{\left(\overrightarrow{\varphi_{s0}^s} + A_s^s\right)(\tau_s'^{-1} - j\delta)}{R_s} e^{-t/\tau_s'^{-1}} e^{j\delta t} - \frac{A_s^s\left(\tau_r'^{-1} - j(\omega_r - \delta)\right)}{R_s} e^{-\frac{t}{\tau_r'^{-1}}} e^{j(\omega_r - \delta)t} (F.69)$$

This shows the stator current to display the same frequency components as the stator flux linkage although with different coefficients. Neglecting the small frequency adjustment parameters and terms of the order τ^{-2}:

$$\delta \approx \frac{(1-\sigma)}{\omega_r \tau_s \tau_r} \approx \tau^{-2}{}_{\mathrm{x}} \approx 0 \qquad (F.70)$$

and noting the transient operational inductance $\tau_s = \frac{L_s'}{R_s}$, $\tau_r = \frac{L_r'}{R_r}$:. The stator current approximates to a simpler form relating chiefly to the effective transient inductance:

$$\overrightarrow{i_s^s}(t) \approx \frac{1}{L_s'}\overrightarrow{\varphi_{s0}^s} e^{-\frac{t}{\tau_s'^{-1}}} e^{j\delta t} - \frac{k_r}{L_s'} e^{-\frac{t}{\tau_r'^{-1}}} e^{j(\omega_r-\delta)t} \qquad (F.71)$$

or, equally:

$$\overrightarrow{i_s^s}(t) \approx \frac{1}{L_s'}\overrightarrow{\varphi_{s0}^s} e^{-\frac{t}{\tau_s'^{-1}}} e^{j\delta t} - \frac{k_s}{L_r'} e^{-\frac{t}{\tau_r'^{-1}}} e^{j(\omega_r-\delta)t} \qquad (F.72)$$

Where $k_s = \frac{L_m}{L_s}$.

Initial conditions

One can check the derivation Eq. F.69 against the initial conditions, using the earlier definitions of A_s, α and β:

$$\overrightarrow{i^s}(t=0) = \frac{\left(\overrightarrow{\varphi_{s0}^s} + A_s^s\right)\alpha}{R_s} - \frac{A_s^s \beta}{R_s} \qquad (F.73)$$

$$\overrightarrow{i_s^s}(t=0) = \frac{\overrightarrow{\varphi_{s0}^s}\alpha}{R_s} + \frac{1}{R_s}\left(\overrightarrow{k_f \varphi_{s0}^s} - \frac{k_r}{\tau_s}\overrightarrow{\varphi_{r0}^r}\right) \qquad (F.74)$$

$$\overrightarrow{i_s^s}(t=0) = \frac{1}{\sigma L_s}\left(\overrightarrow{\varphi_{s0}^s} + \frac{L_m}{L_r}\overrightarrow{\varphi_{r0}^r}\right) \qquad (F.75)$$

The validity of Eq. F.75 is evident from the flux linkage definitions (Eqs. F.2) and the leakage constant definition (Eq. F.3).

F.1.5. Rotor flux linkage natural response

Similarly to the solution for stator flux linkage, Eqs. F.16 & F.17 can be solved for rotor flux linkage.

$$k_s = \frac{L_m}{L_s} \tag{F.76}$$

$$\overrightarrow{\Psi_r^s} = \frac{(\rho_s + v)\overrightarrow{\varphi_{r0}^s} + ({}^{k_r}/_{\tau_s})\overrightarrow{\varphi_{s0}^s}}{[(\rho_r + v)(\rho_s + v) - k_\sigma]} + \frac{(\rho_s + v)\overrightarrow{U_r^s}(v)}{[(\rho_r + v)(\rho_s + v) - k_\sigma]} \tag{F.77}$$

which has the same form as Eq. F.24. Using a partial fraction expansion as before:

$$\overrightarrow{\Psi_r^s}_{\,natural} = \frac{(\rho_s + v)\overrightarrow{\varphi_{r0}^s} + ({}^{k_r}/_{\tau_s})\overrightarrow{\varphi_{s0}^s}}{(\alpha + v)(\beta + v)} = \frac{A_r^s}{(\alpha + v)} + \frac{\overrightarrow{\varphi_{r0}^s} + B_r^s}{(\beta + v)} \tag{F.78}$$

Equating the first order terms in v:

$$B_r^s = -A_r^s \tag{F.79}$$

Equating the zero order terms in v:

$$A_r^s = \frac{(\rho_s - \alpha)\overrightarrow{\varphi_{r0}^s} + \left({}^{k_r}/_{\tau_s}\right)\overrightarrow{\varphi_{s0}^s}}{(\beta - \alpha)} \tag{F.80}$$

Using the frequency adjustment parameters (Eqs. F.37) with the root definitions (Eqs. F.41, F.42):

$$A_r^s = \frac{-(\delta + j\kappa)\overrightarrow{\varphi_{r0}^s} + j\left({}^{k_r}/_{\tau_s}\right)\overrightarrow{\varphi_{s0}^s}}{(\omega_r - 2\delta) + j(\tau_r'^{-1} - \tau_s'^{-1})} \tag{F.81}$$

As previously discussed, the reciprocals of the transient machine time constants are far smaller than rotor speed. Using the approximation, therefore:

$$A_r^s \approx j\frac{k_s\overrightarrow{\varphi_{s0}^s}}{\omega_r\tau_r} \tag{F.82}$$

The natural response (or zero rotor voltage response) of rotor flux linkage in the stator reference frame becomes:

$$\overrightarrow{\varphi_r^s}(t) = A_r^s e^{-t/\tau_s'^{-1}} e^{j\delta t} + \left(\overrightarrow{\varphi_{r0}^s} - A_r^s\right) e^{-t/\tau_r'^{-1}} e^{j(\omega_r - \delta)t} \qquad (F.83)$$

Transforming into the rotor reference frame:

$$\overrightarrow{\varphi_r^r} = \overrightarrow{\varphi_r^s} e^{-j(\omega_r t - \theta_{r0})} \qquad (F.84)$$

Hence:

$$A_r^r = \frac{-(\delta + j\kappa)\overrightarrow{\varphi_{r0}^r} + j\left(k_r/\tau_s\right)\overrightarrow{\varphi_{s0}^r}}{(\omega_r - 2\delta) + j(\tau_r'^{-1} - \tau_s'^{-1})} \qquad (F.85)$$

and finally:

$$\overrightarrow{\varphi_r^r}(t) = A_r^r e^{-t/\tau_s'^{-1}} e^{-j(\omega_r - \delta)t} + \left(\overrightarrow{\varphi_{r0}^r} - A_r^r\right) e^{-t/\tau_r'^{-1}} e^{-j\delta t} \qquad (F.86)$$

Or, redefining roots α, β for the rotor reference frame:

$$\alpha^r = \tau_s'^{-1} + j(\omega_r - \delta), \qquad \beta^r = \tau_r'^{-1} - j\omega_r + \varsigma_f = (\tau_r^{-1} + \kappa) + j\delta \qquad (F.87, F.88)$$

Hence the natural response of the rotor flux in the rotor reference frame approximates to:

$$\overrightarrow{\varphi_r^r}(t) = A_r^r e^{-\alpha^r t} + \left(\overrightarrow{\varphi_{r0}^r} - A_r^r\right) e^{-\beta^r t} \qquad (F.89)$$

F.1.6. Rotor current natural response

Using the rotor voltage equation in the rotor reference frame (Eq. F.90) and the rotor flux derivation (Eq. F.89), the natural response (or zero rotor voltage response) of the rotor current can then be derived:

$$0 = R_r \vec{\imath_r^r} + \frac{d\overrightarrow{\varphi_r^r}}{dt} \qquad (F.90)$$

$$\vec{\imath_r^r}(t) = \frac{\beta^r}{R_r}\left(\overrightarrow{\varphi_{r0}^r} - A_r^r\right) e^{-\frac{t}{\tau_r'^{-1}}} e^{-j\delta t} \ldots\ldots\ldots\ldots\ldots Near - DC$$

$$-\frac{\alpha^r}{R_r} A_r^r e^{-\frac{t}{\tau_s'^{-1}}} e^{-j(\omega_r - \delta)t} \ldots\ldots\ldots\ldots Near - rotor\ speed \qquad (F.91)$$

This shows that the rotor current frequency components will exhibit the same time dependence as the stator current, although the directions of rotation are reversed with respect to the stator. Explicitly, this involves a near-dc (negative) frequency component decaying with the rotor leakage time-constant and a near-rotor-frequency (negative) component decaying with the stator leakage time-constant.

Neglecting the frequency adjustment parameter and terms of the order τ^{-2} as for the stator: $\delta \approx \frac{(1-\sigma)}{\omega_r \tau_s \tau_r} \approx \tau^{-2}{}_{\mathrm{x}} \approx 0$. And noting the transient operational inductance: $\tau_s = \frac{L_s{}'}{R_s}$, $\tau_r = \frac{L_r{}'}{R_r}$. The rotor current therefore approximates to a simpler form:

$$\vec{\imath_r^r}(t) \approx \frac{1}{L_r{}'} \overrightarrow{\varphi_{r0}^r} e^{-\frac{t}{\tau_r'^{-1}}} e^{-j\delta t} - \frac{k_s}{L_r{}'} e^{-\frac{t}{\tau_s'^{-1}}} e^{-j(\omega_r - \delta)t} \qquad (F.92)$$

F.1.7. Torque during a short circuit

As well-known, torque can be derived by considering the stator and rotor fields as two magnetic dipoles. The result is proportional to the vector cross product determinant, i.e. the sine of the angle between the current vectors. The p.u torque is equal to the torque per pole-pair:

$$T = L_m \overline{\imath_r} \wedge \overline{\imath_s} \qquad (F.93)$$

The full derivation of torque as a function of initial flux linkages is lengthy. A reasonable estimate can be made by using the approximate expressions for rotor and

stator current from Eqs. F. 72 & F.92. Converting the rotor current approximation into the stator reference frame and noting that the cross product of a vector with itself is zero:

$$\overline{\imath_r} \wedge \overline{\imath_s} = \left[\frac{\overline{\varphi_{r0}^s}}{L_r'} e^{-t/\tau_r'} e^{j(\omega_r-\delta)t} - \frac{L_m \overline{\varphi_{s0}^s}}{L_r L_s'} e^{-t/\tau_r'} e^{j\delta t}\right] \wedge \left[\frac{\overline{\varphi_{s0}^s}}{L_r'} e^{-t/\tau_r'} e^{j\delta t} - \frac{L_m \overline{\varphi_{r0}^s}}{L_s L_r'} e^{-t/\tau_r'} e^{j(\omega_r-\delta)t}\right] \quad (F.94)$$

$$\overline{\imath_r} \wedge \overline{\imath_s} = \left[\frac{L_m}{L_s L_r'} e^{-t/\tau_r'}\right]\left(\overline{\varphi_{r0}^s} \wedge \overline{\varphi_{r0}^s}\right) + \left[\frac{L_m}{L_r L_s'} e^{-t/\tau_r'}\right]\left(\overline{\varphi_{s0}^s} \wedge \overline{\varphi_{s0}^s}\right) + \cdots\cdots + \left[\frac{1}{L_s' L_r'} e^{-\left(1/\tau_r'+1/\tau_s'\right)t}\right]\left[1 - \frac{L_m^2}{L_s L_r}\right]\left(\overline{\varphi_{r0}^s} e^{j(\omega_r-\delta)t} \wedge \overline{\varphi_{s0}^s} e^{j\delta t}\right) \quad (F.95)$$

$$\overline{\imath_r} \wedge \overline{\imath_s} = \left[\frac{\sigma}{L_s' L_r'} e^{-\left(1/\tau_r'+1/\tau_s'\right)t}\right]\left(\overline{\varphi_{r0}^s} e^{j(\omega_r-2\delta)t} \wedge \overline{\varphi_{s0}^s}\right) \quad (F.96)$$

and finally:

$$T = \left[\frac{L_m}{\sigma L_s L_r} |\overline{\varphi_{r0}}||\overline{\varphi_{s0}}| e^{-t/\tau_T'}\right] \sin\left(-(\omega_r - 2\delta)t - \theta_{\varphi 0}\right) \quad (F.97)$$

$$T = \left[\frac{-L_m}{\sigma L_s L_r} |\overline{\varphi_{r0}}||\overline{\varphi_{s0}}| e^{-t/\tau_T'}\right] \sin\left((\omega_r - 2\delta)t + \theta_{\varphi 0}\right) \quad (F.98)$$

where we have defined the initial phase separation of the rotor and stator flux linkages and a torque transient timescale. The initial flux separation angle is:

$$\theta_{\varphi 0} = \theta\left(\overline{\varphi_{r0}^g}\right) - \theta\left(\overline{\varphi_{s0}^g}\right) \quad (F.99)$$

The torque transient timescale is a parallel combination of the stator and rotor timescales indicating a very fast decay of torque:

$$1/\tau_T' = (1/\tau_r' + 1/\tau_s') \quad (F.100)$$

Leakage parameter approximation

The leakage inductance values are significantly smaller than the mutual inductance for all practical machines. As such we can approximate the value of the leakage parameter, utilising a unit-less variable for the leakage inductance:

$$L_s = (1 + \chi_s)L_m \qquad (F.101)$$

$$L_r = (1 + \chi_r)L_m \qquad (F.102)$$

$$\chi_s, \chi_r \ll 1 \qquad (F.103)$$

Returning to the leakage parameter definition: $\sigma = 1 - \frac{L_m^2}{L_s L_r}$

$$\sigma = 1 - (1 + \chi_s)^{-1}\ (1 + \chi_r)^{-1} \qquad (F.104)$$

Using a Taylor series expansion:

$$\sigma \approx 1 - (1 - \chi_s - \chi_r) \qquad (F.105)$$

$$\sigma \approx \chi_s + \chi_r = \frac{L_{es} + L_{er}}{L_m} \qquad (F.106)$$

Torque approximation

As introduced above, an approximation for the torque expression using the leakage parameter approximation showed from Eq. F.106 and estimated the pre-fault flux magnitude product at 1.1 p.u. This approximation is reproduced in Eq. F.107.

$$T \approx \left[\frac{-1.1}{L_{es} + L_{er}} e^{-t/\tau'_T}\right] \sin\left((\omega_r - 2\delta)t + \theta_{\varphi 0}\right) \qquad (F.107)$$

F.2. Forced response – non-zero rotor voltage

Here the doubly-fed induction machine is fed with a slip-speed rotating voltage to maintain stable operation in the steady-state. In the excitation reference frame, the rotor voltage vector will appear constant. A Laplace transform solution can be derived, similar to the natural response above, this time starting in the excitation reference frame:

$$\overrightarrow{u_s^e} = R_s\overrightarrow{i_s^e} + \frac{d\overrightarrow{\varphi_s^e}}{dt} + j\omega_e\overrightarrow{\varphi_s^e} \qquad (F.108)$$

$$\overrightarrow{u_r^e} = R_r\overrightarrow{i_r^e} + \frac{d\overrightarrow{\varphi_r^e}}{dt} - j\omega_\chi\overrightarrow{\varphi_r^e} \qquad (F.109)$$

Eq. F.109 includes the excitation-frame relative rotor speed, ω_χ (the exact negative of slip-speed). The sign of ω_χ is chosen such that the value is normally positive for a generator.

$$\omega_\chi = \omega_r - \omega_e \qquad (F.110)$$

Substituting for current using the inductance definitions F.2 and using the transient time constant definitions:

$$\overrightarrow{u_s^e} = \frac{1}{\tau_s}\left(\overrightarrow{\varphi_s^e} - \frac{L_m}{L_r}\overrightarrow{\varphi_r^e}\right) + \frac{d\overrightarrow{\varphi_s^e}}{dt} + j\omega_e\overrightarrow{\varphi_s^e} \qquad (F.111)$$

$$\overrightarrow{u_r^e} = \frac{1}{\tau_r}\left(\overrightarrow{\varphi_r^e} - \frac{L_m}{L_s}\overrightarrow{\varphi_s^e}\right) + \frac{d\overrightarrow{\varphi_r^e}}{dt} - j\omega_\chi\overrightarrow{\varphi_r^e} \qquad (F.112)$$

Now, setting the excitation-frame rotor voltage to be constant, and taking Laplace transforms of Eqs. F.8 & F.9:

$$\Gamma\left\{\overrightarrow{u_r^e} = const.\right\} = \frac{\overrightarrow{u_r^e}}{\nu} \qquad (F.113)$$

$$0 = \frac{1}{\tau_s}\left(\overline{\Psi_s^e} - \frac{L_m}{L_r}\overline{\Psi_r^e}\right) + \left(\nu\overline{\Psi_s^e} - \overline{\varphi_{s0}^e}\right) + j\omega_e\overline{\Psi_s^e} \qquad (F.114)$$

$$\frac{\overrightarrow{u_r^e}}{\nu} = \frac{1}{\tau_r}\left(\overline{\Psi_r^e} - \frac{L_m}{L_s}\overline{\Psi_r^e}\right) + \left(\nu\overline{\Psi_r^e} - \overline{\varphi_{r0}^e}\right) - j\omega_\chi\overline{\Psi_r^e} \qquad (F.115)$$

F.2.1. Stator circuit solution

Take the Laplace equations F.114 & F.115 and rearrange for stator flux:

$$\overline{\Psi_s^e}(\nu) = \frac{\left(\frac{1}{\tau_r} - j\omega_\chi + \nu\right)\overline{\varphi_{s0}^e} + \frac{L_m}{L_r\tau_s}\left(\overline{\varphi_{r0}^e} + \frac{\overrightarrow{u_r^e}}{\nu}\right)}{\left[\left(\frac{1}{\tau_s} + j\omega_e + \nu\right)\left(\frac{1}{\tau_r} - j\omega_\chi + \nu\right) - \frac{(1-\sigma)}{\tau_s\tau_r}\right]} \qquad (F.116)$$

This form can be simplified, using certain constants as introduced in Section F.1.2 and defining the complex roots in the excitation frame:

$$\rho_s^e = \frac{1}{\tau_s} + j\omega_e, \quad \rho_r^e = \frac{1}{\tau_r} - j\omega_\chi \qquad (F.117, F.118)$$

$$k_r' = \frac{L_m}{L_r\tau_s} \qquad (F.119)$$

$$\overline{\Psi_s^e}(\nu) = \frac{(\rho_r^e + \nu)\overline{\varphi_{s0}^e} + k_r'\left(\overline{\varphi_{r0}^e} + \frac{\overrightarrow{u_r^e}}{\nu}\right)}{[(\rho_s^e + \nu)(\rho_r^e + \nu) - k_\sigma]} \qquad (F.120)$$

The denominator of Eq. F.120 lends itself to the ‘natural response roots’ and ‘complex frequency adjustment’ of Section F.1.3. The roots are here in the excitation-frame, rotated by $\omega_e t$ radians with respect to the stator-frame roots of Section F.1.3. The complex frequency adjustment has exactly the same form.

$$(\rho_s^e + \nu)(\rho_r^e + \nu) - k_\sigma = (\alpha^e + \nu)(\beta^e + \nu) \qquad (F.121)$$

where:

$$\alpha^e = ({\tau_s}^{-1} - \kappa) + j(\omega_e - \delta), \qquad \beta^e = ({\tau_r}^{-1} + \kappa) - j\left(\omega_\chi - \delta\right) \qquad (F.122, F.123)$$

and

$$\varsigma_f = \frac{(1-\sigma)/\tau_s\tau_r}{(1/\tau_r - 1/\tau_s - j\omega_r)} = \kappa + j\delta, \qquad (\kappa, \delta) \in Re \qquad (F.124)$$

Hence:

$$\overline{\Psi_s^e}(\nu) = \frac{(\rho_r^e + \nu)\overline{\varphi_{s0}^e}\nu + k_r'\left(\overline{\varphi_{r0}^e}\nu + \overrightarrow{u_r^e}\right)}{(\alpha^e + \nu)(\beta^e + \nu)\nu} \qquad (F.125)$$

Eq.F.125 can be solved by partial fractions:

$$\overline{\Psi_s^e}(\nu) = \frac{{A_1}^e}{(\alpha^e + \nu)} + \frac{{B_1}^e}{(\beta^e + \nu)} + \frac{{C_1}^e}{\nu} \qquad (F.126)$$

resulting in:

$${A_1}^e = \left(1 - \frac{\varsigma_f}{(\beta^e - \alpha^e)}\right)\overline{\varphi_{s0}^e} + \frac{k_r'}{(\beta^e - \alpha^e)}\left(\overline{\varphi_{r0}^e} - \frac{\overrightarrow{u_r^e}}{\alpha^e}\right) \qquad (F.127)$$

$${B_1}^e = \frac{\varsigma_f}{(\beta^e - \alpha^e)}\overline{\varphi_{s0}^e} - \frac{k_r'}{(\beta^e - \alpha^e)}\left(\overline{\varphi_{r0}^e} - \frac{\overrightarrow{u_r^e}}{\beta^e}\right) \qquad (F.128)$$

$${C_1}^e = \frac{k_r'}{\alpha^e\beta^e}\overrightarrow{u_r^e} \qquad (F.129)$$

The coefficients of Eqs. F.127 – F.129 provide the coefficients of the stator flux linkage solution:

$$\overline{\varphi_s^e}(t) = {A_1}^e e^{-\alpha^e t} + {B_1}^e e^{-\beta^e t} + \frac{k_r'}{\alpha^e\beta^e}\overrightarrow{u_r^e} \qquad (F.130)$$

In the stator reference frame, this becomes:

$$\overline{\varphi_s^s}(t) = {A_1}^s e^{-\alpha t} + {B_1}^s e^{-\beta t} + \frac{k_r'}{\alpha^e \beta^e}\overrightarrow{u_r^e} e^{+j(\omega_e t + \theta_{e0})} \qquad (F.131)$$

with,

$${A_1}^s = \left(1 - \frac{\varsigma_f}{(\beta^e - \alpha^e)}\right)\overline{\varphi_{s0}^s} + \frac{k_r'}{(\beta^e - \alpha^e)}\left(\overline{\varphi_{r0}^s} - \frac{\overrightarrow{u_r^e} e^{+j\theta_{e0}}}{\alpha^e}\right) \qquad (F.132)$$

$${B_1}^s = \frac{\varsigma_f}{(\beta^e - \alpha^e)}\overline{\varphi_{s0}^s} - \frac{k_r'}{(\beta^e - \alpha^e)}\left(\overline{\varphi_{r0}^s} - \frac{\overrightarrow{u_r^e} e^{+j\theta_{e0}}}{\beta^e}\right) \qquad (F.133)$$

or, more explicitly:

$$\overline{\varphi_s^s}(t) = {A_1}^s e^{-t/\tau_s'} e^{+j\delta t} + {B_1}^s e^{-t/\tau_s'} e^{+j(\omega_r - \delta)t} + \frac{L_m}{L_r \tau_s \alpha^e \beta^e}\overrightarrow{u_r^s} \qquad (F.134)$$

with:

$$\overrightarrow{u_r^s} = \overrightarrow{u_r^e} e^{+j(\omega_e t + \theta_{e0})} \qquad (F.135)$$

The expression for stator flux linkage therefore contains two decay components (at near-dc and near-rotor speed) and a continuous term driven by the rotor excitation. The two decay components have the same roots and are similar in magnitude to those of the natural response solution. Using the stator voltage equation, we can derive the stator current:

$$\overline{i_s^s} = \frac{-1}{R_s}\frac{d\overline{\varphi_s^s}}{dt} \qquad (F.136)$$

$$\overline{i_s^s}(t) = \frac{\alpha {A_1}^s}{R_s} e^{-t/\tau_s'} e^{+j\delta t} + \frac{\beta {B_1}^s}{R_s} e^{-t/\tau_s'} e^{+j(\omega_r - \delta)t} - \frac{j\omega_e L_m}{L_r \tau_s \alpha^e \beta^e}\overrightarrow{u_r^s} \qquad (F.137)$$

Making approximations as per Section F.1.4, neglecting terms of the order τ^{-2} and approximating the product of the natural response roots (Eq. F. 138) we can produce a simpler form of the stator current solution (Eq. F.143).

$$\alpha^e \beta^e \approx j\omega_e \beta^e \qquad (F.138)$$

$$A_1{}^s \approx \overline{\varphi_{s0}^s} \qquad (F.139)$$

$$\dots \frac{\alpha A_1{}^s}{R_s} \approx \frac{\overline{\varphi_{s0}^s}}{\tau_s' R_s} = \frac{\overline{\varphi_{s0}^s}}{\sigma L_s} \qquad (F.140)$$

$$B_1{}^s \approx \frac{-jk_r}{\tau_s \omega_r}\left(\overline{\varphi_{r0}^s} - \frac{\overrightarrow{u_r^e} e^{+j\theta_{e0}}}{\beta^e}\right) \qquad (F.141)$$

$$\dots \frac{\beta B_1{}^s}{R_s} \approx \frac{-j\omega_r(-jk_r)}{R_s \tau_s \omega_r}\left(\overline{\varphi_{r0}^s} - \frac{\overrightarrow{u_r^e} e^{+j\theta_{e0}}}{\beta^e}\right) = \frac{-k_r}{\sigma L_s}\left(\overline{\varphi_{r0}^s} - \frac{\overrightarrow{u_r^e} e^{+j\theta_{e0}}}{\beta^e}\right) \qquad (F.142)$$

Hence:

$$\overline{i_s^s}(t) \approx \frac{1}{\sigma L_s}\left(\overline{\varphi_{s0}^s} e^{-t/\tau_s'} e^{+j\delta t} - \frac{L_m}{L_r}\left(\overline{\varphi_{r0}^s} - \frac{\overrightarrow{u_r^e} e^{+j\theta_{e0}}}{\beta^e}\right) e^{-t/\tau_s'} e^{+j(\omega_r - \delta)t} - \frac{L_m}{L_r}\frac{\overrightarrow{u_r^s}}{\beta^e}\right) \qquad (F.143)$$

F.2.2. Rotor circuit solution

In the same manner as above, we take Laplace transforms of voltage equations in the excitation frame (F.111 & F.112) with constant rotor voltage. The resulting Laplace equations (Eqs. F.114 & F.115) are rearranged for rotor flux linkage, using the following derived parameters:

$$\rho_s^e = \frac{1}{\tau_s} + j\omega_e, \quad \rho_r^e = \frac{1}{\tau_r} - j\omega_\chi \qquad (> F.117, F.118)$$

$$k_s' = \frac{L_m}{L_s \tau_r} \qquad (F.144)$$

$$\overline{\Psi_r^e}(\nu) = \frac{(\rho_s^e + \nu)\left(\overline{\varphi_{r0}^e} + \frac{\overrightarrow{u_r^e}}{\nu}\right) + k_s' \overline{\varphi_{s0}^e}}{[(\rho_s^e + \nu)(\rho_r^e + \nu) - k_\sigma]} \qquad (F.145)$$

This rotor flux linkage expression can be solved with partial fractions, using the natural response roots and complex frequency adjustment exactly as shown for the stator circuit (Eqs. F.121 – F.124):

$$\overline{\Psi_r^e}(\nu) = \frac{(\rho_s^e + \nu)\left(\overline{\varphi_{r0}^e}\nu + \overrightarrow{u_r^e}\right) + k_s'\overline{\varphi_{s0}^e}\nu}{(\alpha^e + \nu)(\beta^e + \nu)\nu} \qquad (F.146)$$

$$\overline{\Psi_r^e}(\nu) = \frac{{A_2}^e}{(\alpha^e + \nu)} + \frac{{B_2}^e}{(\beta^e + \nu)} + \frac{{C_2}^e}{\nu} \qquad (F.147)$$

resulting in:

$${A_2}^e = \frac{\varsigma_f}{(\beta^e - \alpha^e)}\left(\overline{\varphi_{r0}^e} - \frac{\overrightarrow{u_r^e}}{\alpha^e}\right) + \frac{k_s'}{(\beta^e - \alpha^e)}\overline{\varphi_{s0}^e} \qquad (F.148)$$

$${B_2}^e = \left(1 - \frac{\varsigma_f}{(\beta^e - \alpha^e)}\right)\left(\overline{\varphi_{r0}^e} - \frac{\overrightarrow{u_r^e}}{\beta^e}\right) - \frac{k_s'}{(\beta^e - \alpha^e)}\overline{\varphi_{s0}^e} \qquad (F.149)$$

$${C_2}^e = \frac{\rho_s^e}{\alpha^e\beta^e}\overrightarrow{u_r^e} \qquad (F.150)$$

The coefficients of Eqs. F. 148 – F.150 provide the coefficients of the rotor flux linkage solution:

$$\overline{\varphi_r^e}(t) = {A_2}^e e^{-\alpha^e t} + {B_2}^e e^{-\beta^e t} + \frac{\rho_s^e}{\alpha^e\beta^e}\overrightarrow{u_r^e} \qquad (F.151)$$

In the rotor reference frame, this becomes:

$$\overline{\varphi_r^r}(t) = {A_2}^r e^{-\alpha^r t} + {B_2}^r e^{-\beta^r t} + \frac{\rho_s^e}{\alpha^e\beta^e}\overrightarrow{u_r^e}e^{-j(\omega_\chi t + \theta_{\chi 0})} \qquad (F.151)$$

Where

$$\alpha^r = \tau_s'^{-1} + j(\omega_r - \delta), \qquad \beta^r = \tau_r'^{-1} - j\omega_r + \varsigma_f = (\tau_r^{-1} + \kappa) + j\delta \qquad (> F.87, F.88)$$

And

$$A_2{}^r = \frac{\varsigma_f}{(\beta^e - \alpha^e)}\left(\overline{\varphi_{r0}^r} - \frac{\overrightarrow{u_r^e}e^{-j\theta_{\chi 0}}}{\alpha^e}\right) + \frac{k_s'}{(\beta^e - \alpha^e)}\overline{\varphi_{s0}^r} \qquad (F.152)$$

$$B_2{}^r = \left(1 - \frac{\varsigma_f}{(\beta^e - \alpha^e)}\right)\left(\overline{\varphi_{r0}^r} - \frac{\overrightarrow{u_r^e}e^{-j\theta_{\chi 0}}}{\beta^e}\right) - \frac{k_s'}{(\beta^e - \alpha^e)}\overline{\varphi_{s0}^r} \qquad (F.153)$$

or explicitly:

$$\overline{\varphi_r^r}(t) = B_2{}^r e^{-t/\tau_s'}e^{-j\delta t} + A_2{}^r e^{-t/\tau_s'}e^{+j(\omega_r - \delta)t} + \frac{(\tau_s^{-1} + j\omega_e)}{\alpha^e\beta^e}\overrightarrow{u_r^r} \qquad (F.154)$$

with:

$$\overrightarrow{u_r^r} = \overrightarrow{u_r^e}e^{-j(\omega_\chi t + \theta_{\chi 0})} \qquad (F.155)$$

The expression for rotor flux linkage, just as for the stator, contains two decay components (at near-dc and near-rotor speed) and a continuous term driven by the rotor excitation. The two decay components have the same roots and are similar in magnitude to those of the natural response solution. Using the rotor voltage equation, we can derive the rotor current:

$$\overline{i_r^r} = \frac{1}{R_r}\left(\overrightarrow{u_r^r} - \frac{d\overline{\varphi_r^r}}{dt}\right) \qquad (F.156)$$

$$\overline{i_r^r}(t) = \frac{\beta^r B_2{}^r}{R_r}e^{-t/\tau_s'}e^{-j\delta t} + \frac{\alpha^r A_2{}^r}{R_r}e^{-t/\tau_s'}e^{-j(\omega_r - \delta)t} - \frac{1}{R_r}\left(1 + \frac{j\omega_\chi\rho_s^e}{\alpha^e\beta^e}\right)\overrightarrow{u_r^r} \qquad (F.157)$$

Making approximations as per Section F.1.4, neglecting terms of the order τ^{-2}, we can produce a simpler form of the rotor current solution (Eq. F.164).

$$A_2{}^r \approx \frac{jk_s}{\tau_r\omega_r}\overline{\varphi_{s0}^r} \qquad (F.160)$$

$$\therefore \frac{\alpha^r A_2{}^r}{R_r} \approx \frac{jk_s}{R_r\tau_r\omega_r}\overline{\varphi_{s0}^r} = \frac{-k_s}{\sigma L_r}\overline{\varphi_{s0}^r} \qquad (F.161)$$

$$B_2{}^r \approx \left(\overline{\varphi_{r0}^r} - \frac{\overrightarrow{u_r^e} e^{-j\theta_{\chi 0}}}{\beta^e}\right) \qquad (F.162)$$

$$\therefore \frac{\beta^r B_2{}^r}{R_r} \approx \frac{1}{R_r \tau_r}\left(\overline{\varphi_{r0}^r} - \frac{\overrightarrow{u_r^e} e^{-j\theta_{\chi 0}}}{\beta^e}\right) = \frac{1}{\sigma L_r}\left(\overline{\varphi_{r0}^r} - \frac{\overrightarrow{u_r^e} e^{-j\theta_{\chi 0}}}{\beta^e}\right) \qquad (F.163)$$

Hence:

$$\overline{i_r^r}(t) \approx \frac{1}{\sigma L_r}\left(\left(\overline{\varphi_{r0}^r} - \frac{\overrightarrow{u_r^e} e^{-j\theta_{\chi 0}}}{\beta^e}\right) e^{-t/\tau_s'} e^{-j\delta t} - \frac{L_m}{s}\overline{\varphi_{s0}^s} e^{-t/\tau_s'} e^{+j(\omega_r - \delta)t} + \frac{\overrightarrow{u_r^r}}{\beta^e}\right) \qquad (F.164)$$